THE DYNAMICS AND PHYSICAL PROCESSES OF THE COMOROS BASIN.

Charine Collins

27th October 2013

A thesis presented for the Degree of

Doctor of Philosophy

Department of Oceanography

University of Cape Town

South Africa

Abstract

The main objective of this thesis was to investigate the circulation in the Comoros Basin using observed and model datasets. These data were used to establish whether or not a Comoros Gyre exists and to investigate the nature of the eddy variability in the basin.

The water masses in the Comoros Basin emulate those found further south in the Mozambique Channel. The presence of AAIW north of Madagascar confirmed that this water mass enters the Comoros Basin from the east while the presence of North Atlantic Deep Water showed that this water mass is capable of spreading northward over the Davie Ridge. The main currents in the Comoros Basin, the westward flowing NEMC and a poleward current along the western boundary, are under the influence of the monsoon winds. The NEMC intensifies during the Southwest monsoon in response to a strong wind jet which develops off the northern tip of Madagascar, whereas the poleward current weakens due to the opposing force imposed by the southwesterlies.

Additionally, the circulation in the basin consist of meso-scale eddies of both polarities. Anti-cyclonic eddies, with lifespans of ~80 days, are generated at the northern tip of Madagascar due to barotropic instabilities associated with the NEMC flowing past Cape Amber. The anti-cyclones have a residence time in the Comoros Basin which spans approximately half of their lifespan. Initially the anti-cyclones, with translation speeds of 6-8km·day^{-1}, follow the trajectory of the NEMC and turn south upon reaching the African coast propagating into the Mozambique Channel. In the Comoros Basin, the anti-cyclonic eddies have a mean effective radius of 80-100km and can attain diameters of 600km when located in the center of the basin.

The primary location of cyclonic eddy generation is along the northwest coast of Madagascar. The majority of these eddies, formed as a result of baroclinic instabilities,

remain in the Comoros Basin over their entire lifetime. The cyclonic eddies have weaker translation speeds (2.5-3.5km·day^{-1}) than their anti-cyclonic counterparts and also tend to be smaller.

Declaration

This thesis is a presentation of my original research work which includes all analyses of the data, creating of the figures, and writing the discussions of the results. Where-ever contributions of others are involved, every effort is made to clearly acknowledge this, with due reference to the literature. Aside from the guidance provided by my supervisors, I have received no assistance, except as acknowledged.

Supervisors

Prof. Chris J. C. Reason

Department of Oceanography, University of Cape Town, South Africa

Dr. Juliet C. Hermes

South African Environmental Observation Network (SAEON), Egagasini node, South Africa

Acknowledgments

Firstly, I would like to thank my supervisors, Chris Reason and Juliet Hermes for the opportunity to pursue this PhD and for their continued support and guidance. I am also grateful to them for always being available and making it possible for me to attend numerous conferences and workshops during the course of my PhD.

I am grateful to Arne Biastoch for granting me access to his model data. I also thank him and Jonathan Durgadoo for their hospitality at the GEOMAR Helmholtz Centre for Ocean Research in Kiel, Germany and for all the assistance they provided during my visit there. I thank Raymond Roman for processing the ADCP data and providing me with the cruise data. I am also grateful for all the valuable discussions we had about the cruise data.

To my friends, thank you for all the animated discussions we shared and for playing an integral part in keeping me motivated and excited about a future in marine science.

Last, but definitely not least I want to thank my family and friends for their support. I am especially grateful to my mom and sisters for believing in me even when I did not and for always being there when needed. Also, a big, big "thank-you" to my mom for almost working just as hard on this thesis as I have.

Contents

List of Figures

List of Tables

Chapter 1

Introduction

The Agulhas Current, the western boundary current of the South Indian Ocean and the strongest such current in the Southern Hemisphere, plays an important role in the global redistribution of mass, heat and freshwater. Traditionally, the Agulhas Current was thought to be an extension of the continuous flow in the Mozambique Channel, historically known as the Mozambique Current. However, recently it was discovered that strong meso-scale activity characterizes the flow through the Mozambique Channel instead of a continuous current there (de Ruijter et al., 2002; Ridderinkhof and de Ruijter, 2003; Schouten et al., 2003; de Ruijter et al., 2005). The meso-scale activity, dominated by anti-cyclonic eddies, transports tropical and subtropical water into the Agulhas Current. Apart from the role eddies play in transporting tropical and subtropical waters into the Agulhas Current, the eddies in the Mozambique Channel are of interest for a number of other reasons ranging from air-sea exchanges to ecosystem interactions.

At the Agulhas Retroflection region, eddies, rings and filaments are shed which transport warm, saline Indian Ocean water into the South Atlantic Ocean (Schouten et al., 2002a; Pen-

ven et al., 2006c; Biastoch et al., 2008b). This leakage of warm, saline water into the Atlantic, plays an important role in the Atlantic meridional overturning circulation (AMOC) which, in turn, forms an important part of the global climate system (Weijer et al., 1999; Biastoch et al., 2008b; Beal et al., 2011). It has been shown that the interaction of the Mozambique Channel eddies with the Agulhas Current, modulates the timing and frequency of Agulhas ring shedding events, thus impacting the AMOC and the climate system (Schouten et al., 2002a).

Furthermore, the environmental conditions of the tropical South Indian Ocean are favorable for atmospheric cyclogenesis with an average of 12 tropical cyclones per year generated during summer and early autumn (November-April; Fink and Speth, 1998). Tropical cyclones have a profound impact on the physical properties of the underlying ocean but are also influenced by these oceanic conditions. Goni et al. (2009) demonstrated that, under favourable atmospheric conditions, high values of ocean heat content contained in meso-scale features, specifically warm core eddies, can lead to a sudden intensification of tropical cyclones passing over them. Therefore, it is possible that Mozambique Channel eddies could result in the intensification of tropical cyclones passing over the channel, despite empirical evidence of this still lacking.

Meso-scale eddies play a key role in biological processes, especially in the oligotrophic open ocean, by means of converting the mechanical energy of the physical system into trophic energy. Furthermore, eddies are also associated with mechanisms of enrichment (e.g. upwelling), concentration (e.g. convergence) and retention of nutrients as well as marine organisms (Bakun, 2006). Numerous studies have demonstrated the link between meso-scale eddies and the distribution of marine organisms (e.g. Falkowski et al., 1991 and Seki et al., 2002). Cyclonic eddies, with a divergent radial flow and upward circulation in the centre (Tew-Kai and Marsac, 2010), are associated with upwelling of deep, nutrient-rich waters

into the euphotic zone (McGillicuddy et al., 1998; Bakun, 2006) which enhances local primary production. The centres of anti-cyclonic eddies, on the other hand, are characterized by warm, chlorophyll-depleted water; however, high turbulence along the isopycnal slope can result in local nutrient enrichment around the outer edge (Falkowski et al., 1991). Studies into the ecosystem response to meso-scale eddies in the Mozambique Channel, revealed that, coincident with theory (and other localities), cyclonic eddies are conducive for phytoplankton enhancement through upwelling (Tew-Kai and Marsac, 2009) and also influence the distribution of top marine predators such as Great Frigatebirds which frequented the frontal zones between anti-cyclonic and cyclonic eddies during foraging while avoiding the centres (Weimerskirch et al., 2004).

The Mozambique Channel as a whole is divided into two basins by the Davie Ridge (~16°S), with the Comoros Basin (9-15°S) located north of the ridge (Figure 1.1). The interaction of Mozambique Channel eddies with the Agulhas Current and the influence they have on the shedding of Agulhas rings and in turn the AMOC, as well as the impact the eddies have on the biological processes in the Mozambique Channel has attracted a lot of research attention in recent years. Further upstream, very few studies have focused on the processes within the Comoros Basin, an area where the majority of purse-seine fishing activities are located (Tew-Kai and Marsac, 2010) and a potentially key source region of variability for the rest of the Mozambique Channel and subsequently the Agulhas Current (Schouten et al., 2002a). It is not known to what extent eddy processes are important in the Comoros Basin.

The contemporary understanding of the circulation in the Comoros Basin is that it consists of a single large anti-cyclonic cell, the Comoros Gyre. The notion of a single large anti-cyclonic cell is mainly based on three historical studies of the Mozambique Channel utilizing temporally and spatially sparse hydrographic data. Harris (1972), Sætre and da Silva (1984)

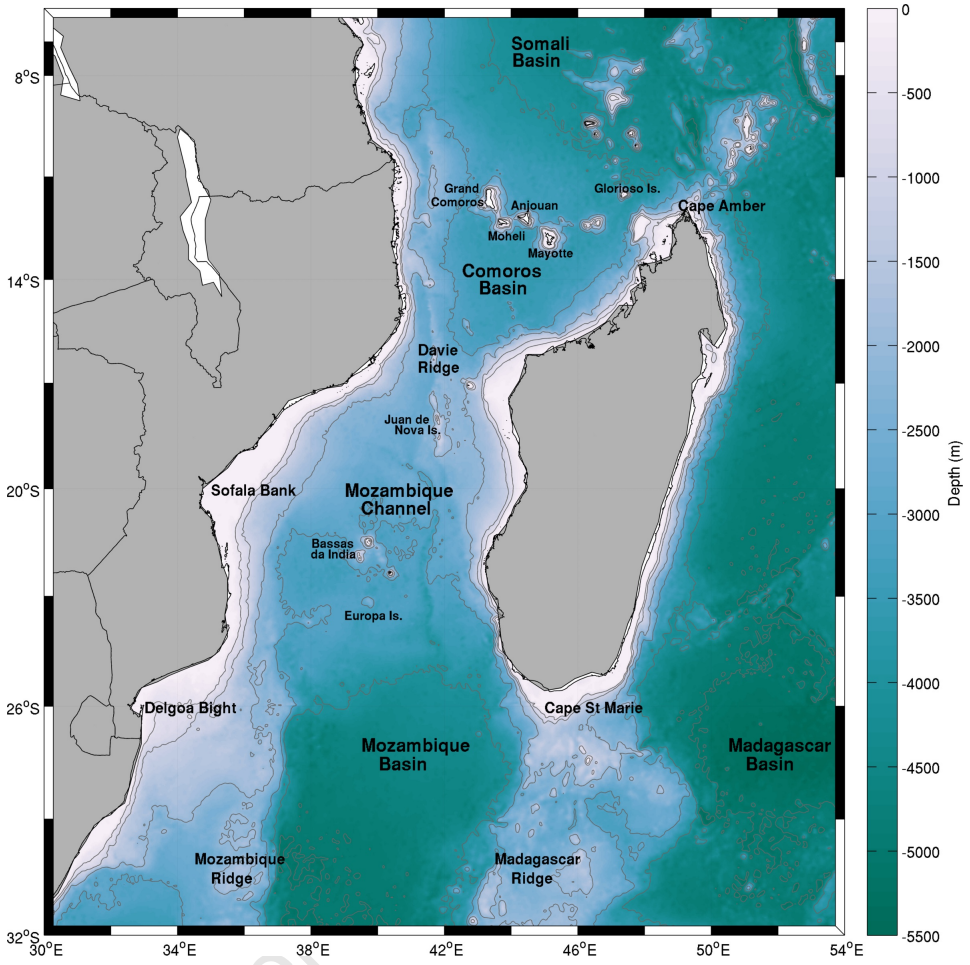

Figure 1.1: *Bathymetry (m) of the Mozambique Channel (Data source: ETOPO2).*

and Donguy and Piton (1991) independently analysed hydrographic data from various research cruises in the Mozambique Channel and from their results inferred that the circulation in the Comoros Basin consists of a single anti-cyclonic cell. Additionally, the latter two studies suggest a seasonality of the circulation in the basin. More recently Biastoch and Krauss (1999) noted an anti-cyclonic loop in the Comoros Basin in their eddy-permitting model configured to simulate the meso-scale eddies in the Mozambique Channel. On the other hand, using a regional model based on HYCOM, Backeberg and Reason (2010) showed that anti-

cyclonic eddies, related to transport pulses in the South Equatorial Current, are generated at the northern tip of Madagascar. Similarly, van der Werf et al. (2010) concluded, from various high-resolution models and observational data, that eddies in the northern Mozambique Channel are generated at the northern tip of Madagascar. However, none of these studies confirmed or denied the notion of the Comoros Gyre.

1.1 Questions

So far there has been no study solely dedicated to the circulation in the Comoros Basin and a detailed description of the dynamics in the basin is still incomplete. Therefore, this study aims to provide a detailed description and analysis of the circulation in the Comoros Basin through a combination of observational and satellite derived data as well as two realistic model configurations for the Greater Agulhas Current System. More specifically this thesis will address the following questions:

- What is the general circulation pattern in the Comoros Basin? Does the circulation in the Comoros Basin consist of a prominent, permanent anti-cyclonic gyre as originally thought or is it comprised of meso-scale eddies as more recent studies suggest? In the case of the latter, are the meso-scale eddies mainly anti-cyclonic or do cyclonic eddies also occur in the Comoros Basin?

- What are the physical properties of the anti-cyclonic gyre, if it exists, or the meso-scale eddies in the Comoros Basin? In the case of the latter, what is the fate of the meso-scale eddies in the Comoros Basin?

- What is the wind forcing over the Comoros Basin and how is it resolved by different wind products?

1.2 Outline of the Dissertation

The western Indian Ocean is a region of complex dynamics and strong variability on a range of scales that impact substantially on the climates of eastern and southern Africa yet it is a region of sparse observational data. The recent increased interest in the Mozambique Channel has led to increased direct observations in the region particularly in the form of a long-term mooring array (LOCO) at the narrowest part of the channel (~16°S; Ridderinkhof and de Ruijter, 2003; Harlander et al., 2009; Ridderinkhof et al., 2010) and a number of cruises undertaken south of 15°S (di Marco et al., 2002; Donohue and Toole, 2003). A region in the Mozambique Channel that is especially lacking in observations is the Comoros Basin (Figure 1.1). In an attempt to begin to fill the gap in the observational record of the northern Mozambique Channel, a dedicated cruise in the Comoros Basin was conducted in late 2009. This observational data, in conjunction with satellite altimetery data, is presented in Chapter 3. This chapter is preceded by a detailed literature review of the oceanography of the Indian Ocean with an emphasis on the south western Indian Ocean, and more particularly, on the greater Agulhas Current System which includes the Mozambique Channel and the Comoros Basin.

Surface wind stress forms an integral part of all ocean circulation models and thus before attempting a realistic model simulation it is necessary to assess the availability of reliable wind stress data, particularly in complex areas such as the Mozambique Channel where islands and other topographic features may cause meso-scale variability in the surface winds

that are not well resolved by the various wind products available. Thus, in Chapter 4, three different wind products, two reanalyses and one satellite derived product, are analysed over the western Indian Ocean, with a focus on the Comoros Basin. The different wind products are assessed based on their representation of the annual and seasonal cycles of velocity, wind stress curl and Ekman pumping. Since the southwestern Indian Ocean is a region of high tropical cyclone activity, which has a tremendous impact on the underlying oceanic conditions, the wind products are also assessed based on their ability to capture this synoptic scale variability.

The limited temporal and spatial resolution of the observational and satellite data used in Chapter 3 renders it insufficient for a complete, detailed description of the circulation in the Comoros Basin. Therefore, two high resolution model simulations, a Regional Ocean Modelling System (ROMS) simulation and a simulation based on the "Nucleus for European Modelling of the Ocean" (NEMO), are used to further investigate the circulation in the basin. Chapter 5 provides a detailed description of the two numerical models as well as the data sets used to evaluate the models. The evaluation of the two models is presented in Chapter 6. Subsequently, the data from the two models are used in Chapter 7 to obtain a detailed description of the circulation and the physical properties of the meso-scale activity in the Comoros Basin. The results of all the aforementioned chapters are summarised in Chapter 8 along with suggestions for future studies.

Chapter 2

Literature Review

2.1 Indian Ocean Overview

The Indian Ocean, the third largest of the major ocean basins, has a unique geographical setting (Rao and Ram, 2005). Unlike the Pacific and Atlantic Oceans, the Indian Ocean is land locked in the north due to the Asian continent extending from the northern tropics to the high latitudes (Palmer, 2005) and as a result it has no connection with the Arctic Ocean (Figure 2.1). As a result, the Indian Ocean differs from the Atlantic and Pacific Oceans in that the circulation patterns north of the equator do not mirror those south of the equator. The presence of the Asian continent results in a strong meridional land-sea contrast leading to a seasonal reversal of the winds, known as the monsoon. This monsoon system is the strongest on Earth (Schott et al., 2009) and generates large seasonal variations in ocean circulation (see section 2.1.1.1 for a detailed description of the monsoonal winds and section 2.1.3 for the associated ocean circulation). The seasonal changes in the monsoonal winds force the wind-driven circulation of the North Indian Ocean, whereas in the South Indian Ocean the

conventional anti-cyclonic, wind-driven circulation persists throughout the year (Lutjeharms, 2006b). In addition, heat exchange of the Indian Ocean to the north is constrained by the presence of the Asian continent and thus ventilation of the thermocline from the north is weak (Schott et al., 2009).

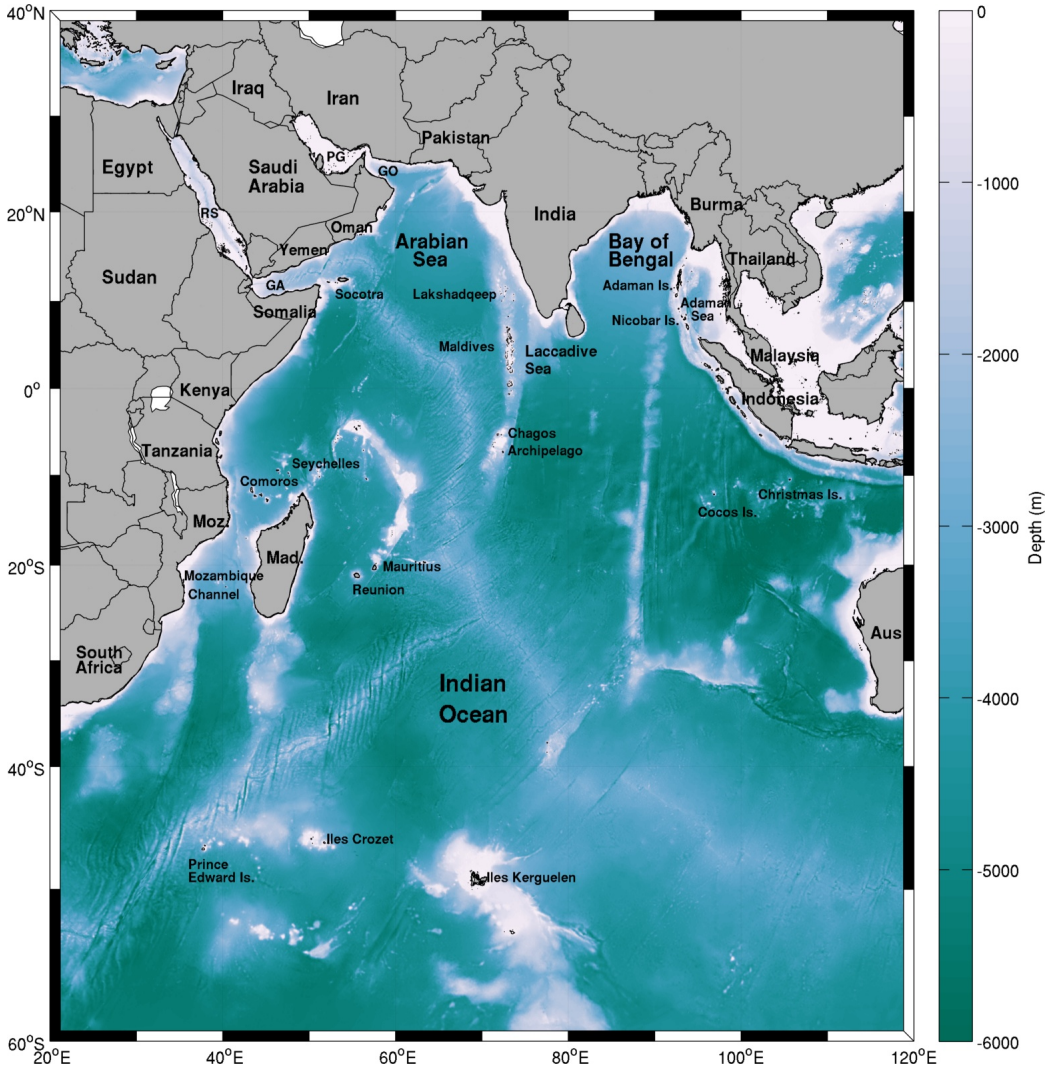

Figure 2.1: *Bathymetry (m) of the Indian Ocean. The abbreviations are as follows: Aus - Australia, Moz - Mozambique, Mad - Madagascar, RS - Red Sea, PG - Persian Gulf, GO - Gulf of Oman, GA - Gulf of Aden (Data source: ETOPO2).*

The Indian Ocean covers an area of $48 \times 10^6 km^2$ excluding the Southern Ocean, the inclusion of which increases the area to $74.1 \times 10^6 km^2$. Its north-south extent, from the inner Bay of Bengal to Antarctica, is 9600km and its east-west extent, from southern Africa to western Australia, is 7800km (Tomczak and Godfrey, 2003) resulting in a volume of ~$18.7 \times 10^6 km^3$. The hydrographic properties of Indian Ocean water masses are influenced by three Mediterranean seas: the Persian Gulf, the Red Sea, and the Australasian Mediterranean Sea consisting of a number of deep basins (Tomczak and Godfrey, 2003). In the east, the Indian Ocean is connected to the Pacific Ocean via the Indonesian Throughflow, and in the south west it has a connection with the South Atlantic Ocean in the form of rings and filaments shed from the Agulhas Current (Lutjeharms and van Ballegooyen, 1988; Gordon, 1985). The Antarctic Circumpolar Current in the south, consisting of a number of fronts, connects all three ocean basins and transports deep and intermediate water between the three ocean basins (Tomczak and Godfrey, 2003).

The Indian Ocean is divided into three parts of about the same size by two roughly meridional ridge systems, the Central Indian Ridge and the Ninety East Ridge (Figure 2.1). The former is a northward extension of the interoceanic ridge system that consistently rises above 4000m, however numerous fractures and depressions allow for the passage of water through the ridge (Tomczak and Godfrey, 2003). The nearly north-south orientated Ninety East Ridge is narrower and less fractured than the Central Indian Ridge with occasional gaps in the 3000m contour north of 10°S. This ridge system consistently reaches the 3000m level south of 10°S and rises above 1500m south of 30°S where it merges with the Southeast Indian Ridge, an extension of the Central Indian Ridge (Tomczak and Godfrey, 2003). Single basins of large meridional extent dominate the central and eastern parts of the Indian Ocean, whereas the western part is divided into a series of smaller deep basins by secondary ridges and the

island of Madagascar (Tomczak and Godfrey, 2003). The presence of Madagascar is another unique Indian Ocean feature, modifying its western boundary in the Southern Hemisphere with implications for the ocean circulation (Fieux and Reverdin, 2001).

2.1.1 Forcing Mechanisms

The primary forces generating ocean currents are the wind exerting a stress on the sea surface and buoyancy fluxes between the atmosphere and ocean which alters the density of the surface water. The former induces what is referred to as wind driven ocean circulation and the latter thermohaline circulation. The wind driven circulation, confined for the most part in the upper kilometer, is the more energetic of the two. The thermohaline circulation, associated with the overturning circulation, is linked to the formation and spreading of the major water masses of the global ocean, such as North Atlantic Deep Water and Antarctic Bottom Water.

2.1.1.1 Winds

Surface winds play a significant role in the energy exchange that occurs at the air-sea interface as they determine sea surface roughness and also generate ocean waves. Surface winds are also an important forcing mechanism for upper ocean circulation (Rao and Ram, 2005).

The South Indian Ocean, south of 10°S, is dominated by the Southeast Trade winds that persist year round (Figure 2.2). During the austral winter, these winds attain their maximum speed and most northerly extent (Schott et al., 2009). On the other hand, the wind patterns north of 10°S are determined by the monsoon circulation which is a major feature of the tropical atmosphere (Figure 2.2). The monsoon mostly affects the North Indian Ocean but its effects extend to ~10°S (Annamalai and Murtugudde, 2004). However, in the Mozambique

Channel the monsoon influence is visible as far south as 15°S (Woodberry et al., 1989).

Monsoonal climates occur where a tropical continent lies poleward of an equatorial ocean (Clift and Plumb, 2008). A seasonal reversal in the direction of the winds is considered to be the distinguishing feature of the monsoonal regions of the world (Cadet, 1979; Gadgil, 2003) which extends over large parts of the tropics (25°S-35°N, 30°W-170°E; Ramage, 1971) including a large part of the Indian Ocean. The climate of the North Indian Ocean is dominated by the monsoon but significant variability in the subtropical and midlatitude South Indian Ocean can also, in part, be attributed to the monsoons (Schott and McCreary, 2001). The two primary mechanisms that drive the monsoon are: differential (land-ocean) sensible heating and tropospheric latent heating (Clemens et al., 1991).

Three climatic situations are observed in regions affected by the monsoon, the Northeast monsoon, Southwest monsoon and the inter-monsoon. The Northeast monsoon (Indian winter monsoon), occurring from December to March, is characterized by a north-south pressure gradient of ~6hPa, between Arabia and Madagascar (Tomczak and Godfrey, 2003). The prevailing winds during this period are northeasterlies over the North Indian Ocean (Figure 2.2a and 2.3; Woodberry et al., 1989) which, upon crossing the equator change to northwesterlies that converge with the southeast trade winds of the South Indian Ocean at ~10°S (Hastenrath and Greischar, 1991). The rising branch of the Indian Ocean Walker circulation is anchored over the maritime continent and as a consequence the Indian Ocean lacks steady equatorial easterlies (Schott et al., 2009).

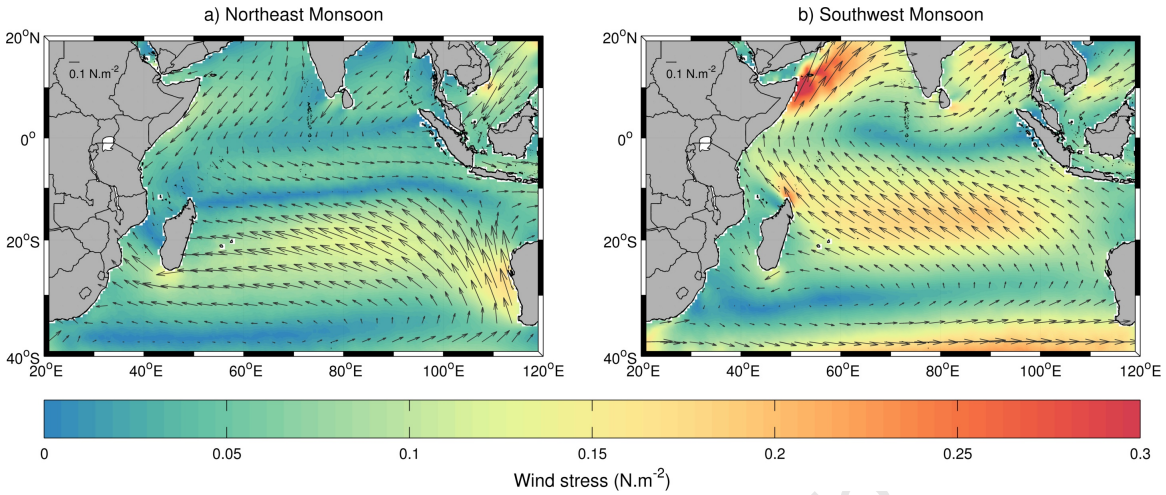

Figure 2.2: *Wind stress ($N{\cdot}m^{-2}$) over the Indian Ocean for the a) Northeast monsoon and b) Southwest monsoon (Data Source: QuikSCAT).*

The Southwest monsoon (Indian summer monsoon), which dominates the annual cycle of the Indian Ocean (Yamagata et al., 2004), is characterized by a 22hPa south-north pressure gradient between June and September (Tomczak and Godfrey, 2003). This results in a complete reversal of the winds over the North Indian Ocean (Rao and Ram, 2005). The stronger southeast trade winds in the Southern Hemisphere extend north to ~5°S and re-curve upon crossing the equator, becoming southwesterlies (Figures 2.2b and 2.3). During this season, a low-level atmospheric jet of intense southwesterlies, known as the Findlater (Findlater, 1971) or Somali Jet is formed along the Somali coast and causes strong upwelling. The inter-monsoon periods occur from April-May and October-November and are characterized by a strong westerly flux that dominates in the equatorial regions (Payet et al., 2004). During the inter-monsoon periods, the winds along the Somali coast weaken which, in turn, decreases the upwelling giving rise to warmer SSTs. This warmer water is transported eastward by

strong equatorial currents known as the Yoshida-Wyrtki jet. This jet is generated by the strong equatorial westerlies (Yamagata et al., 2004).

In addition to the seasonal reversal of surface winds, the monsoon is also characterised by a distinct seasonality of precipitation (Pfeiffer and Dullo, 2006) and drives the annual cycle of sea surface temperatures (SSTs) in the Indian Ocean. During the southwest monsoon the Southern Hemisphere trade winds, forming a continuous air stream extending into south Asia, transport large amounts of water vapour from the Indian Ocean towards the Asian continent resulting in extensive precipitation over land. In the Arabian Sea and western equatorial Indian Ocean, wind-induced evaporation and upwelling associated with the Southwest monsoon results in a large summer cooling (Rao and Sivakumar, 2000; Vinayachandran, 2004). On the other hand, the dry north-easterly winds of the northeast monsoon flow from the cold Asian continent toward the warm, tropical Indian Ocean and maximum precipitation occurs along the Intertropical Convergence Zone (ITCZ) which is located at about 5-10°S (Rao and Ram, 2005).

At times, wind bursts occur during the Northeast monsoon when the atmospheric pressure gets very low in association with the Inter-tropical Convergence Zone (ITCZ). As a result, cyclones may form in the areas of atmospheric depression and instability (Payet et al., 2004). Active tropical cyclone formation in the South Indian Ocean occurs from December to April with a peak in cyclone formation during January and February. Tropical cyclones forming over the Southwest Indian Ocean, ranging from tropical depressions to very intense tropical Cyclones, generally have a westward track towards the east coast of Madagascar and typically recurve towards the south and southeast (Shanko and Camberlin, 1998). While landfall along the east coast of Madagascar is common, only about 5% of tropical cyclones make landfall on the southern African mainland (Reason and Keibel, 2004). These synoptic-scale systems

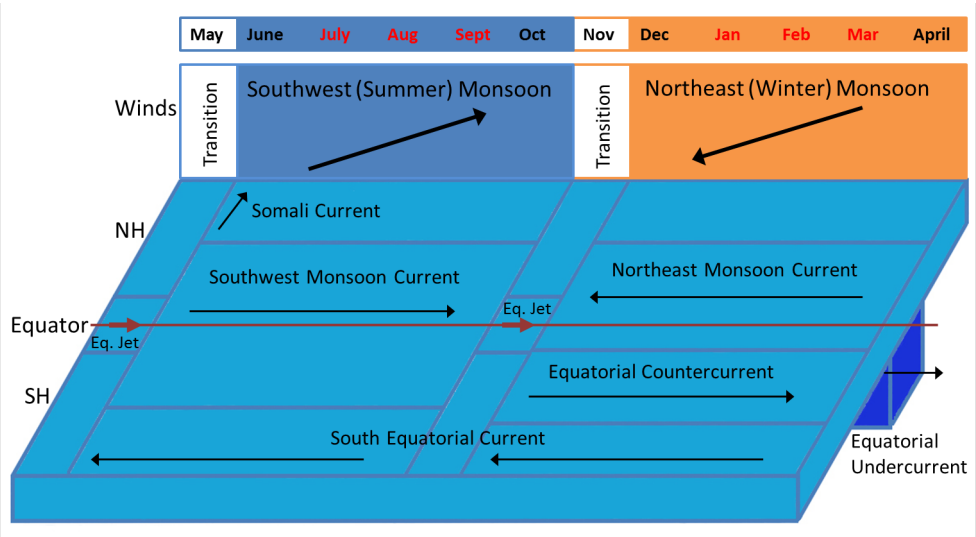

Figure 2.3: *Schematic of the monsoon system of the Indian Ocean. The wind cycle is shown in the top part and the lower part shows the major currents that develop in response to the wind.\ (Adapted from Tomczak and Godfrey (2003)).*

have profound impacts on the underlying ocean such as causing an increase in the mixed layer depth (Dickey et al., 1998), a decrease in SST due to upwelling (Price, 1981), and near-inertial surface currents of 1-2m·s^{-1}, detectable at depths up to ~500m (Withee and Johnson, 1976).

2.1.1.2 Sea Surface Temperature

Sea surface temperature (SST) plays a significant role in the exchange of moisture, heat and gases across the ocean-atmosphere interface since it influences the generation of turbulent eddies in the lower atmosphere. SST also provides an indication of processes and features occurring in the surface layers of the ocean. In particular, SST can provide information on upwelling, eddies, fronts and current boundaries (Rao and Ram, 2005).

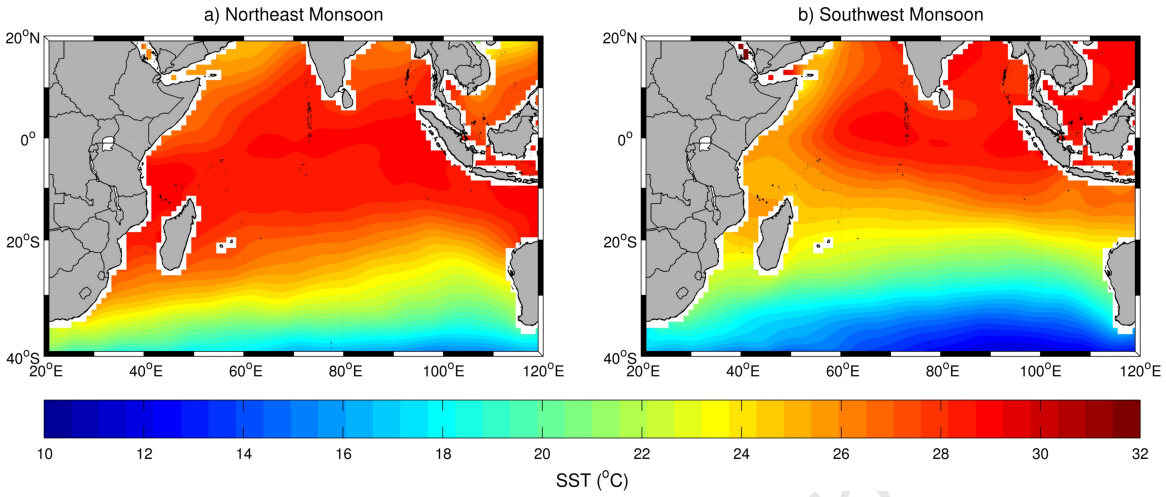

Figure 2.4: *Sea surface temperature (°C) of the Indian Ocean for the a) Northeast monsoon and b) Southwest monsoon (Data source: World Ocean Atlas 2009).*

SST can be influenced by air-sea exchange, and horizontal and vertical ocean advections. These SST anomalies occur at time scales long enough to affect climate. Changes in the upwelling of cool subsurface water can have profound affects on SST. Atmospheric forcing can directly result in changes in upwelling through modification of the winds that drive upwelling. Changes in upwelling can also be forced oceanographically through a change in the temperature of the upwelled water (Schott et al., 2009). Wind-driven upwelling only occurs near the surface (upper 100-200m), thus a modest change in the depth of the thermocline can change the temperature of the upwelled water significantly and subsequently impact SST.

The climatological SST of the tropical Indian Ocean is warm (22-28°C; Figure 2.4) with magnitudes comparable to that of the western Pacific warm pool. However, during the Southwest monsoon, the western sector experiences cooling (Figure 2.4b; Behera et al., 2000). In the North Indian Ocean (north of 10°S), the annual reversal of the monsoon winds cause dra-

matic changes (Behera et al., 2000) and the winds, as well as the associated currents, have a significant influence on the SST (Rao and Ram, 2005). The influence of the monsoon winds on SST in the northern and equatorial Indian Ocean is so dramatic that the seasonal cycle in the SSTs are larger than in any other tropical ocean (Slingo et al., 2005). The strong south-westerlies of the Southwest monsoon cause a cooling of the sea surface through evaporation and entrainment (Behera et al., 2000). This cooling is more pronounced along the Somali coast, where the Somali Jet drives strong coastal upwelling (Slingo et al., 2005). Other key areas of upwelling occur off Sumatra and in the band 5-10°S (Schott et al., 2009).

2.1.1.3 Sea Surface Salinity

Salinity together with temperature are determinants of density and thus play an important role in ocean dynamics. Changes in salinity in the open ocean mainly depend on the difference between precipitation and evaporation. However, sea surface salinity (SSS) values are also affected by advection and mixing processes (Rao and Ram, 2005). In the Indian Ocean, additional factors influencing the salinity are river inflow, the influx of more saline water from the Red Sea and Persian Gulf, and the influx of less saline water from the Indonesian Throughflow (Han and McCreary, 2001).

The precipitation over most of the South Indian Ocean (~10-40°S) is similar to what is observed in other tropical regions where precipitation in the west exceeds the precipitation in the east (Figure 2.5). However, in the northern Indian Ocean the situation is reversed and the annual mean precipitation in the west is much lower than the precipitation received in the east (Figure 2.5; Tomczak and Godfrey, 2003).

In the Indian Ocean, as in the other oceans, SSS (Figure 2.6) closely follows the precipitation-evaporation (P-E) distribution (Figure 2.5). A SSS maximum occurs near 30°S, correspond-

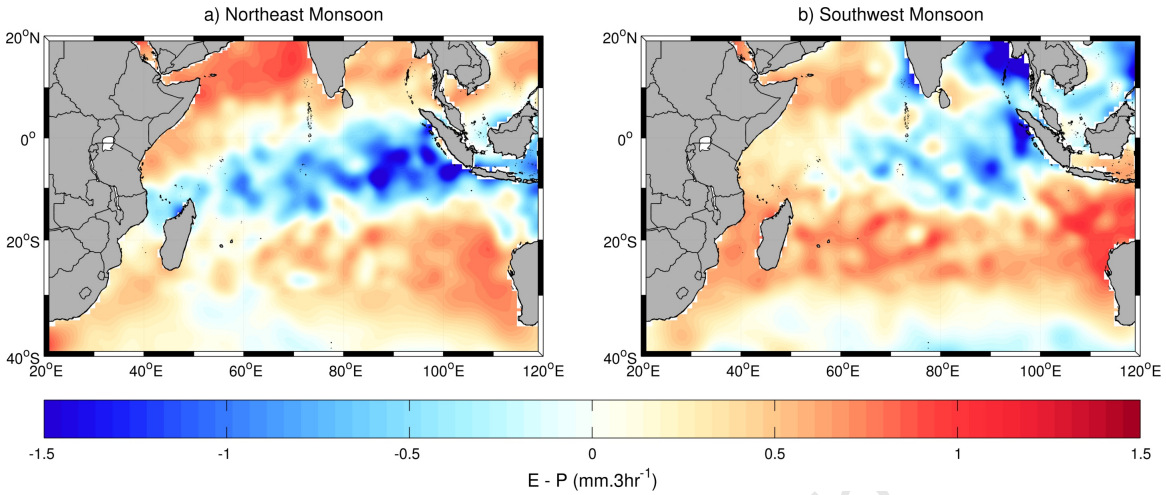

Figure 2.5: *Evaporation - Precipitation (mm·3hr^{-1}) over the Indian Ocean for the a) Northeast monsoon and b) Southwest monsoon (Data source: Comprehensive Ocean-Atmosphere Data Set).*

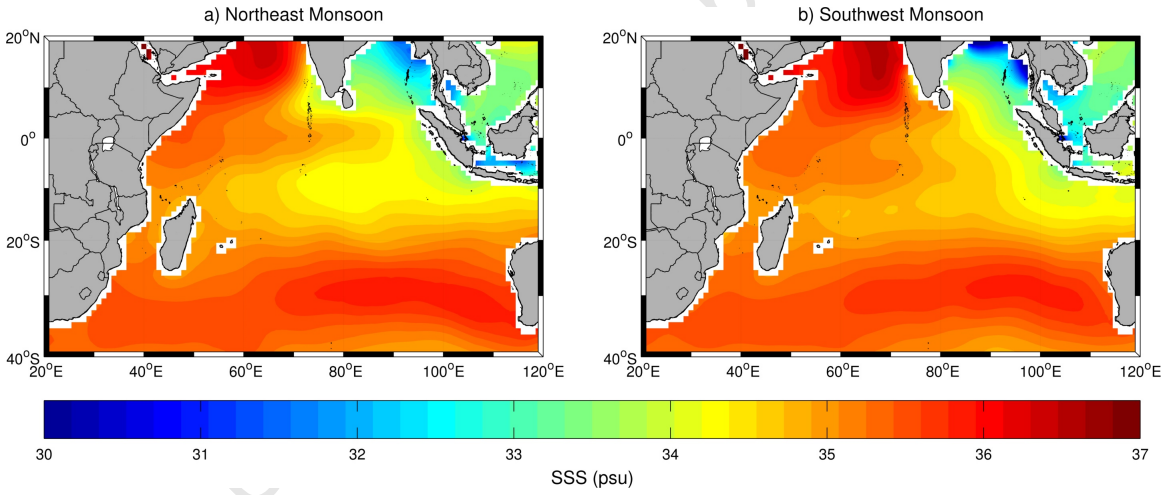

Figure 2.6: *Sea surface salinity (psu) of the Indian Ocean for the a) Northeast monsoon and b) Southwest monsoon (Data source: World Ocean Atlas 2009).*

ing with the P-E minimum. SSS decreases south of 30°S and into the Southern Ocean reflecting the influx of freshwater from the melting of Antarctic sea ice. The eastern tropical Indian Ocean display surface salinities near and below 34.5psu. There is an increase in SSS towards

the coast of Africa as well as north into the Arabian Sea (Figure 2.6). The great excess in evaporation over precipitation experienced by the Red Sea and Persian Gulf results in very saline water (Tomczak and Godfrey, 2003).

2.1.2 Water masses

In the Indian Ocean, three basic kinds of water masses can be distinguished: those entering from the outside, those generated by subduction within the open Indian Ocean, and those generated by mixing of other water masses (Schott and McCreary, 2001). In the northwest Indian Ocean, evaporation exceeds precipitation resulting in high-salinity waters in the Arabian Sea, Red Sea and Persian Gulf (Morales et al., 1996). These water masses are subducted and can be traced as they spread out from their source regions (Quadfasel and Schott, 1982; Swallow et al., 1983). Low-salinity waters from the eastern Indian Ocean are transported into the western Indian Ocean by the South Equatorial Current, whereas low-salinity waters from the Southern Ocean enter the Indian Ocean through subduction at the Subtropical Convergence (Warren et al., 1976; Wyrtki et al., 1971).

A hydrological front, separating the northern and southern water masses, occurs between 5-12°S and designates the differential influence of the subtropical gyre and the monsoon system (Wyrtki, 1973b). In the northern Arabian Sea, Arabian Sea High Salinity Water (ASHSW), characterized by temperatures around 26.8°C and salinity around 36.5psu (Figure 2.7), is formed during the northeast monsoon (Kumar and Prasad, 1999) and spreads underneath the surface-mixed layer as a salinity maximum (Morrison, 1997; Schott and Fischer, 2000). The strong northwestward coastal current along the west coast of India limits the eastern extent of this water mass to the west of 67°E while the equatorial currents inhibit the

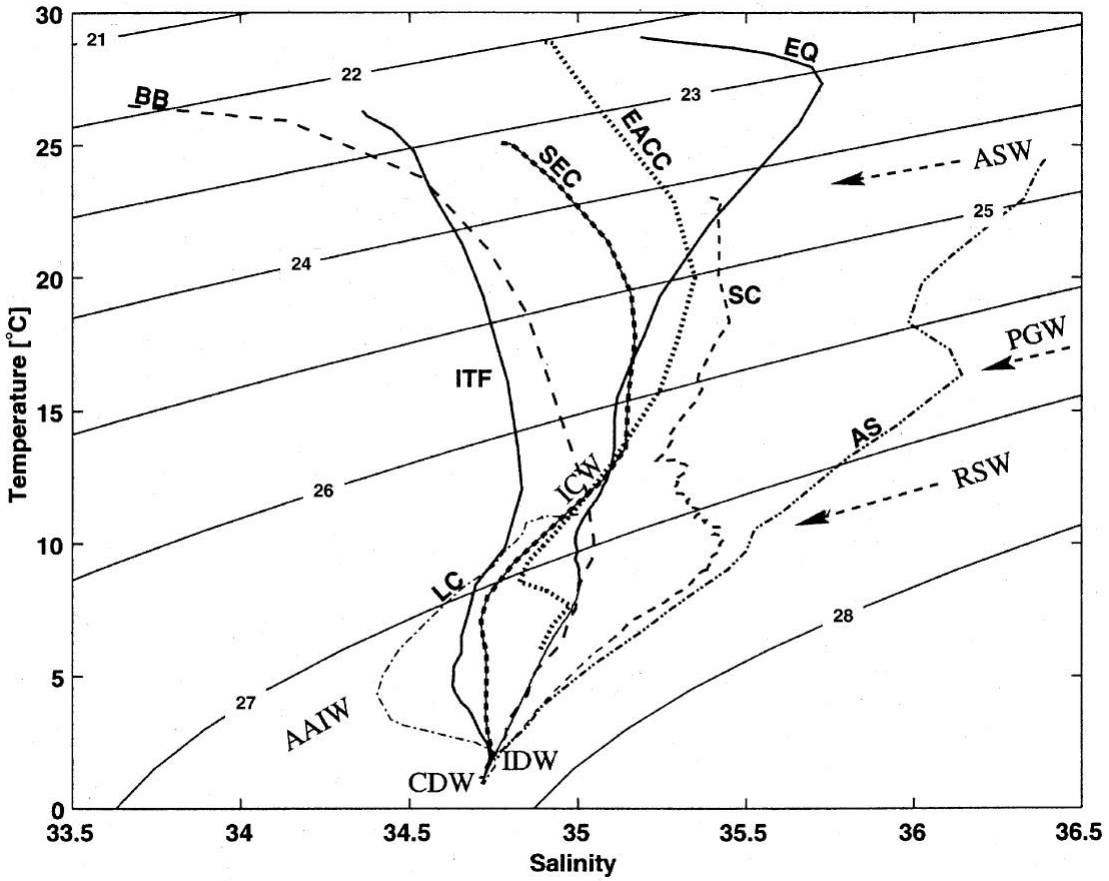

Figure 2.7: *Temperature-Salinity diagram of the Indian Ocean water masses for the Bay of Bengal (BB), northern Arabian Sea (AS), equatorial region of the western basin (EQ), South Equatorial Current (SEC), western exit of the Indonesian Throughflow (ITF), and Leeuwin Current (LC). The Somali Current (SC) curve is from August 1993 measurements in the northern upwelling wedge. Core water masses indicated are Circumpolar Deep Water (CDW), Indian Deep Water (IDW), Antarctic Intermediate Water (AAIW), Indian Central Water (ICW), Red Sea Water (RSW), Persian Gulf Water (PGW), and Arabian Sea Water (ASW). Profiles are for respective winter seasons in each hemisphere (After Schott and McCreary (2001)).*

southward spreading of ASHSW (Kumar and Prasad, 1999).

Warm, saline Red Sea Intermediate Water (RSIW), formed in the Mediterranean basin of the Red Sea, spreads from the north through the strait of Bab el Manded into the Gulf of

Aden where it is modified through mixing (Beal et al., 2000). This water mass is characterized by temperatures of around 22°C, a salinity maximum of around 39psu (Figure 2.7) and an oxygen minimum and often occur as patches or lenses over large parts of the Indian Ocean (Shapiro and Meschanov, 1991). The preferred spreading route of RSIW, after emerging from the Gulf of Aden into the Arabian Sea, is southwestward through the passage between the African Continent and Socotra along the African continental shelf with enhanced inflow during the Northeast Monsoon (Beal et al., 2000; Schott and Fischer, 2000). RSIW crosses the equator and spreads southward into the Agulhas Current via the flow in the Mozambique Channel (Roman and Lutjeharms, 2009) and within the East Madagascar Current (Donohue and Toole, 2003).

A specific thermocline water mass occurs in the equatorial regime of the Indian Ocean. Indian Equatorial Water (IEW), characterized by small vertical salinity differences, is a mixing product of Indian Ocean waters from the north and south and Indonesian Throughflow Water (ITW) coming from the east (You and Tomczak, 1993). IEW, extending from about 150 to 2000m depth, has a temperature and salinity range of 8.0-25°C and 34.6-35.2psu, respectively (Rao and Ram, 2005). ITW, derived from Pacific Ocean central water, is modified in the Indonesian Seas (Song et al., 2004) and flows into the Indian Ocean throughout the thermocline, with stronger flow in the upper thermocline and weaker flow in the lower thermocline (You and Tomczak, 1993). As this water mass is advected westward within the South Equatorial Current it slowly dilutes (Song et al., 2004). ITW spreads, during the Southwest Monsoon, into the tropical Indian Ocean along the east coast of Africa, within the northward flowing Somali Current. The southward transport of ITW occurs through the Mozambique Channel and along the east coast of Madagascar (Song et al., 2004).

In the tropics, excess precipitation over evaporation in the northeastern part of the Indian

Ocean, surface warming, and the influx of fresh ITW all contributes to the formation of warm, fresh Tropical Surface Water (TSW; New et al., 2007). This water mass, found between 0 and 20°S, within or north of the SEC, is flanked by more saline water masses to the north and south (New et al., 2007). TSW, characterized by temperatures warmer than 24°C and salinities in the range 34.5-34.6psu (Figure 2.7; Morales et al., 1996), spreads westward with the South Equatorial Current (SEC) and, where it bifurcates along the east coast of Madagascar, this water mass can be transported into the Mozambique Channel or southward with the poleward branch of the East Madagascar Current (Swallow et al., 1988; Gründlingh et al., 1991). Strong evaporation between 25°- 35°S in the subtropical, anticyclonic gyre of the Southern Hemisphere leads to the formation of an additional salinity maximum-water, Subtropical Surface Water (STSW; Morales et al., 1996; Schott and McCreary, 2001) which subducts below the fresher TSW in the north (Wyrtki, 1973a; Karstensen and Quadfasel, 2002). This water mass is characterized by a subsurface salinity maximum with a core density of $\sigma\Theta = 25.8 kg{\cdot}m^{-3}$ (Lutjeharms, 2006d; Song et al., 2004). The STSW spreads towards the western boundary, at a core depth of 200-250m, within the SEC and shallows as it spreads to a depth of about 100m (Swallow et al., 1988). Upon reaching the western boundary, northward spreading across the equator takes place within the Somali Current (Schott and McCreary, 2001). The salinity maximum of this water mass erodes northward, but remains distinguishable due to southward Ekman transport of fresher tropical waters in the upper layer (Song et al., 2004).

At the Subtropical Convergence of the Southern Hemisphere, a subtropical water mass, Indian Central Water (ICW) originates (Tomczak and Godfrey, 2003). This water mass is generally found below 200m and is characterized by a near-linear T/S relation for temperature above ~7°C and a temperature/salinity (T/S) maximum associated with STSW for tempera-

tures below 7°C (Figure 2.7; Schott and McCreary, 2001). ICW recirculates in the subtropical gyre and is the dominant water mass that can be found in the thermocline south of the front at 10°C (Morales et al., 1996). The entry of ICW into the North Indian Ocean during the South-west monsoon via the western boundary current is associated with a rapid decrease in oxygen indicative of rapid aging en route (You and Tomczak, 1993; Morales et al., 1996). This aged form of ICW is referred to as North Indian Central Water (NICW; Schott and McCreary, 2001).

Antarctic Intermediate Water (AAIW), formed at the Antarctic Convergence, enters the basin at intermediate depths from the southeast (Fine, 1993). This water mass, generated in the subfrontal zone through subduction, is characterized by an oxygen maximum and salinity minimum. The low salinities are a result of excess precipitation over evaporation in the area of formation (Schott and McCreary, 2001). In the Indian Ocean, AAIW has the same properties as in the Pacific and Atlantic oceans, i.e. temperatures in the range 2-2.5°C and salinity of about 33.8psu (Figure 2.7). However, when it enters the subtropical gyre, the temperature and salinity of AAIW increase to approximately 3-4°C and 34.3psu, respectively (Tomczak and Godfrey, 2003). AAIW is present between depths of 800 and 1200m (Donohue and Toole, 2003) which is within reach of the equatorial current system and as a result the distribution of AAIW in the Indian Ocean is limited to south of 10°S (Tomczak and Godfrey, 2003).

The net heat and buoyancy gain experienced by the North Indian Ocean due to the presence of the Asian continent inhibits the formation of bottom and deep waters generated through convection. Thus, bottom and deep waters are formed in-situ by mixing or imported into the Indian Ocean from other basins and as a result the thermocline circulation of the Indian Ocean represents a conversion of cold, dense, imported waters to warmer waters (Toole and Warren, 1993).

Circumpolar Deep Water (CDW) fills the Indian Ocean at depths below approximately 3800m and its properties (0.3°C, 34.7psu) correspond to those of Antarctic Circumpolar Water by the time it leaves the Circumpolar Current (Tomczak and Godfrey, 2003). Entry of CDW into the Madagascar and West Australian Basins occurs at a depth of more than 4000m. This water mass, characterized by high salinity and oxygen concentrations (Toole and Warren, 1993), enters the respective basins through gaps in the Southwest Indian Ridge and the Southeast Indian Ridge (Tomczak and Godfrey, 2003). These deep ridges prevent the direct entry of CDW into the central Indian Ocean Basin (Schott and McCreary, 2001).

Specific to the North Indian Ocean is North Indian Deep Water (NIDW; Schott and McCreary, 2001) which occupies the depth range from about 1500-2000m to 3800m (Tomczak and Godfrey, 2003). This water mass is oxygen-poor and, due to mixing with older intermediate waters, has a high salinity. NIDW, thought to form in the low and northern latitudes through deep upwelling (Schott and McCreary, 2001), is considered to be an aged form of CDW (You, 2000) and leaves the northern and equatorial Indian Ocean through southward transport (Park et al., 1993). In the southwest, the increased oxygen and salinity gives NIDW the characteristics of diluted North Atlantic Deep Water (NADW). NADW is confined to the extreme southwest of the Indian Ocean, in particular the Natal Valley and the Mozambique Basin, by the presence of the Madagascar and Davie ridges (Toole and Warren, 1993).

Cold, saline NADW is formed in the North Atlantic Ocean through convection and spreads, at depth, into the Indian and Pacific Oceans via the Southern Ocean (van Aken et al., 2004). This water mass is transformed to fresher Lower Circumpolar Deep Water (LCDW) in the Southern Ocean through upwelling and mixing with other water masses (Callahan, 1972; Park et al., 1993). NADW and LCDW are assumed to rise to shallower depths, in the Indian and Pacific Oceans, through large-scale upwelling (Stommel, 1958) and in the process are

transformed and heated by diapycnal mixing with the overlaying less dense water (Munk, 1966). NIDW is distinguished from NADW by its lower oxygen and higher nutrient content (Park et al., 1993; You, 2000). Upper Circumpolar Deep Water (UCDW), distinguished from LCDW by its lower oxygen and higher nutrient concentrations, is thought to originate within the Pacific and Indian Oceans.

2.1.3 General Circulation

2.1.3.1 North Indian Ocean

The circulation of the North Indian Ocean is under the direct influence of the monsoon winds and as such undergoes a seasonal reversal (Lutjeharms, 2006b; Schott and McCreary, 2001; Shetye and Gouveia, 1998). The monsoonal winds drive a series of coastal currents around the North Indian Ocean in a generally anti-clockwise (clockwise) direction during the North-east (Southwest) monsoon (New et al., 2007). The north-easterly winds of the Northeast monsoon (December-February) drive the monsoonal gyre situated north of the equator. During this season, the Northeast Monsoon Current flows westward across the Indian Ocean basin carrying water from the Bay of Bengal to the Arabian Sea. Upon reaching the coast of Africa this flow turns south as the Somali Current and converges, in a confluence zone at 2-4°S, with the northward flowing East Africa Coastal Current (EACC) to supply water to the eastward flowing South Equatorial Counter Current (SECC; Schott and McCreary, 2001; Swallow et al., 1988; Schott et al., 2009). The EACC, the only major coastal current in the tropical Indian Ocean that does not display a seasonal reversal in direction, flows northward between ~3-11°S (Shetye and Gouveia, 1998). The Equatorial Counter Current (ECC), generally occurs between 3°N and 5°S, but moves as far south as 10°S between January and

April (Lutjeharms, 2006b).

The strong southwesterly winds that dominate over the North Indian Ocean during the Southwest monsoon (July-August; New et al., 2007) induce a number of changes in the circulation. The Somali Current changes direction, becoming a northward flowing current that is supplied with water from the westward flowing South Equatorial Current (SEC) and the northward flowing EACC. During this season, the Somali Current can appear as a set of different cells and gyres depending on the driving wind field and the time of season (Schott et al., 2009). At about 4°N, a part of the Somali Current turns offshore forming a cold upwelling wedge on its left shoulder; the other part forms the 'Southern Gyre' through recirculation across the equator (Schott and McCreary, 2001). A second gyre, the 'Great Whirl', is formed in the north, while a third, the 'Socotra Eddy', forms northeast of Socotra during many but not all Southwest monsoons (Schott and McCreary, 2001). Along the eastern boundary of the Arabian Sea, the Northeast Monsoon Current changes direction and becomes the Southwest Monsoon Current which flows eastward from the Arabian Sea, south past Sri Lanka where it turns northward into the Bay of Bengal (Schott et al., 2009).

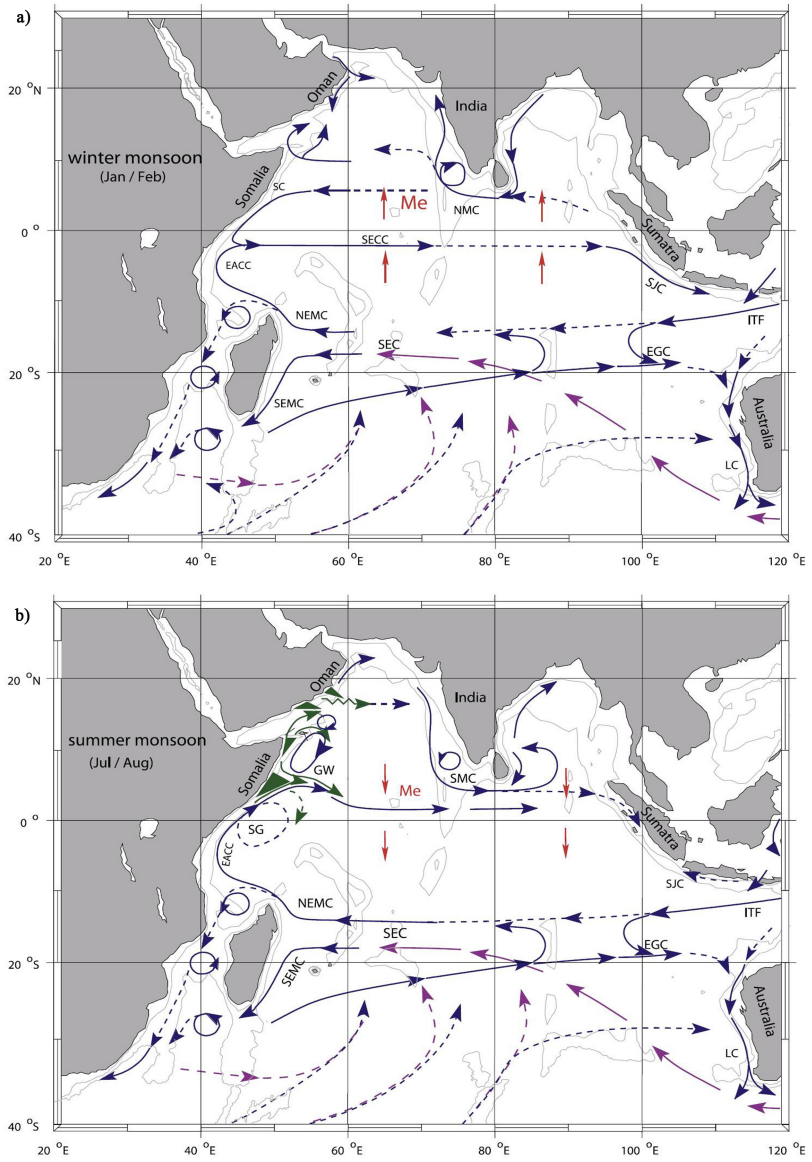

Figure 2.8: *Schematic of the Indian Ocean circulation during the a) Northeast monsoon and b) Southwest monsoon identifying the following features: the South Equatorial Current (SEC), South Equatorial Countercurrent (SECC), Northeast and Southeast Madagascar Current (NEMC and SEMC), East African Coastal Current (EACC), Somali Current (SC), Southwest and Northeast Monsoon Currents (SMC and NMC), South Java Current (SJC), East Gyral Current (EGC), Leeuwin Current, Indonesian Throughflow (ITF) and the Southern Gyre (SG) and Great Whirl (GW) with their associated upwelling wedges (green shades). The magenta lines indicate the subsurface return flow of the super gyre. The red vectors (Me) represent the direction of meridional Ekman transports (After Schott et al. (2009)).*

2.1.3.2 South Indian Ocean

The general circulation of the South Indian Ocean consists of a basin-wide, wind-driven subtropical anticyclonic gyre and a tropical cyclonic gyre. The basin-wide tropical wind-driven gyre consists of the eastward flowing South Equatorial Countercurrent (SECC) in the north, the seasonally reversing South Java Current (SJC) in the east, the westward flowing South Equatorial Current (SEC) in the south, and the North East Madagascar Current (NEMC) and the northward flowing East African Coastal Current (EACC) in the west (Figure 2.8; Schott et al., 2009). This tropical gyre is similar to a mid-latitude wind-driven gyre in that it responds to the basin-wide wind stress curl distribution and has a western boundary region that is characterized by intense eddy formation (Woodberry et al., 1989). However, it differs from a mid-latitude gyre in its proximity to the equatorial wave guide and in the extreme seasonal wind variations with the changing monsoons (Woodberry et al., 1989). The seasonal cycle in the winds results in a migration of the northern limit of this gyre, the SECC, between the Northern and Southern hemispheres. Consequently, the EACC crosses the equator during the southwest monsoon, feeding into the northwestward Somali Current (SC; Woodberry et al., 1989). The presence of the equatorial wave guide allows energy to propagate away from the western boundary via equatorial Kelvin waves and mixed Rossby-gravity waves which are not available in a mid-latitude western boundary region (Woodberry et al., 1989).

The subtropical gyre, driven by the anti-cyclonic wind forcing of the South Indian Ocean (Ffield et al., 1997), is the dominant feature of the South Indian Ocean circulation (Woodberry et al., 1989) and it comprises of the westward flowing South Equatorial Current (SEC) in the north, the strong poleward flowing Agulhas Current as a western boundary current and the eastward flowing South Indian Ocean Counter Current in the south . The SEC is dominant

in the area south of 8°S and flows westward at velocities that rarely exceed 0.3m·s^{-1} (Payet et al., 2004). The Mascarene Plateau lies directly in the path of the SEC at 60°E and strongly affects its flow. The flow of the SEC is constrained to passing through two gaps in the plateau even at a depth of 50m. This severely alters the distribution of the meridional current structure (Lutjeharms, 2006b). The Agulhas Current is the strongest western-boundary current in the Southern Hemisphere (Quartly and Srokosz, 2004) reaching at least 1000m in depth (Beal and Bryden, 1999) and transports between 66 and 70Sv (Beal and Bryden, 1997). Most of the Agulhas waters are fed by the subtropical gyre with a fraction (20-25Sv) being supplied by either the Mozambique Channel or the East Madagascar Current (Stramma and Lutjeharms, 1997).

An inherent dynamic of subtropical gyres is that they exhibit some degree of asymmetry, with concentrated flow toward the western side. However, the westward intensification of the subtropical circulation in the South Indian Ocean, in the form of the Agulhas Current, is extreme and unusual for a subtropical gyre (de Ruijter et al., 1999a). The consequence of this extreme concentrated flow is a distinct southwest Indian Ocean subgyre that extends to ~60°E (Stramma and Lutjeharms, 1997).

2.2 South West Indian Ocean

The main current transporting water to the South West Indian Ocean is the South Equatorial Current (SEC; van der Werf et al., 2009; Nauw et al., 2008). This current, driven by the wind stress curl (Schott and McCreary, 2001), flows westward across the Indian Ocean in the upper 600m between about 10°S and 20°S (Chapman et al., 2003; di Marco et al., 2000; Schott and McCreary, 2001). The Mascarene Plateau (4 - 20°S) lies directly in the path of the SEC and

extends for over 2000km between the Seychelles in the north (4°S, 56°E) and Mauritius in the south (20°S, 57°E). Upon encountering the Plateau, the SEC splits into two cores centred near 12°S and 18°S each with an estimated westward transport of about 20-25Sv at 57°E (New et al., 2007; Chapman et al., 2003). The bifurcation of the SEC into two main streams near 8-12°S and 19-22°S has been attributed to the fact that the ridge can only be crossed in two places, the wide sill between 5-8°S or the narrow gaps at 18-21°S (Chapman et al., 2003).

The land mass of Madagascar imposes another barrier for the wind driven circulation between 12°S and 25°S (Palastanga et al., 2009), preventing a large part of the SEC from reaching the east coast of Africa (Lutjeharms, 2006d). The presence of Madagascar causes the SEC to diverge, between 17°S-20°S, into the Southeast Madagascar Current (SEMC) and the Northeast Madagascar Current (NEMC; Nauw et al., 2008; Palastanga et al., 2009; van der Werf et al., 2009; Chapman et al., 2003). New et al. (2007) suggest that the northern and southern cores of the SEC formed at the Mascarene Plateau form the NEMC and SEMC, respectively. The estimated transports of the NEMC and the SEMC are approximately 20 and 30Sv (Swallow et al., 1988; Schott et al., 1988), indicating that a total transport of about 50Sv for the SEC upstream of Madagascar is plausible.

The NEMC follows the northeast coast of Madagascar (van der Werf et al., 2009), flowing past the northern tip of Madagascar (Schott and McCreary, 2001; Lutjeharms, 2006c) and meanders westward toward the east coast of Africa (Quadfasel and Swallow, 1986) where it bifurcates to supply water to the East African Coastal Current (EACC; Stramma and Lutjeharms, 1997; Shetye and Gouveia, 1998) and the flow in the Mozambique Channel (Schott and McCreary, 2001; Schott et al., 2009; Shetye and Gouveia, 1998).

The SEMC, with its narrow, intense flow (Lutjeharms et al., 1981) characteristic of a

western boundary current (di Marco et al., 2000), flows southward along the east coast of Madagascar following the continental shelf break to the southern tip of Madagascar (Schott et al., 2009; di Marco et al., 2000). The classic view of the fate of the SEMC is a straight zonal flow past the southern tip of Madagascar towards the African coast. However, the more contemporary view of the fate of the SEMC is one of numerous diverse paths (di Marco et al., 2000), each of which may only exist intermittently (Quartly and Srokosz, 2004). One possible route for the SEMC is, as per the classical view, to flow due west past the southern tip of Madagascar and into the southern part of the Mozambique Channel (Lutjeharms, 1988a; Gründlingh, 1985, 1987, 1993). An alternative route that has been proposed is that after rounding the southern tip of Madagascar at Cape St. Marie, the SEMC curves northwest into the southern Mozambique Channel and subsequently turns anticyclonically southwestward towards Africa (Tomczak and Godfrey, 2003; di Marco et al., 2002). Based on the analysis of satellite derived sea surface temperature, chlorophyll concentrations, and drifter data, it has been suggested that, similar to the behaviour of the Agulhas Current south of South Africa, the SEMC retroflects or breaks up south of Madagascar and shed rings and filaments into the Mozambique Basin that ultimately join with the Agulhas Current System (di Marco et al., 2000; de Ruijter et al., 2002, 2004; Quartly and Srokosz, 2002; Lutjeharms, 1988a,b). A different interpretation of this data is the counter-clockwise advection of high chlorophyll surface waters from the continental slope into the interior of the subtropical gyre by transient anticyclonic eddies in the area (Quartly et al., 2006). Moreover, using combined satellite and in-situ observations, de Ruijter et al. (2004) found that regular pairs of contra-rotating eddies occur south of Madagascar and that these eddies generally propagate to the southwest at speeds of 5-10cm$\cdot s^{-1}$. De Ruijter et al. (2004) also observed a subsurface salinity maximum, characteristic of Subtropical Surface Waters, in the upper layers of both the anticyclonic and

cyclonic eddy sampled during the hydrographic survey which suggests that waters contained with in the eddy pair are almost completely derived from the SEMC.

The large-scale background flow of the southwest Indian Ocean subgyre is westward, and as such it has been suggested that no persistent retroflection can exist south of Madagascar because there is no long-term eastward flow between 25-30°S to which it could link (de Ruijter et al., 2004; Quartly et al., 2006). However, Siedler et al. (2006) and Palastanga et al. (2007) have shown that a narrow, eastward flowing current, the South Indian Ocean Counter Current (SICC), exists between 22 and 26°S. Analysis of altimeter-derived and high resolution model data have shown that the SICC receives a substantial amount of water from the SEMC region (Siedler et al., 2009).

2.2.1 Sources of the Agulhas Current

The greater Agulhas Current system in the Southwest Indian Ocean plays a key role in the global ocean circulation (Gordon et al., 1992; de Ruijter et al., 1999a; Lutjeharms, 2006b). The Agulhas Current flows southwestward along the east coast of South Africa closely following the coast line (Figure 2.9; de Ruijter et al., 1999b). South of South Africa, the continental shelf extends offshore steering the Agulhas Current away from the continent. After separating from the continent, the Agulhas Current retroflects and feeds back into the South Indian Ocean as the eastward flowing Agulhas Return Current (Figure 2.9; Beal et al., 2011). The retroflection, known as the Agulhas Retroflection, sheds eddies, rings and filaments which transport warm, saline Indian Ocean water into the South Atlantic Ocean (Biastoch et al., 2008b). The leakage of water from the Indian Ocean to the Atlantic feeds into the upper arm of the meridional overturning circulation of the Atlantic (AMOC), which, in turn,

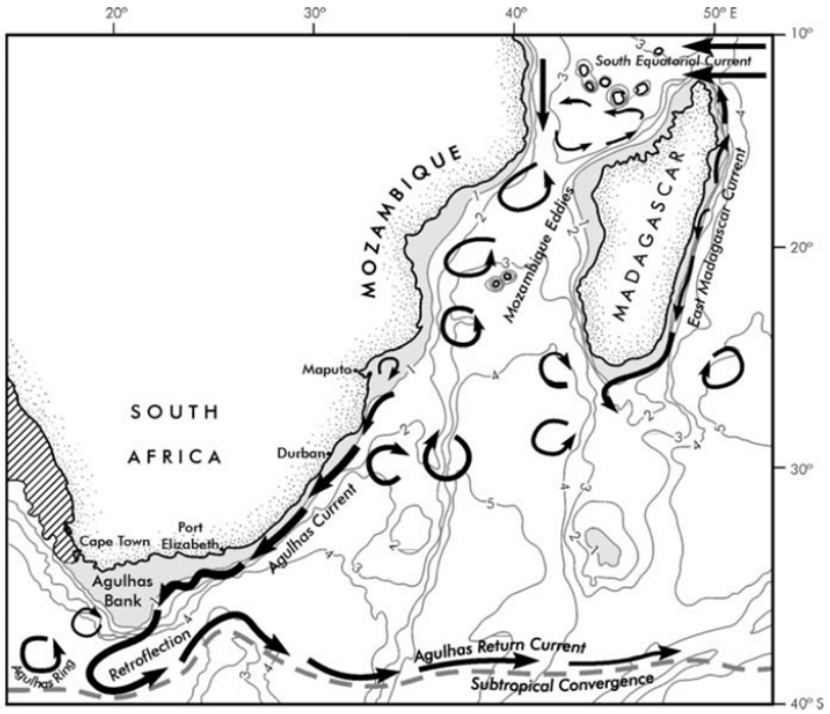

Figure 2.9: *Schematic of the circulation of the greater Agulhas Current System. The arrows represent ocean currents and the curvilinear features portrays meso-scale eddies. The bathymetric contours are expressed in km (After Lutjeharms (2006c)).*

has implications for global climate (Peeters et al., 2004).

Contrary to classical portrayals, the dominant sources of the Agulhas Current are not the flow through the Mozambique Channel (Sætre and da Silva, 1984) nor the East Madagascar Current (Sætre and da Silva, 1984; Lutjeharms, 1988b) but the recirculation in the South West Indian Ocean subgyre (Harris, 1972; Stramma and Lutjeharms, 1997). The greater part, ~40Sv, of the total volume flux of the upper 1000m of the Agulhas Current (~65Sv) is derived from the recirculation in the above mentioned subgyre. The rest of the volume flux is derived from east of Madagascar and from the southward flow through the Mozambique Channel.

The modelling results of Biastoch and Krauss (1999) indicate that the flow east of Mada-

gascar contributes about 20Sv to the Agulhas Current, 5Sv is supplied from the southward flow through the Mozambique Channel and the rest of the Agulhas Current is derived from re-circulation of the Agulhas Current waters in the subtropical gyre of the Indian Ocean. These volume contributions are in close agreement with the rough estimates provided by Harris (1972) (35Sv from east of Madagascar, 10Sv from the Mozambique Channel, 27Sv from the southwest Indian Ocean subgyre) and the geostrophic transport (upper 1000m) estimates of Stramma and Lutjeharms (1997). Even though the Mozambique Channel is not a dominant source of the Agulhas Current, the amount of thermocline and surface waters transported poleward by meso-scale eddies in the Mozambique Channel is large enough to play a significant role in the global thermohaline circulation (de Ruijter et al., 2002). Furthermore, the merging of eddies from the Mozambique Channel into the Agulhas Current have been shown to trigger the formation of a Natal Pulse (Lutjeharms and Roberts, 1988), a growing solitary meander, which subsequently triggers the shedding of Agulhas rings at the Agulhas Retroflection (Schouten et al., 2002a). A detailed description of the Mozambique Channel is presented below as the knowledge on the circulation in the Comoros Basin, located in the northern Mozambique Channel, is limited.

2.2.2 The Mozambique Channel

Classically, the flow in the Mozambique Channel was depicted as a continuous, intense western boundary current along the east coast of Mozambique that flowed directly into the Agulhas Current (Lutjeharms, 2006c,d; Schumann, 1998). This notion was based on early observations of ship's drift (Sætre, 1985; Lutjeharms et al., 2000) and on occasional observations of sea surface temperatures (Lutjeharms, 2006d). Past portrayals of the circulation in the

Mozambique Channel, based on non-synoptic hydrographic observations vary significantly (e.g. Harris, 1972; Sætre and da Silva, 1984) and cast doubt upon the circulation patterns within the channel. A number of recent studies based on satellite data (Gründlingh, 1995), in-situ observations (di Marco et al., 2002) and numerical modelling (Biastoch and Krauss, 1999) have shown that the circulation in the Mozambique Channel is considerably more complicated than a simple western boundary current and that it in fact consists of a train of cyclonic and anti-cyclonic eddies (de Ruijter et al., 2002; Ridderinkhof and de Ruijter, 2003).

After separating from the northern tip of Madagascar, the NEMC generates large anti-cyclonic eddies (LaCasce and Isachsen, 2007) some of which drift south into the Mozambique Channel (de Ruijter et al., 2002; Ridderinkhof and de Ruijter, 2003). Additional anti-cyclonic eddies are formed at the narrows of the Mozambique Channel and are the most intense (de Ruijter et al., 2002). The flow on the western side of the channel is highly variable and eddy kinetic energy is high while that on the eastern side is low (Lutjeharms, 2006a,d). The high variability and the strong currents at the shelf edge agree with the concept of a train of poleward moving eddies through the channel. The eddies from the Mozambique Channel flow southward along the shelf edge and may meet with the SEMC in the southern part of the channel and move into the Agulhas Current (van der Werf et al., 2009).

2.2.2.1 Eddy Characteristics and Transport Estimates

The anticyclonic eddies that dominate the flow in the Mozambique Channel are deep reaching eddies that have a diameter of about 300-350km (Harris, 1972; de Ruijter et al., 2002; Schouten et al., 2003) and propagate southward at a translation speed of ~4.5km·day^{-1} (de Ruijter et al., 2002). This would result in a train of approximately three anti-cyclonic eddies throughout the channel at any one time. Analysing sea surface height anomalies, Schouten

et al. (2003) showed an increase in SSH anomalies from ~20cm in the north to 35cm in the central and southern regions of the channel. The increase in SSH anomalies was attributed to a strengthening of the eddies, part, but not all, of which can be explained by the latitudinal displacement of an eddy through the planetary vorticity gradient (Schouten et al., 2003). Furthermore, these authors found that north of the narrows of the channel (north of 16°S) eddies form at a frequency of 6-7 per year equating to a 55 day period which is also the dominant period of the barotropic instability of the SEC north of Madagascar (Schott et al., 1988; Quadfasel and Swallow, 1986). The frequency of eddy formation decreases to 4-7 per year in the centre of the channel with a further reduction (4 per year) towards the southern end of the channel.

Lowered ADCP current measurements of an eddy located at the narrows of the channel (17°S) and at the southern entrance to the Mozambique Channel (24°S), have revealed that the Mozambique Channel eddies, with speeds exceeding $10cm{\cdot}s^{-1}$ and reaching to the bottom (~2000m), have a significant barotropic component despite being surface intensified (de Ruijter et al., 2002). The water mass and velocity structure of eddies in the Mozambique Channel indicates that the eddies trap water to below the intermediate water mass level and, with regular generation (~ 4 per year; Schouten et al., 2002a) and water trapping down to 1500m, the estimated volume transport for the the eddies is about 15Sv (Table 2.1; de Ruijter et al., 2002).

Historical transports for the Mozambique Channel, based on hydrographic data, range from 5Sv northward to 26Sv southward depending on the time of year and reference level used to calculate the transports (see di Marco et al. 2002 for an overview). More recent transport estimates calculated from hydrographic data and a reference level of 2500m (the sill depth in the channel), show a net southward transport of 29.1Sv in the northern Mozambique

Table 2.1: *Historical volume transport estimates in the Mozambique Channel.*

Transport (Sv)	Data source	Reference
15 south	ADCP	de Ruijter et al. (2002)
29.1 south[a]	Hydrography	di Marco et al. (2002)
5.9 south[b]	Hydrography	di Marco et al. (2002)
14 south	ADCP	Ridderinkhof and de Ruijter (2003)
8.6 south	ADCP	Harlander et al. (2009)
16.7 south	ADCP	Ridderinkhof et al. (2010)

[a]Northern Mozambique Channel
[b]Southern Mozambique Channel

Channel and 5.9Sv in the southern Mozambique Channel (di Marco et al., 2002). The discrepancy in the transport between the north and south was attributed to the seasonality and eddy variability superimposed on the mean southward flow. Analysing current observations for 1 year obtained from a mooring array at the narrowest section of the channel, Ridderinkhof and de Ruijter (2003) have shown the transport to fluctuate between 20Sv northward and 60Sv southward at the frequency of eddy passages, with an estimated mean southward transport of 14Sv (Table 2.1). Harlander et al. (2009) expanded on this study, analysing two and a half years of current observations from the same mooring array as Ridderinkhof and de Ruijter (2003) and found a mean volume transport of 8.6Sv southward (Table 2.1). These authors found a northward transport of 5.9Sv in the eastern part and a 15.7Sv southward transport in the western part for the top 1200m.

In addition, Harlander et al. (2009) also observed a deep northward undercurrent of 1.5Sv. de Ruijter et al. (2002) also showed the existence of a northward flowing Mozambique undercurrent with two cores which is probably an extension of the Agulhas undercurrent (Beal and Bryden, 1997). One core of the undercurrent is located at intermediate level with speeds ranging between 0.1 and 0.2m$\cdot$s^{-1}. This core weakens northward, carrying Antarctic intermediate

water along the continental slope. The other core, with maximum equatorwards speeds near 0.2m·s^{-1}, is located below 2000m and transports North Atlantic Deep Water northwards. A longer time series of current measurements from the long-term mooring array in the narrows of the Mozambique Channel (~17°S) revealed a mean southward volume transport of 16.7Sv (Table 2.1) through the channel with daily transport values ranging from 45.4Sv northward to 67.2Sv southward (Ridderinkhof et al., 2010). In addition, Ridderinkhof et al. (2010) found a seasonal and interannual variability in the transport with magnitudes of about 4.1Sv and 8.9Sv, respectively.

2.2.2.2 Variability in the Mozambique Channel

As mentioned above, the variability observed in the transport estimates through the Mozambique Channel comprises at least seasonal variation, interannual variability as well as the quasi-regular passage of eddies. The seasonal variability can be attributed to the variability of the wind field over the western Indian Ocean while large-scale physical phenomena are the most likely source of interannual variability (Ridderinkhof et al., 2010). It is possible that lower frequency variability may exist in the Mozambique Channel given the presence of this type of variability in the atmospheric circulation over the region (e.g. Allan et al., 1995; Reason and Mulenga, 1999).

The monsoon winds, mentioned in section 2.1.1.1, have a direct influence on the northern part of the Mozambique Channel as well as its main source, the South Equatorial Current. During the Northeast monsoon (austral summer), the northern part of the Mozambique Channel is under the influence of northwesterly winds and the southern part experiences southeasterly winds. However, southeasterly winds dominate over the entire Mozambique Channel during the Southwest Monsoon (austral winter; Lutjeharms, 2006b). Thus it appears that the

northern part of the channel is influenced by the monsoonal wind system of the Indian Ocean (Sætre and da Silva, 1984) whereas the southern part is not. The Inter Tropical Convergence Zone (ITCZ) forms the border between these two systems (Lutjeharms, 2006b).

As such, past studies have attributed most of the inter-annual and seasonal variability of the circulation in the northern Mozambique Channel to the variations in the wind field (Donguy and Piton, 1991). Model simulations of the Mozambique Channel have demonstrated that there is a marked seasonality to the flow in the Mozambique Channel with very low to no transport during the Northeast monsoon and very high transport values during the Southwest monsoon (Biastoch and Krauss, 1999; Biastoch et al., 1999). Biastoch et al. (1999) suggest that the position of the core of the South Indian Anticyclone may be responsible for this seasonality. During the Southwest monsoon, the core of the South Indian Anticyclone lies between approximately 5-20°S and the associated Ekman transport can flow north of Madagascar and into the Mozambique Channel. Therefore, the increased transport during this season is a result of the combined effect of the occurrence of a wind stress maximum at the northern tip of Madagascar and the northward shift in the southeast trade winds (Biastoch and Krauss, 1999). The South Indian Anticyclone shifts southward during the northeast monsoon and a buffer zone occurs between the westerlies along the equator and the southeast trade winds, thus inhibiting the barotropic transport from extending into the Mozambique Channel (Biastoch et al., 1999). Similarly, Matano et al. (2008) and Matano et al. (2002) showed that the seasonal variability in the southwest Indian Ocean is controlled by a regional barotropic mode located in the western portion of the basin. The barotropic mode, defined as the depth-averaged response (Kindle, 1991), is a consequence of relatively fast changes in the wind forcing which initiate barotropic currents that rapidly propagate the wind forcing within the subregions of the basin (Matano et al., 2002). This barotropic mode extends from

the equator, encompassing the SEC, south through the Mozambique Channel and up to the Agulhas Current.

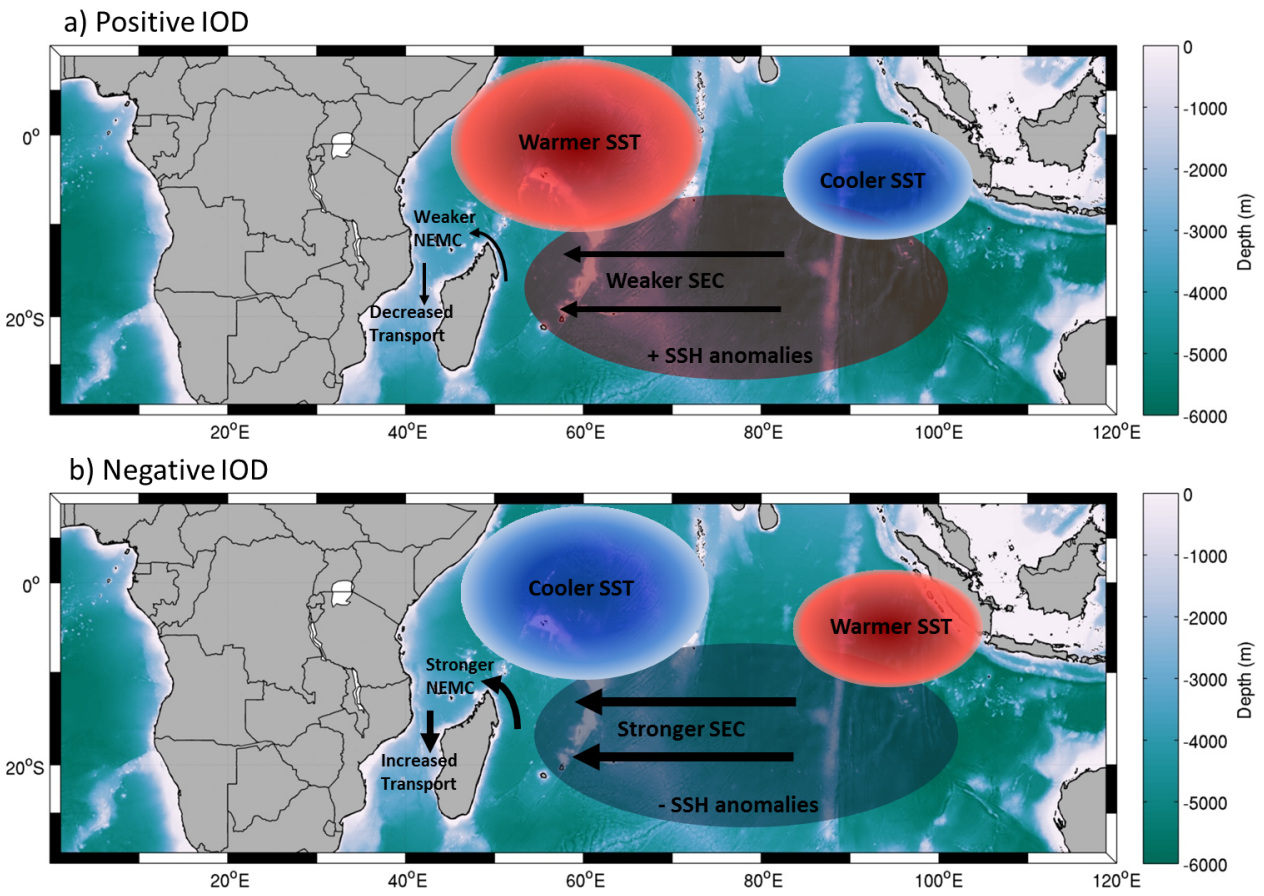

Figure 2.10: *Schematic of the relationship between the IOD and SSH anomalies in the Indian Ocean and the subsequent influence on the SEC and NEMC.*

The interannual variability in the transport in the Mozambique Channel appears to be related to the variability of the Indian Ocean Dipole (Ridderinkhof et al., 2010). Palastanga et al. (2006) found that similar interannual fluctuations are exhibited by the SSH in the central Mozambique Channel and northern Mozambique Channel and that they can be related to the occurrence of Indian Ocean Dipole events in the tropical Indian Ocean. The sea level anoma-

lies associated with positive (negative) IOD events induce a weakening (strengthening) of the SEC which subsequently lead to a decrease (increase) in the strength of the NEMC (Figure 2.10). The decrease (increase) in the NEMC is followed by a weakening (strengthening) of the flow through the Mozambique Channel (Figure 2.10). Thus, a positive correlation exists between the Mozambique Channel transport and the IOD with a lag of about 1 year (Ridderinkhof et al., 2010).

2.2.2.3 Eddy formation

Based on current data obtained from a long term mooring array deployed in the narrowest part of the Mozambique Channel near 16°S, Ridderinkhof and de Ruijter (2003) suggest that the eddies are formed at the narrows of the channel as a result of instabilities that pinch off the current that penetrates across the Davie Ridge. The inference made by Ridderinkhof and de Ruijter (2003) is based on data from a single mooring array and therefore is not that reliable. Biastoch and Krauss (1999), through an eddy-permitting numerical model, successfully simulated a series of shallow, southward moving, meso-scale eddies in the Mozambique Channel in agreement with hydrographic observations (de Ruijter et al., 2002) and long-term satellite altimetery analyses (Schouten et al., 2003). This model's data suggested that the eddies in the Mozambique Channel are formed north of the narrows of the channel. Moreover, a numerical model simulation investigating the role of Madagascar on the formation of Mozambique Channel eddies showed that Madagascar plays a key role in the formation of eddies. Without Madagascar, a continuous western boundary current, similar to the continuous Mozambique Current described in textbooks, flows along the east coast of southern Africa (Penven et al., 2006c).

A number of mechanisms have been suggested for the formation of Mozambique Chan-

nel eddies, one of which is the interaction of baroclinic Rossby waves with Madagascar (Schouten et al., 2002b). Equatorial Kelvin waves arriving at the Indonesian coast at a periodicity of about 90 days (4 per year) split into north and southward travelling coastal Kelvin waves. At about 10-12°S, the southward traveling coastal Kelvin waves trigger Rossby waves at about the same 90-day periodicity. These westward-propagating Rossby waves cross the Indian Ocean at frequencies of two per year (semi-annual; Morrow and Birol, 1998) and four per year (Schouten et al., 2002b). The train of Rossby waves, travelling west at speeds of ~20cm·s^{-1} along 12°S, encounter Madagascar and Schouten et al. (2002b) suggested that the interaction of the incoming Rossby waves with the high shear regions of the SEC north of Madagascar may act as a trigger for the formation of anti-cyclonic eddies in the northern Mozambique Channel that subsequently propagate south through the narrowest part of the channel and into the rest of the Mozambique Channel at a frequency of 4 per year.

Another mechanism that has been proposed for the formation of Mozambique Channel eddies from both observational data and numerical simulations is barotropic instability in the NEMC. Both Quadfasel and Swallow (1986) and Swallow et al. (1988) suggested, from observations, that eddies forming west of the northern tip of Madagascar are a result of barotropic instability of the NEMC after its separation from the coast. Biastoch and Krauss (1999) analysed the energy interaction terms of a numerical simulation of the Mozambique Channel region and found that in the northern Mozambique Channel, the barotropic instability term exceeded the baroclinic instability term, and concluded that barotropic instability is important here. Using a flat bottom, barotropic model, LaCasce and Isachsen (2007) also showed that anti-cyclonic eddies west of the northern tip of Madagascar are a result of the barotropic instability of the NEMC.

2.2.2.4 Water masses in the Mozambique Channel

The waters in the Mozambique Channel consist of a mixture of different water masses (van der Werf et al., 2009); however the water masses are characteristic of those found at these latitudes in the rest of the Indian Ocean (Lutjeharms, 2006d). The waters of the upper layers in the Mozambique Channel lie in a salinity band between 35 and 35.4psu (Lutjeharms, 2006d). In the channel, there are two different water masses at temperatures exceeding ~18°C that are identifiable by distinct salinities. These water masses are Tropical Surface Water (TSW) which generally occurs in the northern part of the channel and Subtropical Indian Ocean Water (STSW) which occurs in the southern part (Lutjeharms, 2006d). Subtropical Surface Water (STSW), Tropical Surface Water (TSW) along with Indonesian Throughflow Water (ITW) are the main source waters in the upper layers (van der Werf et al., 2009).

A meridional variation is observed at intermediate levels (~5°C) with Antarctic Intermediate Water in the south and Red Sea Intermediate Water in the north (Clowes and Deacon, 1935). The salinity values associated with RSIW in the northern Mozambique Channel are in the range 34.7-34.8psu (di Marco et al., 2002), but can exceed 34.8psu (de Ruijter et al., 2002). As the Red Sea Water travels south through the channel within the Mozambique Channel eddies, there is a reduction in the salinity. However, by the time this water mass reaches 10-12°S, it is still more saline than AAIW by about 0.2-0.3psu (di Marco et al., 2002). On the other hand, the intermediate core of the Mozambique Undercurrent transports AAIW, with a salinity minimum of <34.5psu, north into the Mozambique Channel (de Ruijter et al., 2002).

South of 20°S, the deep water in the Mozambique Channel, with an oxygen and salinity maximum and silicate minimum, indicates the presence of North Atlantic Deep Water (di Marco et al., 2002; van Aken et al., 2004) while the low oxygen and salinity and high sil-

icate bottom waters suggest the presence of Circumpolar Deep Water (di Marco et al., 2002; Swart et al., 2010).

2.2.3 The Comoros Basin

Research in the Comoros Basin, the region 9-15°S between northern Madagascar and Mozambique, is very limited and mostly based on sparse observational data. Typically, the circulation in the region is only mentioned in passing in studies focusing elsewhere in the Mozambique Channel.

Harris (1972) analyzed hydrographic data of the Mozambique Channel and northern Agulhas Current (5-40°S and 30-70°E) collected during six different cruises on-board three different vessels during the spring of 1964. This author found that the circulation in the Mozambique Channel consists of deep anti-cyclonic vortices with diameters of ~300km and estimated volume transports of about 10-20Sv. The northernmost position of these vortices was found to be located in the Comoros Basin while the southernmost was located off the coast of Durban.

Sætre and da Silva (1984) presented results from several research cruises carried out during 1977-1980 along the coast of Mozambique. Similar to Harris (1972), these authors found that the circulation pattern along the Mozambican coast is characterized by three propagating anti-cyclonic cells with additional smaller cyclonic eddies also present (Figure 2.11). Sætre and da Silva (1984) also suggested a seasonality to the circulation in the northern half of the Mozambique Channel. A quasi-stationary anti-cyclonic gyre dominates in the northern part of the Mozambique Channel, and is also characteristic of the central Mozambique Channel during the austral summer. These two anti-cyclones, separated by a cyclonic eddy during the

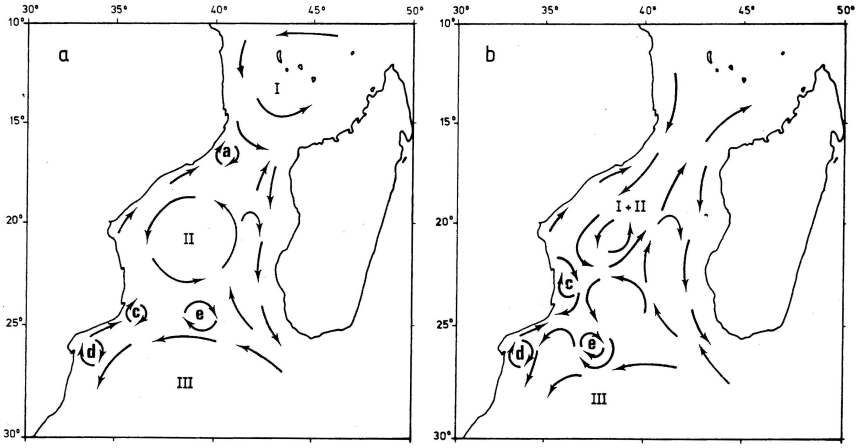

Figure 2.11: *The circulation in the Mozambique Channel according to Sætre and da Silva (1984).*

summer, appear to be connected during the austral winter and extend into the central part of the channel as an anticyclonic tongue (Figure 2.11).

Geostrophic current determinations, as well as absolute surface current measurements obtained from three research cruises in the Mozambique Channel, two during the austral summer (March 1974 and 1975) and one during the austral winter (June-July 1974), were analyzed by Donguy and Piton (1991). These authors reported a distinct anti-cyclonic eddy in the northern part of the Mozambique Channel that is fed in the north by the westward flowing SEC while a northward current along the coast of Madagascar constitutes the eastern part. In addition, they also found a well established southeastward flowing current in the central part of the channel. In accordance with Sætre and da Silva (1984), Donguy and Piton (1991) also suggested a seasonal variability to the anti-cyclonic eddy in the northern Mozambique Channel as well as interannual variability, both of which they attribute to the influence of wind. All three of the above mentioned studies are based on hydrographic data with limited spatiotemporal coverage which calls into question the robustness of the results.

Using an eddy-permitting numerical model, Biastoch and Krauss (1999) simulated a series of shallow, southward moving, meso-scale eddies in the Mozambique Channel. These authors noted an anti-cyclonic loop in the northern Mozambique Channel which pinches off anti-cyclonic eddies that travel southward into the Mozambique Channel. These results suggest that the formation of eddies within the Mozambique Channel, can in part, be attributed to the dynamics in the northern Mozambique Channel. On the other hand, from the analysis of high-resolution models and satellite data (AVISO sea surface height anomalies), van der Werf et al. (2010) concluded that eddies in the northern Mozambique Channel are formed near Cape Amber, the northern tip of Madagascar. These authors also found that the eddies simulated in the numerical models propagated south through the narrows of the channel while those observed in the satellite data dissipated and new eddies are formed at the narrows of the channel. The difference in behaviour of the modeled and observational eddies were attributed to the interaction of the eddies with the Comoros Islands, which is not correctly represented in the models. Furthermore, using an eddy resolving model and satellite altimetery data, Backeberg and Reason (2010) showed that anti-cyclonic eddies formed at the northern tip of Madagascar are related to transport pulses in the SEC and travel westward to the coast of Mozambique with subsequent poleward flow into the Mozambique Channel.

In all of the above mentioned studies, the area generally referred to as the northern Mozambique Channel is more specifically known as the Comoros Basin and the anti-cyclonic circulation observed by Harris (1972), Sætre and da Silva (1984), Donguy and Piton (1991) and Biastoch and Krauss (1999) in this region has been termed the "Comoros Gyre" (Lutjeharms, 2006a). The surface currents that make up the gyre are not strong (Sætre, 1985), except near the coast of Africa where mean speeds greater than $0.5 m \cdot s^{-1}$ have been recorded (Lutjeharms et al., 2000). In addition, an along-slope, poleward boundary current has been

observed in the western part of the basin and has a total transport of ~30Sv (de Ruijter et al., 2002). The temperature-salinity characteristics indicated that the 30Sv consisted of 15Sv Indian Central Water in the upper 450m layer, 11Sv in the Intermediate Water layer, and 4Sv of Circumpolar Deep Water. These temperature and salinity characteristics are consistent with those of the East African Coastal Current (Schott and McCreary, 2001) and indicate a common point of origin, the northern limb of the East Madagascar Current. As noted by the authors, this section was too short to confirm whether the current observed was part of a western boundary current or part of an eddy.

The Comoros Basin is not an isolated ocean basin and large scale modes of variability such as the IOD and ENSO will have an influence on this region. There is also a possibility that signals from the east Indian Ocean influence this region. As mentioned in section 2.2.2.2, negative IOD events result in a strengthening of the NEMC and subsequently increase the transport through the Mozambique Channel. Similarly, de Ruijter et al. (2004) have suggested La Niña/negative IOD events act to strengthen the South East Madagascar Current which in turn, is associated with periods of regular dipole formation south of Madagascar. Therefore, it is likely that La Niña/negative IOD events can result in more regular formation of the anti-cyclonic eddy in the Comoros Basin, however the impact on the basin have not, as yet, been investigated. The next subsection discusses ENSO and the IOD in more detail.

2.2.4 Climate Variability

The variability of the tropical Indian Ocean is influenced by a number of climate modes occurring in a range of scales from intraseasonal to interannual and longer time scales. Most of these modes are coupled to the strong seasonal cycle of the Indian Ocean (Schott et al.,

2009). The El Niño Southern Oscillation (ENSO) and the Indian Ocean Dipole (IOD) are the two most prominent modes of interannual variability that impact the Indian Ocean.

2.2.4.1 ENSO

The El Niño-Southern Oscillation (ENSO), a coupled instability of the tropical Indo-Pacific ocean-atmosphere system (Chen and Cane, 2008), is the primary mode of variability in the tropics and influences the global climate (Yoo et al., 2010). The oceanic part is characterized by anomalous warming (El Niño) and cooling (La Niña) events of the eastern equatorial Pacific (Schott et al., 2009). The atmospheric counterpart, the Southern Oscillation, is characterized by a fluctuation of the atmospheric pressure between the eastern and western tropical Pacific (Chen and Cane, 2008) and is a result of the ocean-atmosphere interaction. Sea level pressure tends to be lower (higher) in the eastern Pacific during El Niño (La Niña), and higher (lower) in the western Pacific (Rasmusson and Carpenter, 1982).

For the Indian Ocean, it has been noted that most of the observed interannual variability can be attributed to the ENSO. During an El Niño (La Niña) event, the Indian Ocean north of 30-35°S tends to warm (cool), while cooling (warming) occurs in the southern mid-latitudes (Chambers et al., 1999; Reason et al., 2000). In addition, a southward shift in the Inter-Tropical Convergence Zone (ITCZ) occurs during an El Niño event. This results in a southward shift of the anomalous easterlies near the equator to ~10°S. The wind stress curl associated with the anomalous winds leads to the formation of westward traveling downwelling Rossby waves (Xie et al., 2002). A positive SST anomaly propagates to the west along with the Rossby wave resulting in a basin wide warming which in turn leads to increased convection (Tourre and White, 1995, 1997) and increased cyclone activity (Xie et al., 2002). The positive SST anomalies lag the warming of the central Pacific Ocean by one to two seasons

(3-6 months; Lanzante, 1996; Klein et al., 1999; Saji and Yamagata, 2003b; Reason et al., 2000). In the Atlantic and South China Sea, SST anomalies associated with the ENSO are a result of changes in cloud cover and evaporation which, in turn, alter the net heat flux (Klein et al., 1999). However, the SST anomalies over the Indian Ocean associated with the ENSO are not correlated with anomalous cloud cover or latent heat flux and Klein et al. (1999) suggests that the SST anomalies might be a result of altered ocean dynamics caused by changes in the wind field.

Sea surface height anomalies are rapidly transported across the Indian Ocean by sequences of Kelvin and Rossby waves and have an important influence on the interocean exchange between the Indian and Atlantic oceans. The strong westerlies dominating over the equatorial Indian Ocean during the inter-monsoon periods force strong downwelling equatorial Kelvin waves at semi-annual time scales (Wyrtki, 1973a). Upon reaching the Indonesian coast, the equatorial Kelvin waves bifurcate into north- and southward traveling coastal Kelvin waves which are partially reflected as westward travelling Rossby waves. The anomalously strong easterlies that occur over the equatorial Indian Ocean during El Niño inhibits the Kelvin wave signal resulting in a temporary absence of the Rossby wave trigger (Schouten et al., 2002a). Large anticyclonic eddies form in the Mozambique Channel due to the interaction of Rossby waves with Madagascar. These eddies play an important role in the interocean exchange as they influence the shedding of Agulhas rings. Schouten et al. (2002b) found that the temporary absence of a Rossby wave during the 1994 and 1997/1998 ENSO/IOD events coincided with a temporary absence of Mozambique Channel eddies and subsequently Agulhas rings. Therefore, reduced eddy formation in the Mozambique Channel and subsequently that from the Agulhas Retroflection may be a lagged response to SSH anomalies in the equatorial Indian Ocean generated by anomalous easterlies during El Niño events.

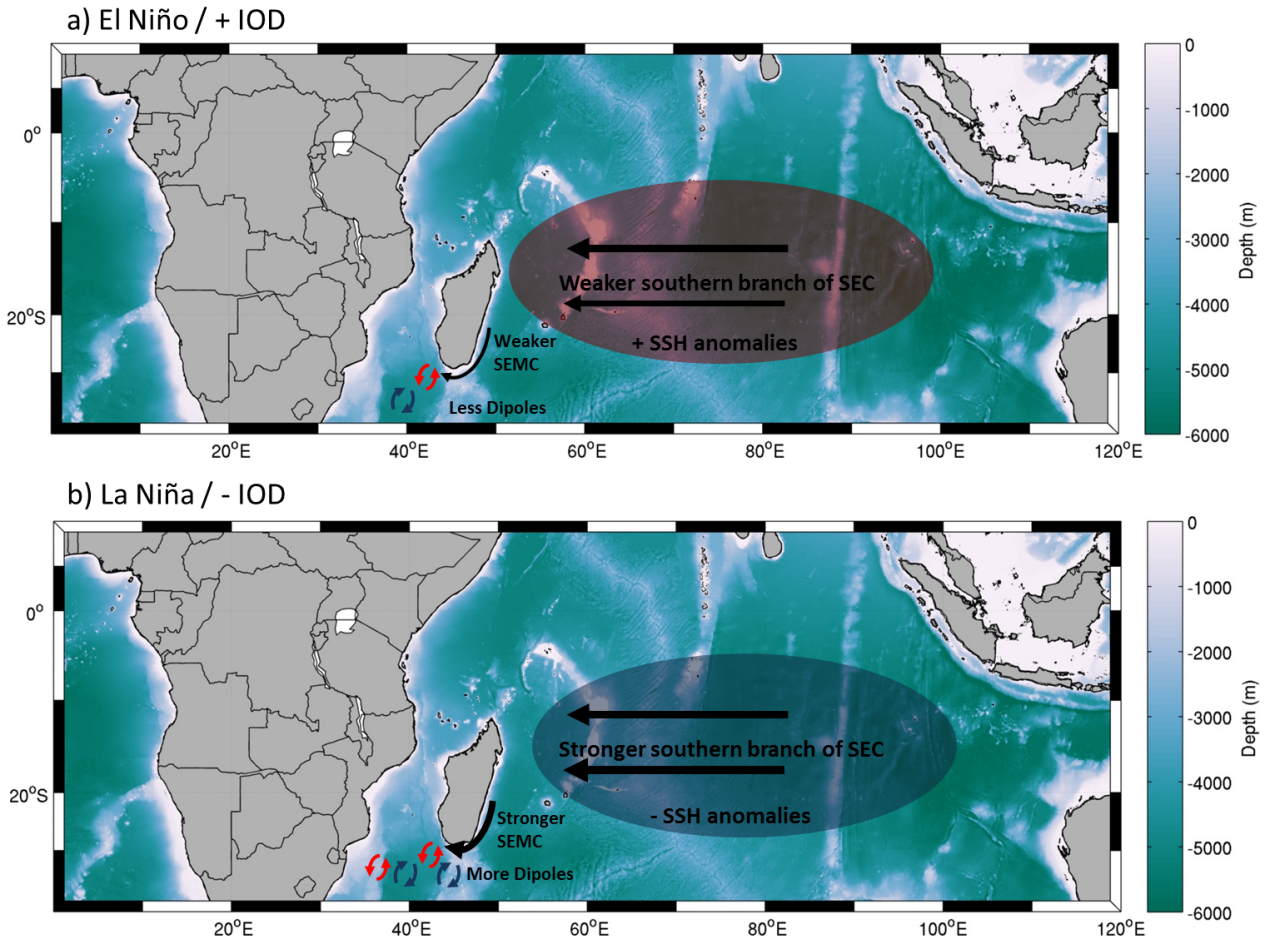

Figure 2.12: *Schematic of the relationship between ENSO/IOD and SSH anomalies in the Indian Ocean and the subsequent influence on the SEC and SEMC.*

de Ruijter et al. (2004) correlated SSH of the South Indian Ocean with SSH south of Madagascar and found that the period of highest SSH anomalies south of Madagascar coincides with La Niña/ negative IOD conditions over the Indian Ocean (Figure 2.12). The results of this study indicate that the southern branch and subsequently the SEMC, after separating from the Madagascan coast, intensifies during La Niña (Figure 2.12). Furthermore, increased dipole formation south of Madagascar were observed during La Niña periods, which, as theo-

retical studies have suggested (e.g Ou and de Ruijter, 1986), can be attributed to a stronger jet at separation which stimulates vortex formation (Figure 2.12). Additionally de Ruijter et al. (2004) suggests that reduced dipole formation during El Niño events is a result of a weaker, more stable jet. At the time of writing, no information was available on the response of the northern branch of the SEC and the NEMC jet to the ENSO.

2.2.4.2 IOD

Another example of a large scale mode of variability in the Indian Ocean is the Indian Ocean Dipole (IOD; Saji et al., 1999; Yamagata et al., 2003, 2004; Webster et al., 1999) which is defined by an east-west dipole pattern in sea surface temperature (SST) anomalies (Chang et al., 2006) and is phase-locked to the boreal summer and fall (Saji et al., 1999; Webster et al., 1999; Murtugudde et al., 2000). The independence of the IOD from ENSO has been an issue of much debate with some studies arguing that it is dependent on ENSO (Allan et al., 2003; Baquero-Bernal et al., 2002) while others claim it is an internal mode of the Indian Ocean (Saji et al., 1999; Webster et al., 1999; Rao et al., 2002).

The Dipole Mode Index (DMI), first introduced by Saji et al. (1999), represents the strength or phase of the IOD. The DMI is calculated as the difference between the area-averaged SST anomalies of the tropical western Indian Ocean (50°E-70°E, 10°S-10°N) and the tropical southeastern Indian Ocean (90°E-110°E, 10°S-0°; Saji et al., 1999). A positive (negative) IOD event is characterized by warmer (cooler) than normal SSTs in the western equatorial Indian Ocean and cooler (warmer) than normal SSTs in the eastern equatorial Indian Ocean (Saji et al., 1999). The atmospheric response to the anomalous SST is a basin-wide anomalous Walker circulation (Yamagata et al., 2002, 2003), which causes a reversal in the direction of the equatorial winds, from westerlies to easterlies during the peak phase

of positive events (Rao et al., 2002). These wind anomalies have a strong influence on thermocline (Feng and Meyers, 2003) and sea level anomalies (Rao et al., 2002). In the east, the sea level is anomalously lowered during positive IOD events while it is raised in the western and central Indian Ocean (Saji and Yamagata, 2003b). Theory predicts a baroclinic ocean response to wind anomalies in equatorial regions (McCreary and Anderson, 1984) and, in accordance, the thermocline anomalies have a sign opposing that of sea level (Saji and Yamagata, 2003b).

The initiation of the warming in the western Indian Ocean is a consequence of the changes in the eastern Indian Ocean. Positive IOD events are initiated by anomalous cooling of SSTs along the Sumatra-Java coast during May-June (Saji et al., 1999) which is a result of anomalous upwelling (Feng and Meyers, 2003). The enhanced cooling in the eastern Indian Ocean coupled with a westward wind anomaly over the equator incites rapid growth of the IOD (Feng and Meyers, 2003) which peaks in September-October with anomalously warmer SSTs over large parts of the western Indian Ocean (Saji et al., 1999). The lagged peak of a positive IOD event is a result of westward propagating, off-equatorial Rossby waves generated by the wind anomaly and associated Ekman pumping. These Rossby waves deepen the thermocline and warm the western Indian Ocean. A slow eastward propagation of the warm anomaly along the equator characterizes the decay of a positive IOD event (Feng and Meyers, 2003).

In "normal" years, the westerly winds in the equatorial Indian Ocean excite strong eastward surface jets during the monsoon transition periods known as Wyrtki jets (Wyrtki, 1973a). These jets accumulate warm water in the eastern equatorial Indian Ocean (Wyrtki, 1973a; Clarke and Liu, 1993; Yamagata et al., 1996) resulting in increased SSTs, sea level, and mixed layer thickness and a deeper thermocline in the east (Vinayachandran et al., 1999; Schott et al., 2009). This inhibits the cooling along the coast of Sumatra brought about by

evaporation, coastal upwelling and oceanic heat advection due to strong alongshore winds off the coast (Saji et al., 1999). During a positive IOD event, the Wyrtki jets are absent (Vinayachandran et al., 1999) and cooling dominates off Indonesia due to the extended trade winds with an easterly component along the Equator which prevents the intrusion of the equatorial current (Saji et al., 1999). The cooling off Indonesia is further enhanced by upwelling favourable alongshore winds (Vinayachandran et al., 1999). Thus, the normal heat supply to the coast off Sumatra is interrupted by the abnormally extended trade winds associated with positive IOD events.

The cooling in the eastern Indian Ocean associated with positive IOD events weakens the convection at the Intertropical Convergence Zone (ITCZ; Saji et al., 1999) which is normally associated with the convergence of the northeast and southeast trade winds. Subsequently, there is a northward extension of the southeast trade winds and convergence with the northeast trade winds occurs further downstream in response to the surface pressure modification. Convergence and moisture supply at the extended downstream end of the trade winds is enhanced by the altered large-scale wind pattern and encourages precipitation northwest of the normal position of the ITCZ (Saji et al., 1999). In the west, increased convergence, a result of the shifting trade winds, lead to reduced wind speed and reduced evaporation, consequently aiding in warming the SSTs. Increased rainfall, in turn, reduces the salinity of the surface waters which increases the stability of the surface waters and inhibits entrainment. The altered trade winds also result in reduced eastward transport which causes an anomalous deepening of the thermocline in the west. The warmer SST in the west introduces a positive feedback mechanism by increasing the precipitation anomaly and consequently the wind anomaly to its east (Saji et al., 1999). Therefore, precipitation increases over the western Indian Ocean and decreases over the ITCZ during positive IOD events.

The climate of many regions around the globe are significantly affected by the IOD (e.g. Ashok et al., 2003; Clark et al., 2003; Black et al., 2003; Ashok et al., 2001; Saji and Yamagata, 2003a; Behera et al., 2003; Saji et al., 1999) through changes in the global atmospheric circulation. For example, countries to the west of the Indian Ocean have anomalously high precipitation during positive IOD events (Clark et al., 2003; Black et al., 2003; Saji and Yamagata, 2003a; Behera et al., 2003; Singh, 2008) with anomalously low precipitation over countries to the east (Ashok et al., 2003, 2001; Saji and Yamagata, 2003a). This pattern of precipitation is a result of the underlying SST anomalies with cooler SSTs leading to less rainfall due to decreased evaporation and warmer SSTs enhancing precipitation due to enhanced evaporation. The enhanced rainfall also coincides with anomalous surface convergence and updrafts, while the decreased precipitation corresponds to anomalous surface divergence and downdrafts (Saji and Yamagata, 2003a). Not only does the IOD impact the Indian Ocean rim countries, it may also impact more remote regions. For instance, Saji and Yamagata (2003a) suggest that positive IOD events are associated with warm land surface anomalies and reduced rainfall over Europe, northeast Asia and South Africa.

Apart from the atmospheric response to the IOD, there is also an oceanic response. Palastanga et al. (2006) analysed the geostrophic anomalies of the subtropical gyre and the circulation in the western Indian ocean resulting from the large sea level anomalies associated with the IOD. These authors found that the SSH anomalies associated with the IOD resulted in a shift in the location and intensity of the tropical and subtropical gyres. More specifically, the positive (negative) SSH anomalies associated with positive (negative) IOD events weakens (strengthens) the surface flow of the SEC west of the Mascarene Plateau as well as the NEMC and SEMC. Subsequently, there is an intensification and northward (southward) extension of the subtropical (tropical) gyre.

Having discussed the oceanography and climate of the Comoros Basin and more broadly, the Indian Ocean, the next chapter presents analysis of some recent observations in the Comoros Basin.

Chapter 3

Observational Analysis

The majority of research efforts in the Mozambique Channel have been dedicated south of 15°S, in the form of a long term mooring array (LOCO) at the narrowest part of the channel (~16°S; Ridderinkhof and de Ruijter, 2003; Harlander et al., 2009; Ridderinkhof et al., 2010) and numerous cruises (e.g. di Marco et al., 2002, Donohue and Toole, 2003). The current knowledge on the circulation in the Comoros Basin, the region 9-15°S between northern Madagascar and Mozambique, is very limited and based on sparse observational data collected during the late 20th Century. These observational studies along with a recent modelling study (Biastoch and Krauss, 1999) imply that the circulation in the Comoros Basin consists of a large anti-cyclonic gyre termed the "Comoros Gyre" (Lutjeharms, 2006a). However, more recent studies have suggested that the circulation in the basin consists of meso-scale eddies that originate at the tip of Madagascar (Backeberg and Reason, 2010; van der Werf et al., 2010).

It is possible that, instead of a permanent feature, the "Comoros Gyre" inferred from sparse observational data, is a more sporadic occurrence and that the circulation in the Co-

moros Basin is dominated by meso-scale activity. Therefore, the objective of this chapter is to use hydrographical data from a dedicated cruise in the Comoros Basin and 19 years of satellite altimeter data to investigate the circulation in the basin. The hydrographic data, limited in its temporal and spatial resolution, provides a first glance of the water mass properties, and vertical structure in the Comoros Basin. The altimetry data, while providing only surface information, provides an indication of the permanence of the "Comoros Gyre" as well as the longer term meso-scale activity.

3.1 Data and Methods

3.1.1 Comoros Basin Cruise

A dedicated cruise took place in the Comoros Basin from 6 October to 3 November 2009 on board the *R/V Dr Fridtjof Nansen* as part of the Agulhas Somali Current Large Marine Ecosystem (ASCLME) Project (hereafter referred to as the Comoros Cruise). The location of the 133 hydrographic stations sampled during the cruise were designed to encompass the "Comoros Gyre", situated between 10°S and 15°S, as well as the inflow from the North-east Madagascar Current (NEMC; Figure 3.1). Station sampling, with the stations located 1-500km apart, commenced on 6 October 2009 with the stations along the inter-island transects S1 and S2 which were followed by a meridional section (S3) north of Grand Comoros. Sampling continued from the Comoros Island of Moheli to the west coast of Madagascar along a south-west section (S4 and S5). This was followed by a meridional section (S6) north off the northern tip of Madagascar. After transect S6, sampling continued between Madagascar and Mayotte along a zonal section (S7) which was followed by sections S8, S9

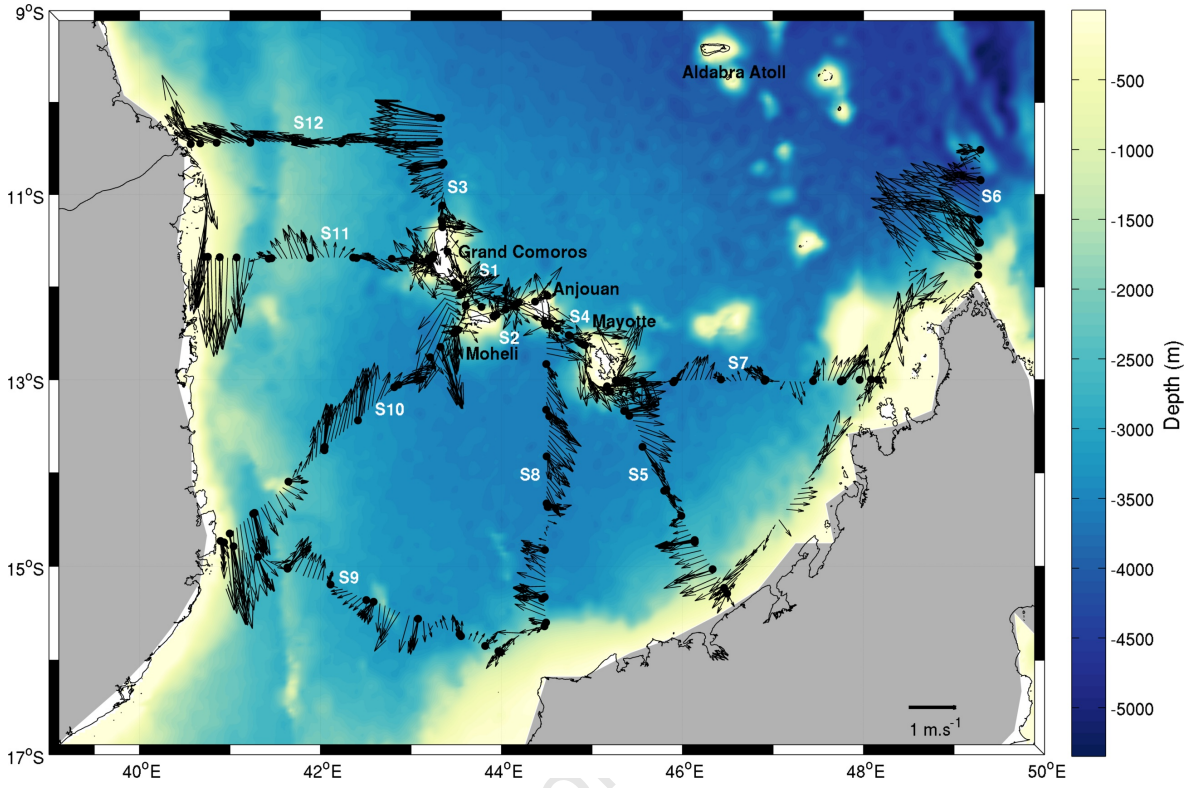

Figure 3.1: *Bathymetry (m) of the northern Mozambique Channel showing the location of the stations for which hydrographic data are presented. The vectors represent the ADCP velocities ($m{\cdot}s^{-1}$) averaged between 30-100m.*

and S10. The survey was completed with two zonal sections, S11 and S12, at approximately 11.7°S and 10.4°S, respectively. In total, 27 days were required to complete the hydrographic survey.

Hydrographic casts were performed with a 12-bottle rosette/CTD at each hydrographical station at depths up-to 3000m. In addition to temperature, and conductivity measurements, discrete measurements of oxygen were obtained for all stations through sub-sampling of the water samples collected in the Niskin bottles. Water samples were collected at a maximum of 12 depths distributed throughout the water column. The vertical profiles of current speed

and direction in the upper 300m were obtained from a vessel mounted 150-kHz Acoustic Doppler Current Profiler (ADCP). The ship's relative velocities were converted into absolute velocities using the Common Ocean Data Access System (CODAS) software package.

The ADCP data were averaged into 20 minute ensembles with depth bins set to 4m. Since the measurements were collected in regions where the depth exceeded the range of the ADCP bottom tracking, navigational data, provided by a Seapath DCPS system, and water tracking were used as reference to calculate the misalignment angle. ADCP currents include ageostrophic flows such as tides, drift currents and internal wave or inertial oscillations. Thus, relating ADCP currents to geostrophic velocities is fairly complicated. Donohue and Toole (2003) showed a tidal influence of around 5cm·s^{-1} in the Mozambique Channel and southeast of Madagascar. The barotropic tidal component was removed from the ADCP velocities using estimates from the OSU TOPEX/Poseidon Cross-over Global Inverse Solution, Version 6.2 (Egbert and Erofeeva, 2002). Geostrophic velocities in the bottom triangle were filled by extrapolating the velocity at the deepest common depth.

The method described in Osiński et al. (2003) were used to calculate the ADCP-referenced geostrophic velocities. This method uses a combination of CTD and ADCP measurements to compute the absolute ADCP-referenced velocity. The absolute ADCP-referenced velocity, $V_{abs}(p)$, is calculated as

$$V_{abs}(p) = V_R(p) + (V_{ADCP} - < V_R(p) >),$$

where $V_R(p)$ is the vertical profile of the baroclinic velocity and $<V_R(p)>$ is the baroclinic velocity averaged in the depth range 50-150m (Meinen et al., 2000). V_{ADCP}, the averaged ADCP velocity, is calculated as

$$V_{ADCP} = \frac{1}{X_2 - X_1} \times \frac{1}{Z_2 - Z_1} \int_{X_1}^{X_2} \int_{Z_1}^{Z_2} V \, dx dz,$$

where V is the measured ADCP velocity, X_1 and X_2 are the locations of two adjacent CTD stations and Z_1 and Z_2 are 50 and 150m, respectively. The depth range 50–150m was chosen as the layer where consistently accurate data is provided by the ADCP and where the ageostrophic signal is particularly weak.

3.1.2 Altimetry Data

Absolute dynamic topography (ADT), sea level anomalies (SLA) and absolute geostrophic velocities (AGV), obtained from the SSALTO/DUACS gridded data products were used in addition to the hydrographic data to investigate the circulation in the Comoros Basin. The absolute dynamic topography is calculated as the sum of the mean dynamic topography and satellite-observed sea level anomalies. The mean dynamic topography is calculated as the difference between the mean sea surface height and the geoid.

The SSALTO/DUACS gridded products were generated through the near-real time and delayed mode multi-mission altimeter data processing system at the Centre National d'Etudes Spatiales (CNES). The gridded data, merged from the multiple altimeter missions Jason-1, ERS-1/2, GFO, TOPEX/Poseidon and ENVISAT are binned into 7-day averages for the period 18 October 1992 to 28 December 2011 and have a 1/4° horizontal resolution. The altimetry data were firstly analysed for the four week period spanning the duration of the cruise (30 September 2009-04 November 2009) and subsequently for a 19 year (1993-2011) time period of weekly satellite derived data.

The SLA data were used to calculate the eddy kinetic energy (EKE) which can be used as

a measure of meso-scale variability (Ladd, 2007). EKE is estimated, assuming geostrophy, from the SLA (η') as

$$EKE = \frac{1}{2}\left[\left\langle U_g'^2 \right\rangle + \left\langle V_g'^2 \right\rangle\right]$$

where $\langle\rangle$ denotes the time average, and $U_g^{'}$ and $V_g^{'}$ are the geostrophic velocities calculated as

$$U_g^{'} = -\frac{g}{f}\frac{\triangle \eta'}{\triangle y}$$

$$V_g^{'} = \frac{g}{f}\frac{\triangle \eta'}{\triangle x}$$

where f is the Coriolis parameter.

3.1.2.1 Eddy detection and tracking Scheme

In addition to the aforementioned analyses, the long-term meso-scale activity in the Comoros Basin was assessed through an eddy identification and tracking scheme (Halo et al., 2013). This scheme was applied to the ADT data and uses physical criteria as well as geometric techniques to identify and track meso-scale eddies. A combination of positive values of the Okubo-Weiss parameter and the largest closed contour of ADT is used by the eddy identification scheme to detect both cyclonic and anti-cyclonic eddies. The Okubo-Weiss parameter (Okubo, 1970; Weiss, 1991) aims to separate a velocity field into regions of high deformation (strain) and high vorticity. By definition, an eddy consists of a region of high vorticity (eddy core) surrounded by an area experiencing high rates of strain (circulation cell). The Okubo-Weiss parameter (W) allows for the determination of regions that are either vorticity-

dominated (W<0) or strain-dominated (W>0; Henson and Thomas, 2008) and is calculated as

$$W = s_n^2 + s_s^2 - \omega^2$$

where ω is the vorticity, and s_n and s_s represents the normal and shear components of the strain, respectively. Vorticity, and the strain components are determined as follows

$$\omega = \frac{\partial v}{\partial x} - \frac{\partial u}{\partial y},$$

$$s_n = \frac{\partial u}{\partial x} - \frac{\partial v}{\partial y},$$

$$s_s = \frac{\partial v}{\partial x} + \frac{\partial u}{\partial y}.$$

The above mentioned eddy identification procedure was developed to increase the objectivity of eddy detection by minimizing the number of parameters. The selection criteria for the eddies specified by the user are in the form of a minimum or maximum size and minimum amplitude. From one time step to the next, the eddies which are closest in terms of spatial distance, shape and strength are considered to be the same eddy that has evolved with time. Eddies are filtered based on a minimum life-span to eliminate eddies of too short duration. As described in Chapter 2 section 2.2.2, eddies in the Mozambique Channel have diameters of between 300 and 350km (Harris, 1972; de Ruijter et al., 2002; Schouten et al., 2003) and sea surface height anomalies in the northern part of the channel have an amplitude of ~20cm (Schouten et al., 2003). Therefore, the maximum diameter and minimum amplitude was set

to 400km and 0.2m, respectively, and only eddies with a lifespan longer than 30 days were tracked.

3.2 Results

3.2.1 Hydrography

3.2.1.1 Surface and Central Waters (0-600m)

The surface water of the Comoros Basin displayed a spread of characteristics during the Comoros cruise that is typical of Tropical and Subtropical Surface waters (di Marco et al., 2002; Lutjeharms, 2006b). The upper 100m of the Comoros Basin is characterised by warm (Figure 3.2), high oxygen (4.4-5.2ml·m^{-1}), low salinity (Figure 3.3) Tropical Surface Water (Table 3.1; Figure 3.4). The low salinity of this water mass can be attributed to the influx of low-salinity Indonesian Throughflow Water (ITW) transported westward from the Pacific via the SEC (Wyrtki et al., 1971; Gordon et al., 1997) as well as surface warming and excess precipitation in the tropics, especially in the Bay of Bengal (Baumgartner and Reichel, 1975).

The freshest TSW (35psu) occurs at the air-sea interface along the southern part of section S6 (Figure 3.3f), indicating that this water mass enters the Comoros Basin via the northwestward flowing NEMC which obtains maximum surface velocities of >1m·s^{-1}. At approximately 10.8°S, the NEMC bifurcates along the African continent (Figure 3.1) into an equatorward and poleward branch which has mean surface velocities of ~0.7m·s^{-1}. The poleward branch transports TSW deeper into the Comoros Basin and Mozambique Channel where meso-scale eddies assist in mixing this water mass with more saline water masses and spreading it throughout the Mozambique Channel. Along section S12 (Figure 3.3l), TSW is

Table 3.1: *The depth, temperature and salinity ranges of the major water masses in the Comoros Basin.*

	Depth (m)	Temperature (°C)	Salinity (psu)
Upper layers			
TSW	0-100	24-30	34.9-35.1
ASHSW	0-100	24-28	35.1-35.5
STSW	100-400	14-22	35.2-35.5
EIOW	100-400	14-22	35-35.2
SICW	300-600	9-14	34.7-35.2
NICW	300-600	9-14	34.7-35.2
Intermediate layers			
AAIW	600-1500	4-9	34.6-34.8
RSIW	600-1500	4-9	34.7-35
Bottom layers			
NADW	1500-2500	1.5-2.5	34.75-34.77
LCDW	>2500	<3	<34.75

confined to the inshore stations (Figure 3.3l) coinciding with strong ($0.9 m \cdot s^{-1}$) equatorward flow suggesting that the northward transport of TSW into the East African Coastal Current (EACC) occurs primarily along the coast. The rest of the surface layer (0-100m) of section S12 is occupied by warm, saline Arabian Sea High Salinity Water (ASHSW; Table 3.1) which is found along all the sections (Figures 3.2, 3.3 and 3.4). This water mass, with oxygen concentrations similar to TSW, is formed in the Arabian Sea (Kumar and Prasad, 1999) and forms a shallow salinity maximum in the upper 50-100m. As ASHSW spreads south-southeastward it may reach as far south as the northern limit of the SEC (~10°S) where it may occur beneath or alongside TSW (New et al., 2007).

In the Comoros Basin, the strongest ASHSW signal is observed at the northernmost stations of sections S6, along part of S3 and along S12 (Figure 3.3c, f , l). Westward flow associated with the NEMC is observed along all three of these sections (Figure 3.1) indicating that the ASHSW entrained within the SEC flows into and across the Comoros Basin via

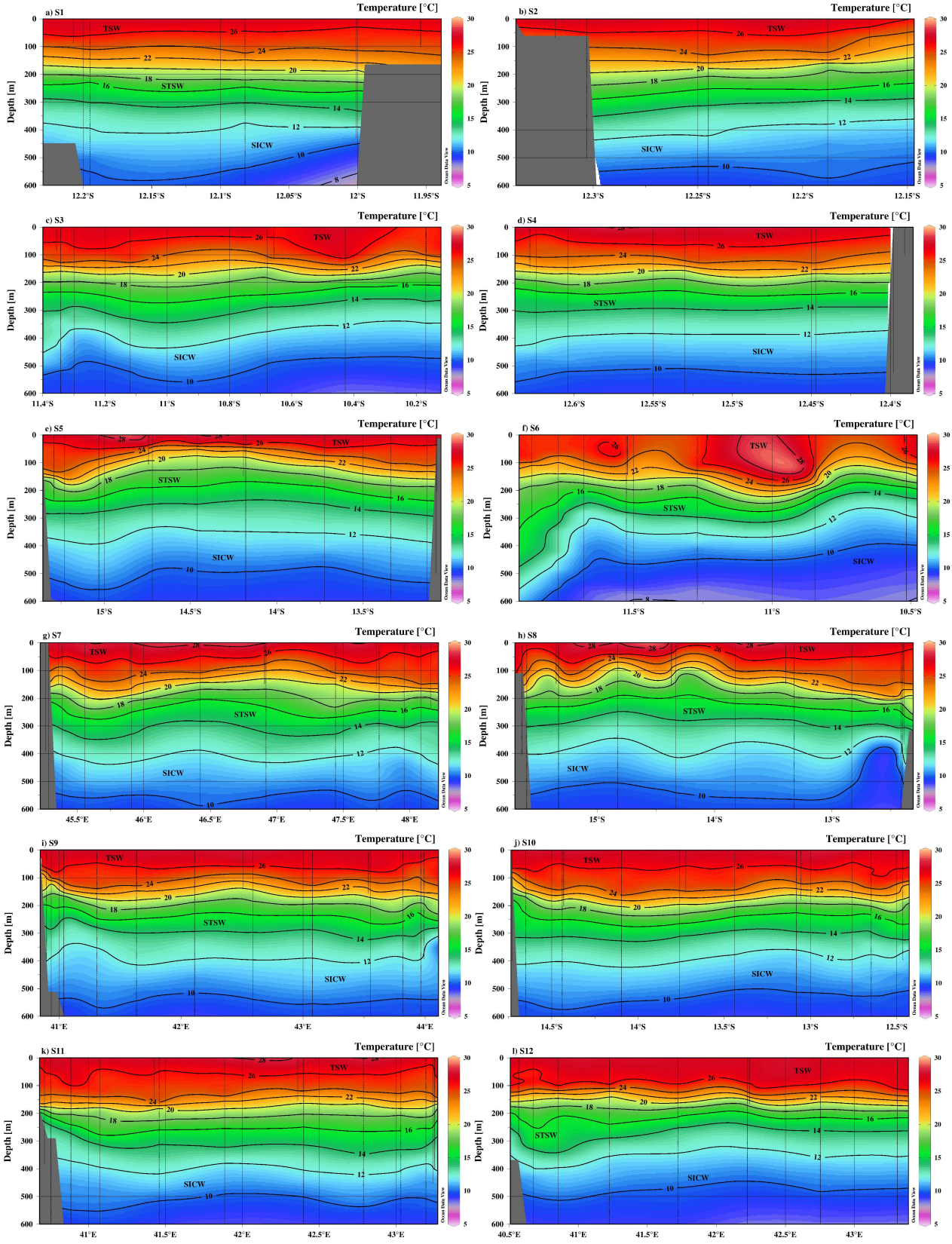

Figure 3.2: *The temperature (°C) in the upper 600m for transects S1 through S12. The contour interval is 2°C.*

the NEMC.

Most of the Comoros Basin below the surface layers of TSW and ASHSW, is dominated by high salinity, low oxygen Subtropical Surface Water (STSW; Table 3.1 and Figure 3.4). This water mass forms as a result of excess evaporation over precipitation in the subtropics (25-35°S; Baumgartner and Reichel, 1975; Warren, 1981). STSW reaches as far north as 15°S where it encounters the fresher ITW and TSW and is turned westward by the flow in the SEC (Wyrtki et al., 1971). The STSW enters the Comoros Basin via the NEMC as is evident from the westward flow dominating from the surface to ~250m at S6 (Figure 3.1) where high salinity values are also observed (Figure 3.3f). During the cruise, the most saline STSW within the Comoros Basin was found around the Comoros Islands and in the deep channels between the islands (Figure 3.3). The STSW can also influence the upper 100m as is observed along sections S5 and S8 (Figure 3.3e, h). In approximately the middle of section S5, there is a core of STSW that upwelled from a depth of about 200m (Figure 3.3e). The flow along the northern part of this section is towards the northeast while flow in the southern part is towards the southwest (Figure 3.1) suggesting that the upwelling of the high salinity water is a result of cyclonic circulation. Similarly, the flow pattern, eastward (westward) in the north (south) along the meridional transect S8 (Figure 3.1), as well as the upwelling of the isotherms and isohalines from a depth of about 200m in the southern most part of this section (Figures 3.2h and 3.3h) indicates that this section partially crossed a cyclonic eddy with an average speed of ~0.4m·d^{-1}. The sea level anomalies and geostrophic velocities confirm that transect S8 crossed the western edge of a cyclonic eddy centred at roughly 45.5°E (see section 3.2.2.1). This eddy appears to be the same eddy sampled during transect S5 that traveled southwest.

The influence of Equatorial Indian Ocean Water (EIOW) as termed by Lutjeharms (1991) can also be observed at depths of 100-400m (Figures 3.2 and 3.3). This water mass, also

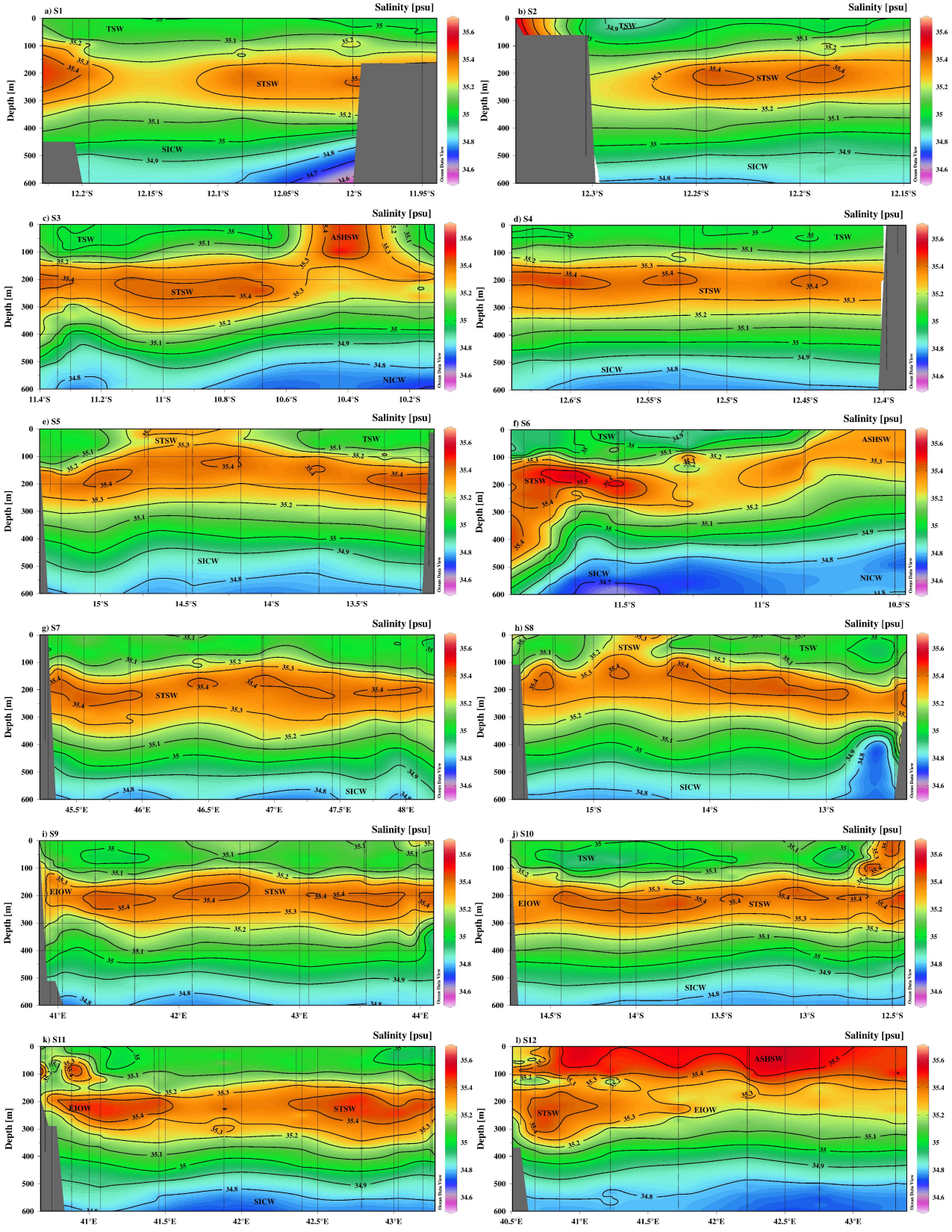

Figure 3.3: *The salinity (psu) in the upper 600m for transects S1 through S12. The contour interval is 0.1psu.*

known as Indian Equatorial Water (IEW; Sverdrup et al., 1942), has elevated nutrient values compared to TSW (Donohue and Toole, 2003) but, with temperatures similar to that of STSW, has a less extreme salinity maximum and lower oxygen values compared to STSW (Table 3.1 and Figure 3.4). The formation mechanism for EIOW has not been established as yet, but it has been suggested that this water type is simply a mixture of water masses from the Southern Hemisphere, Northern Hemisphere and from the Pacific (Sharma, 1976; Quadfasel and Schott, 1982; You and Tomczak, 1993). Within the Comoros Basin, this water mass is almost exclusively found hugging the African shelf along sections S9, S10 and S11 (Figures 3.2i, j, k and 3.3i, j, k) where strong southward flow ($0.7 m \cdot s^{-1}$) suggests that this water mass is transported south across the narrows into the southern part of the Mozambique Channel (Figure 3.1). Along section S12, there is a reversal with STSW along the shelf and EIOW off-shore (Figure 3.3l) as would be expected with a northward turning NEMC.

The major water mass around the thermocline depth (300-600m) is South Indian Central Water (SICW) with its characteristic oxygen maximum (Table 3.1 and Figure 3.4). In the Comoros Basin, SICW is recognised by its relatively linear θ/S relationship (Gründlingh et al., 1991) between approximately 9°C and 14°C (Figure 3.4). SICW dominates the central waters of all sections with the exception of transects S6 and S12 (Figures 3.2 and 3.3). At transect S6 high oxygen, low salinity South Indian Central Water (SICW) dominates in the southern part of the transect while North Indian Central Water (NICW), distinguished from SICW by its lower oxygen concentrations, dominates in the north (Figures 3.3f and Figure 3.4f). The low oxygen concentration associated with NICW stretches all the way to the surface while just to the south high oxygen concentrations associated with the water in the surface layers penetrates to a depth of 500m. The influence of NICW is also evident at the northernmost stations of transect S3 and along the inter-island sections.

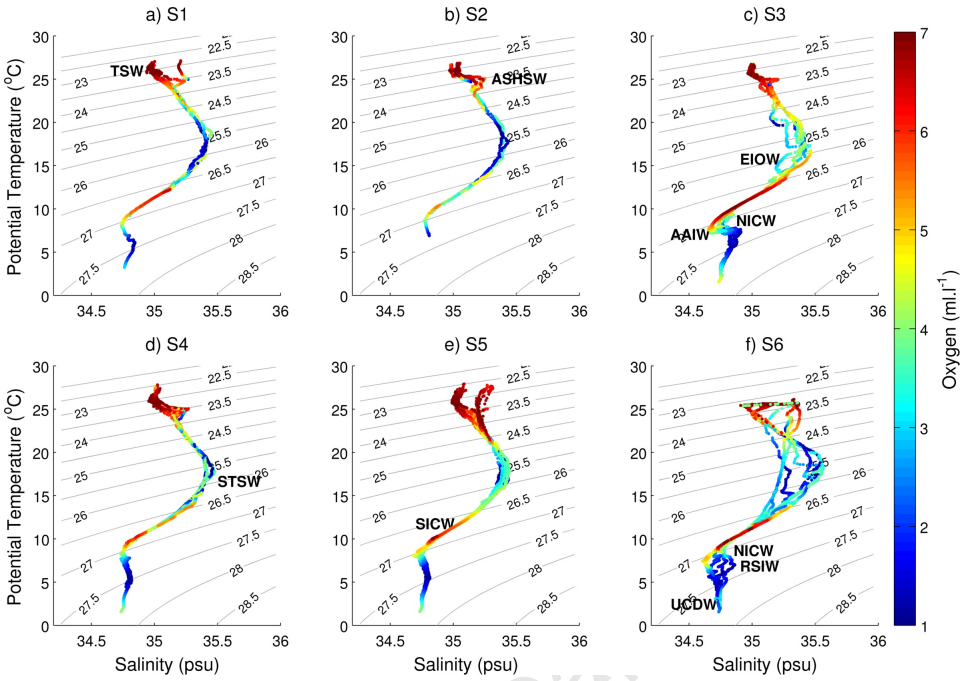

Figure 3.4: *Individual θ-S diagram for the all stations sampled along transects S1 to S6. The color represents oxygen concentration (ml·l^{-1}).*

3.2.1.2 Intermediate Waters (600-1500m)

The intermediate layers in the Comoros Basin during the Comoros Cruise consisted of low-salinity Antarctic Intermediate Water (AAIW) and high-salinity Red Sea Intermediate Water (RSIW; Table 3.1). AAIW, characterized by a salinity minimum and oxygen maximum (Figure 3.7), originates at the Sub-Antarctic Front as a result of excess precipitation over evaporation and enters the Indian Ocean from the southeast (Fine, 1993). RSIW is formed in the northern Red Sea where evaporation rates exceed precipitation rates resulting in the formation of this high salinity, low oxygen water mass (Morcos, 1970; Bower et al., 2000).

AAIW is transported within the equatorward Mozambique Undercurrent (de Ruijter et al., 2002) which, flowing along the continental slope, consists of two cores. The one core, flowing

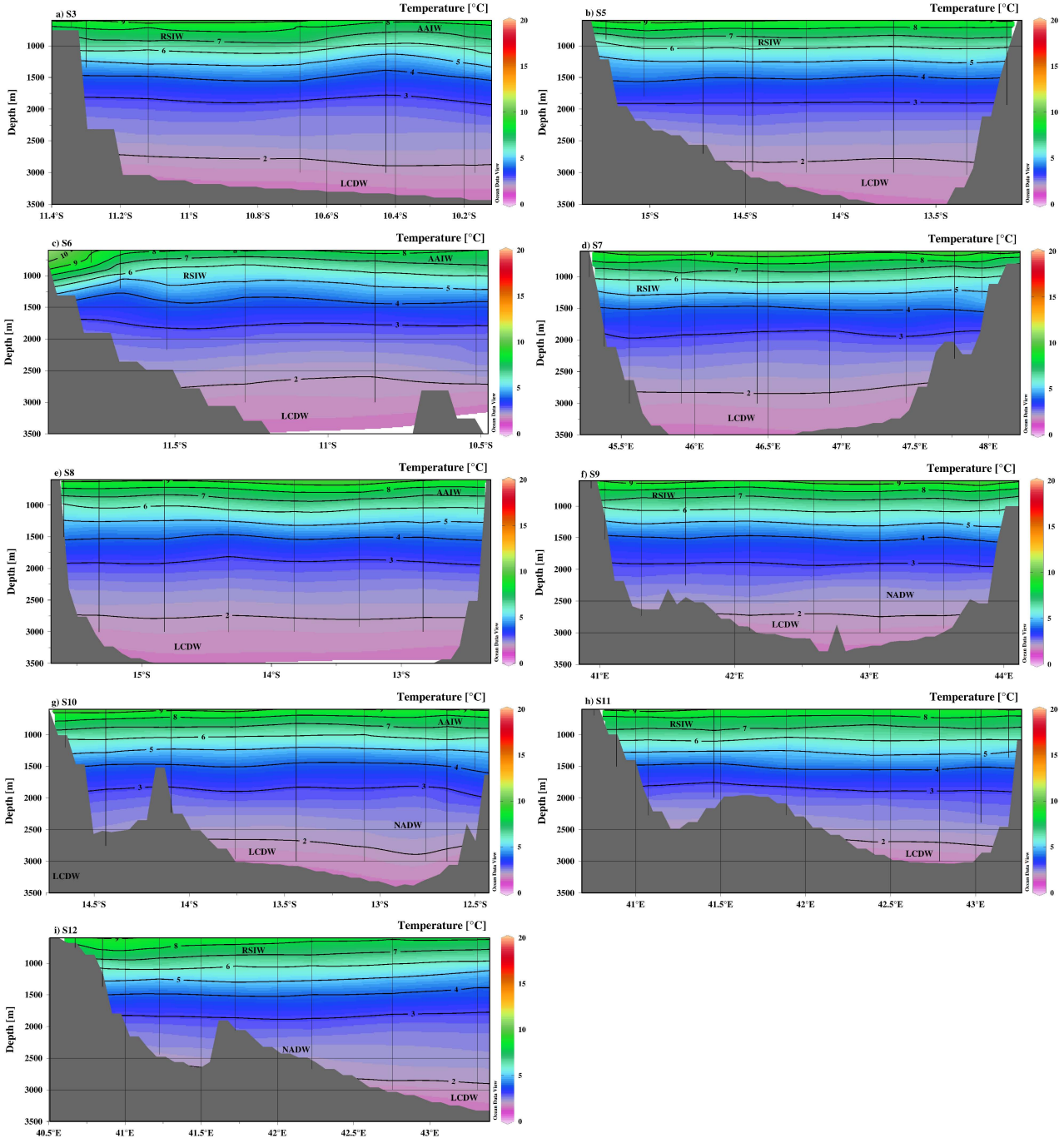

Figure 3.5: *The temperature (°C) at depths greater than 600m for transects S3 and S5 through to S12. The inter-island transects (S1, S2 and S4) only sampled to depths of ~600m and therefore are not presented here. The contour interval is 1°C.*

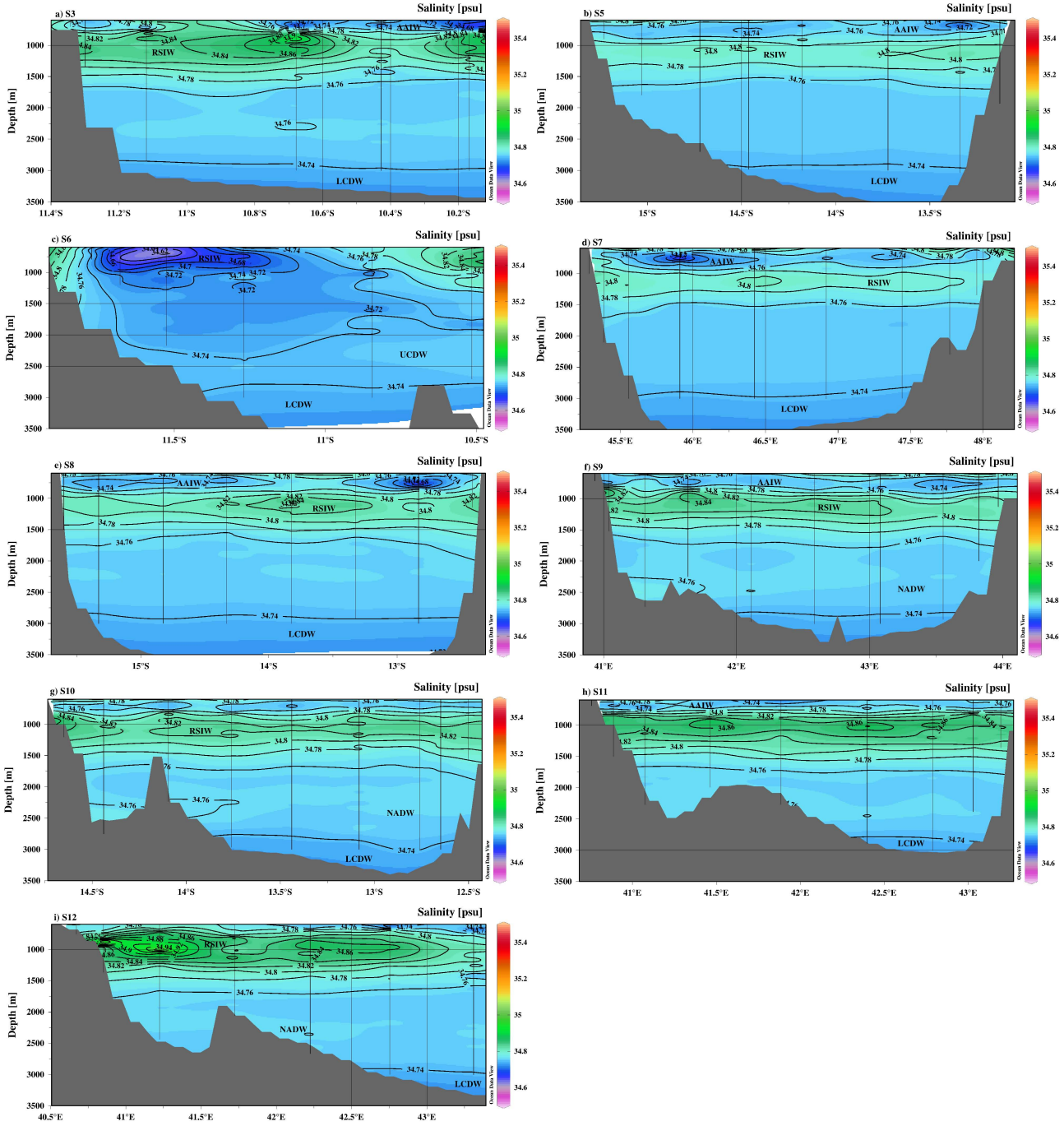

Figure 3.6: *The salinity (psu) at depths greater than 600m for transects S3 and S5 through to S12. The inter-island transects (S1, S2 and S4) only sampled to depths of ~600m and therefore are not presented here. The contour interval is 0.02psu.*

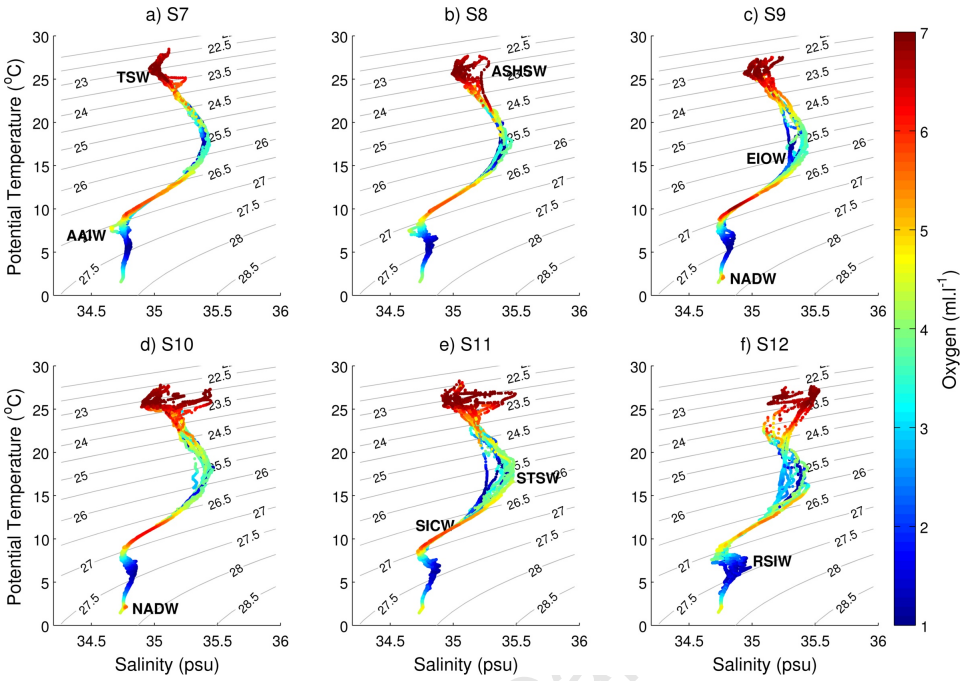

Figure 3.7: *Individual θ-S diagram for all stations sampled along transects S7 to S12. The color represents oxygen concentration (ml·l^{-1}).*

at intermediate levels, transports AAIW northward along the continental slope into the Comoros Basin. Di Marco et al. (2002) proposed a secondary route of AAIW into the Comoros Basin. These authors suggest that AAIW moves north within the interior of the Indian Ocean and continues west around Cape Amber, the northern tip of Madagascar, within the SEC. During the Comoros cruise, the freshest AAIW occurred in the northern parts of transect S3 and along transect S6 (Figure 3.6a and c) indicating that this water mass enters the Comoros Basin within the westward flowing NEMC supporting the route proposed by di Marco et al. (2002). More saline AAIW were observed along sections S5, S7 and S8 (Figure 3.7b, d, e) which suggests mixing of this water mass with RSIW. As noted above, sections S5 and S8 sampled through a cyclonic eddy indicating that the mixing of AAIW and RSIW may have

occurred within this eddy. Section S7 was sampled after the passing of the eddy and therefore the mixed AAIW is evident at this section as well.

RSIW was observed along all the sections over the neutral density layer 27.2-27.55kg·m^{-3} (Figure 3.7) with the most saline RSIW observed along transect S12 (Figure 3.6i). The more pronounced signal of RSIW in the west indicates that the southward spreading of this water mass occurs primarily between the African continent and the Comoros Islands. This is consistent with the southward spreading of this water mass from the north into the Mozambique Channel along the western boundary of the Indian Ocean as noted by Beal et al. (2000). The influence of RSIW is observed throughout the Comoros basin, indicating that similar to the transport of this water mass through the Mozambique Channel (de Ruijter et al., 2002; Roman and Lutjeharms, 2009), it spreads throughout the basin at intermediate levels within the core of meso-scale eddies.

3.2.1.3 Deep and Bottom Waters (1500-3500m)

At the time of the cruise, the deep and bottom waters of the Comoros Basin comprised of high salinity, oxygen rich North Atlantic Deep Water (NADW), the saline, nutrient rich North Indian Deep Water (NIDW) as well as Upper (UCDW) and Lower Circumpolar Deep Water (LCDW; Table 3.1). Similar to AAIW, NADW is transported equatorward within the Mozambique Undercurrent but within the core flowing below 2000m as a narrow jet (de Ruijter et al., 2002). The Madagascar Ridge south of Madagascar, and the Davie Ridge in the north of the Mozambique Channel, significantly constrain the northward spreading of NADW (Ullgren et al., 2012). A number of authors (e.g. Toole and Warren, 1993; Mantyla and Reid, 1995) assume that this water mass cannot pass over the Davie Ridge and therefore is assumed to be absent from the Comoros Basin. However, van Aken et al. (2004) noted the influence of

NADW to depths of ~2000m, and with a sill depth of ~2500m in the Mozambique Channel this water mass is capable of spreading northward through the Mozambique Channel and into the Comoros Basin. During the time of the cruise, the high salinity, oxygen rich signature of NADW was strongest along sections S9 and S10 (Figure 3.7c and d) but its influence could be seen as far north as section S12 at 10.5°S in the depth range 2400-2600m (Figure 3.6i). This signal of NADW within the Comoros Basin suggests that, initially, it flows along the African slope and the western slope of the Davie Ridge. After passing over the ridge, as suggested by van Aken et al. (2004), this water mass flows along the eastern slope of the ridge probably due to a topographic blockage at 14°S.

LCDW was observed along all the sections below 2500m. UCDW influence can be clearly observed in the NEMC (S6) characterized by significantly fresher salinities over the potential temperature range 2.2-4°C (Figure 3.4f). Within the basin, an almost isohaline layer is observed between 2.2-3°C which lies either between the intermediate water and LCDW or NADW (Figure 3.6). This layer has a higher salt content than the UCDW observed in the NEMC (S6) indicating the influence of NIDW. The slight salinity minimum around ~3°C however, still indicates some UCDW influence, whilst the salinity maximum between 2-2.5°C shows stronger NIDW influence. In this range, NIDW can be clearly distinguished from NADW by its lower oxygen signature.

3.2.2 Altimetry

3.2.2.1 Cruise Altimetry

In the time-mean ADT and AGV for the period surrounding the Comoros Cruise (30 September - 4 November 2009) two strong currents are observed: the NEMC flowing west past the

tip of Madagascar and a southward flowing current along the coast of Mozambique (Figure 3.8). In the altimeter data, the NEMC bifurcates at the East African coast at ~10.8°S (Figure 3.8) which is in good agreement with the bifurcation point observed in the ADCP data (Figure 3.1). The mean geostrophic velocity ($0.5 m \cdot s^{-1}$) of the NEMC is comparable to the mean speed calculated from the ADCP data at a depth of ~30m (Table 3.2). However, the maximum velocity measured by the ADCP at the northern tip of Madagascar is twice that observed in the altimetry data.

The poleward flowing current along the western boundary of the Comoros Basin is in agreement with the southward flow observed at the coastal stations along sections S11 and S10 (Figure 3.1) as well as with the strong southward current that Harlander et al. (2009) and Ridderinkhof et al. (2010) found in the current meter data from a mooring across the Mozambique Channel. As observed for the NEMC, the mean geostrophic velocity of this current is comparable to the mean speed calculated from the ADCP data while the maximum geostrophic velocity is slightly lower than the maximum speed measured during the Comoros cruise (Table 3.2). Although the ADCP velocity field contains ageostrophic contributions other than the barotropic tide which was removed, the good agreement between the ADCP velocity field and the satellite derived geostrophic velocities indicate that these contributions are small in comparison to the main westward and southward flow in the Comoros Basin. The underestimation of the maximum velocity of both the NEMC and southward current in the altimetry data can possibly be attributed to the fact that this data has a temporal resolution of seven days, whereas the cruise measurements were instantaneous. In addition, the spatial smoothing of the altimeter data can also result in an underestimation of the maximum velocities.

At the start of the Comoros Cruise, an anti-cyclonic eddy was present in the southern part

Table 3.2: *The mean and maximum geostrophic and ADCP velocities ($m \cdot s^{-1}$) of the NEMC and the poleward current as well as the cyclonic eddy.*

	Maximum	Mean (std)
NEMC at 49.2°E		
AVISO	0.7	0.5 (0.2)
ADCP	1.4	0.5 (0.3)
NEMC at 43.4°E		
AVISO	0.7	0.5 (0.2)
ADCP	0.7	0.5 (0.2)
Poleward Current at ~11.7°S		
AVISO	0.5	0.4 (0.1)
ADCP	0.7	0.4 (0.2)
Poleward Current at ~15°S		
AVISO	0.5	0.4 (0.1)
ADCP	1.0	0.6 (0.3)
Cyclonic westward		
AVISO	0.7	0.6 (0.1)
ADCP	1.1	0.7 (0.3)
Cyclonic eastward		
AVISO	0.6	0.5 (0.1)
ADCP	0.9	0.5 (0.3)

of the Comoros Basin, centred at about 42.5°E, 15°S, and traveled south through the narrows of the channel (Figures 3.9). The absolute geostrophic velocities show that relatively strong (0.4-0.7$m \cdot s^{-1}$) anti-cyclonic circulation is associated with this eddy which dissipates along its southward trajectory (Figures 3.9). Even though this anti-cyclonic eddy was located in the basin during the cruise, it was not sampled and therefore no evidence of it was present in the hydrographic data.

During the time of the cruise, a cyclonic eddy is evident in the Comoros Basin confirming the cyclonic circulation observed in the ADCP data (Figure 3.8). The weekly averaged ADT and AGV for the cruise period reveals that the cyclonic eddy had a southwestward trajectory

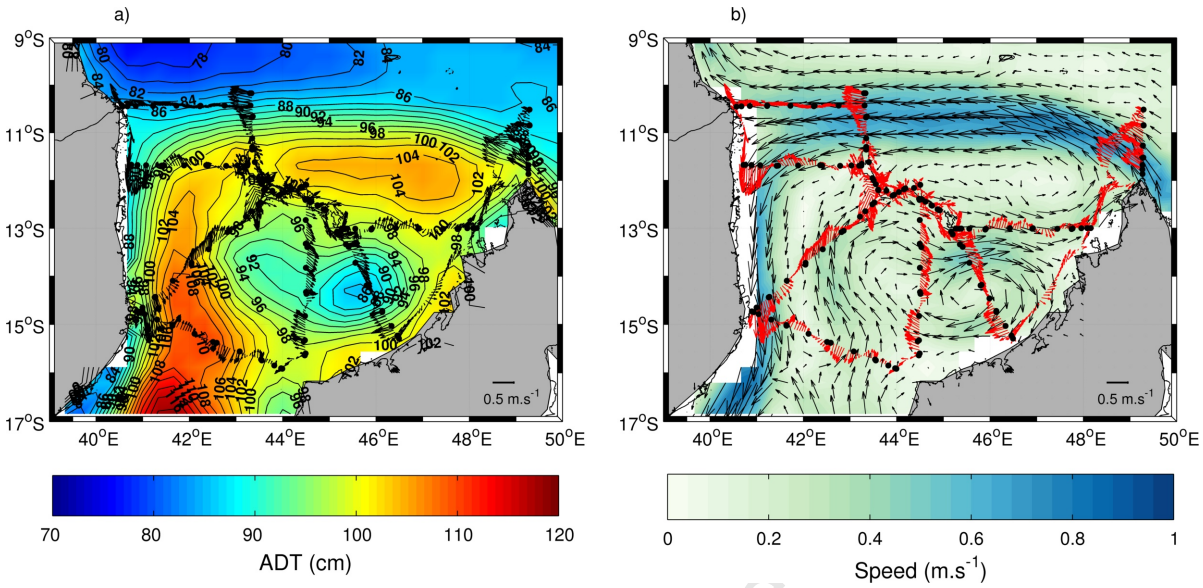

Figure 3.8: *a) Time averaged absolute dynamic topography (cm) and b) absolute geostrophic velocities (m·s^{-1}) for the time period 30 September - 4 November 2009. The black circles indicate the position of the cruise hydrographic stations. The contours in (a) are at 2cm intervals. The black and red vectors in (a) and (b) represent the ADCP velocities (m·s^{-1}) averaged between 30-100m.*

and weakened as it propagated (Figures 3.9). At the start of the cruise (late September to early October), this cyclone, centred at approximately 46°E and 13.5°S obtained maximum speeds of roughly 0.8m·s^{-1} with an average of about 0.7m·s^{-1} (Figures 3.9 a). At the end of the cruise period (early November), the velocities of the cyclone, now centred at about 44°E, 14.5°S, had decreased to an average of about 0.6m·s^{-1} (Figures 3.9 d). The mean westward and eastward geostrophic velocities of the cyclonic eddy, corresponding temporally and spatial with the cruise transect S5 which sampled the eddy, is in good agreement with the mean velocities calculated from the ADCP data at ~30m (Table 3.2). However, as observed for the two main currents, the altimeter data underestimates the maximum velocities.

The eddy detection scheme, described in section 3.1.2, first detected the cyclonic eddy present in the basin during the cruise on 17 June 2009 and it had dissipated by 4 November

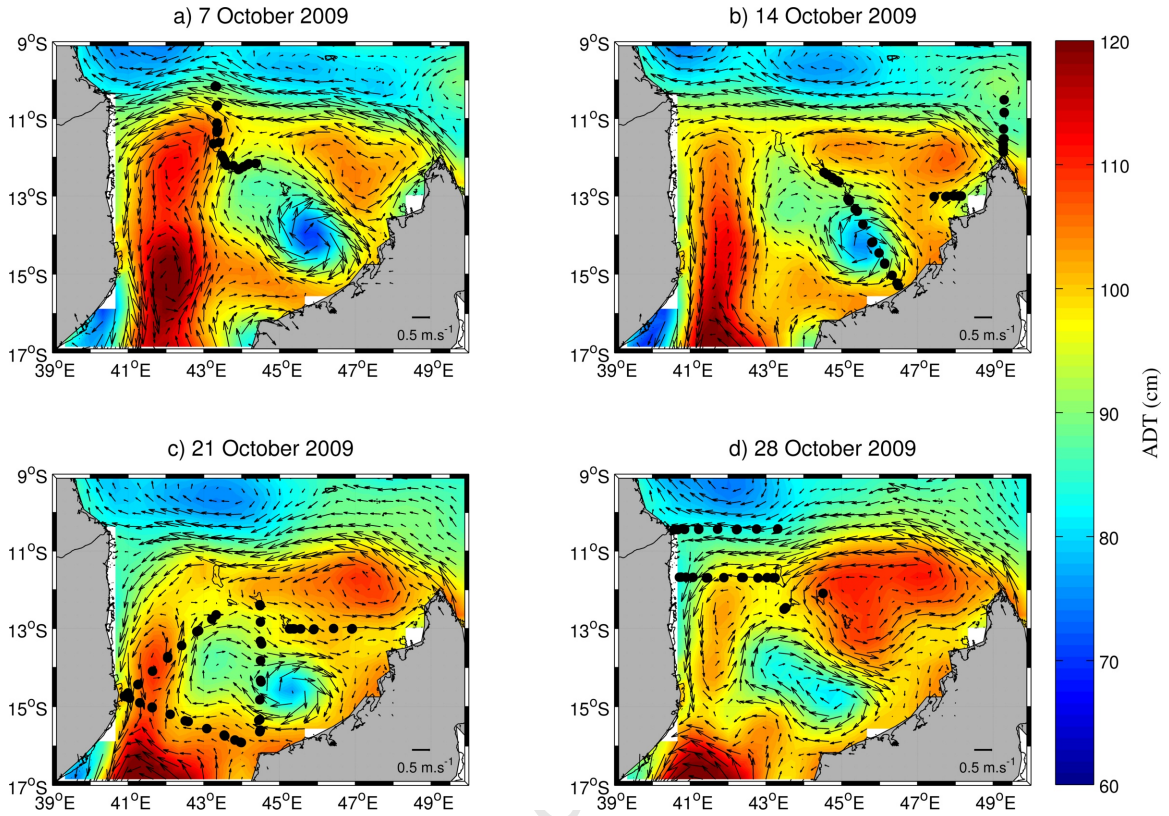

Figure 3.9: *Weekly means of absolute dynamic topography (cm) for the duration of the cruise and the hydrographic stations (black circles) sampled during the respective weeks. The vectors indicate the absolute geostrophic velocities (m·s^{-1}).*

2009. This cyclonic eddy, with a translation speed of 1.5km·day^{-1} and mean diameter of 160km, had a lifespan of 133 days all of which were spent in the Comoros Basin. The amplitude of this cyclonic eddy, which is an indicator of the strength of the eddy, decreased from 0.2m at the start of the cruise (30 September 2009) to 0.1m at the end of October (28 October 2009) confirming that it weakened along its southwestward trajectory.

The altimeter data, for the period of the Comoros cruise, indicates that the circulation in the Comoros Basin consists of both anti-cyclonic and cyclonic eddies. Even though, eddies of both polarities were present during the time of the cruise, only the cyclonic eddy was

sampled. The hydrographic data, therefore is not representative of both meso-scale eddies as a result of the timing of the sampling.

3.2.2.2 Variability in the Comoros Basin

Sætre and da Silva (1984) as well as Donguy and Piton (1991), analysing various hydrographic data sets, alluded to a seasonality of the circulation in the Comoros Basin as a result of the wind forcing. Wavelet analysis (described in detail in Chapter 4, section 4.3.2) of the monthly means of each observation in the domain 6-20°S and 35-55°E for the period 1993-2011 indicates a strong annual, semi-annual and 3-monthly (meso-scale) signal in the Comoros Basin (not shown). The semi-annual signal is related to the monsoonal winds which influence the Mozambique Channel as far south as 15°S (Woodberry et al., 1989). Seasonal means of ADT and AGV for the two monsoon seasons, the Southwest (JAS) and Northeast (JFM) monsoon, is used to further investigate the semi-annual signal. Individual monthly means for the period 1993-2011, derived from the weekly averaged ADT data, were used to compute seasonal means of ADT and AGV.

The seasonal mean absolute geostrophic velocities confirm that the circulation in the Comoros Basin is dominated by the northwest flowing NEMC and a strong poleward current along the east coast of Mozambique (Figure 3.10) as observed during the Comoros Cruise (Figure 3.1) and in the altimeter data covering the cruise period (Figure 3.8b). The NEMC has an increased intensity during the southwest monsoon (Figures 3.10b), while the poleward current along the coast of Mozambique is stronger during the Northeast monsoon (Figures 3.10a). The intensification of the NEMC coincides with increased wind speed at the northern tip of Madagascar (Figure 3.11a) due to a strong wind jet of southeasterlies which develops during the Southwest monsoon (see Chapter 4, section 4.4.2). The strengthening (weakening)

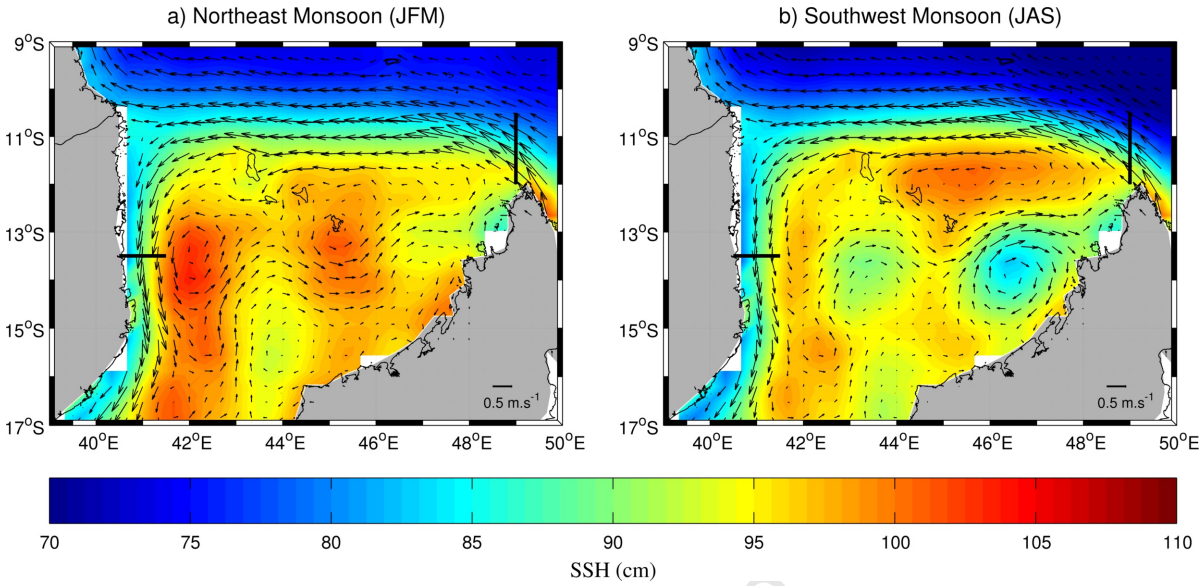

Figure 3.10: *Absolute dynamic topography (cm) for the a) Northeast monsoon and b) Southwest monsoon with the absolute geostrophic velocities ($m{\cdot}s^{-1}$) overlaid (vectors). The black lines indicate the meridional and zonal sections used to calculate the annual cycle of the NEMC and poleward current presented in Figure 3.11.*

of the poleward current during the Northeast (Southwest) monsoon coincides with decreased (increased) wind speeds (Figure 3.11b). Northwesterlies dominate over the Comoros Basin during the Northeast monsoon and flowing in the direction of the poleward current act to strengthen the poleward flow along the east coast of Mozambique. Conversely, southwesterlies dominate over the basin during the Southwest monsoon which exert an opposing force on the poleward current, thus weakening it.

In addition to the above mentioned currents, the seasonal means of ADT and AGV indicate that both anti-cyclonic and cyclonic eddies occur in the Comoros Basin (Figure 3.10). During the Northeast monsoon (Figure 3.10a), two anti-cyclones dominate in the basin. On the other hand, two cyclonic eddies, dominate in the Comoros Basin during the Southwest Monsoon (Figure 3.10b). In addition, anti-cyclonic circulation is observed north of 13°S

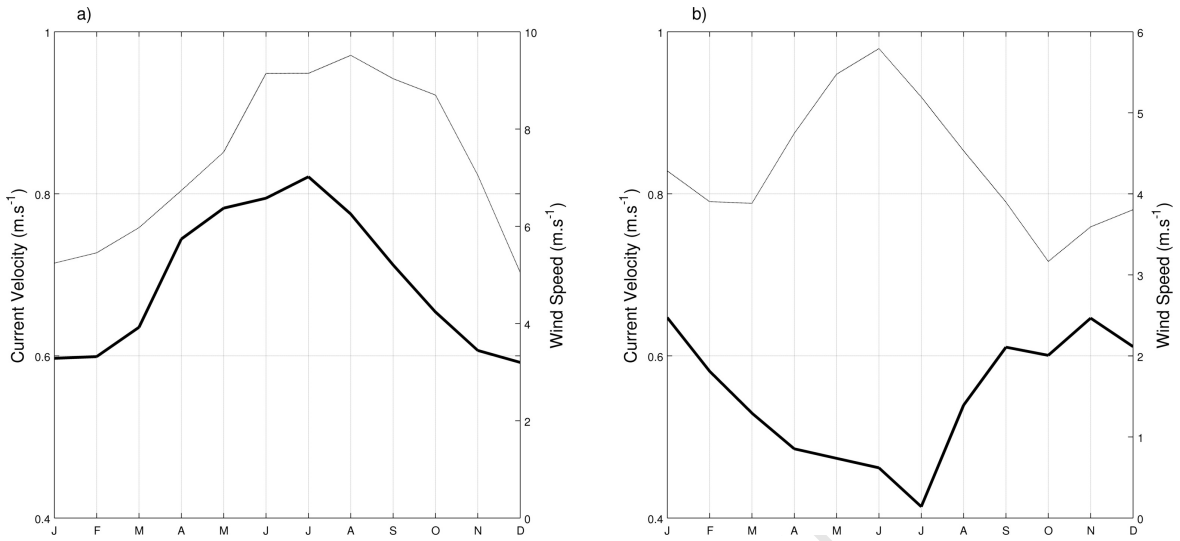

Figure 3.11: *The annual cycle of geostrophic velocities (solid line) and wind speed (dashed line) averaged over the a) NEMC and b) poleward current.*

during the Southwest monsoon.

To further investigate the meso-scale variability in the Comoros Basin, weekly averages of ADT and AGV were visually analysed. Several co-occurring cyclonic, and anti-cyclonic features dominate the flow field of the basin. However, at times, no distinct meso-scale eddies are evident in the weekly averages. Occasionally, the flow of the meso-scale eddies as well as that of the two main currents, the NEMC and the poleward current along Mozambique, appear to interact to form a large recirculation feature in the Comoros Basin. This recirculation feature does not occupy the whole of the basin all of the time. To illustrate the interaction of the meso-scale features, two weekly means (6 December 2000 and 26 September 2007) representing the two scenarios are considered in detail.

A prominent anti-cyclonic eddy (AC1) along the coast of Mozambique and a cyclonic eddy (C1) to the east of it is displayed in the weekly mean ADT and AGV of 6 December 2000 (Figure 3.12a). In addition, there are two weak anti-cyclonic features, one to the north

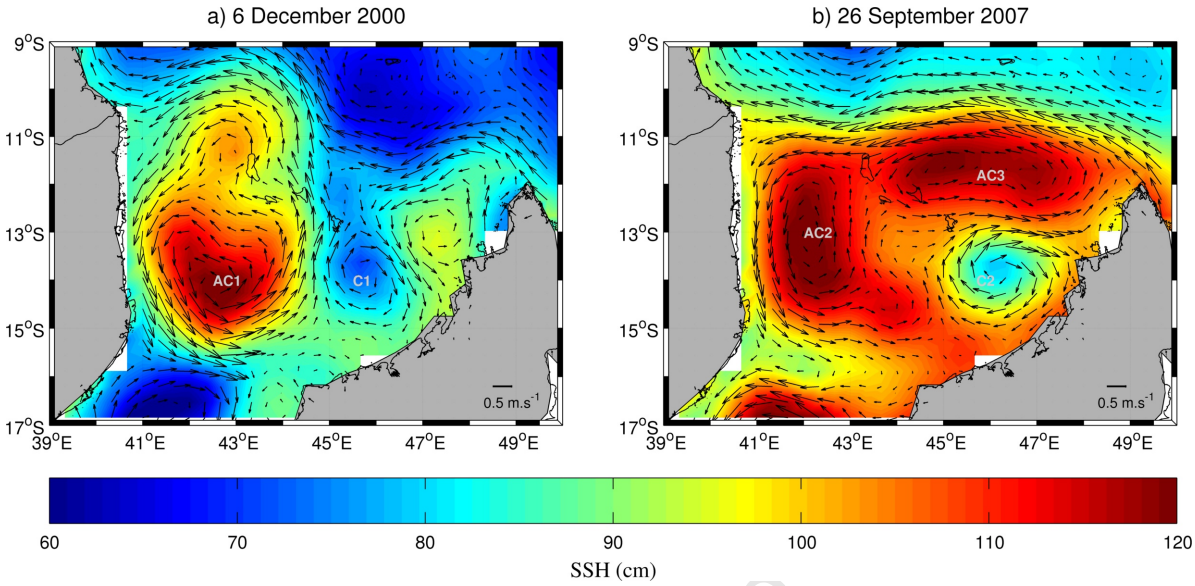

Figure 3.12: *Weekly snapshots of absolute dynamic topography (cm) and absolute geostrophic velocities ($m{\cdot}s^{-1}$) for a) 6 December 2000 and b) 26 September 2007.*

of AC1 and the other to the northeast of C1. The southward current along the Mozambique coast forms the western edge of AC1. South of 15°S, AC1 interacts with a cyclone where the channel is narrowest and this results in a more southeastward flow along the coast of Mozambique (Figure 3.12a). Part of the northward eastern edge of AC1 continues north to merge with the westward flow in the NEMC and is recirculated in AC1 thus creating a large anti-cyclonic recirculation cell in the western part of the Comoros Basin (Figure 3.12a).

The weekly mean ADT and AGV of 26 September 2007 displays two large anti-cyclonic eddies in the Comoros Basin, one along the coast of Mozambique (AC2) and the other west of the tip of Madagascar (AC3; Figure 3.12b). In addition, a cyclonic eddy (C2) is present along the northwest coast of Madagascar. The northern edge of both AC2 and AC3 is formed by the NEMC and the poleward current along the Mozambican coast forms the western edge of AC2. Part of the poleward flow turns eastwards north of 15°S forming the southern edge of

AC2 while the rest continues south into the Mozambique Channel (Figure 3.12b). Part of the eastern flow turns north to complete the recirculation of AC2, while the rest continues to the east. At approximately 45°E, the eastward flow from AC2 encounters the westward flow of C2 which steers it to the north and, subsequently, it circulates back into AC2. The northward flow of AC2 interacts with the southward edge of AC3 at about 12.5°S and merges with the eastward edge of the latter. The eastward northern edge of C2 also interacts with the eastward southern edge of AC3 (Figure 3.12b). As the eastward flow of AC3 and the C2 encounters the shelf edge of Madagascar, it is steered towards the north merging with the westward flow of the NEMC and completing the recirculation.

3.2.2.3 Eddy Kinetic Energy

Globally, eddy kinetic energy ranges from 0 to approximately 2000$cm^2 \cdot s^{-2}$ (Shum et al., 1990; Thoppil et al., 2011) with the highest EKE values associated with the variability of western boundary current systems. The mean EKE in the Comoros Basin, calculated for the 19 year period 1993-2011, ranges from 100 to 1200$cm^2 \cdot s^{-2}$ with a mean value of approximately 400$cm^2 \cdot s^{-2}$ (Figure 3.13a). These values are comparable with the EKE associated with the Gulf Stream (Shum et al., 1990; Brachet et al., 2004) and the Kurishio Current (Shum et al., 1990), however the maximum EKE values observed in the Comoros Basin are slightly lower than that of these two currents. The lowest energies (<300$cm^2 \cdot s^{-2}$) are observed to the north of the tip and along the northwest coast of Madagascar while the highest energies (>600$cm^2 \cdot s^{-2}$) occur south of the Comoros Islands (south of 13°S) along the coast of Africa. The area of maximum EKE (>1000$cm^2 \cdot s^{-2}$), along the African coast in the narrows of the channel, is associated with the southward propagation of Mozambique Channel eddies from the Comoros Basin into the channel (Harlander et al., 2009). North of the Comoros Is-

lands there is a region of moderately high energy (>400cm^2·s^{-2}) which corresponds with the meso-scale activity associated with the NEMC. Another region of moderately high energy is located along the west coast of Madagascar associated with a recurrent cyclonic eddy. The high mean EKE in the Comoros Basin suggests that this region is highly dynamic and the variability is dominated by meso-scale features.

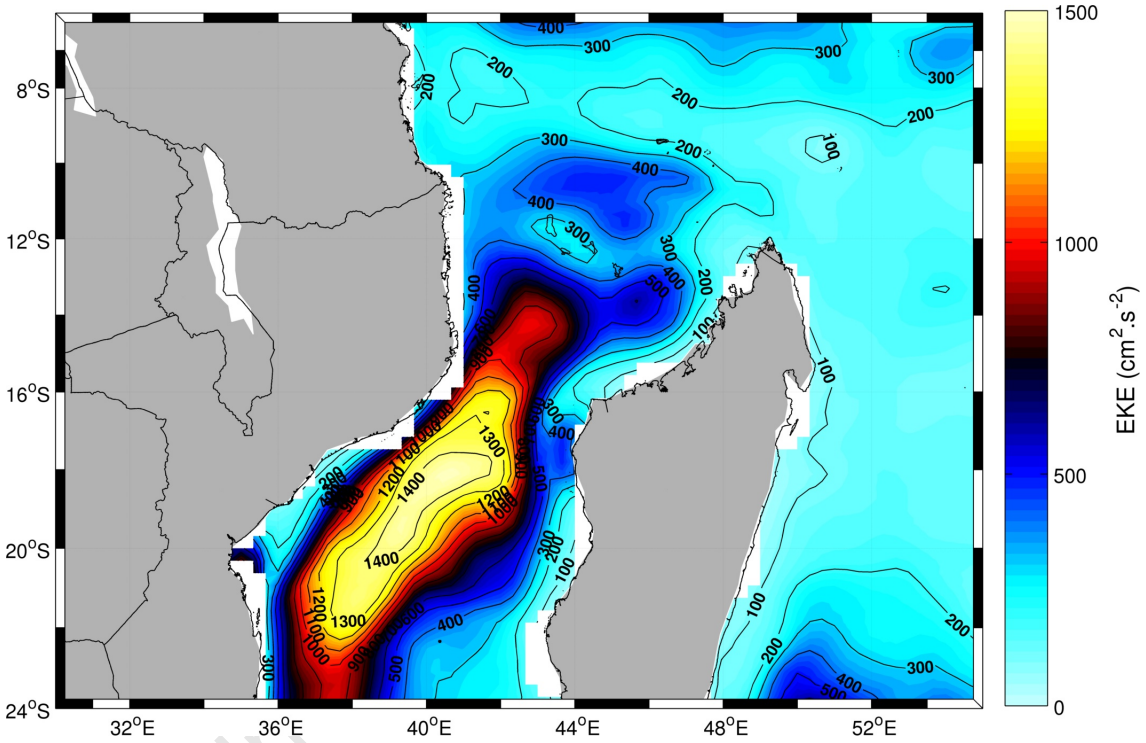

Figure 3.13: *The mean EKE (cm^2·s^{-2}) for the period 1993-2011. The contour interval is 100cm^2·s^{-2}.*

The seasonal mean EKE in the Comoros Basin for the period 1993-2011 shows that lower energies occur north of the Comoros Islands during the Northeast monsoon compared to the Southwest monsoon (Figure 3.14). The stronger (weaker) EKE during the Southwest (Northeast) monsoon appears to be related to the strengthening (weakening) of the NEMC as dis-

cussed in the previous section. This suggests that a stronger NEMC during the Southwest monsoon results in either increased eddy activity or more intense eddies. The seasonal EKE associated with the cyclonic eddy along the northwest coast of Madagascar noted in the previous sections displays relatively similar values during both monsoon seasons. Coinciding with a weaker poleward flow along the western boundary of the Comoros Basin, the region of high energy north of the narrows of the Mozambique Channel is slightly reduced during the Southwest monsoon (Figure 3.14b and c). This imply fewer or less intense eddies along the coast of Mozambique during the Southwest monsoon when the poleward current is weaker.

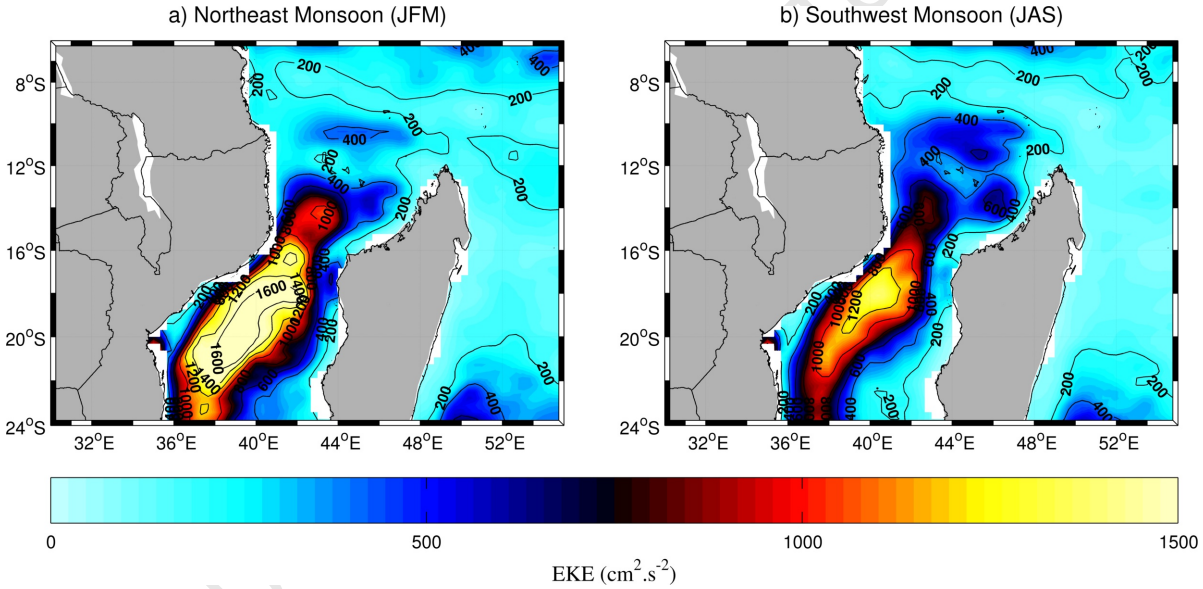

Figure 3.14: *The mean EKE ($cm^2 \cdot s^{-2}$) for the a) Northeast monsoon and b) Southwest monsoon calculated over the period 1993-2011. The contour interval is 200$cm^2 \cdot s^{-2}$.*

3.2.3 Eddy Identification and Tracking

The analyses of the altimeter data presented in the previous section indicate that the Comoros Basin is a region of high eddy activity with both cyclonic and anti-cyclonic eddies generated

in the basin. In this section, the automated eddy tracking scheme described in section 3.1.2 is used to determine the characteristics of the eddies generated in the Comoros Basin.

3.2.3.1 Eddy Genesis and Propagation

High eddy numbers are observed in the Comoros Basin, in the Mozambique Channel and east of Madagascar. In the Comoros Basin, the highest concentration of eddies occurs directly north of the narrows of the channel (Figure 3.15a). A high number of eddies is also observed around the Comoros Islands and along the northwest coast of Madagascar. The highest concentration of eddy activity in the Mozambique channel is observed along the western boundary with increased eddy activity along the west coast of Madagascar as well.

The high number of eddies west of the tip of Madagascar can be attributed to anti-cyclonic eddies which appear to form throughout the Comoros Basin but the most clearly defined area of formation is west of the northern tip of Madagascar between 11° and 12°S (Figure 3.15b). The majority of the eddies formed west of the tip of Madagascar, following the trajectory of the NEMC, travel westward with velocities of 1.9-14.4cm·s^{-1}. West of 43°E, these eddies turn south and appear to propagate into the Mozambique Channel at velocities in the range 1-13.8cm·s^{-1}. The anti-cyclonic eddies forming in the rest of the Comoros Basin display very diverse trajectories with some even flowing northward. However, very few anti-cyclonic eddies appear to travel between the Comoros Islands.

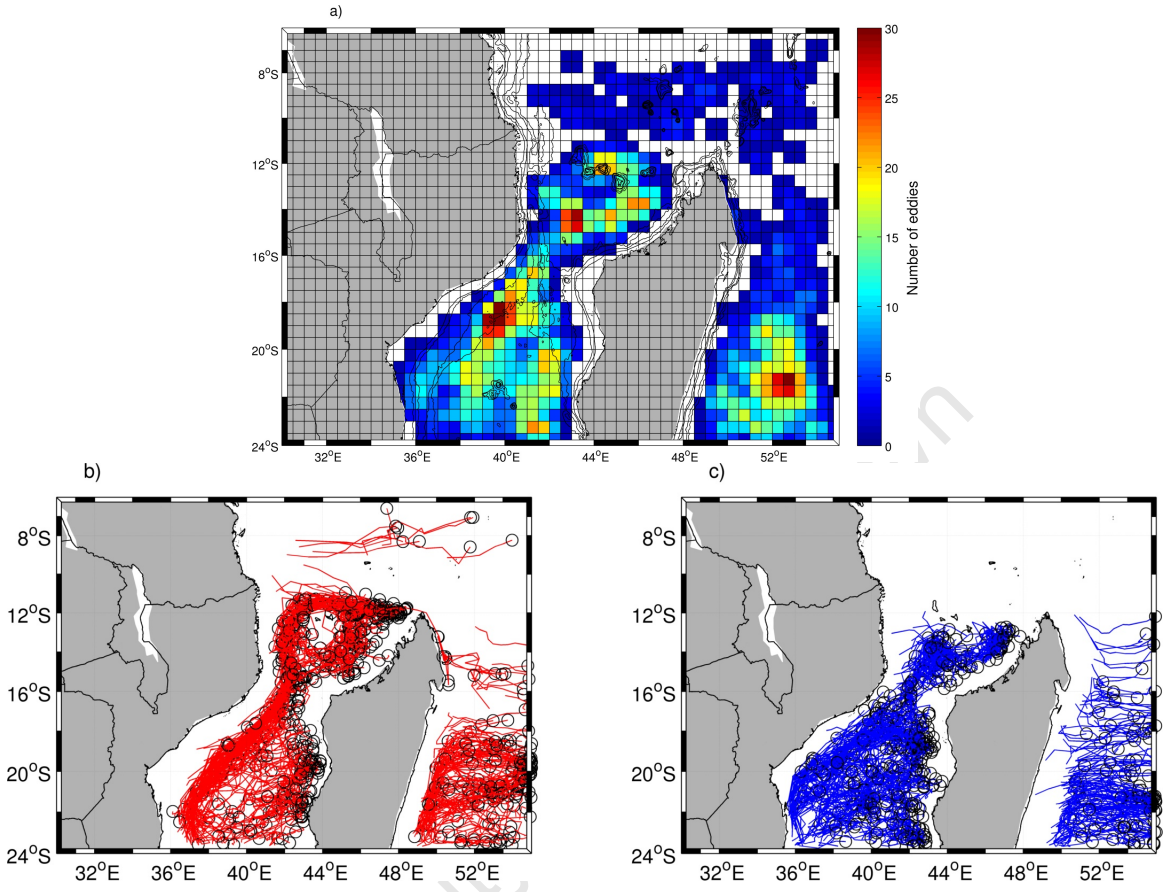

Figure 3.15: *a) Spatial distribution of the total number of eddies calculated within each 0.5 x 0.5° and the generation sites and trajectories of b) anti-cyclonic and c) cyclonic eddies. Only eddies with a lifespan exceeding 30 days are considered.*

The generation sites of cyclonic eddies formed in the Comoros Basin suggest two prominent areas of formation, one south of 12°S along the west coast of Madagascar and another south of 13°S centred around ~43°E (Figure 3.15c). Therefore, the high concentration of eddies north of the narrows of the channel and along the northwest coast of Madagascar can be attributed to the genesis of cyclonic eddies at these locations. The majority of the cyclonic

eddies formed along the west coast of Madagascar, with mean velocities of 2.5cm·s^{-1}, appear to have very limited trajectories and remain close to their point of origin. The rest of the cyclonic eddies generated in the Comoros Basin do not show a general trajectory pattern and appear to travel throughout the basin at velocities in the range 1.1-10.5cm·s^{-1}, but are limited to south of 12°S.

In the Mozambique Channel, the high eddy activity along the western boundary can be attributed to the southward passage of anti-cyclonic eddies generated in the Comoros Basin whereas the eddy activity along the eastern boundary can be ascribed to the generation of eddies of both polarities. Similarly, the high eddy numbers east of Madagascar can be attributed to both anti-cyclonic and cyclonic eddy activity.

The region of interest is the Comoros Basin and therefore all subsequent analyses were carried out on eddies generated in the Comoros Basin (39°-50°E and 11°-16°S). A total of 299 eddies, consisting of 201 anti-cyclonic and 98 cyclonic eddies, were generated in the basin during the 19 years (1993-2011) under consideration. This amounted to an average of 12 anti-cyclonic and 8 cyclonic eddies being generated in the Comoros Basin per year.

3.2.3.2 Eddy Lifespan and Retention time

The lifespan of an eddy is defined as number of days between the generation and termination of an eddy, whereas retention time refers to the number of days an eddy spent in the Comoros Basin. The average lifespan of an eddy generated in the Comoros Basin is 91 days. More specifically, anti-cyclonic eddies generated in the Comoros Basin have an average lifespan of 85 days and remains in the Comoros Basin ~50 days. Cyclonic eddies, on the other hand, spending on average 80 days in the Basin, have a mean lifespan of 102 days. Roughly 75% of the cyclonic eddies generated in the Comoros Basin remain there over their entire lifespan.

Anti-cyclonic eddies generated in the Comoros Basin have a residence time of between 1 week and six months whereas cyclonic eddies have a maximum residence time of more than a year.

Table 3.3: *The mean lifespan and retention times in days of anti-cyclonic and cyclonic eddies generated in the Comoros Basin.*

	Anti-cyclonic	**Cyclonic**
Mean Lifespan	85±63	102±72
Mean Retention time	60±46	80±65
Min residence time	7	7
Max residence time	182	378

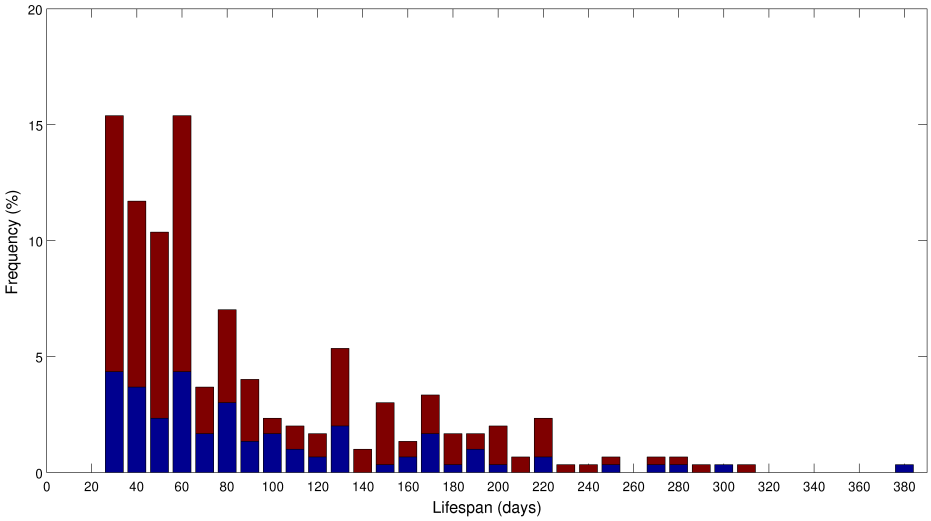

Figure 3.16: *The lifespan of anti-cyclonic eddies (red bars) and cyclonic eddies (blue bars) in the Comoros Basin.*

Slightly more than half of the eddies generated in the Comoros Basin have lifespans shorter than 60 days and consist mainly of anti-cyclonic eddies. A quarter of the eddies generated in the Comoros Basin obtained lifespans between 100 and 200 days, constitut-

ing roughly equal proportions of cyclonic and anti-cyclonic eddies. Eddies generated in the Comoros Basin rarely live longer than 200 days and those that do are predominantly anti-cyclonic eddies.

The majority of the anti-cyclonic eddies generated in the Comoros Basin remain in the basin for less than 50 days whereas only half of the cyclonic eddies remain in the basin for less than 50 days. Anti-cyclonic eddies with a retention time exceeding 100 days accounts for less than 6% of the anti-cyclones generated in the basin whereas more than a quarter of the cyclonic eddies have retention times of more than 100 days.

3.2.3.3 Eddy translation speed

Anti-cyclonic eddies generated in the Comoros Basin have a mean translation speed of ~6km·day^{-1} which is almost double that of their cyclonic counterparts which have mean translation speeds of ~3.5km·day^{-1}. The translation speed of anti-cyclonic eddies in the Comoros Basin is slightly higher than the estimated translation speed of ~4.5km·day^{-1} for anti-cyclonic eddies propagating southwards through the Mozambique Channel (de Ruijter et al., 2002).

Table 3.4: *The mean translations speed, advective time scale, area and transport of anti-cyclonic and cyclonic eddies generated in the Comoros Basin.*

	Anti-cyclonic	**Cyclonic**
Mean Translation Speed (km·day^{-1})	6.3±3.6	3.5±2.6
Mean Advective Time scale (days)	39±29	99±90
Mean Area (10^3km^2)	24.3±8.7	18.2±5
Mean Transport (Sv)	5.7±4.3	2.3±1.9

Assuming the eddies in the Comoros Basin are circular and extend to the bottom (3000m), as previously noted by Harris (1972) for a deep anti-cyclonic vortex in the Comoros Basin, the volume transport can be estimated based on the area and translations speeds (Vásquez

et al., 2013). The estimated volume transport for anti-cyclonic eddies in the Comoros Basin range from 0.2 to 25Sv with a mean volume transport of 5.7Sv. Cyclonic eddies, with a mean volume transport of 2.3Sv, have slightly lower volume transports which range from 0.1 to 12Sv. The volume transport estimated for anti-cyclonic eddies in the Comoros Basin from the altimeter data is in good agreement with the 10-20Sv estimated by Harris (1972) from hydrographic data.

3.2.3.4 Eddy Kinematic Properties

The automated eddy identification and tracking scheme described in section 3.1.2 provides estimates of the following kinematic properties: eddy amplitude, scale and rotational speed. In this section, these properties will be used to characterize the anti-cyclonic and cyclonic eddies generated in the Comoros Basin.

Eddy Amplitude

The eddy amplitude (A) can be used as a proxy for the strength of an eddy and is defined as the difference between the extremum SSH value within the eddy and the estimated basal height (h_0) of the eddy boundary (Chelton et al., 2011). Thus, the amplitude of a cyclonic eddy, calculated as $A = h_0 - h_{min}$, is the difference between the averaged SSH value around the outermost closed contour that defines the eddy perimeter, h_0, and the minimum SSH within the eddy, h_{min}. Similarly, the amplitude of an anticyclonic eddy, calculated as $A = h_{max} - h_0$, is the difference between the maximum SSH within the eddy, h_{max}, and h_0.

The anti-cyclonic (0.1±0.05cm) and cyclonic eddies (0.09±0.03cm) generated in the Comoros Basin have similar mean amplitudes indicating that eddies of both polarities are of similar strength. The majority of the anti-cyclonic and cyclonic eddies retained in the Co-

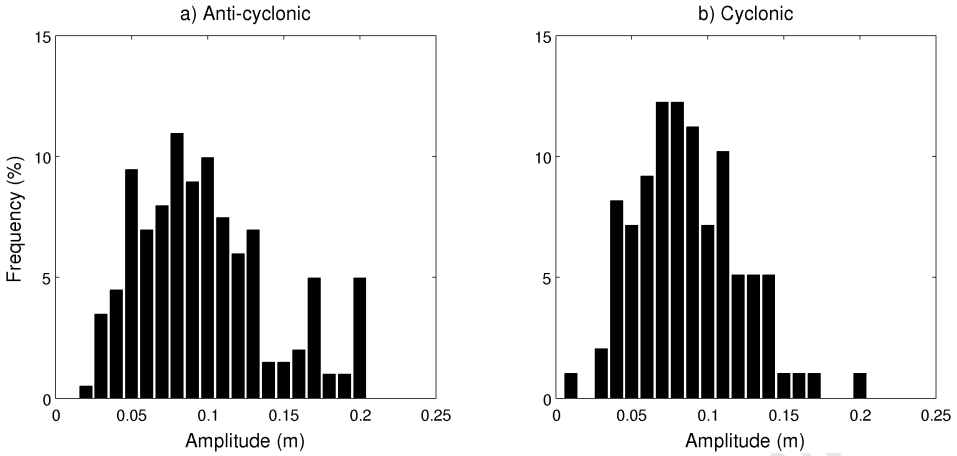

Figure 3.17: *The distribution of the eddy amplitude (m) for a) anti-cyclonic and b) cyclonic eddies while residing in the Comoros Basin.*

moros Basin have amplitudes in the range 5-10cm (Figure 3.17). More than a quarter of the eddies of both polarities have amplitudes greater than 10cm (Figure 3.17). Globally, eddies with amplitudes exceeding 10cm are mainly associated with highly unstable currents such as the Agulhas Current and the Gulf Stream (Chelton et al., 2011).

Eddy Scale

Eddy scale is an important statistical property of variability (Beckmann et al., 1994). The definition of eddy scale adopted here is the speed-based radius estimate which is the definition preferred by Chelton et al. (2011). The eddy scale is defined as the radius of a circle of equal area to that within the closed SSH contour that has the maximum average geostrophic speed (Chelton et al., 2011). This definition of the eddy scale which makes no assumption, a priori, about the structure of the eddy provides a better measure of eddy size than for example the e-folding scale which is based on the axially symmetric Gaussian (Chelton et al., 2011).

Anti-cyclonic eddies generated in the Comoros Basin, obtaining an average eddy scale of

~80km while residing in the Comoros Basin, are larger than their cyclonic counter parts with an average eddy scale of ~60km. Eddies of both polarities predominantly have eddy scales in the range 50-100km (Figure 3.18). Slightly more than 10% of the anti-cyclonic eddies retained in the Comoros Basin obtain eddy scales larger than 100km. The aforementioned results are in good agreement with Chelton et al. (2011), who found that more than 90% of eddies, globally, have scales between 50 and 150km and eddies in the Southern Hemisphere have a mean eddy scale of 87km.

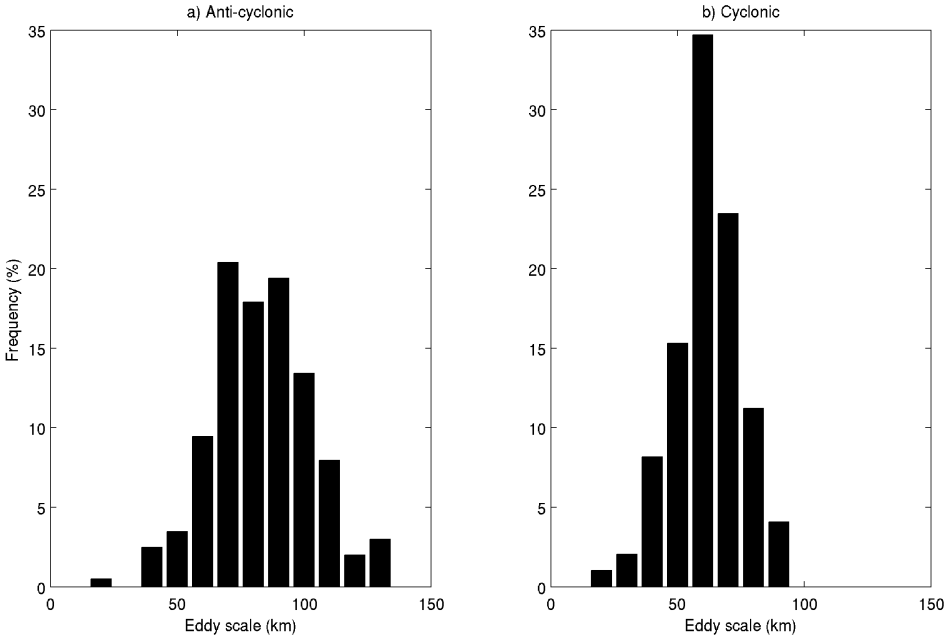

Figure 3.18: *The distribution of the eddy scale (km) for a) anti-cyclonic and b) cyclonic eddies while residing in the Comoros Basin.*

Eddy Rotational Speed

The rotational speed (U) of an eddy is defined as the maximum average geostrophic speed around all closed SSH contours within the eddy. Thus, U is determined by the average geostrophic speed around the same SSH contour used to calculate the eddy scale (Chelton et al., 2011).

The rotational speed of eddies in the Comoros Basin range between 0.1 to 1.1m·s^{-1}. Anti-cyclonic eddies generated in the Comoros Basin have rotational speeds (0.5m·s^{-1}) similar to their cyclonic counter parts (0.4m·s^{-1}) while residing in the basin. The majority of cyclonic and anti-cyclonic eddies in the Comoros Basin have rotational speeds less than 0.5m·s^{-1} (Figure 3.19). Only 1% of the cyclonic and anti-cyclonic eddies have rotational speeds in excess of 1m·s^{-1} while confined in the Comoros Basin.

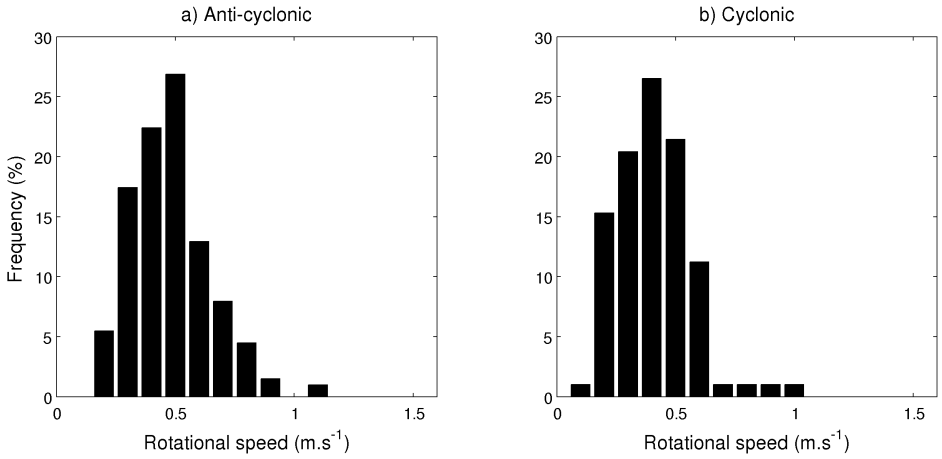

Figure 3.19: *The distributions of the eddy rotational speed (m·s^{-1}) for a) anti-cyclonic and b) cyclonic eddies while residing in the Comoros Basin.*

3.3 Summary

The limited studies of the past on the circulation in the Comoros Basin (e.g. Harris, 1972; Sætre and da Silva, 1984; Donguy and Piton, 1991 and Biastoch and Krauss, 1999) suggested that it consists of an anti-cyclonic gyre that displays seasonal variability due to the influence of wind. The analyses of this chapter, utilizing hydrographic and altimeter data, were aimed at determining whether the circulation in the Comoros Basin consists of a permanent "Comoros Gyre" or whether it is more variable. In addition, the seasonal and interannual variability of the circulation in the Comoros Basin was also investigated. Analysis of the interannual variability in relation to two major climate modes, the ENSO and IOD, yielded no significant results and are therefore not discussed in this chapter (see Appendix A).

3.3.1 Water Masses

All of the upper ocean water masses enter the Comoros Basin from the east within the NEMC. This current, with a core speed exceeding 0.6m·s^{-1}, bifurcates along the East African coast at ~10.8°S (Figure 3.1 and 3.8). The strong southward branch (>0.5m·s^{-1}; Figure 3.1 and 3.8) transports the upper ocean water masses further into the Comoros Basin where meso-scale eddies aid in distributing these water masses throughout the basin and into the rest of the Mozambique Channel (de Ruijter et al., 2002).

The intermediate layers of the Comoros Basin are dominated by AAIW and RSIW, with the latter spreading primarily southwards between Africa and the Comoros Islands. This is consistent with the southward spreading of this water mass from the north into the Mozambique Channel along the western boundary of the Indian Ocean noted Beal et al. (2000). The influence of RSIW throughout the Comoros Basin, indicates that similar to the transport

of this water mass through the Mozambique Channel (de Ruijter et al., 2002; Roman and Lutjeharms, 2009), it spreads throughout the basin at intermediate levels within the core of meso-scale eddies.

In the literature two routes are proposed for the transport of AAIW into the Comoros Basin. According to de Ruijter et al. (2002), AAIW is transported northward along the continental slope into the basin via the equatorward Mozambique Undercurrent. Di Marco et al. (2002), however proposed that AAIW moves north within the interior of the Indian Ocean and continues west around Cape Amber, the northern tip of Madagascar, within the SEC. During the Comoros Cruise, the freshest AAIW was observed north of Madagascar within the NEMC confirming the route proposed by di Marco et al. (2002) as a possible route of AAIW into the Comoros Basin.

NADW, which is also transported within the Mozambique Undercurrent (de Ruijter et al., 2002), is assumed by a number of authors (e.g. Toole and Warren, 1993; Mantyla and Reid, 1995) to be absent from the Comoros Basin due to the topographic constrain imposed by the Davie Ridge. However, during the Comoros Cruise, NADW was present at the southern most sections (S9 and S10; Figures 3.7i-j and 3.6f-g) and at the sections along the African coast (S11 and S12; Figures 3.7k-l and 3.6h-i). This indicates, as suggested by van Aken et al. (2004), that this water mass is capable of spreading northward through the Mozambique Channel and into the Comoros Basin.

3.3.2 Circulation

Both the cruise and the altimeter data indicates that the flow field of the Comoros Basin consists of two strong currents: the westward flowing NEMC and a poleward current along

the western boundary (Figures 3.1, 3.9 and 3.10). The NEMC, flowing west past the tip of Madagascar with an average velocity of 0.5m·s^{-1} (Table 3.2), bifurcates along the East African coast at ~10.8°S. The strong poleward current, with an average velocity similar to that of the NEMC, has been observed previously in current meter data from a mooring across the Mozambique Channel (Harlander et al., 2009; Ridderinkhof et al., 2010). Both currents display a strong seasonal signal in response to the wind forcing over the Comoros Basin. Increased intensity is observed in the NEMC during the Southwest monsoon (Figure 3.11a) in response to a strong wind jet which develops off the northern tip of Madagascar. The poleward current, on the other hand, is weaker during the Southwest monsoon (Figure 3.11b) as a result of the southwesterlies dominating over the basin which exert an opposing force on the poleward current.

At the time of the cruise, a cyclonic eddy was present along the west coast of Madagascar as is evident in the ADCP and the weekly altimeter data. Upwelling was observed in the centre of the cyclonic eddy in the hydrographic data. The region where the cyclonic eddy was located during the cruise, is a region of moderately high eddy kinetic energy (Figures 3.13 and 3.14) and the automated eddy tracking scheme identified this region as a primary location of cyclonic eddy formation (Figure 3.15b) suggesting the cyclonic eddy is a recurrent feature.

Maximum EKE (>600cm^2·s^{-2}) in the Comoros Basin occur south of 13°S extending through the narrows into the Mozambique Channel (Figures 3.13). According to Ridderinkhof and de Ruijter (2003), Mozambique Channel eddies are formed at the narrows of the channel suggesting that the maximum EKE observed here is a result of eddy formation. However, the primary location of anti-cyclonic eddy generation in the Comoros Basin, identified by the eddy tracking scheme, is west of Madagascar and most of the anti-cyclonic eddies dis-

play a westward trajectory north of the Comoros Islands (Figure 3.15a). Upon reaching the East African coast the eddies travel south along the Davie Ridge through the narrows of the Channel, confirming the findings of LaCasce and Isachsen (2007). Therefore, the maximum EKE does not necessarily indicate an area of formation but could rather indicate where there is a regular passage of eddies or an intensification due to "funneling" of eddies through the narrows of the channel.

A statistical census of the eddies tracked by the automated eddy tracking scheme shows that 20 eddies are generated in the Comoros Basin per year of which the majority (12 per year) are anti-cyclonic eddies. These findings are in agreement with the 18 eddies per year (12 anti-cyclonic and 6 cyclonic) reported by Halo (2012) using the same automated eddy tracking scheme with slightly different values for the parameters. Furthermore, Halo (2012) also found that anti-cyclonic eddies in the Comoros Basin are preferentially generated west of the tip of Madagascar and propagate west towards the African coast, where after they are deflected southwards. The high rate of anti-cyclonic eddy formation in the Comoros Basin can possibly be attributed to the positive vorticity extending from the tip of Madagascar into the Comoros Basin (Figure 3.20). This also explains the preferential formation of anti-cyclonic eddies west of the tip of Madagascar.

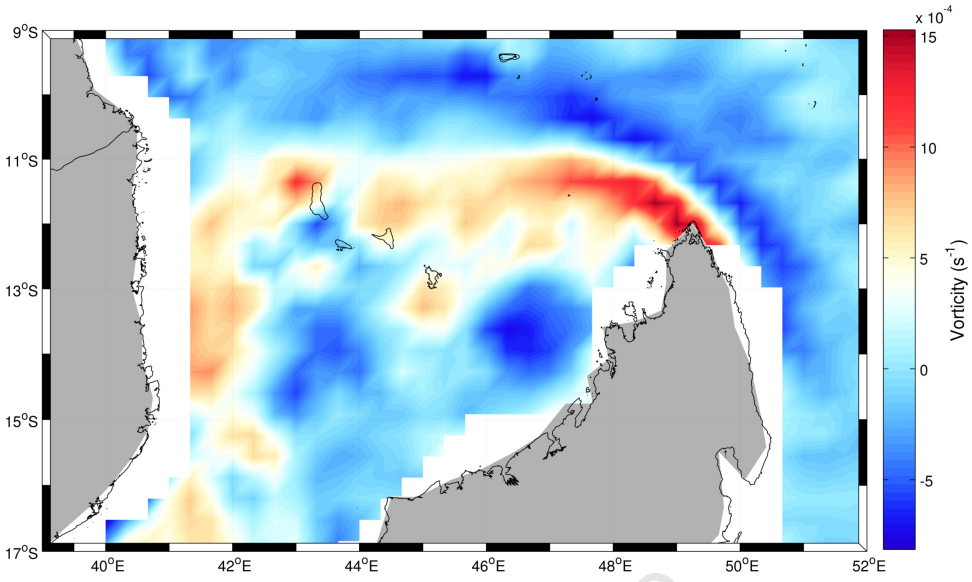

Figure 3.20: *Annual mean vorticity calculated from the satellite altimetery data for the period 1993-2011.*

Van der Werf et al. (2010), found that eddies formed west of the tip of Madagascar in the satellite data decayed north of the narrows of the channel while simulated eddies propagated through the narrows. The difference between the observational data and model data was ascribed to the unrealistic topography of the Comoros Islands in the models. The authors suggest that the eddies pass between the islands causing them to dissipate; however, in the models, the islands are not represented correctly and therefore the eddies are able to pass through the narrows. To the contrary, the results presented in this chapter, indicate that the majority of the altimeter derived anti-cyclonic eddies generated west of the tip of Madagascar propagate southward through the narrows of the Mozambique Channel and do not appear to pass through the Comoros Islands.

3.3.3 Mean Characteristics of eddies in the Comoros Basin

Anti-cyclonic eddies generated in the Comoros Basin, with a mean lifespan of ~80 days, are retained within the basin for more than half of their lifespan. The cyclonic eddies generated in the basin, on the other hand, with mean lifespans longer than their anti-cyclonic counterparts, remain in the basin for the more than three quarters of their lifespan (Table 3.3). A quarter of the cyclonic eddies generated in the basin propagate through the narrows of the Mozambique Channel while the rest spend their entire lifespan in the basin.

Anti-cyclonic eddies in the Comoros Basin, with translation speeds of ~6km·day^{-1}, have mean volume transports of ~6Sv whereas cyclonic eddies with lower translations speeds (~3km·day^{-1}) have lower volume transports (~2Sv). Eddies of both polarities generated in the Comoros Basin are of similar strength as indicated by the comparable mean amplitudes. Even though, eddies of both polarities have similar mean rotational speeds, cyclonic eddies in the Comoros Basin have a mean eddy scale of 60km which is slightly smaller than the mean eddy scale of 80km attained by their anti-cyclonic counterparts.

3.4 Conclusion

The hydrographic and altimeter data presented in this chapter has filled an important knowledge gap in a historically under sampled region, showing that the circulation in the Comoros Basin is highly variable and consists of numerous cyclonic and anti-cyclonic eddies as well as a well defined southward current along the East African coast. The anti-cyclonic eddies in the Comoros Basin are primarily formed at the northern tip of Madagascar and propagate across the Comoros Basin into the Mozambique Channel. Cyclonic eddies are primarily generated along the northwest coast of Madagascar and the majority remain in the basin over their en-

tire lifespan. The results presented here indicate that the anti-cyclonic feature perceived in past studies as a gyre, and subsequently termed the "Comoros Gyre", was most likely a large anti-cyclonic eddy.

Even though a better idea of the circulation in the Comoros Basin has been obtained from the cruise and altimeter data, these results are not without their caveats. The hydrographic data are limited in its temporal resolution while the altimeter data at a 1/4° horizontal resolution do not provide any information regarding the vertical structure of the eddies. Therefore, in order to determine the vertical structure of the eddies in the Comoros Basin numerical modelling is employed in Chapter 7. However, before the modelling can be attempted an investigation into the appropriate wind products for modelling the region of interest is presented in the next chapter.

Chapter 4

Wind Product Comparisons[1]

The western Indian Ocean is a region of complex dynamics and strong variability on a range of scales that impact substantially on the climates of eastern and southern Africa. However, a complete understanding of the variability at all scales is precluded by the limited spatio-temporal resolution of available observational and satellite derived data. As discussed in Chapter 3, neither satellite derived data nor observational data are capable of providing a comprehensive representation of the ocean circulation. Even though satellites provide global coverage, the resolution of the data obtained is often very coarse and data is not available near the coast. Furthermore, a limited number of variables can be measured by satellites and these can only be measured at the surface. The monetary and time constraints associated with in-situ data collection means that, even though vertical profiles can be obtained, it provides only an instantaneous snap-shot and the measurements within a region are limited in their spatial and temporal resolution. Therefore, in order to overcome the aforementioned hurdles,

[1]This chapter is based on: C. Collins, C.J.C. Reason, and J.C. Hermes (2012). Scatterometer and reanalysis wind products over the western tropical Indian Ocean. *Journal of Geophysical Research*, ***117***, C03045, doi:10.1029/2011JC007531.

ocean circulation models are a useful tool in interpreting sparse observational data as well as improving the understanding of basic processes and their interconnectedness. Several ocean circulation models have been used to improve understanding of the ocean circulation in the tropical southwest Indian Ocean and more specifically the greater Agulhas Current System including the Mozambique Channel (Biastoch and Krauss, 1999; Backeberg et al., 2008; Hermes et al., 2007; Penven et al., 2006a). However, a feature in the Mozambique Channel that is especially lacking in observations and understanding is the Comoros Basin (Figure 4.1).

An integral part of ocean circulation models is the surface forcing, of which wind stress forms an important part, as currents and property transports can change significantly in response to modified surface forcing. Therefore, before attempting a realistic ocean circulation simulation, it is necessary to assess the availability of reliable wind stress data, particularly in complex areas such as the Mozambique Channel where islands and other topographic features may cause meso-scale variability in the surface winds that are not well resolved by the various wind products available. Therefore, this chapter investigates how three different wind products resolve the wind features of the western Indian Ocean, with a focus on the Comoros Basin region.

4.1 Wind stress in numerical models

Surface wind stress and its curl form part of all large-scale ocean basin circulation theories and models (Harrison, 1989). Wind stress, acting on the sea surface, is a fundamental forcing agent for dynamical ocean processes (Petit et al., 2006) and is the most important driving force behind upper-ocean circulation (Trenberth et al., 1990). The exchange of momentum

between the ocean and atmosphere via wind stress is important for the study of air-sea interactions, climate variability and ocean processes (Kara et al., 2007).

Surface wind stress is required by all ocean circulation models as specified boundary conditions (Trenberth et al., 1990). In the past, inadequate spatial and temporal sampling of surface winds made a reliable estimate of the mean stress very difficult, however the accuracy of climatologies has increased during the last decade now that climatologies can be derived from satellite scatterometry and operational forecast models (Trenberth et al., 1990). Currently, ocean modellers have a choice between observation-based wind climatologies such as Hellerman and Rosenstein (1983) and the University of Wisconsin-Milwaukee/Comprehensive Ocean-Atmosphere Data set (da Silva et al., 1994), wind climatologies obtained from numerical weather prediction models such as the National Centers for Environmental Prediction (NCEP) and the European Centre for Medium-Range Weather Forecasts (ECMWF), and wind climatologies derived from satellite data such as QuikSCAT. All three types of data sets are subject to their own error/biases (Metzger, 2003) which raises the question: what are the similarities and differences of these products?

Several studies report on the variation between different wind products for various parts of the world oceans (Annamalai et al., 1999; Metzger, 2003; Palma et al., 2004). In comparing NCEP-NCAR and ECMWF re-analyses over the Indian Ocean during the Southwest monsoon, Annamalai et al. (1999) found that the Somali Jet is stronger and more zonal in NCEP-NCAR, whereas it extends further north over the Arabian Sea and into northwest India in ECMWF. Metzger (2003) showed that significant differences exist in the wind stress curl patterns in ECMWF and NCEP over the South China Sea. In addition, this author also showed that the differences in the wind stress curl patterns were reflected in the upper ocean model response and advocated that atmospheric forcing products for high-resolution ocean

models should be chosen with care. A modelling study of the ocean circulation patterns of the Southwestern Atlantic Shelf demonstrated that significantly different circulation patterns can be obtained using different wind stress climatologies (Palma et al., 2004). The differences in circulation patterns were attributed to differences in wind magnitude and time periods of the different products. Therefore, an increase in sophistication and resolution of global and regional ocean general circulation models results in an increasing sensitivity to accurate surface wind stress curl forcing (Milliff et al., 2004).

In an attempt to evaluate some of the similarities and differences of different wind products for the western Indian Ocean, a comparison is made between three different products (NCEP II, ERA-interim and QuikSCAT). The three products are evaluated based on the representation of large-scale wind patterns as well as their ability to resolve small-scale features such as corner accelerations due to the island effect. Focus is placed on the western Indian Ocean since it displays a dramatic seasonal variation in both wind and circulation patterns. Furthermore, it is an important region of air-sea interaction (Benny, 2002) and contains areas such as the Mozambique Channel/Comoros Basin which are not well understood.

4.2 Datasets

In this study, three different wind products, QuikSCAT (QSCAT), NCEP/DOE AMIP-II Reanalysis (NCEP II), and ERA-interim (ERA), were compared for the western Indian Ocean region (20°N-40°S, 30°E-80°E, Figure 4.1). A description of the different wind products is provided below. The wind products were compared with respect to wind speed, wind stress curl, wind stress divergence, and associated Ekman pumping.

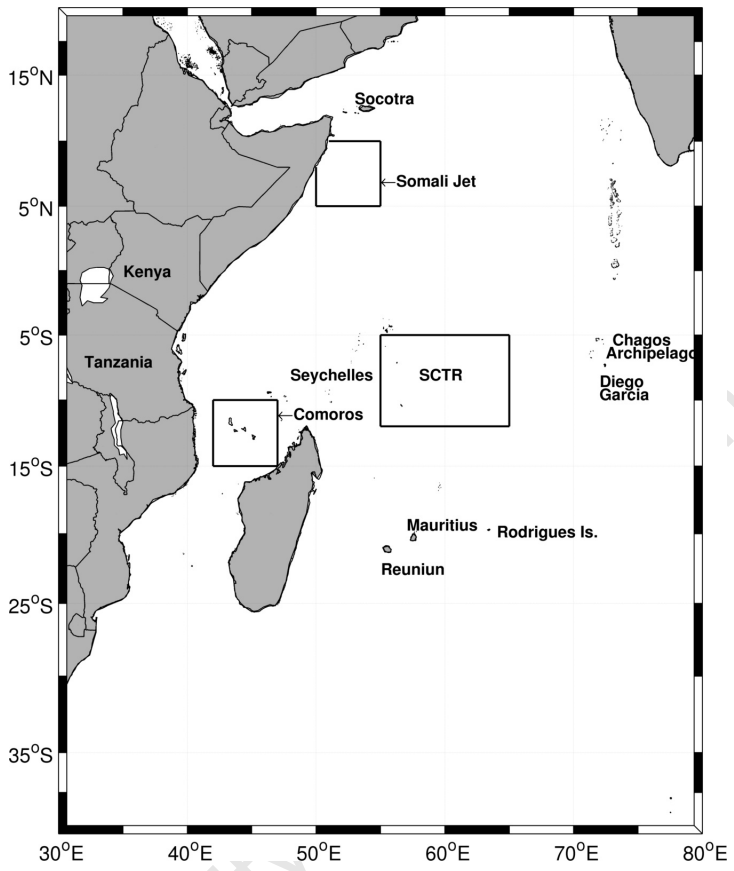

Figure 4.1: *Location of the three sample areas used in the wavelet analyses. The top box indicates the area for the Somali Jet, the middle box indicates the area of the Seychelles-Chagos Thermocline Ridge (SCTR), and the bottom box indicates the location of the Comoros Basin.*

4.2.1 QuikSCAT

The QuikSCAT satellite, fitted with the SeaWinds scatterometer, was launched on 19 June 1999 into a sun-synchronous, 803km circular orbit (Sharma and D'Sa, 2008). QuikSCAT provides accurate data over a 1600km-wide swath (Chelton and Freilich, 2005) and its 101 minute orbit period allows it to sample ~90% of the global ocean daily (Schlax et al., 2001). The SeaWinds scatterometer, a scanning microwave radar, measures the electromagnetic backscatter from sea surface roughness and the angle of incidence of the transmitted pulse to

infer surface wind stress magnitude and direction (Milliff et al., 2004). The QuikSCAT data used here are the Level 3 data with a 0.25° x 0.25° spatial resolution (Table 4.1). Swath-by-swath averaging of QuikSCAT derived wind stress curl is crucial to resolve small-scale wind features (Chelton et al., 2004). Therefore, wind speed and wind stress curl were calculated within each measurement swath and averaged daily on a 0.25° grid for the period August 1999 to November 2009. The QuikSCAT mission requirements specify the error figures within the speed range 3-30m·s^{-1} to be less than 2m·s^{-1} and 20° in the derived wind speed and wind direction, respectively. However, a comparison of QuikSCAT with in-situ data from moored buoys over the Indian Ocean showed a bias of 0.37m·s^{-1} and 5.8° and a root mean square deviation of 1.57m·s^{-1} and 44.1° for QuikSCAT wind speed and wind direction, respectively (Satheesan et al., 2007).

4.2.2 NCEP/NCAR reanalysis

NCEP/DOE AMIP-II Reanalysis data are based on the widely used NCEP/NCAR Reanalysis, using a 3D-variational analysis scheme, with 28 sigma levels in the vertical and a horizontal resolution of ~210km (T62; Kistler et al., 2001). The wind data assimilated for the NCEP/NCAR Reanalysis are Special Sensor Microwave Imager (SSM/I) surface winds. A detailed description of the assimilation system is provided by Kalnay et al. (1996). The spatial resolution of the NCEP II wind data is 2.5˚ x 2.5˚ with a daily and monthly temporal resolution available for the period January 1979 to July 2010 (Table 4.1).

Table 4.1: *Spatial and temporal resolution of the different wind products.*

	QuikSCAT	**NCEP/NCAR**	**ERA-Interim**
Time period	Jul 1999 - Nov 2009	Jan 1979 - Jul 2010	Jan 1989 - Dec 2009
Spatial resolution	0.25° x 0.25°	2.5° x 2.5°	0.75° x 0.75°
Temporal resolution	Daily	Daily and Monthly	6 hourly

4.2.3 ERA-interim

ERA-interim, produced by the European Centre for Medium range Weather Forecasting (ECMWF), uses a 4D-variational analysis on a spectral grid at T255 (corresponds to ~80km) and a hybrid vertical coordinate system with 60 levels (Mooney et al., 2011). The forward integration in the 4D-variational analysis uses the ECMWF global model and incorporates QuikSCAT, ERS-1 and ERS-2 recalibrated data, as well as EUMETSAT (European Organisation for the Exploitation of Meteorological Satellites) re-processed wind data (Simmons et al., 2007). The ERA-interim data used in this study have a 0.75° x 0.75° spatial resolution and a 6-hourly temporal resolution for the period January 1989 to December 2009 (Table 4.1).

4.3 Methods

4.3.1 Wind stress curl and Ekman pumping

Firstly, wind stress and its derivatives (wind stress curl and Ekman pumping) were computed daily for QSCAT and NCEP II and 6-hourly for ERA. The daily (6-hourly) data were then used to calculate individual monthly means for the period January 2000 to December 2008 for all three wind products. Subsequently, these monthly means were used to compute climatological means.

Wind stress, a measure of the momentum transferred from the atmosphere to the ocean, was calculated using the bulk aerodynamic formula

$$\tau = (\tau_x, \tau_y) = \rho_a C_d \mid W \mid (u, v)$$

where τ_x and τ_y are the zonal and meridional wind stress components, respectively. Air density, ρ_a, is taken as 1.225kg·m^{-3}, C_d is the drag coefficient and W is the magnitude (wind speed) of the zonal (u) and meridional (v) components of the wind. The value of C_d is dependent on atmospheric stability and wind speed (Petit et al., 2006) and several formulations are in common use with no general consensus on which is most accurate. In this study, the Large and Pond (1981) formulation was used to calculate C_d,

$$C_d = \begin{cases} 0.0012 & 4 \leq U_{10} < 11 m \cdot s^{-1} \\ 0.0049 + 0.000065 U_{10} & 11 \leq U_{10} \leq 25 m \cdot s^{-1} \end{cases}$$

where U_{10} is the wind speed at 10m height measured in meters per second. These estimates of C_d are based on the ratio of the directly measured Reynolds stress to the square of the wind speed. The wind speeds used in calculating C_d were limited to speeds above 4m·s^{-1}, since the drag coefficient increases with increasing wind speeds. A constant C_d of 0.0012 was used for wind speeds less than 4m·s^{-1}. Wind speeds over the western Indian Ocean rarely exceed 25m·s^{-1} and therefore the above C_d formulation was deemed adequate.

Wind stress curl is important dynamically as it is a source of vorticity. The vertical component of the wind stress curl for each of the wind products was calculated using the equation

$$curl\,\tau = \frac{\partial \tau_y}{\partial x} - \frac{\partial \tau_x}{\partial y}.$$

Wind stress curl generates open ocean upwelling and downwelling, also known as Ekman pumping (Pedlosky, 1996). The Ekman upwelling velocity for each wind product was

calculated as

$$W_e = \frac{1}{\rho_w f} curl\,\tau$$

where ρ_w is the density of sea water, assumed to be 1025kg·m^{-3}, and f is the Coriolis parameter.

4.3.2 Annual and semi-annual cycles

The evolution in relative strength of the dominant modes of the time series through the data record can be visualized using wavelet analysis, rather than the more traditional methods such as Fourier analysis (Hermes et al., 2007). Hence, wavelet analysis is utilized to investigate the annual and semi-annual cycles of wind speed and wind stress curl computed for QSCAT, NCEP II and ERA. Wavelet analysis has been successfully applied in many meteorological and oceanographic applications. One example is Risien et al. (2004) who investigated the intraseasonal variability of surface winds over the Benguela upwelling system using wavelet analysis.

The present study makes use of the Morlet wavelet as it allows for the detection of both time-dependent amplitude and phase for different frequencies exhibited in the time series:

$$\psi(t) = \pi^{\frac{1}{4}} e^{\frac{-t^2}{2}} e^{i\omega_0 t}$$

where $i = (-1)^{\frac{1}{2}}$ and $\omega = \pi(\frac{2}{ln2})^{\frac{1}{2}}$, the plane wave of the frequency (Daubechies, 1992) is chosen to be large enough to ensure that $\psi(t)$ satisfies the wavelet admissibility condition. The local wavelet power spectrum is calculated as the square of the wavelet coefficients and

the global wavelet power spectrum is the average of the wavelet power spectrum over time (Torrence and Compo, 1998).

The wavelet power expresses the variance of the time series and therefore a high significance line in the global wavelet power spectrum is indicative of a noisy time series whereas a low significance line indicates a smooth time series. The significance lines are calculated using an appropriate background spectrum (white noise or red noise) that serves as a "null hypothesis". In this study, a red noise spectrum was chosen. It is assumed that different realizations of the geophysical process will be randomly distributed about this expected background, and the actual spectrum can be compared against this random distribution. A feature can be assumed to be true with a certain percent of confidence if the peak in the wavelet power spectrum is significantly above the background spectrum (Torrence and Compo, 1998). The 95% significance level determined from a chi-squared distribution, as well as the region of the wavelet analysis not subjected to edge effects, denoted by the cone of influence (COI; Torrence and Compo, 1998), are indicated on the wavelet figures.

Wavelet analyses were performed on the normalized monthly time series of QSCAT, ERA, and NCEP II for the time period 2000 to 2008. This time period was based on the fact that it is the only continuous time period for which QSCAT has a full complement of monthly data. Time series of wind speed and wind stress curl magnitude were created by computing monthly averages of these variables for three regions in the western Indian Ocean (Figure 4.1): 5-10°N, 50-55°E (Somali Jet) and 10-15°S, 42-47°E (Comoros) and 5-12°S, 55-65°E (Seychelles-Chagos Thermocline Ridge (SCTR; Hermes and Reason, 2008, 2009) . The first two regions were selected to identify discrepancies in the annual and semi-annual cycles of the wind products, as they represent both hemispheres and are also regions in which modelling is essential due to lack of observations. The SCTR region was selected since it

constitutes a region of upwelling in the southwest tropical Indian Ocean and is important for regional climate, especially with regard to cyclogenesis (Xie et al., 2002).

4.4 Results

In this section, the three wind products, QSCAT, NCEP II and ERA, are compared based on their dominant modes of variability and annual cycles of wind speed and wind stress curl. The dominant modes of variability are assessed through wavelet analysis. Furthermore, the wind products are also compared with respect to their seasonal representation of wind speed, wind stress curl and upwelling velocities.

4.4.1 Annual and Semi-annual cycles

4.4.1.1 Somali Jet

The three wind products display similar annual cycles for wind speed (Figure 4.2a) over the Somali Jet. Over the Somali Jet, wind speeds are strongest during the Southwest monsoon (June-September), with the wind speeds of ERA and NCEP II almost 50% stronger than that of QSCAT. Maximum wind speed occurs during July in NCEP II and QSCAT, while ERA wind speed peaks in June. Minimum wind speed occurs during the monsoon transition months of April and October in QSCAT and NCEP II and April and November in ERA. The transition to the Southwest monsoon occurs about a month earlier in ERA than in the other two products and is also stronger. Time series of weekly averaged wind speed indicates that at the end of the Southwest monsoon, the transition to the inter-monsoon period occurs almost two weeks later in ERA than in NCEP II and QSCAT. These results indicate that the

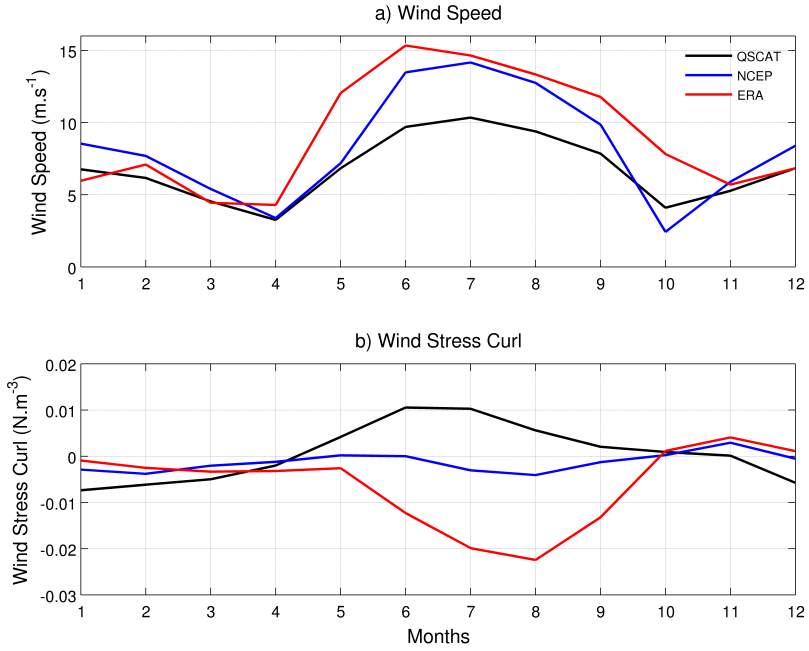

Figure 4.2: *The annual cycle of a) wind speed ($m{\cdot}s^{-1}$) and b) wind stress curl ($N{\cdot}m^{-3}$) over the Somali Jet. The black, blue and red lines represent QSCAT, NCEP and ERA, respectively.*

duration of Southwest monsoon over the Somali Jet is approximately 1-1.5 months longer in ERA than in QSCAT and NCEP II.

The wind stress curl of the three different products, especially QSCAT, over the Somali jet display different annual cycles (Figure 4.2b). QSCAT wind stress curl displays cyclonic (anti-cyclonic) curl over the Somali Jet (Figure 4.2b) coinciding with the period of maximum (minimum) wind speed (Figure 4.2a). On the other hand, NCEP and ERA display anti-cyclonic curl associated with the period of maximum wind speed. Time series of monthly wind stress curl of the three wind products (not shown) indicate that the ERA wind stress curl is consistently anti-cyclonic during the Southwest monsoon and QSCAT wind stress curl is consistently cyclonic. In NCEP II, anti-cyclonic wind stress curl dominates during the

Southwest monsoon and is of greater amplitude than the cyclonic wind stress curl that occurs during some years (e.g. 2000 and 2001). The box representing the Somali Jet straddles an area of anti-cyclonic (cyclonic) wind stress curl along the Horn of Africa and an offshore area of cyclonic (anti-cyclonic) wind stress curl during the Northeast (Southwest) monsoon. The discrepancy in the annual cycle of wind stress curl between the scatterometer and reanalysis wind products is most notable during the Southwest monsoon and is a result of stronger along-shore cyclonic wind stress curl in the former and stronger offshore anti-cyclonic wind stress curl in the latter.

Figure 4.2 indicates that the wind speed and wind stress curl over the Somali Jet have a strong annual cycle in all three wind products, but it is unclear whether the variance is stronger at annual time-scales compared to seasonal or semi-annual time-scales. In order to determine which signal/s dominate the intraseasonal variability, the wind speed and wind stress curl were subjected to wavelet analysis as described in section 4.3.2.

The wavelet power spectrum and global wavelet power spectrum of wind speed for the three different products over the Somali Jet display similar distributions of power (Figure 4.3). All three wind products display significant variability in wind speed at semi-annual (6 months) as well as annual (12 months) time scales. However, the time-frequency patterns of the three products are not the same (Figure 4.3a-c). The annual cycle of QSCAT and ERA wind speed are stronger during late 2004-2006 and 2002, respectively. Despite the short duration of the power peak in ERA, the average significance of the annual cycle of ERA wind speed is higher than that of NCEP II and QSCAT (Figure 4.3d-f). The stronger average annual cycle of ERA wind speed can be attributed to the higher wind speeds displayed by this product during the Southwest monsoon (Figure 4.2a). The semi-annual signal of QSCAT wind speed is weaker during 2002-2004, while the semi-annual signal of ERA wind speed

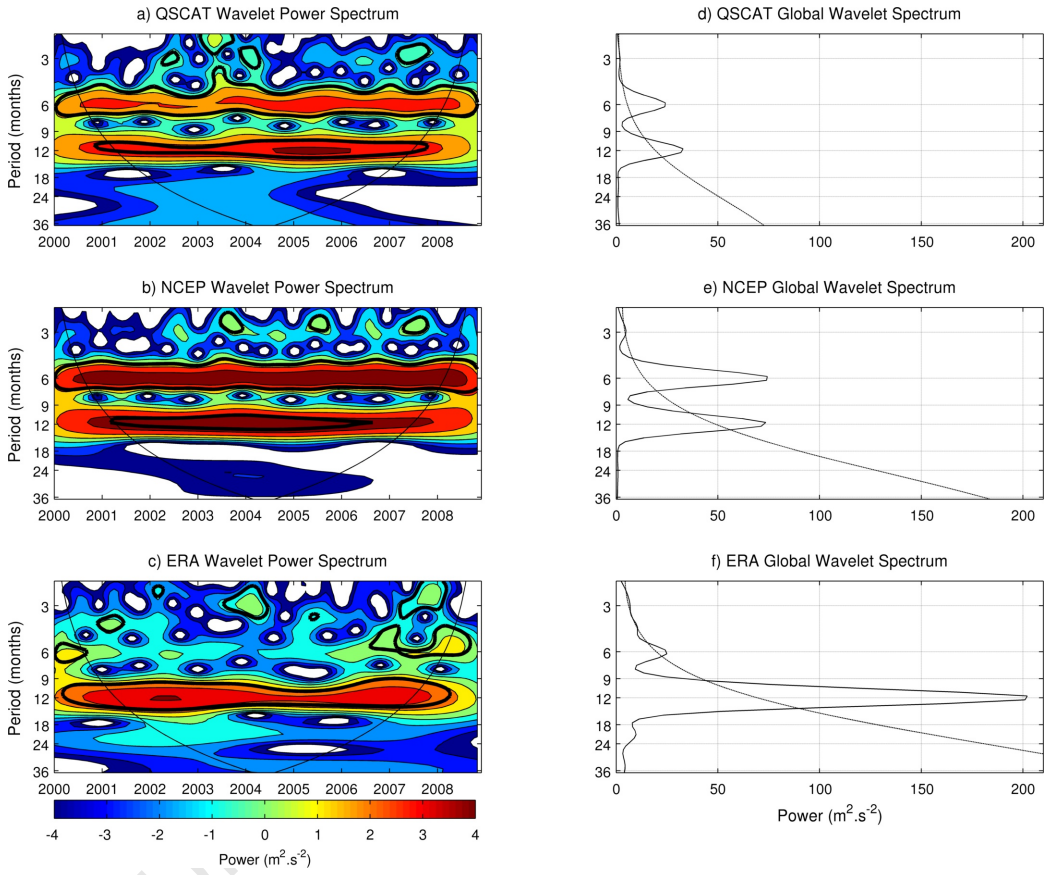

Figure 4.3: *Wavelet power spectrum (left) and power (right) of the wavelet analysis of wind speed over the Somali Jet (5-10°N, 50-55°E) for a) QSCAT, b), NCEP, c) ERA. The cone of influence (COI) is indicated by the thin black line, and the thick black contours indicate the 95% significance levels. Significance in the Global wavelet spectrum is indicated by the black dashed line.*

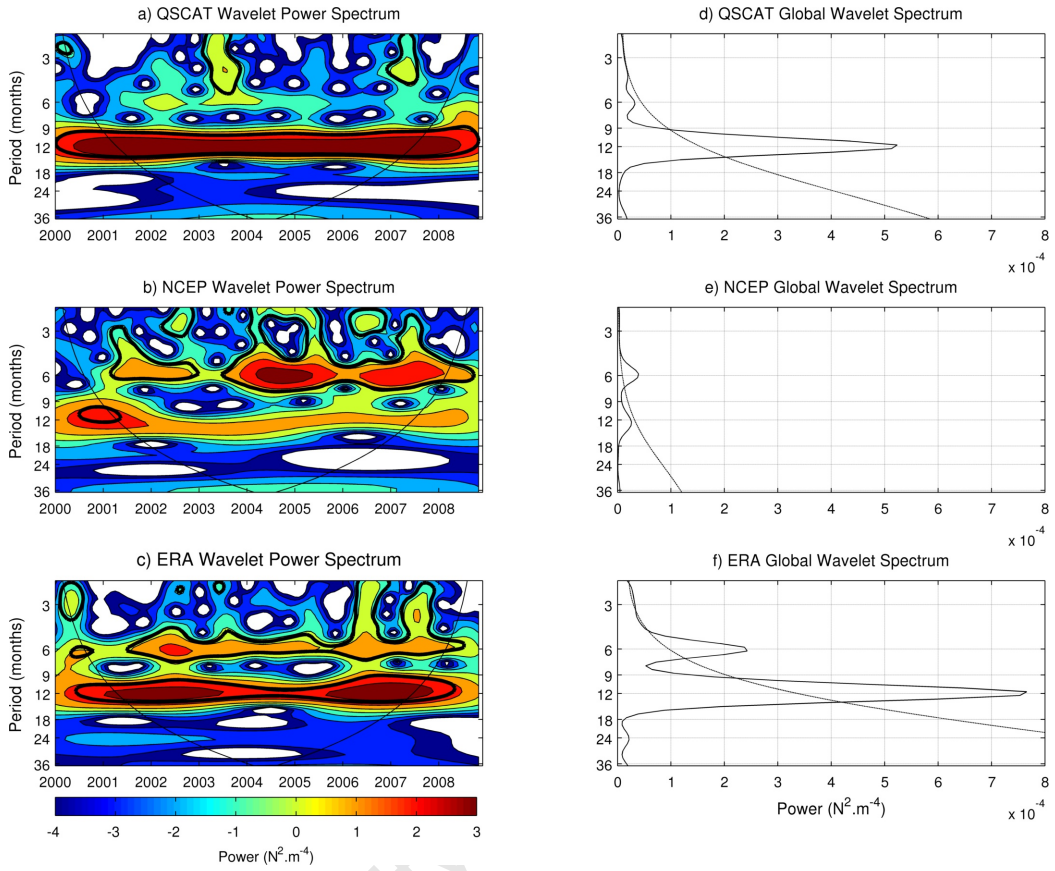

Figure 4.4: *Same as Figure 4.3 but for wind stress curl over the Somali Jet.*

only occurs during 2007-2008. Therefore, it is not surprising that the uninterrupted semi-annual cycle of NCEP II wind speed is stronger than that of ERA and QSCAT. Additionally, a small but significant 2-4 month signal is observed for ERA wind speed.

The wind stress curl of both QSCAT and ERA over the Somali Jet have a significant annual signal (Figure 4.4) whereas this frequency is not significant in NCEP II (strong power only occurs during 2000-2002). The absence of a significant annual signal in NCEP can be attributed to the low variability observed in the annual cycle of the wind stress curl of this wind product (Figure 4.2b). As with wind speed, the time-frequency patterns are not com-

parable (Figure 4.4a, c, d and f). A weakening in the annual cycle of ERA wind stress curl occurred during 2004-2006, yet it has a higher average significance than the uninterrupted annual cycle of QSCAT wind stress curl. The strong annual signal of ERA wind stress curl is a result of the strong negative wind stress curl displayed by this product during the Southwest monsoon whereas the annual signal of QSCAT wind stress curl can be attributed to positive wind stress curl during this season (Figure 4.2b). All three products display a peak in variability at semi-annual time scales, however it is only significant for NCEP II and ERA (Figure 4.4). The average semi-annual cycle of ERA wind stress curl is stronger than NCEP II, despite the latter having a stronger semi-annual cycle during 2004 and 2006-2008 while the former exhibits a power peak during 2002 only.

4.4.1.2 Comoros Basin

The annual cycle of wind speed for the three products over the Comoros Basin also show rather different patterns (Figure 4.5a). Over the Comoros Basin, QSCAT wind speed exhibits less monthly variation compared to NCEP II and ERA wind speeds. Wind speeds over the Comoros Basin attain greatest speeds during May to August. Maximum wind speed for QSCAT and NCEP II occurs in June whereas in ERA, maximum wind speed occurs a month earlier with additional peaks in January, July and October. Wind speeds in NCEP II and ERA exhibit minimum values in March whereas in QSCAT, minimum values occur in October.

QSCAT and ERA wind stress curl over the Comoros Basin exhibit comparable patterns, while NCEP II wind stress curl displays an opposing annual cycle. Over the Comoros Basin, the annual cycle of NCEP II wind stress curl is dominated by anti-cyclonic curl, with strongest anti-cyclonic curl occurring from June to October (Figure 4.5b). A clear shift from anti-cyclonic curl in January-March to cyclonic curl in April-August and then back to anti-

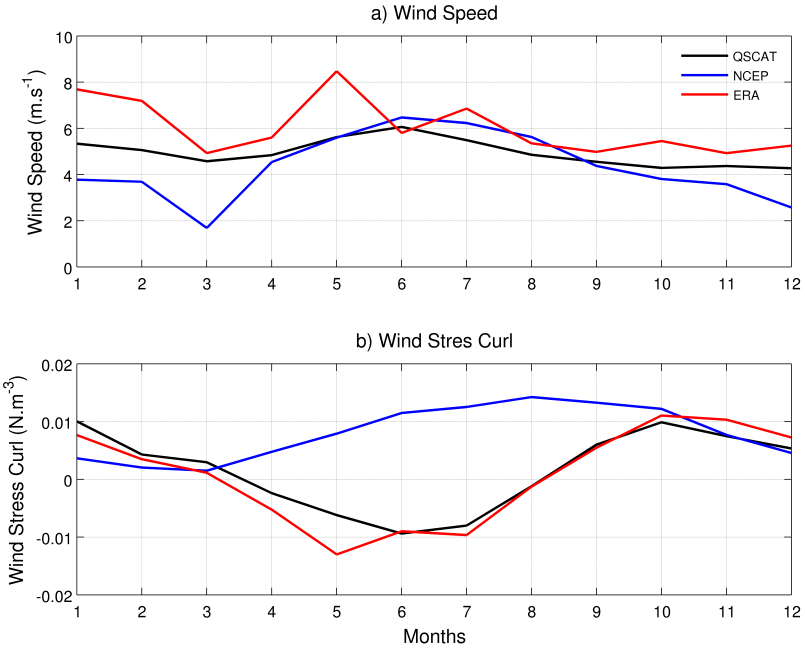

Figure 4.5: *The annual cycle of a) wind speed ($m{\cdot}s^{-1}$) and b) wind stress curl ($N{\cdot}m^{-3}$) over the Comoros Basin. The black, blue and red lines represent QSCAT, NCEP and ERA, respectively.*

cyclonic is evident in QSCAT and ERA. The discrepancy between NCEP II wind stress curl and wind stress curl of the other two wind products is also evident in the monthly time series of wind stress curl over the Comoros Basin. Changing winds in the northern Mozambique Channel associated with the monsoon seasons, described in section 2.2.2.2, are responsible for the change from anti-cyclonic wind stress curl during austral summer to cyclonic during austral winter. The opposing annual cycle of NCEP II wind stress curl can be attributed to the inability of NCEP II to resolve small-scale features described in more detail in section 4.4.2. The stronger annual cycles in QSCAT and ERA wind stress curl noted in the wavelet analysis are a result of stronger wind stress curl during the Southwest monsoon.

Noticeably different distributions of power are evident in the wavelet power spectrum and

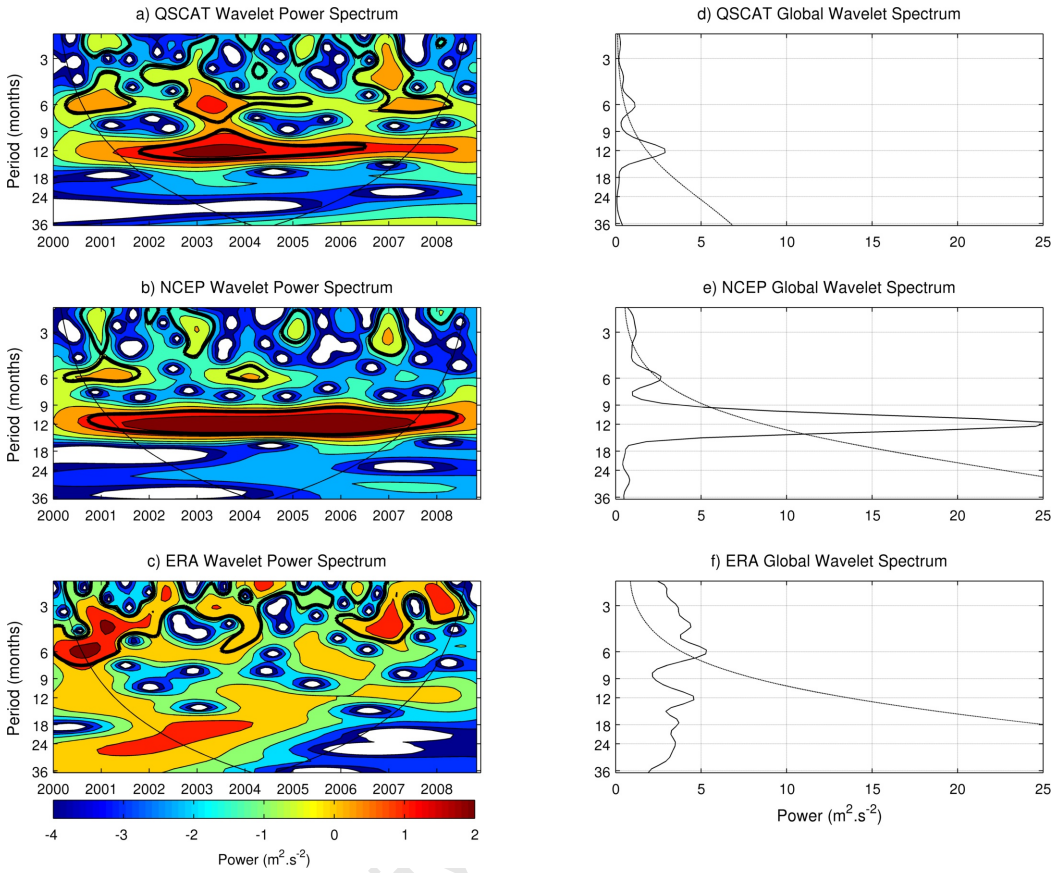

Figure 4.6: *Same as Figure 4.3 but for the Comoros (10-15°S, 42-47°E).*

global wavelet power spectrum of wind speed (Figure 4.6) for the different wind products over the Comoros, while the wind stress curl plots show similar distributions (Figure 4.7). The wind speeds of both QSCAT and NCEP II have a significant annual cycle, however the annual cycle of the latter is noticeably stronger (Figure 4.6d and e). The stronger annual cycle of NCEP II can be attributed to the stronger winds during the southwest monsoon. Compared to QSCAT and NCEP II, daily and monthly time series of ERA wind speeds (not shown) display consistently higher wind speeds and therefore a stronger than observed annual cycle is expected, however the greater variability of this product dampens the strength of its annual

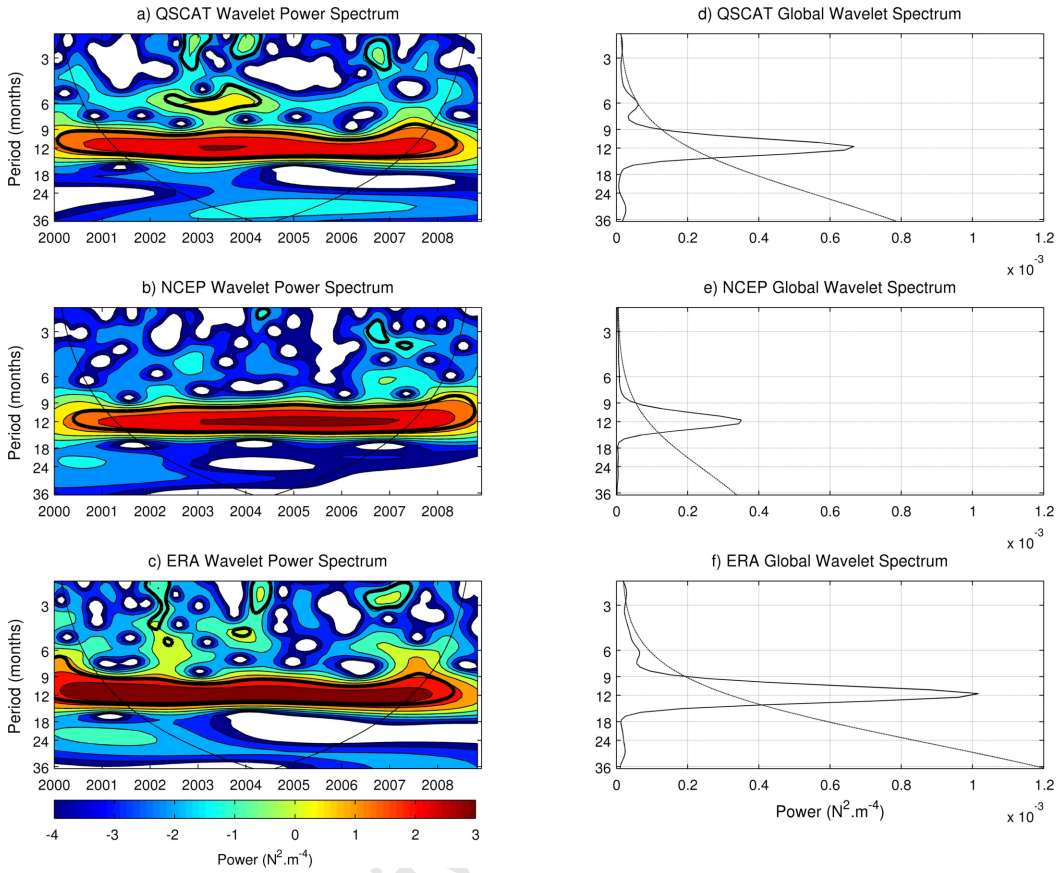

Figure 4.7: *Same as Figure 4.3 but for wind stress curl over the Comoros.*

cycle. Significant peaks in wind speed variability over the Comoros also occur at 3 months and semi-annual time scales in all three wind products, with the signals being much stronger in ERA compared to the other two products (Figure4.6). The semi-annual cycles of both ERA and QSCAT exhibit noticeable power peaks, during 2001 and 2003, respectively (Figure 4.6a and c). The stronger power peak of ERA results in a stronger average significance compared to QSCAT. Furthermore, ERA and QSCAT wind speed display a significant 4-5 month signal which is stronger in the former, a result of two power peaks, during 2001-2002 and 2006. On the other hand, QSCAT shows a single peak during 2007 (Figure 4.6a and c).

The wind stress curl plots (Figure 4.7) of the three wind products over the Comoros have significant peaks in variability at annual time scales, with this signal being stronger in QSCAT and ERA. The annual cycle of NCEP II wind stress curl is strongest during 2003-2007 (Figure 4.7b), while QSCAT wind stress curl displays strongest power during 2003 (Figure 4.7a). Despite the longer duration of the power peak in NCEP II, the average significance of the annual cycle is lower than that of QSCAT (Figure 4.7d and e). QSCAT also shows a semi-annual signal which is barely significant (Figure 4.7d).

4.4.1.3 Seychelles-Chagos Thermocline Ridge

Wind speed of the three different products over the SCTR display relatively similar annual cycles (Figure 4.8a). Similar to the wind speed over the Somali Jet, the wind speed over the SCTR is strongest during the Southwest monsoon (June-September). During this season, the wind speeds of the different products are comparable in strength, reaching a maximum during July in ERA and NCEP II while QSCAT displays maximum wind speed during August. An additional peak in wind speed is observed in all three products during February, with ERA displaying a third peak during May. During the Northeast monsoon (November-March) and the transition months of April-May and October, the wind speed of NCEP II is about 20-50% weaker than the wind speed of QSCAT and ERA. In all three wind products minimum wind speed occurs during April.

The annual cycle of wind stress curl over the SCTR is dominated by cyclonic wind stress curl (Figure 4.8b). In all three wind products, maximum cyclonic wind stress curl occurs during the Southwest monsoon with NCEP II displaying stronger cyclonic wind stress curl than the other two products. The weakest cyclonic wind stress curl occurs during the Northeast monsoon and minimum wind stress curl is observed during February in all three products.

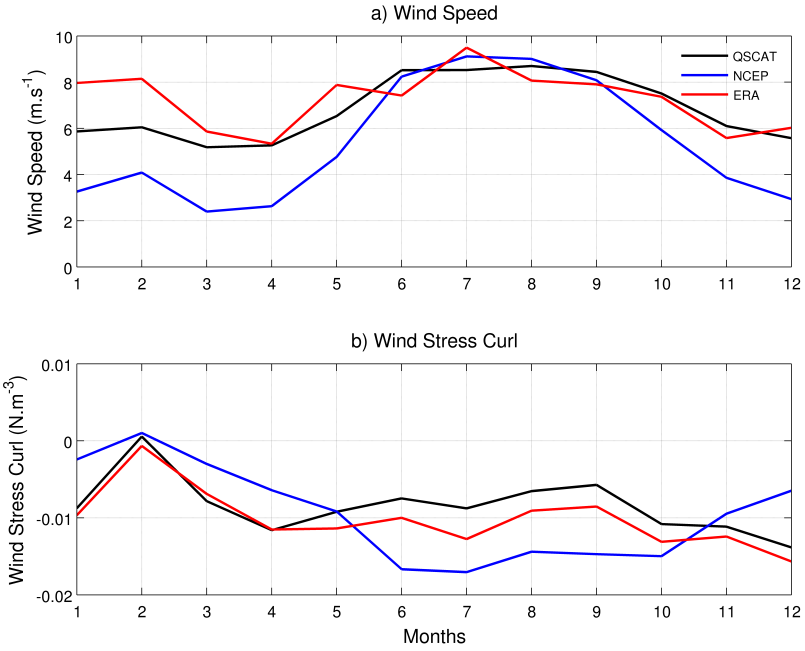

Figure 4.8: *The annual cycle of a) wind speed ($m{\cdot}s^{-1}$) and b) wind stress curl ($N{\cdot}m^{-3}$) over the SCTR. The black, blue and red lines represent QSCAT, NCEP and ERA, respectively.*

ERA and QSCAT wind stress curl display a decrease in wind stress curl from February to April after which there is a slight increase in wind stress curl. In NCEP II, however, wind stress curl decrease lasts an extra two months and only starts increasing again in July.

The wavelet power spectrum and global wavelet power spectrum of NCEP II and QSCAT wind speed over the SCTR display comparable patterns of variability (Figure 4.9). Both products display significant peaks in variability at annual timescales as well as a power peak between 2003 and 2007. Despite the comparable patterns of variability, the average significance of the annual signal of NCEP II wind speed is about three times higher than that of QSCAT. NCEP II wind speeds range from a minimum of $<2 m{\cdot}s^{-1}$ during the Northeast Monsoon to a maximum of $>8 m{\cdot}s^{-1}$ during the Southeast Monsoon, while QSCAT wind speeds

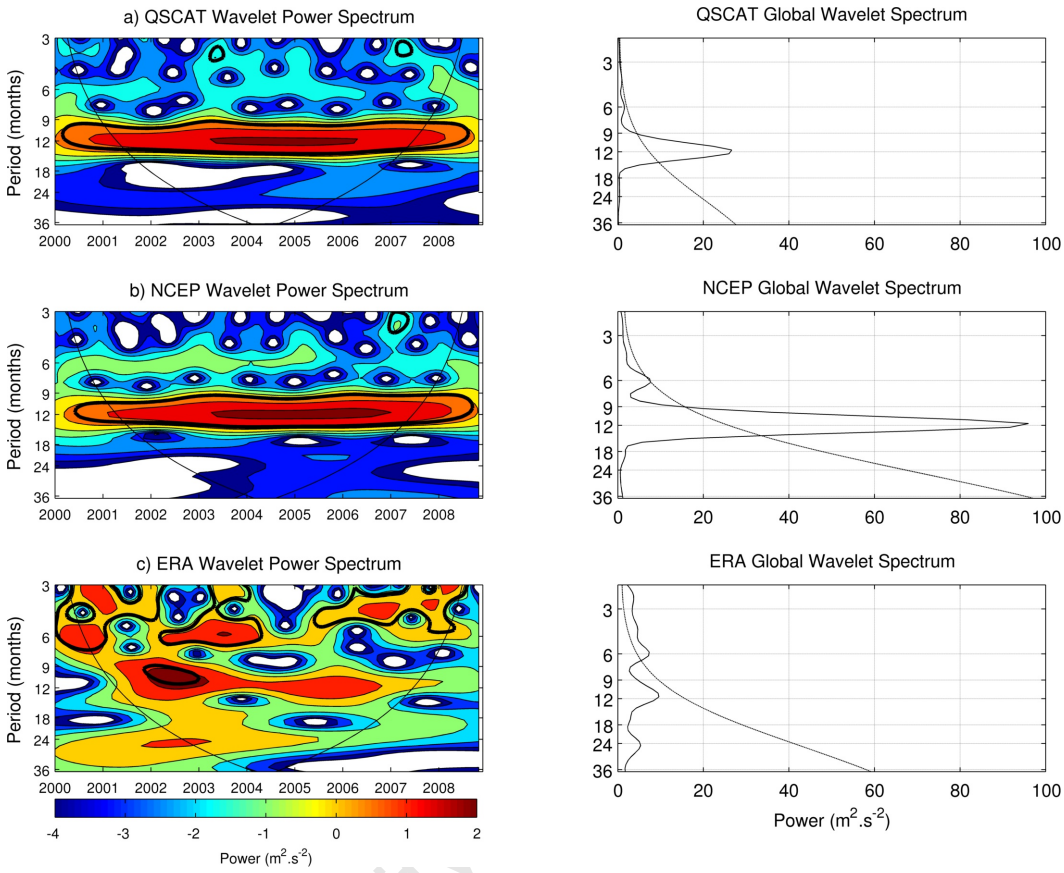

Figure 4.9: *Same as Figure 4.3 but for wind speed over the SCTR (5-12°S, 55-65°E).*

range from 5-9m·s^{-1}. The stronger annual signal of NCEP II wind speed can be attributed to the larger amplitude (3-9m·s^{-1}) compared to QSCAT (5-8.5m·s^{-1}; Figure 4.8a). In contrast to NCEP II and QSCAT, the wind speed of ERA over the SCTR display significant variability at 3 months and semi-annual timescales (Figure 4.9c). The monthly time series of ERA wind speed display higher wind speeds with greater variability than QSCAT and NCEP II for the majority of the time period and thus the greater variability of the ERA wind speed dampens the strength of the annual cycle.

The wind stress curl over the SCTR displays significant variability at semi-annual time

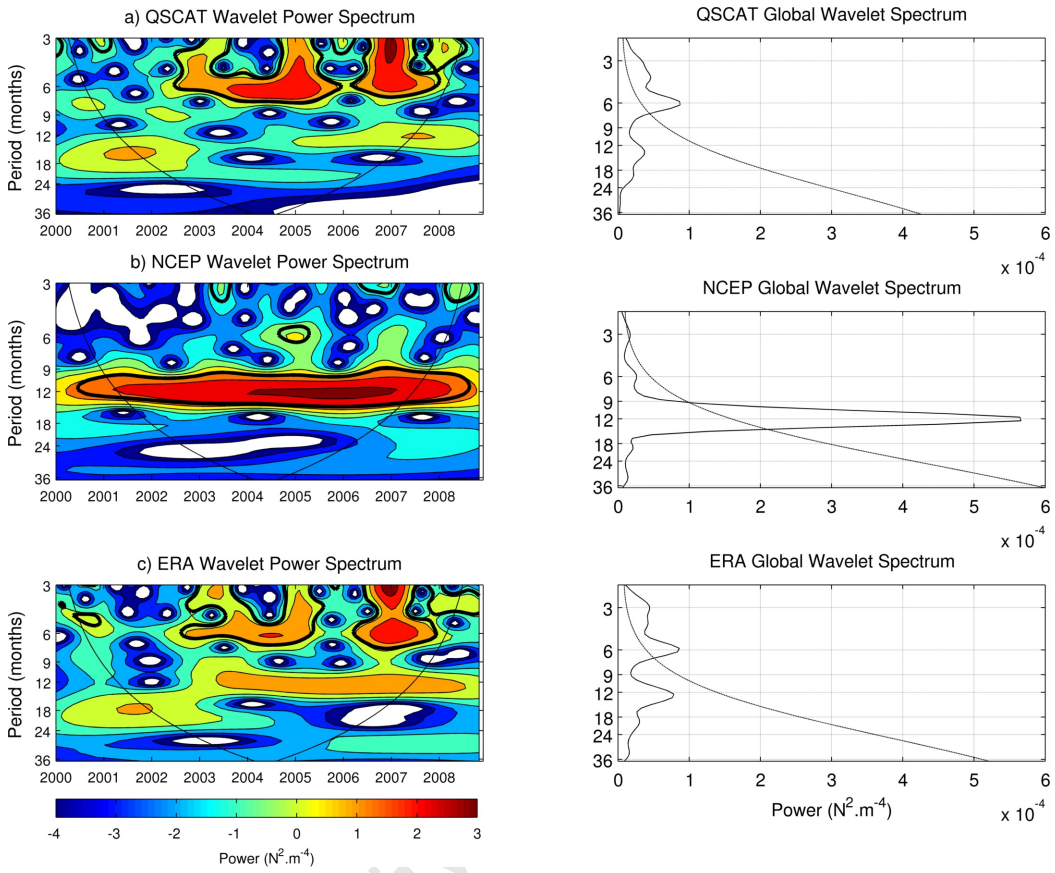

Figure 4.10: *Same as Figure 4.3 but for wind stress curl over the SCTR.*

scales, with comparable average significance, in QSCAT and ERA (Figure 4.10). The semi-annual signal of both QSCAT and ERA display a power peak during 2007 with an additional power peak (2004-2005) observed in QSCAT. Similar to wind speed, NCEP II wind stress curl has a significant annual signal with a power peak between 2004-2007. The stronger annual signal of NCEP II wind stress curl can be attributed to the stronger cyclonic wind stress curl of this product during the Southwest monsoon (Figure 4.8b). On the other hand, the semi-annual signal of ERA and QSCAT can be attributed to an increase in wind stress curl during the Southwest monsoon which does not occur in NCEP.

4.4.2 Seasonal Maps

Seasonal maps (JFM, AMJ, JAS, OND) were created for wind speed, wind stress curl and Ekman pumping but, for brevity, only the Southwest (JAS) and Northeast (JFM) monsoon seasons are considered here.

4.4.2.1 Wind Vectors

In general, all three wind products resolve the large-scale wind patterns of the two monsoon seasons. Southeasterlies dominate over the southwest Indian Ocean (SWIO) during the Southwest monsoon, whereas easterlies dominate during the Northeast monsoon (Figure 4.11). The curl associated with these winds is the driving force behind the South Equatorial Current, the main current transporting water into the SWIO (Schott and McCreary, 2001). The trade winds of the Southwest monsoon are stronger in NCEP II (Figure 4.11f) compared to ERA and QSCAT (Figure 4.11d and e). On the other hand, during the Northeast monsoon, the SWIO easterlies are weaker in ERA compared to QSCAT and NCEP II and are also limited in their extent (Figure 4.11a-c).

The northwest Indian Ocean (NWIO) experiences a drastic change in winds from the Northeast to the Southwest monsoon. Northeasterlies dominate over the NWIO during the Northeast monsoon (DJFM) and change direction upon crossing the equator to become northwesterlies/westerlies over the Comoros Basin and north of Madagascar. The northeasterlies in NCEP II are stronger compared to QSCAT and ERA. Moreover, in NCEP II and QSCAT (Figure 4.11a and c), the area of increased northeasterlies is confined to west of 70°E and 60°E, respectively, and extends north into the Arabian Sea whereas in ERA, they are confined to west of 50°E (Figure 4.11b) and its northward extent is limited to ~10°N.

The prevailing winds over most of the tropical western Indian Ocean change direction

from northeasterlies to southwesterlies during the transition months between the two monsoon seasons (April/May). Strong (~7-8m·s^{-1}) southwesterlies prevail over the NWIO during the Southwest monsoon season, with very strong (~10-15m·s^{-1}) southwesterlies occurring along the coast of Somalia and into the Arabian Sea (Figure 4.11d-f). This narrow band of intense southwesterlies represents the low-level atmospheric jet, known as the Findlater (Findlater, 1971) or Somali Jet. This jet is the driving force behind the intense northeastward flowing Somali Current along the Somali coast with surface speeds in excess of 2m·s^{-1} (Schott, 1983). A more extensive, intensified Somali Jet is evident in ERA and NCEP II (Figure 4.11e and f) compared to QSCAT (Figure 4.11d). During the entire Southwest monsoon season, the north-east extent of the Somali Jet is more tightly confined to the Horn of Africa in QSCAT than in the other wind products.

Due to its higher resolution, it is expected that the small-scale features in wind direction and wind speed will be better resolved by QSCAT than by ERA and NCEP. The most common small-scale features are corner acceleration and orographic effects such as wind shadows, both of which can influence the underlying oceanic circulation patterns. Corner acceleration, in the form of strong southeasterlies, is noticeable off the northern tip of Madagascar during the Southwest monsoon and the winds are also strengthened off the southeastern tip of Madagascar (Figure 4.11d-f). Furthermore, a wind shadow forms over the Comoros Basin perpendicular to the northwest coast of Madagascar. The corner accelerations and wind shadow associated with Madagascar are better resolved by QSCAT and ERA due to the higher resolution of these products.

The wind jets evident off the northern and southern tips of Madagascar are in accordance with the corner accelerations noted by Risien and Chelton (2008) and Chelton et al. (2004) and are analogous to wind jets observed on the flanks of islands situated in regimes of strong

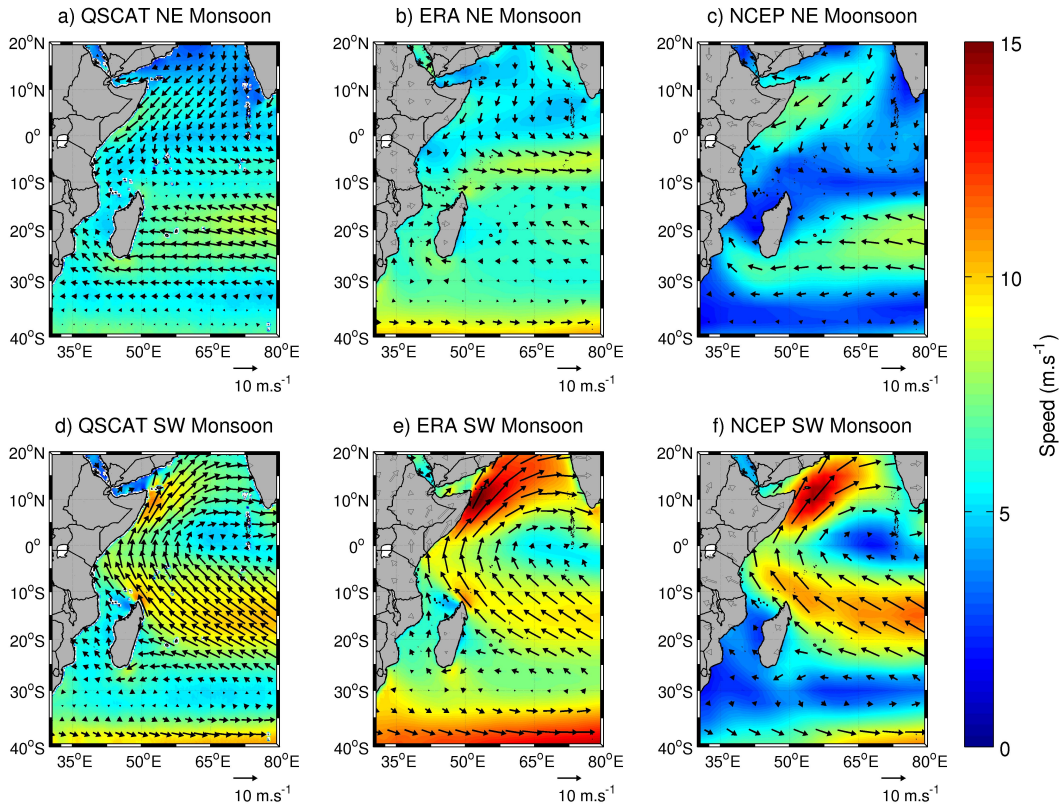

Figure 4.11: *Wind vectors of QSCAT (a, d), ERA (b, e), and NCEP (c, f) for the Northeast monsoon (top panel) and Southwest monsoon (bottom panel).*

trade winds (e.g. Chavanne et al. 2002). Wind jets on the flanks and wind wakes in the lee of islands form in response to the islands acting as a barrier to the trade winds. This results in a bifurcation of the prevailing winds around the islands which is mirrored by the circulation (i.e. SEC bifurcates upon encountering Madagascar). Northwesterlies dominate over the Comoros Basin during the Northeast monsoon and therefore no wind jet is formed off northern Madagascar.

The presence of Socotra Island (12.18-12.42°N, 53.19-54.33°E) with its mountains di-

rectly in the path of the Somali Jet, results in increased wind speeds off the eastern and western tips of this island with decreased wind speeds downstream. Consistent with the findings of Vecchi et al. (2004), under the steady southwesterlies of the Southwest monsoon season, QSCAT reveals that a wind wake bounded by wind jets is generated on the lee side of the mountains on Socotra (Figure 4.11d). The wind jets and wind wake are created in response to a split in the prevailing wind caused by the high elevation mountains on the island (Xie et al., 2001).

4.4.2.2 Wind stress curl and Ekman pumping

Overall, comparable patterns of wind stress curl and Ekman pumping are evident in all three wind products under investigation. However, some notable differences are observed in the small-scale features. ERA and NCEP II display smoother patterns of wind stress curl and Ekman pumping than QSCAT due to the lower resolution of these products.

The large-scale pattern of wind stress curl over the Indian Ocean comprises alternating wide latitudinal bands of negative and positive wind stress curl. As expected, due to the dramatic changes in wind direction associated with the changing monsoon seasons, contrasting wind stress curl patterns are observed for the NWIO (Figure 4.12). Associated with the prevailing northeasterlies of the Northeast monsoon, anti-cyclonic (negative) wind stress curl occurs over the Arabian Sea, the Gulf of Aden, and along the coast of the Arabian Peninsula with cyclonic (positive) wind stress curl occurring over the rest of the NWIO (Figure 4.12a-c). The anti-cyclonic curl extends south past the Horn of Africa and along the Somali east coast with the latter appearing stronger in ERA (Figure 4.12b) than in QSCAT and NCEP II (Figure 4.12a and c). The anti-cyclonic wind stress curl over most of the Gulf of Aden results in negative upwelling velocities (downwelling; Figure 4.13a-c). Along the east coast

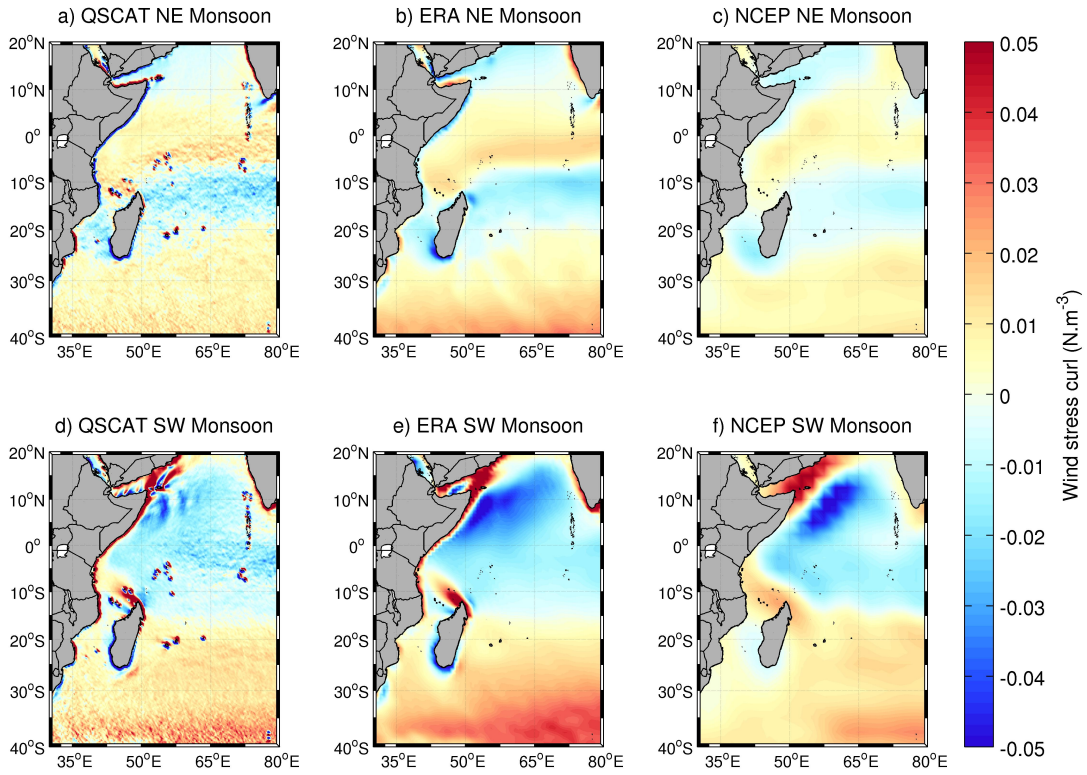

Figure 4.12: *Wind stress curl of QSCAT (a, d), ERA (b, e), and NCEP (c, f) for the Northeast monsoon (top panel) and Southwest monsoon (bottom panel).*

of Somalia, downwelling, a result of the anti-cyclonic wind stress curl, appears more intense in QSCAT and ERA than in NCEP II (Figure 4.13a-c). Note that upwelling velocities are not calculated within 3° of the equator due to the vanishing of the Coriolis parameter there.

The southwesterlies prevailing over the NWIO during the Southwest monsoon result in anti-cyclonic (negative) wind stress curl over most of the NWIO (Figure 4.12d-f). Comparable with the broader and stronger Somali Jet in ERA (Figure 4.11e), the anti-cyclonic curl displayed by ERA for the NWIO appears stronger than the curl of the other two wind prod-

ucts. Positive wind stress curl occurs along the east coast of Africa, over the Gulf of Aden and the western Arabian Sea. This positive curl is stronger in ERA (Figure 4.12e) than in the other wind products. Upwelling is evident along the Somali east coast in response to cyclonic wind stress curl. In ERA and NCEP II, the Ekman pumping extends further offshore and northeast into the Arabian Sea (Figure 4.13e and f) than is evident in QSCAT (Figure 4.13d) due to the coarser resolution of these products.

In QSCAT, the west-east extension of the cyclonic wind stress curl over the western Arabian Sea is not continuous during the Southwest monsoon (Figure 4.12d). A northeast oriented band of cyclonic curl is apparent off the eastern tip of Socotra Island separated from the cyclonic curl off the Horn of Africa by a band of anti-cyclonic wind stress curl. These bands of wind stress curl occur in response to the wind wakes and a wind shadow forms on the lee side of the island. In QSCAT, northeast oriented areas of downwelling and upwelling occur off the western and eastern tips of Socotra, respectively, (Figure 4.13d) in response to the wind stress curl dipole (Figure 4.12d). Downwelling is also observed south of Socotra in response to the anti-cyclonic wind stress curl associated with the Great Whirl. These small-scale features are clearly discernible in QSCAT, however, in ERA and NCEP II, the upwelling along the east coast of Somalia extends north around Socotra (Figure 4.13e and f).

Away from the coast, positive wind stress curl dominates over the NWIO during the Northeast monsoon and extends south to ~7°S over most of the western Indian Ocean but as far as ~15°S in the northern Mozambique Channel (Figure 4.12a-c). This band of anti-cyclonic wind stress curl in the SWIO can be attributed to the directional change experienced by the northeasterlies upon crossing the equator. The negative wind stress curl dominating over the NWIO during the Southwest monsoon extends into the SWIO to ~15°S except in the Mozambique Channel. In addition, cyclonic wind stress curl also occurs over the tropical

SWIO (~10-20°S) during the Northeast monsoon. Anti-cyclonic wind stress curl associated with the trade winds dominates over the rest of the SWIO and is the driving force behind the subtropical anti-cyclonic gyre and, in turn, the Agulhas Current. In ERA, the wind stress curl appears slightly stronger over the SWIO (Figure 4.12b) than in the other two products (Figure 4.12a and c).

Associated with the wind jets north and south of Madagascar during the Southwest monsoon, is a dipole of wind stress curl. A plume of intense anti-cyclonic wind stress curl extends northwest off the northern tip of Madagascar with a parallel band of cyclonic curl to the south evident in QSCAT and ERA (Figure 4.12d-e). NCEP II, however, depicts anti-cyclonic curl over the entire Comoros Basin rather than a distinct plume (Figure 4.12f). The anti-cyclonic plume off the northern tip of Madagascar results in downwelling, evident in all three wind products (Figure 4.13d-f), while the plume of cyclonic wind stress curl to the south results in upwelling depicted in QSCAT and ERA only. This finding is in agreement with studies of other high-topography islands in the Northern Hemisphere (e.g. Hawaiian and Cabo Verde islands (Chavanne et al., 2002); Canary Islands (Barton, 2001)) which display upwelling and downwelling in response to dipoles of positive and negative wind stress curl associated with northern and southern wind jets. No distinct upwelling is associated with the wind jet south of Madagascar.

Mauritius and Reunion are mountainous islands situated in a region of steady trade winds. Therefore, as is observed for other high-topographic islands in the path of trade winds (e.g. Hawaii and Canary Islands), wind jets on the flanks and wind wakes on the lee side of these islands are expected. Due to the coarser resolution of NCEP II and ERA, and the inability of scatterometers to sample data closer than ~30km from the coast, these features are not apparent in Figure 4.11. However, evidence of these wind jets and wind wakes can be found in

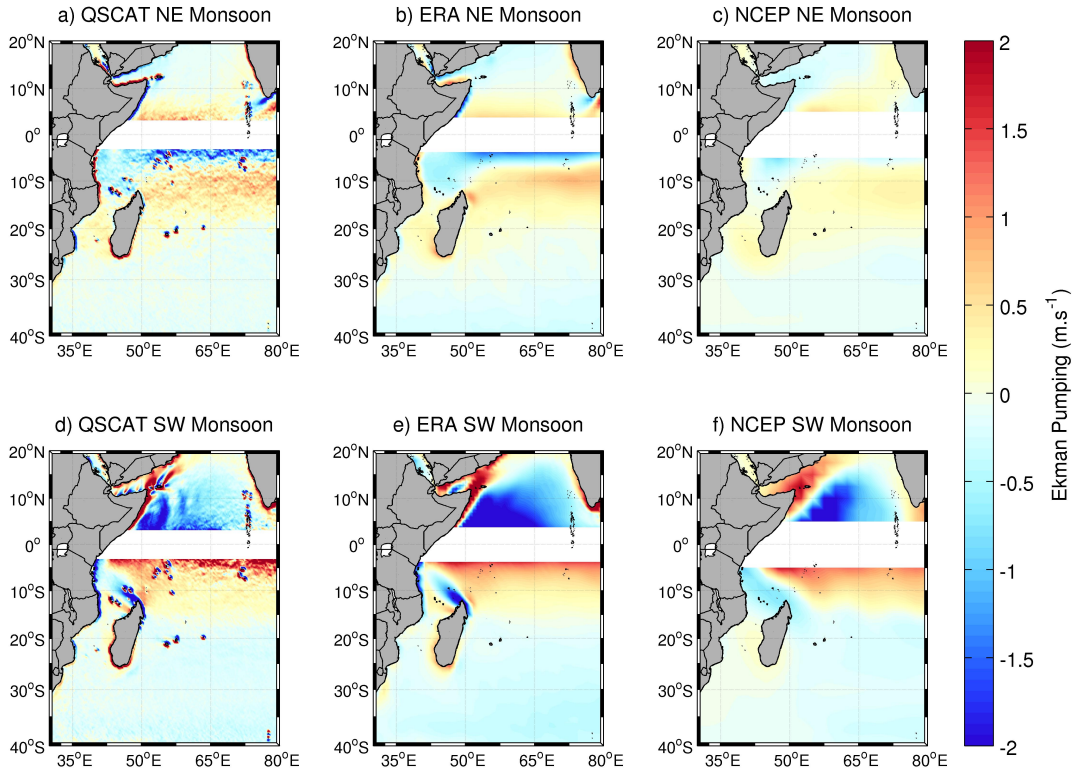

Figure 4.13: *Ekman pumping of QSCAT (a, d), ERA (b, e), and NCEP (c, f) for the Northeast monsoon (top panel) and Southwest monsoon (bottom panel). Positive (negative) Ekman pumping indicates upwelling (downwelling). Ekman pumping near the Equator is undefined and is not plotted between 3°N-3°S.*

the QSCAT derived wind stress curl patterns in the vicinity of these islands (Figure 4.12a and d). A study by Chavanne et al. (2002) reported positive wind stress curl on the northern side and negative curl on the southern side of the lee of the islands in the Hawaiian archipelago. The dipole of wind stress curl associated with these islands was attributed to wind jets and wind wakes occurring on the flanks and lee side of the islands, respectively (Xie et al., 2001). Similarly, a wind stress curl dipole in QSCAT, i.e. anti-cyclonic wind stress curl north of the islands and cyclonic wind stress curl to the south, is associated with Mauritius and Reunion (Figure 4.14a and b). Since the winds in this region only change from easterlies to southeasterlies with the monsoons (Figure 4.11a and d), there is no obvious seasonal shift in the wind stress curl dipole. No wind stress curl or upwelling dipoles are present in ERA and NCEP II.

On the basis of one year (January-December 1994) of ERS-1 scatterometer data, Petit et al. (2006) suggested that a wind stress curl dipole associated with Mauritius and Reunion exists. However, Petit et al. (2006), suggested that the dipole is only evident during February-March. The downwelling (upwelling) associated with the anti-cyclonic (cyclonic) wind stress curl could be due to the formation of anti-cyclonic (cyclonic) eddies in response to the horizontal shear in the wind field. Such wind-driven meso-scale eddies have been found in the lee of the Hawaiian Islands (Yoshida et al., 2010), and the Canary Islands (Arístegui et al., 1994) both of which are situated in the trade wind belt.

Similarly to the wind stress curl and upwelling dipoles associated with Mauritius and Reunion, wind stress curl and upwelling dipoles are also associated with the Comoros Islands (Figure 4.14), an archipelago of mountainous volcanic islands in the Comoros Basin. However, unlike Mauritius and Reunion, there is a seasonal reversal in the dipoles with the monsoons since the islands are located much closer to the equator. During the Southwest monsoon, southeasterlies prevail over the Comoros Basin and anti-cyclonic wind stress curl

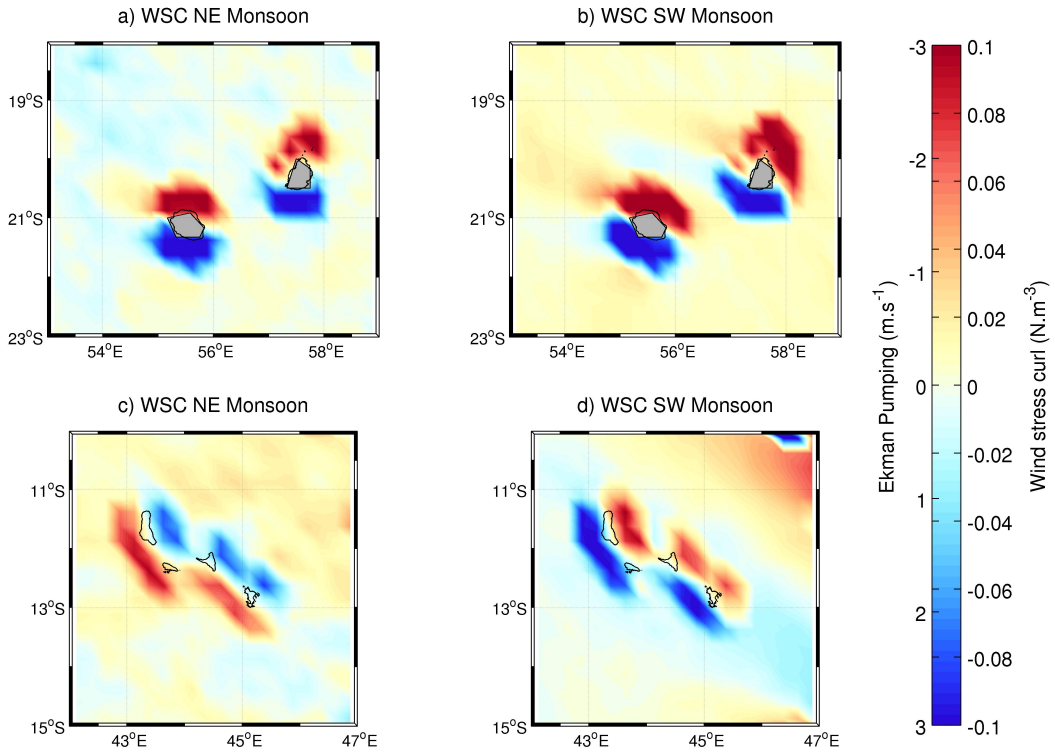

Figure 4.14: *QSCAT wind stress curl (WSC) and Ekman pumping over Mauritius and Reunion (a,b) and the Comoros Islands (c,d) for the Northeast monsoon (left panel) and the Southwest monsoon (right panel). Positive (negative) Ekman pumping indicates upwelling (downwelling).*

occurs to the north and cyclonic wind stress curl occurs to the south of the islands (Figure 4.14b). With the northwesterlies prevailing over the basin during the Northeast monsoon, cyclonic and anti-cyclonic wind stress curl occurs to the north and south of the islands, respectively (Figure 4.14a). The differing wind stress curl patterns of the monsoon seasons drive analogous Ekman pumping patterns (both shown in Figure 4.14).

4.4.3 Synoptic Scale Variability

Tropical cyclones are synoptic scale cyclonic systems characterized by enhanced convection, very strong near surface winds, and centres which are warmer than the surrounding atmosphere (Liu, 2010; McDonald et al., 2005). They represent a very important component of air-sea interactions (Fan et al., 2009; Yin et al., 2007) over regions of high sea surface temperatures in the tropical and subtropical oceans (McDonald et al., 2005). Tropical cyclones result in marked SST cooling, strong ocean current velocities and large surface gravity waves (Fan et al., 2009).

Tropical cyclones are classified based on the maximum sustained wind speed occurring near the centre of the storm. The classification of tropical cyclones generated over the southwestern Indian Ocean are summarised in Table 4.2. The lowest category in the southwest Indian Ocean, namely tropical disturbance are reserved for systems with wind speeds less than 50km·h^{-1}. These systems are upgraded to status of Tropical depression when they reach wind speed greater than 50km·h^{-1} but less than 63km·h^{-1}. Moderate tropical storms are designated as such when tropical depressions reach wind speeds greater than 65km·h^{-1}. Tropical storms with wind speeds in the range 89-117km·h^{-1} are classified as severe tropical storms. Once a severe tropical storm reaches wind speeds in excess of 118km·h^{-1}, it is upgraded to a Tropical cyclone. A tropical cyclone that intensifies further and reaches wind speeds >166km·h^{-1} is classified as an Intense tropical cyclone. A very intense tropical cyclone is classified as such when the system reaches wind speeds greater than 212km·h^{-1}. This is the highest category on the SWIO tropical cyclone scale (Tyson and Preston-Whyte, 2000).

An additional weather disturbance that occurs over the SWIO is the subtropical depression. These are synoptic scale low pressure systems which, during their lives, have charac-

Table 4.2: *Classification of tropical cyclones formed within the southwestern Indian Ocean.*

Classification	Wind Speed ($km \cdot h^{-1}$)	Example
Tropical Disturbance	<50	
Tropical Depression	51-63	
Moderate tropical storm	>65	Tropical storm Celina
Severe tropical storm	89-117	Tropical storm Hennie
Tropical cyclone	>118	Tropical cyclone Kesiny
Intense tropical cyclone	>166	Tropical cyclone Dera
Very Intense tropical Cyclone	>212	Tropical cyclone Hary

teristics belonging to both tropical and extra-tropical depressions (Tyson and Preston-Whyte, 2000). The genesis of such systems are regularly observed over the southern Mozambique Channel. Other important weather systems that affect the Mozambique Channel and neighbouring SWIO but which are not considered here are tropical-extratropical cloudbands (Hart et al., 2010) and Meso-scale Convective Complexes (Blamey and Reason, 2012).

To illustrate how the tropical cyclones generated in the SWIO are represented in the different wind products, a single snapshot of wind speed and wind stress curl of three events are analysed for each of the wind products. The selected events are a tropical disturbance, the severe tropical storm Hennie and the very intense tropical cyclone Hary.

On 3 January 2006, a tropical disturbance developed in the southern Mozambique Channel at approximately 20°S (Figure 4.15a). This weather disturbance had a west-southwestward trajectory moving to the coast of Mozambique before eventually becoming an overland depression on 5 January 2006 and had dissipated by 7 January 2006. The maximum sustained wind speeds of this system was estimated to be $12.9 m \cdot s^{-1}$ occurring while the system was located inland from the channel. This tropical disturbance can clearly be seen in both QSCAT and ERA as localised areas of high wind speeds in the southern Mozambique Channel (Figures 4.15b and c). Even though higher wind speed is also observed in this region in NCEP

(Figures 4.15d), it does not appear as a localised feature, but rather seems to form part of the generally higher wind speed which occurs in the Mozambique Channel. The maximum wind speed observed for this feature in ERA is slightly less (~10m·s^{-1}) than the maximum wind speed observed in QSCAT (22m·s^{-1}). Strong negative wind stress curl is associated with the centre of the tropical disturbance while positive wind stress curl occurs to the east of it, as is evident in QSCAT (Figures 4.15e). ERA derived wind stress curl displays a similar pattern, however the negative wind stress curl associated with the centre of the tropical disturbance is located closer towards the coast than the tropical disturbance is located (Figures 4.15f). No distinct wind stress curl is observed in NCEP associated with the tropical disturbance (Figures 4.15g).

Severe tropical storm Hennie formed west-southwest of Diego Garcia (see Figure 4.1), a tropical coral atoll south of the equator, on 21 March 2005 as a tropical depression with wind speeds less than 15m·s^{-1}. Along its south-southeastward trajectory, it intensified to a severe tropical storm on 24 March 2005, east-northeast of Mauritius with maximum estimated wind speeds in excess of 25m·s^{-1} (Figure 4.16a). Severe tropical storm Hennie is clearly depicted in all three wind products with similar maximum speed and, like the systems described above, this system has a larger horizontal extent in ERA and NCEP compared to QSCAT (Table 4.3 and Figures 4.16b-d). The wind stress curl associated with this storm appears as a centre of negative wind stress curl with positive wind stress curl associated with the southern edge. The negative wind stress curl in QSCAT and ERA are of similar strength while NCEP display slightly weaker wind stress curl (Figures 4.16e-g).

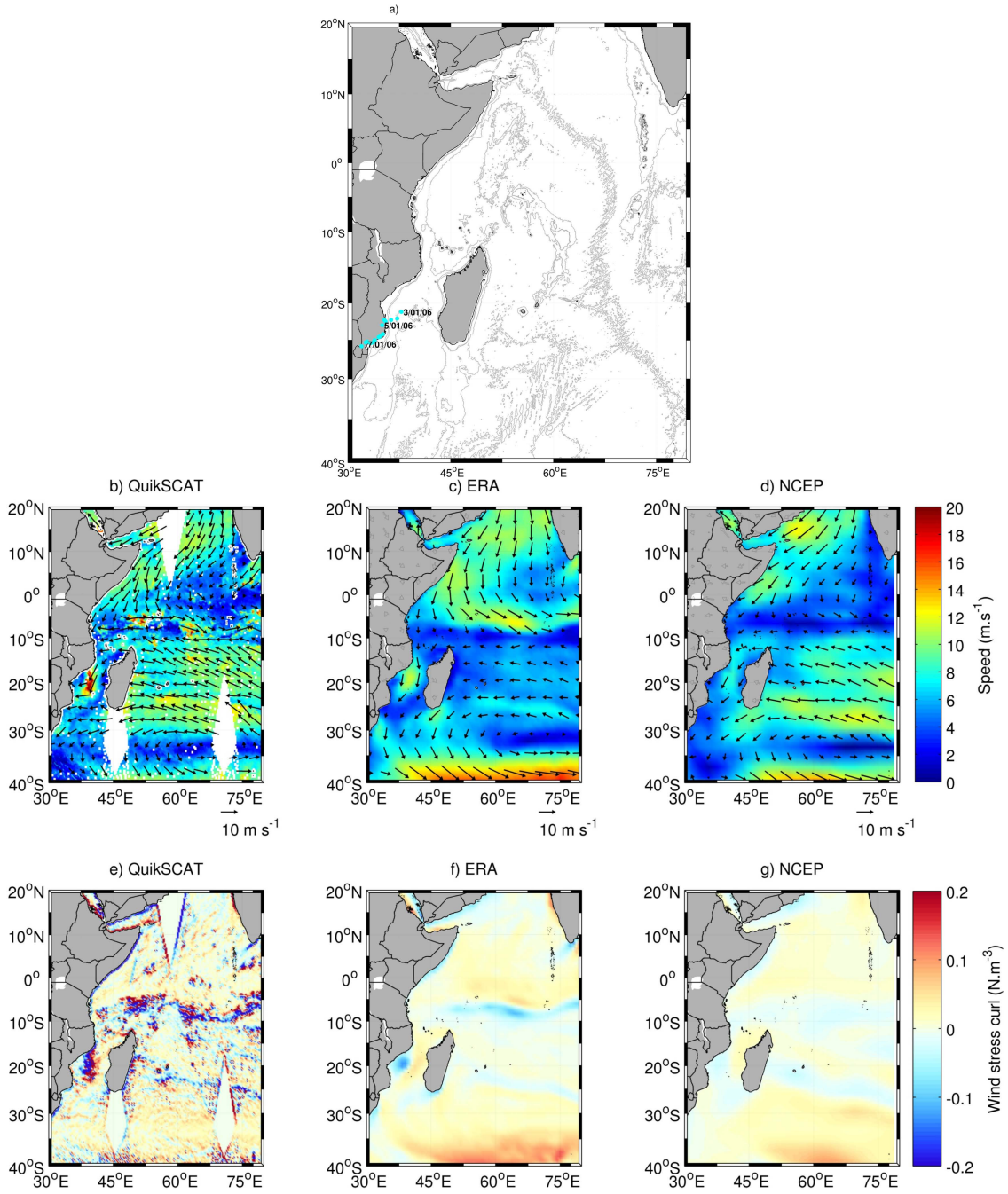

Figure 4.15: *The storm track (a) as well as the wind speed (a-d) and wind stress curl (e-f) of a tropical disturbance formed in the southern Mozambique Channel as reproduced by the three different wind products.*

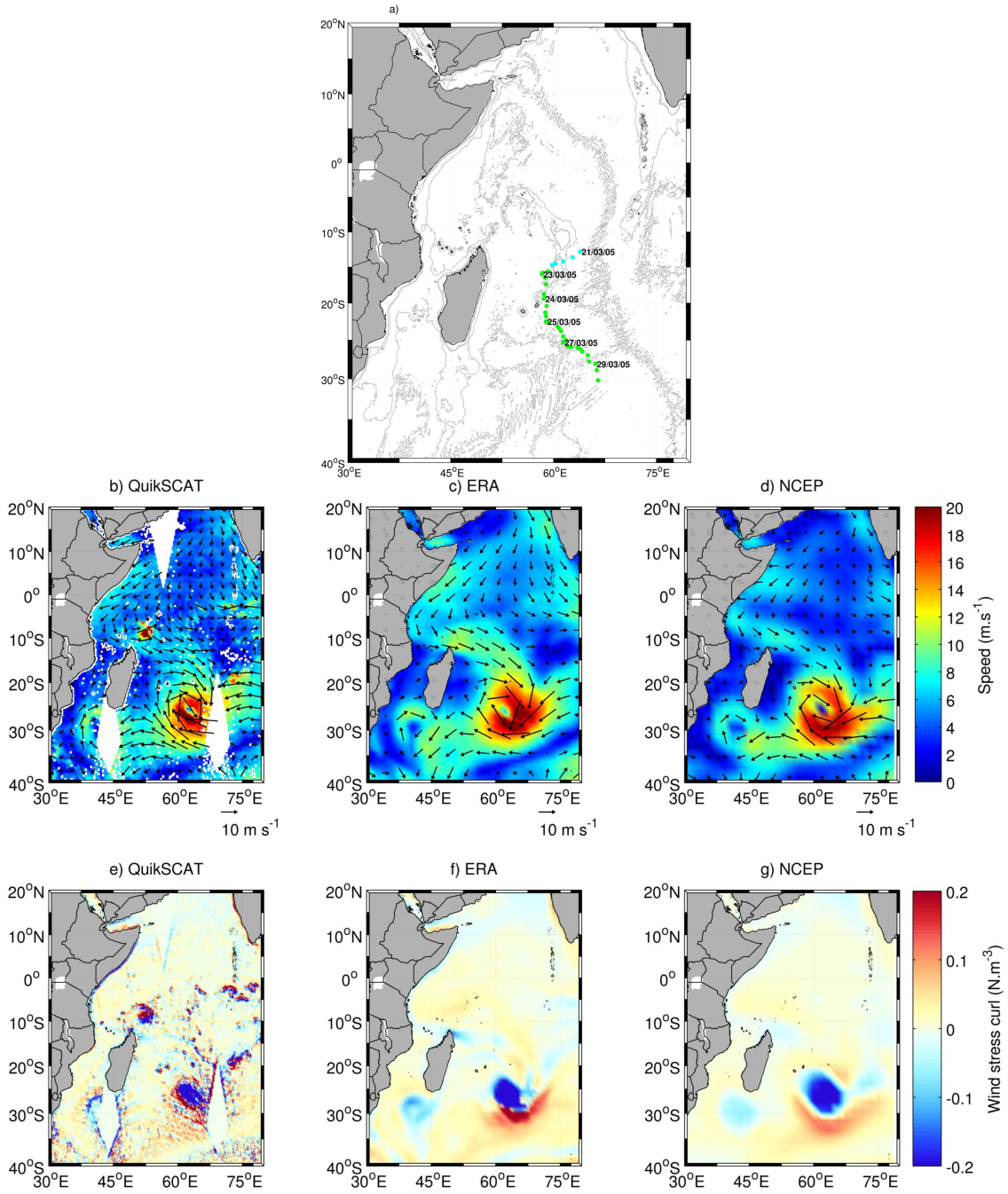

Figure 4.16: *The storm track (a) as well as the wind speed (a-d) and wind stress curl (e-f) of the sever tropical storm Hennie as reproduced by the three different wind products. In (a), the light blue circles indicates wind speeds <33m·s^{-1} and the green indicates wind speeds of 33-63m·s^{-1}.*

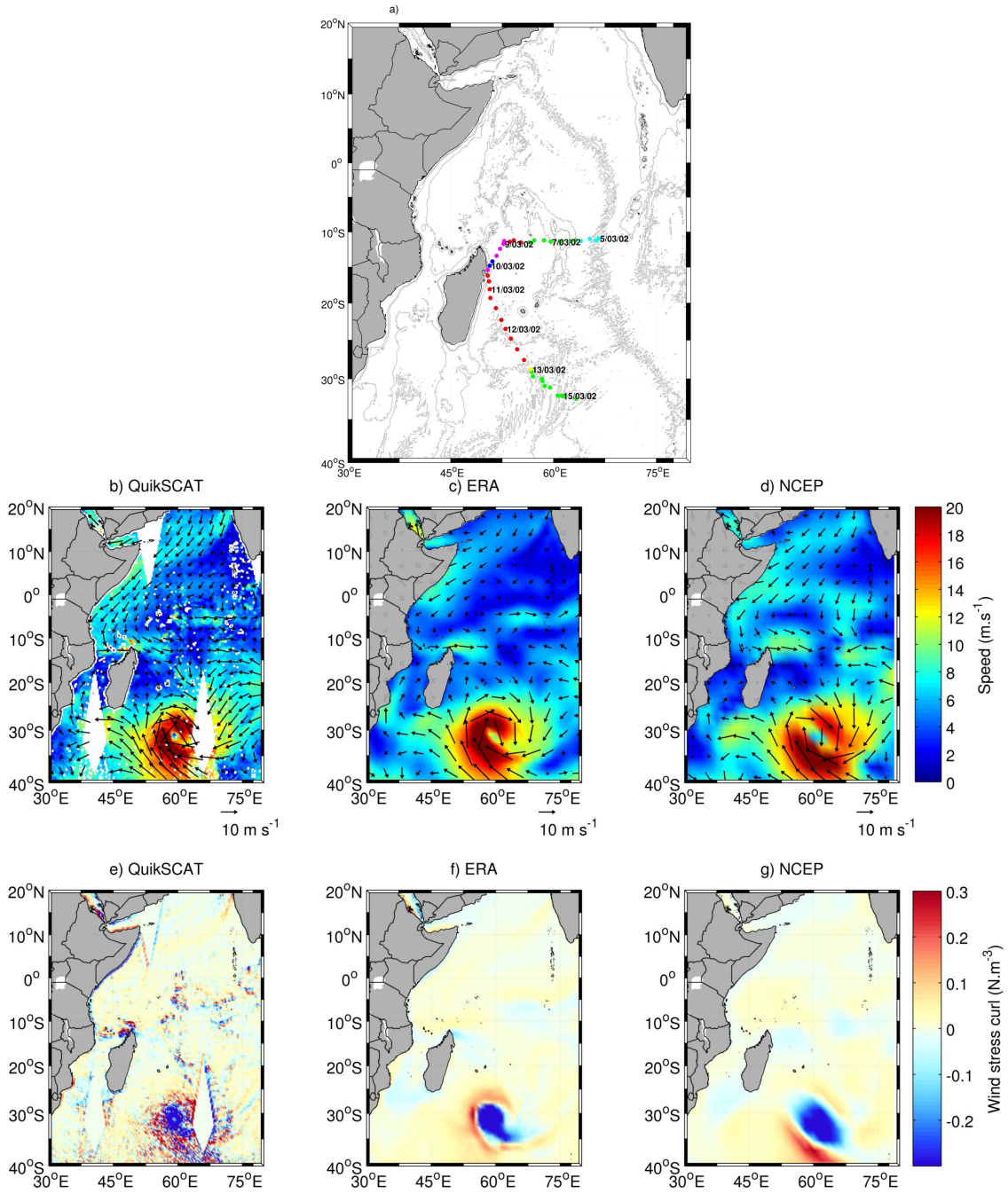

Figure 4.17: *The storm track (a) as well as the wind speed (a-d) and wind stress curl (e-f) of the very intense Tropical Cyclone Hary as reproduced by the three different wind products. In (a), the light blue, green, yellow, red, pink and dark blue circles indicate wind speeds of <33m·s^{-1}, 33-63m·s^{-1}, 64-82m·s^{-1}, 83-95m·s^{-1} and 113-134m·s^{-1}, respectively.*

Cyclone Hary developed on 5 March 2002 west-southwest of Diego Garcia as a tropical depression (Figure 4.17a). This system initially had a westward trajectory and intensified to tropical cyclone strength northwest of the tip of Madagascar were it turned southwestward intensifying further to speeds in excess of $50 m \cdot s^{-1}$ making the storm a "very intense" tropical cyclone. Upon reaching the coast of Madagascar, cyclone Hary turned southeastward and along this trajectory it weakened back to tropical storm intensity. Cyclone Hary is clearly evident in all three wind products and occurs as a slightly larger feature in NCEP (Figure 4.17d) while in ERA and QSCAT (Figures 4.17b and c) it is of similar horizontal extent (Table 4.3). In all three wind products, the maximum wind speed obtained by this tropical cyclone are of similar magnitude. Negative wind stress curl is associated with the core of this feature and is surrounded by positive wind stress curl as is evident in all three wind products (Figure 4.17).

In summary, the synoptic scale variability is better resolved by QSCAT compared to the other two wind products. However, compared to the estimated intensity calculated by the Joint Typhoon Warning Center (JTWC) using the Dvorak technique (Dvorak, 1984), the intensity of the tropical cyclones are underestimated by all three products. The most notable difference in the synoptic variability of the three products is the horizontal extent of the weather systems. This tends to be greater in the reanalysis products compared to QSCAT as expected from the lower resolution of the former. Overall, the intensities of the weather systems are comparable in the three products; however, at maximum speeds of $33 m \cdot s^{-1}$ or more (tropical cyclones) the reanalysis products have greater intensities than QSCAT. The wind stress curl associated with the weather systems is of similar strength in QSCAT and ERA, but weaker in NCEP II. ERA, however does display stronger wind stress curl than QSCAT for maximum wind speeds greater than $33 m \cdot s^{-1}$. The discrepancies between the in-

Table 4.3: *The mean diameter (km) of the selected storm systems for the three different wind products.*

Storm	QSCAT	ERA	NCEP
Tropical disturbance	464	446	Not detected
Severe tropical storm Hennie	778	999	1094
Very intense tropical cyclone Hary	973	993	1197

tensities at maximum wind speeds greater than $33 m \cdot s^{-1}$ could be due to a lack of data and rain contamination resulting in lower intensities in QSCAT. Moreover, the greater intensities of the weather systems in the reanalysis could be a result of the inability of these products to successfully simulate the onset of the systems, thus they may require increased intensity to maintain an energy balance.

4.5 Summary

The main objective of the analysis in this chapter was to compare different wind products over the western Indian Ocean with an emphasis on the Comoros Basin which is not well understood. For comparison, analysis of the wind products over the Somali Jet and Seychelles Chagos Thermocline Ridge regions are also presented. The differences in the three wind products have important implications for the regional ocean dynamics and modelling of the western Indian Ocean, particularly with respect to meso-scale wind differences. Meso-scale wind features are most likely to influence smaller regional ocean circulation patterns such as the circulation in the Comoros Basin. The wind products, each with a different horizontal resolution, were compared in terms of annual cycle, dominant modes of variability and patterns of wind speed and direction, wind stress curl and Ekman upwelling velocities.

Wavelet analyses of wind speed and wind stress curl over three sample regions, the Somali

Table 4.4: *Dominant modes of variability in the wind speed, and wind stress curl of the three different wind products over the Somali Jet (5-10°N, 50-55°E), the Comoros (10-15°S, 42-47°E) and the SCTR (5-12°S, 55-65°E).*

	Somali Jet			**Comoros**			**SCTR**		
	Seas	Semi-ann	Ann	Seas	Semi-ann	Ann	Seas	Semi-ann	Ann
Wind Speed									
QSCAT		x	x	x	x	x			x
NCEP		x	x	x	x	x			x
ERA		x	x	x	x		x	x	
WSC									
QSCAT			x			x	x	x	
NCEP		x				x			x
ERA		x	x			x	x	x	

Jet, SCTR and the Comoros Basin, were used to determine the dominant modes of variability present in the three wind products. This analysis, summarized in Table 4.4, revealed that wind speeds over the Somali Jet display similar modes of variability in all three wind products with the dominant modes being a semi-annual and annual cycle. Similarly, the annual cycle calculated for wind speed over the Somali Jet show similar patterns in all three products even though there is a distinct difference in the strength of wind speed. The variability of wind stress curl over the Somali Jet displays rather different patterns in the three wind products. ERA displays both a semi-annual and annual cycle while NCEP II shows only a semi-annual cycle and QSCAT an annual cycle. The lack of an annual cycle in the wavelet analysis of NCEP II wind stress curl over the Somali Jet is a result of the weak variability of wind stress curl of this product compared to that of QSCAT and ERA. This weak variability could be due to the data assimilated or due to a large deviation of the estimated parameters from observations.

The wavelet analysis of wind stress curl over the Comoros showed similar modes of

variability in the different wind products; however, rather different patterns are evident in wind speed. In addition to a semi-annual cycle displayed by the wind speed of all three products, QSCAT and NCEP II also exhibit a significant annual cycle. The absence of an annual cycle in the wavelet analysis of ERA wind speed over the Comoros can be attributed to the increased higher frequency variability displayed by this product which results in a relative dampening of the annual cycle. Due to the increased variability of ERA wind speed, significant variability at shorter time scales are evident for this product over the Comoros.

For both the Somali Jet and the Comoros, the global wavelet spectrum of QSCAT wind speed is significantly lower compared to that of the reanalysis products. The global wavelet spectrum is a function of variance and the wavelet power spectrum. Compared to the reanalysis products, QSCAT wind speed has a lower variance for both regions. Furthermore, the wavelet power spectrum of wind speed over the Somali Jet is comparable in NCEP II and QSCAT at both annual and semi-annual time scales but that of ERA is lower (higher) at semiannual (annual) time scales. The wavelet power spectrum of ERA wind speed over the Comoros is weaker overall than that of QSCAT and NCEP II, while NCEP II has higher power at annual time scales and weaker power at semi-annual time scales compare to QSCAT. Therefore, it can be concluded that the weaker global wavelet spectrum of QSCAT wind speed can be attributed to the lower variance. The lower variability of QSCAT wind speed is indicative of a smoother time series, and therefore, a signal with lower power compared to the reanalysis products can still be significant.

Wavelet analysis of wind speed over the SCTR region revealed that the dominant mode of variability in NCEP II and QSCAT occurs at annual time-scales while in ERA it occurs at semi-annual and seasonal time-scales. On the other hand, the dominant modes of variability for wind stress curl in QSCAT and ERA occur at seasonal and semi-annual time-scales

whereas NCEP II display significant variability at annual time-scales. Similar to ERA wind speed over the Comoros, the absence of an annual cycle in the wavelet analysis of wind speed over the SCTR in ERA is a result of increased month-on-month variability which diminishes the strength of the annual cycle. The absence of a semi-annual cycle in the wind stress curl of NCEP over the SCTR can be attributed to a steady decrease in wind stress curl commencing at the end of the Northeast monsoon until it starts again. The stronger global wavelet spectrum of NCEP wind speed at annual time-scales over the SCTR compared to that of QSCAT is indicative of the stronger variability of this dataset over the region. The comparable strength of the global wavelet spectrum of ERA and QSCAT wind stress curl over the SCTR indicates that the variability of these two data sets are similar over the SCTR region.

The data sets are in relatively good agreement with regards to the large-scale patterns of wind speed, wind direction, wind stress curl and Ekman pumping. All three wind products reproduce the characteristic features of the two monsoon seasons reasonably well; however, some notable differences are observed. These are the differing strengths and extent of the Somali Jet during the Southwest monsoon and the differing strengths and extent of the easterlies prevailing over the SWIO during the Northeast monsoon. The discrepancy between the annual cycle of the scatterometer and reanalyses wind stress curl over the Somali Jet exemplifies the differences between the products with regard to the strength and expanse of certain large-scale features such as low-level atmospheric jets.

The differences in the annual cycle of wind speed and wind stress curl over the Somali Jet during the Southwest monsoon suggests that the feedback from the ocean on low-level winds may be poorly resolved by the reanalysis products. Both ocean currents and sea surface temperature (SST) gradients have been shown to modify wind stress curl (Chelton et al., 2004). Scatterometers measure backscatter from wind-generated waves and when movement

in the atmosphere and ocean coincide, waves are not generated and hence, no winds are measured by scatterometers (Kelly et al., 2001). Conversely, the winds of numerical weather prediction models are estimated relative to fixed locations, thus the ocean surface is regarded to be motionless (Chelton et al., 2004). Therefore, wind speeds of scatterometers will be lower (higher) than the wind speeds of numerical weather prediction models when the surface currents are flowing in (against) the direction of the wind. The lower wind speed of QSCAT over the Somali Jet (Figures 4.2a and 4.11) supports this and can be attributed to the influence that the strong northward flowing Somali Current has on the QSCAT wind measurements. These differences between scatterometer and reanalysis wind products need to be considered when modelling areas with strong currents.

Since the magnitude of the wind is used to calculate the wind stress which, in turn, is used to calculate wind stress curl, lower wind speeds would result in a decrease in the wind stress curl of the scatterometer. Although the offshore wind stress curl of QSCAT is weaker than that of the reanalyses, the positive wind stress curl along the coast is stronger in QSCAT (Figure 4.11). Risien and Chelton (2008) found that wind stress curl develops over regions of strong crosswind SST gradients, while wind stress divergence develops in regions of strong downwind SST gradients. In the Somali Basin, the crosswind SST gradient is stronger than the downwind SST gradient due to upwelling along the Somali coast. In agreement with the findings of Risien and Chelton (2008), the positive crosswind SST gradient manifest in QSCAT as stronger wind stress curl along the Somali coast. The difference in the annual cycle of wind stress curl during the Southwest monsoon can thus be attributed to the stronger positive wind stress curl of QSCAT along the Somali coast due to the crosswind SST gradient. The stronger negative offshore wind stress curl of the reanalyses may be due to their inability to resolve the ocean feedback on low-level winds.

The Seychelles-Chagos Thermocline Ridge, an upwelling region in the southwest Indian Ocean, forms as a result of the wind pattern: southeasterly winds dominate south of the SCTR driving weak near-surface southward flow due to the Coriolis force, while westerly winds, associated with northward flow, dominates north of the SCTR. This wind pattern results in surface divergence which is compensated for by upwelling (Hermes and Reason, 2008). The discrepancy between NCEP wind stress curl and that of the other two wind products suggests that the atmospheric response to the cooler SST associated with the SCTR may be misrepresented in NCEP. Another source of discrepancy may be the underrepresentation of the strength of the upwelling of the SCTR.

Prominent differences exist in the small scale features of the different wind products. Most notable is the inability of the reanalysis products to resolve the wind stress curl and upwelling dipoles associated with the Comoros islands, Mauritius and Reunion. Additionally, the disparity between the annual cycle of wind stress curl for the higher (QSCAT and ERA) and the low (NCEP II) resolution products over the Comoros, a complex region with island effects, indicates the inability of low resolution products to resolve wind wakes, jets and other local scale features. The coarser resolution of ERA and NCEP II averages out the signature of these local scale features. Since most of the local scale features are caused by an interaction of the wind with orographic features such as high mountains, the smoothed orography of ERA and NCEP II also contributes to their inability to resolve these features.

The corner acceleration off the northern tip of Madagascar and its associated anti-cyclonic wind stress curl may create an instability in the current flowing off the northern tip of Madagascar. In turn, this instability may influence the formation and dynamics of the Comoros Gyre. The wind jet off the northern tip of Madagascar is only present during the Southwest monsoon, and hence could result in an increased frequency of the formation of the gyre dur-

ing this season. In addition, the wind stress curl dipole associated with the Comoros islands could result in the formation of wind-driven meso-scale eddies, as has been observed for other mountainous islands with associated wind stress curl dipoles (Arístegui et al., 1994; Yoshida et al., 2010). The formation of such wind-driven meso-scale eddies in the Comoros Basin could impact the circulation patterns and thereby influence the formation and dynamics of the Comoros Gyre.

Furthermore, the environmental conditions of the southwest Indian Ocean are favorable for cyclogenesis, as such this region experiences an average of 12 tropical cyclones per year during November to April (Fink and Speth, 1998). Tropical cyclones form over most of the world's tropical waters between ~5-22° latitude where sea surface temperatures are sufficiently high (>26°C) and where there is weak vertical wind shear and instability in the moisture flux (Liu, 2010). These synoptic-scale systems have profound impacts on the physical properties of the underlying ocean. Numerous studies (e.g. Dickey et al., 1998) have found that tropical cyclones result in an increase in the mixed layer depth, a decrease in SST by up to 6°C, and near-inertial surface currents of 1-2m·s^{-1}, detectable at depths up to ~500m (Withee and Johnson, 1976). At the base of the mixed layer, strong turbulence is induced by the vertical shear of the horizontal currents. In turn, the strong turbulence drives the mixing of warm water across the mixed layer base (Emanuel, 2005) and entrainment of deeper cold water into the mixed layer (Ginis, 2002) resulting in a cooling of the sea surface temperatures and a deepening of the mixed layer.

Additionally, the strong winds associated with tropical cyclones result in vertical mixing and upwelling which injects cold, nutrient-rich waters from deeper layers into the surface layer (Price, 1981). Son et al. (2006) as well as Yin et al. (2007) found that the entrainment of nutrient-rich waters into the surface layer during the passage of a tropical cyclone coincided

with increased chl-a concentrations, a result of a phytoplankton bloom. In-situ measurements of the physical and biological responses to the passage of tropical cyclones are very limited and the cloud-cover associated with cyclones obscure satellite sensors. Therefore, ocean models coupled with a biochemical model play a crucial part in gaining a better understanding of the ocean responses including the biological responses to tropical cyclones.

The different wind products under consideration differed with respect to the horizontal extent of the weather systems as well as the intensities. The larger horizontal extent of the weather systems in NCEP and ERA would result in larger areas of decreased SST due to vertical mixing and upwelling which in turn might imply larger phytoplankton blooms. On the other hand, the lower wind speeds of the weather systems would result in weaker vertical mixing and upwelling and consequently less intense phytoplankton blooms. Yin et al. (2007) investigated the physical and biochemical responses of the ocean to Typhoon Ketsana using a ROMS simulation forced with QSCAT data and found that the SST cooling and the phytoplankton bloom were weaker in the QSCAT simulation compared to observations. The weaker SST cooling and phytoplankton bloom in the QSCAT simulation can be attributed to contamination of the QSCAT data under heavy rain conditions associated with tropical cyclones. Therefore, it is recommended that modelling studies focusing on the oceanic response to tropical cyclones, both physical and biological, use more accurate wind forcing data.

With its several mountainous islands of different sizes, the tropical western Indian Ocean offers a useful testbed for the comparison of different wind products and their associated ocean circulation patterns. Given that this region feeds into the Agulhas Current, the strongest western boundary current in the Southern Hemisphere, which is known to have important connections with the weather and climate of Southern Africa and the Atlantic Meridional Overturning Circulation (AMOC), the results discussed here may have broader than regional

significance.

4.6 Conclusion

The results presented here suggest that there is a trade-off between spatial resolution and temporal resolution in the wind forcing used for regional ocean modelling. The high resolution QuikSCAT wind data have a low temporal resolution of one day and are only available for the period July 1999-November 2009 (Table 4.1). This dataset, however, can be supplemented by ASCAT which like QuickSCAT has a 0.25° spatial resolution and is available from January 2009 onwards. The two reanalysis data sets with lower spatial resolution compared to QuikSCAT, on the other hand, are available over a longer time period and these products are constantly being improved upon. Therefore, it is recommended that ocean modelling circulation studies that require high temporal resolution should, at present, consider using a wind product of lower spatial resolution but which provides a better temporal data coverage. For studies requiring high spatial resolution such as those focused on meso-scale activity, it is recommended that the high resolution scatterometer data be used. This high resolution product is more reliable in reproducing the meso-scale wind features (e.g. wind jets) producing wind-driven meso-scale eddies which could impact the general circulation patterns of the region.

Furthermore, for studies interested in modelling the physical and biochemical response of the ocean to tropical cyclones, it is recommended that wind data derived from the angular momentum model be used as forcing since QuikSCAT wind data which is affected by rain contamination could under-represent the intensity and size of the cyclones. Conversely, the low resolution of the reanalyses would result in an overestimation of the size. The analysis presented here does not provide a clear cause of the underestimation of the intensity of the

cyclones in the reanalysis products and should be addressed in future studies. It could be a result of the low resolution or a misrepresentation of the air-sea interactions associated with the cyclones or a combination of both.

The Comoros Basin, the region of interest for this dissertation, is located in a region where orography has a strong influence on the wind field. Also, as seen in Chapter 3, the basin is a region of high meso-scale activity and in order to obtain a realistic representation of the circulation in the basin, a high resolution model simulation is needed. Therefore, QuikSCAT wind data, which are capable of reproducing the meso-scale wind features, is the logical choice for surface forcing of a high resolution ocean circulation model of the Comoros Basin.

Chapter 5

Numerical Modelling

A review of the current knowledge of the circulation in the Mozambique Channel, presented in Chapter 2, has shown that this is an area of high meso-scale activity that is still not fully understood due to limited observations. Despite the increased interest in the Mozambique Channel recently, the majority of research efforts have focused on the region south of 15°S (e.g. Ridderinkhof and de Ruijter, 2003; Harlander et al., 2009; Ridderinkhof et al., 2010; di Marco et al., 2002; Donohue and Toole, 2003), leaving the Comoros Basin still largely under-sampled and understudied even though it is an important region for purse-seine fishing (Tew-Kai and Marsac, 2010) and a potentially key source region of variability for the rest of the Mozambique Channel.

In late 2009, a dedicated cruise took place in the Comoros Basin in an attempt to begin bridging the gap in the observational record for the Mozambique Channel. The data collected during this cruise, along with satellite altimetry data, presented in Chapter 3, showed that the circulation in the Comoros Basin is highly variable consisting of eddies of both polarities and a well defined southward current along the East African coast. However, the hydrographic

data provides only an instantaneous representation while the altimeter data only provides information on sea surface height and geostrophic velocities. Therefore, an alternative method of obtaining a broader understanding of the circulation in the Comoros Basin is the use of numerical ocean circulation models.

5.1 Regional Ocean Modelling System (ROMS)

This thesis employs the Regional Ocean Modelling System (ROMS) to investigate the processes and dynamics of the Comoros Basin. A detailed description of this model is provided in Shchepetkin and McWilliams (2003; 2005). ROMS is a split-explicit, free-surface, topographic-following coordinate model that solves the incompressible, hydrostatic, primitive equations on a rotating frame using the hydrostatic vertical momentum balance and the Boussinesq approximation. In the Boussinesq approximation, density variations are disregarded except in their contribution to the buoyancy force in the vertical momentum equation. The hydrostatic approximation assumes that the buoyancy force is balanced by the vertical pressure gradient. ROMS is coupled with a non-linear equation of state and advective/diffusion schemes for potential temperature and salinity. A non-local, K-Profile Parameterization (KPP) boundary-layer scheme (Large et al., 1994) is used to parameterize the subgrid-scale vertical mixing.

5.1.1 Equations of Motion

Taking into account the Boussinesq and hydrostatic approximation, the primitive equations, expressed in Cartesian coordinates, solved by ROMS include the horizontal momentum equations

$$\frac{\partial u}{\partial t} + v \cdot \nabla u - fv = -\frac{\partial \phi}{\partial x} + \frac{\partial}{\partial z} A_v \frac{\partial u}{\partial z} + D_u, \tag{5.1}$$

$$\frac{\partial v}{\partial t} + v \cdot \nabla v + fu = -\frac{\partial \phi}{\partial y} + \frac{\partial}{\partial z} A_v \frac{\partial v}{\partial z} + D_v, \tag{5.2}$$

the time evolution of potential temperature and salinity which is governed by the advective-diffusive equations

$$\frac{\partial T}{\partial t} + v \cdot \nabla T = \mathscr{F}_T + D_T \tag{5.3}$$

$$\frac{\partial S}{\partial t} + v \cdot \nabla S = D_S, \tag{5.4}$$

the hydrostatic balance

$$\frac{\partial \phi}{\partial z} = \frac{-\rho g}{\rho_0}, \tag{5.5}$$

the continuity equation for an incompressible fluid

$$\frac{\partial u}{\partial x} + \frac{\partial v}{\partial y} = -\frac{\partial w}{\partial z}, \tag{5.6}$$

and the equation of state for sea water

$$\rho = \rho(T, S, P). \tag{5.7}$$

In the above equations, u, v, w are the velocity components, measured in m·s^{-1}, in the x, y (horizontal coordinates) and z (vertical coordinate) directions respectively, t is time (s), f is the Coriolis parameter (s^{-1}) and g is acceleration due to gravity (m·s^{-2}). A_v is the vertical

mixing parameter and D_u, D_v are the lateral momentum dissipation terms. T and S are potential temperature (°C), and salinity (psu) respectively and ρ is density measured in kg·m^{-3}. F_T represents the surface forcing term for temperature and includes short- and longwave radiation as well as latent and sensible heat fluxes. D_T, D_S describe the diffusion of temperature and salt. The dynamic pressure, ϕ (m^2·s^{-2}), is calculated as $\frac{P}{\rho_0}$, where P is pressure (N·m^{-2} or kg·m^{-1}·s^{-2}) and ρ_0 is the reference density of sea water (1024kg·m^{-3}).

5.1.2 Vertical Boundary Conditions

ROMS introduces external forcing terms through vertical viscosity and diffusivity by way of surface and bottom boundary conditions. Wind forcing (equations (5.8),(5.9)), heat flux (equations (5.10),(5.15)), salt flux (equations (5.11),(5.16)), vertical velocity (equations (5.12), (5.17)) and bottom stress (equations (5.13), (5.14)) is introduced at the surface $(z = \zeta)$, as

$$A_v \frac{\partial u}{\partial z} = \frac{\tau_s^x}{\rho_o} \tag{5.8}$$

$$A_v \frac{\partial v}{\partial z} = \frac{\tau_s^y}{\rho_o} \tag{5.9}$$

$$A_T \frac{\partial T}{\partial z} = \frac{Q_T}{\rho_0 C_p} \tag{5.10}$$

$$A_s \frac{\partial S}{\partial z} = (E - P)S \tag{5.11}$$

$$w = \frac{\partial \zeta}{\partial t} \tag{5.12}$$

and at the bottom$(z = -h)$, as

$$A_v \frac{\partial u}{\partial z} = \frac{\tau_b^x}{\rho_o} \tag{5.13}$$

$$A_v \frac{\partial v}{\partial z} = \frac{\tau_b^y}{\rho_o} \tag{5.14}$$

$$A_T \frac{\partial T}{\partial z} = 0 \tag{5.15}$$

$$A_s \frac{\partial S}{\partial z} = 0 \tag{5.16}$$

$$-w + v \cdot \nabla h = 0. \tag{5.17}$$

In the above equations, ζ is surface elevation (m), τ_s^x, $\tau_s^y$and τ_b^x, τ_b^y are surface and bottom wind stresses ($N{\cdot}m^{-2}$) respectively in the x- and y-directions and A_v is the vertical viscosity ($m{\cdot}s^{-1}$). A_T is the temperature diffusivity term ($m^2{\cdot}s^{-1}$), T is temperature, Q_T is the surface heat flux ($W{\cdot}m^{-2}$) and C_p is the heat capacity of sea water ($J{\cdot}kg^{-1}{\cdot}°C^{-1}$). A_s is the salinity diffusivity term ($m^2{\cdot}s^{-1}$), E and P denotes evaporation and precipitation, respectively.

5.1.3 Ocean-Atmosphere Feedback

The net surface heat flux (Q_T) consists of the net short wave and net long wave radiative fluxes (IR) at the sea surface plus the sensible (SH) and latent heat flux (LH) exchanges between the ocean and the atmosphere. In the absence of atmospheric feedbacks in an ocean-only model, an undesirable drift of the model fields may occur when surface fluxes alone

are specified. To correct for this, basin scale models are often forced by nudging the model fields towards climatological fields (Penven, 2000). A physically more satisfactory method of representing the model sea surface temperature (T_{model}) feedback on surface heat fluxes is to linearize the thermal forcing around climatological sea surface temperatures (T_{clim}) (Haney, 1971). Thus the total heat flux (Q_{Total}) applied to the surface is thus

$$Q_{Total} = Q_T + \frac{\partial Q}{\partial T_{Clim}}(T_{Model} - T_{Clim}) \tag{5.18}$$

The term $\frac{\partial Q}{\partial T_{Clim}}$ represents the surface net heat flux sensitivity to the sea surface temperature and is calculated from the different contributions of the heat flux as follows (Penven, 2000):

$$IR = -4\sigma T_{Clim}^4 \tag{5.19}$$

$$SH = -\rho_{atm} C_p C_h |U_{10}| (SST - T_{air}) \tag{5.20}$$

$$LH = -\rho_{atm} \times C_e \times L \times |U_{10}| \times 2353 \times log_{10}\left(\frac{q_s}{T_{Clim}^2}\right) \tag{5.21}$$

$$Q = IR + SH + LH \tag{5.22}$$

where σ is the Stefan-Boltzmann constant (5.6697×10^{-8}W·m^{-2}·°C^{-4}) , p_{atm} represents the atmospheric density, C_p denotes the specific heat of the atmosphere at the sea surface (1004.8J·kg^{-1}·°C^{-1}), C_h and C_e represent the sensible and latent heat transfer co-efficients, respectively and the values depend on atmospheric stability and wind speed. ROMS assumes stable atmospheric conditions and thus constant values of 0.66×10^{-3}W·m^{-2}·°C^{-1} and

1.15×10^{-3}W·m^{-2}·°C^{-1}are used for C_h and C_e, respectively. SST denotes the sea surface temperature, while T_{air} represents the air temperature. The latent heat of vaporisation is denoted by L, U_{10} is the wind speed at 10m height and q_s is the specific humidity at sea level.

In ROMS, salt fluxes based on climatological evaporation (E) and precipitation (P) are used to specify the fresh water fluxes. A drift in model-derived salinities can arise due to the use of model independent E-P data (Haidvogel et al., 2000). Therefore, similar to the heat flux correction term, a salt flux correction term formulated as

$$SaltFlux = \frac{S_{Model}(E-P)}{\rho_0} + k(S_{Model} - S_{Clim}) \tag{5.23}$$

has been incorporated into the model formulation, where S_{Clim} and S_{Model} are the climatological and model-derived sea surface salinities, respectively. In order to obtain the coefficient k (in m·s^{-1}), the term $\frac{\partial Q}{\partial Tclim}$ is scaled according to the reference density of seawater and C_p.

5.1.4 Lateral Boundary Conditions

An obstacle that regional ocean models have to overcome is the adequate representation of the influence of dynamical processes occurring outside the computational domain on the dynamics within the domain. Open boundaries are present in most regional numerical simulations and require the application of appropriate open boundary conditions (OBC; Ma and Madsen, 2011). OBCs are considered unsuitable if they do not allow information to exit the computational domain or do not effectively transmit information into the domain, or if they generate or reflect waves that propagate inside the computational domain (Spall and Robinson, 1989). Thus, appropriate OBCs allow outgoing waves to radiate through the boundary to the exterior of the computational domain without creating reflections back into the domain (Ma and Madsen, 2011). OBCs are a combination of adaptive nudging and outward oblique radia-

tion (Marchesiello et al., 2001). Adaptive nudging towards a prescribed external condition is necessary for maintaining stability.

At the open boundaries, sponge layers are assigned in order to coarsen the model solution to conform with the large scale incoming signal (Penven and Tan, 2007). Away from the open boundaries, horizontal viscosity is zero. At the open boundaries, within the sponge layers, lateral viscosity is assigned and it increases smoothly toward the edge of the domain in order to suppress computational noise associated with the radiation condition (Marchesiello et al., 2001). Nudging of the model data towards external data also occurs within the sponge layers.

Closed lateral boundaries, i.e. land, are defined as masked regions. Computations occur over the entire computational domain and values of the variables within the masked regions are set to zero at the end of each time-step. However, the calculated velocity terms at the closed boundaries are corrected for free-slip or no-slip conditions. Hedstrom (1997) provides a more detailed description of the procedure. The ROMS simulation analysed in this thesis, described in section 5.2, incorporates the free-slip condition at the closed boundaries.

5.1.5 Vertical Coordinate System

The three vertical coordinate systems that are commonly available for numerical modelling are the geopotential (z) coordinate system, the isopycnic coordinate system and the terrain-following (sigma) coordinate system. In ROMS, the primitive equations, are descretized in the vertical over variable topography using stretched terrain-following coordinates (Figure 5.1; Song and Haidvogel, 1994) which allows for increased resolution in areas of interest such as the thermocline as well as a better representation of bathymetry-flow interactions

(Marchesiello et al., 1998). The terrain-following coordinates (σ) require the transformation

$$z = z(x, y, \sigma), \tag{5.24}$$

where z is the Cartesian height and σ, the distance from the free surface, is measured as a fraction of the thickness of the water column at a particular location. Therefore, σ ranges from -1 at the bottom ($z = -h(x,y)$) to 0 at the free surface ($z = \zeta$)(Shchepetkin and McWilliams, 2005). In ROMS, the general vertical coordinate system of Song and Haidvogel (1994), a non-linear function of z, is used to obtain uniformly high resolution near the surface, while preserving the terrain-following coordinates in the bottom layers. This method employs surface- and bottom-stretching parameters (θ_s and θ_b, respectively) to stretch the σ coordinates in order to obtain, for example, increased resolution at the surface.

A long standing problem in topography-following coordinate ocean models is the discrete approximation of the horizontal pressure-gradient force. The horizontal pressure-gradient error occurs due to the pressure gradient term being divided in to a "hydrostatic correction" and an "along-coordinate surface" component, both of which are very large (Haidvogel and Beckmann, 1999). Imbalanced numerical truncation errors in the two terms result in an inexact cancellation of the hydrostatic resting pressure. The resulting pressure gradient errors are dependent on the strength of the stratification, both the vertical and horizontal resolution as well as the steepness of the topography (Haidvogel and Beckmann, 1999). Therefore, the horizontal pressure-gradient error can be attributed to hydrostatic inconsistency which results in spurious geostrophically balanced flows (Shchepetkin and McWilliams, 2003). Shchepetkin and McWilliams (2003) developed a pressure-gradient algorithm that more accurately achieves the hydrostatic balance terms for the sigma-coordinate formulation, thus reducing the pressure-gradient error. Their algorithm reconstructs the density field as continuous func-

tions of transformed coordinates into z-coordinates which is subsequently analytically integrated to compute the pressure-gradient force.

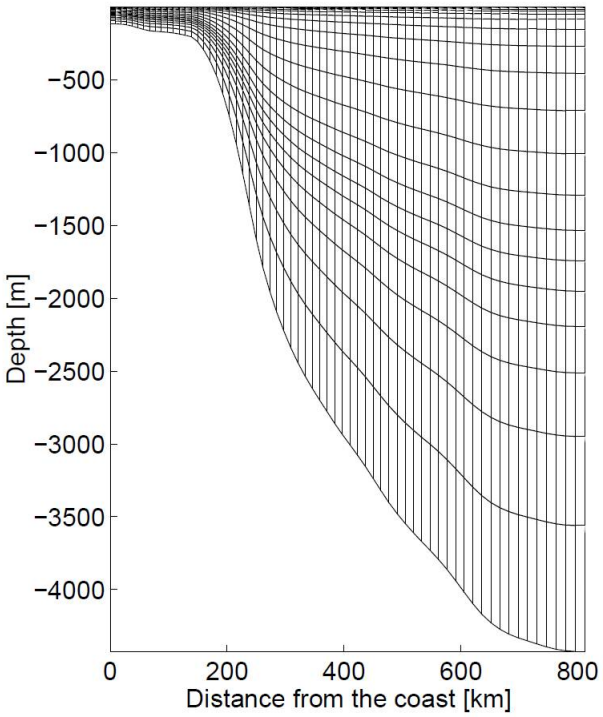

Figure 5.1: *The vertical sigma-coordinate system.*

5.1.6 Temporal, Horizontal and Vertical Temporal Discretization

ROMS uses a split-explicit time-stepping scheme to solve the hydrostatic primitive equations for momentum. This scheme requires special treatment and coupling between the barotropic (slow) and baroclinic (fast) modes. The free-surface and the vertically integrated momentum equations are advanced using a finite number of barotropic time steps within each baroclinic step. The barotropic fields are time averaged before replacing the values obtained with a longer baroclinic step in order to overcome the errors associated with the aliasing of frequen-

cies resolved by the barotropic steps but unresolved by the baroclinic step (Shchepetkin and McWilliams, 2005). Thus, ROMS use short time steps to advance the surface elevation and barotropic momentum equations and larger time steps for temperature, salinity and baroclinic momentum. A special 2-way time-averaging procedure is employed for the barotropic mode which satisfies the 3D continuity equation. A third-order accurate predictor (Leap-Frog) and corrector (Adams-Molton) time-stepping algorithm is used to descretize the baroclinic mode. This algorithm allows a substantial increase in the permissible time-step size (Penven et al., 2006b).

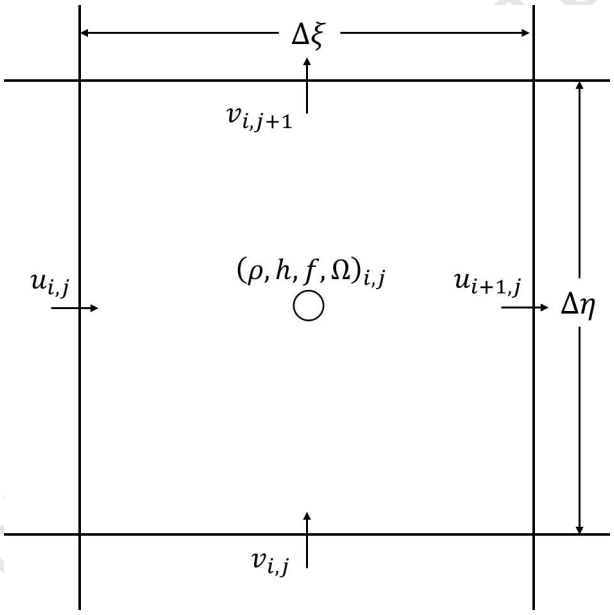

Figure 5.2: *The position of the variables on the Arakawa-C grid used in the horizontal discretization of ROMS.*

In the horizontal, boundary-fitted, orthogonal curvilinear coordinates on a staggered Arakawa C-grid (Arakawa and Lamb, 1977) are used to evaluate the primitive equations. This grid has a characteristic variable-placement scheme (Figure 5.2) and is well suited for problems with

a horizontal resolution finer than the first Rossby radius of deformation (Hedstrom, 1997). In the vertical, the grid is also staggered as shown in Figure 5.3.

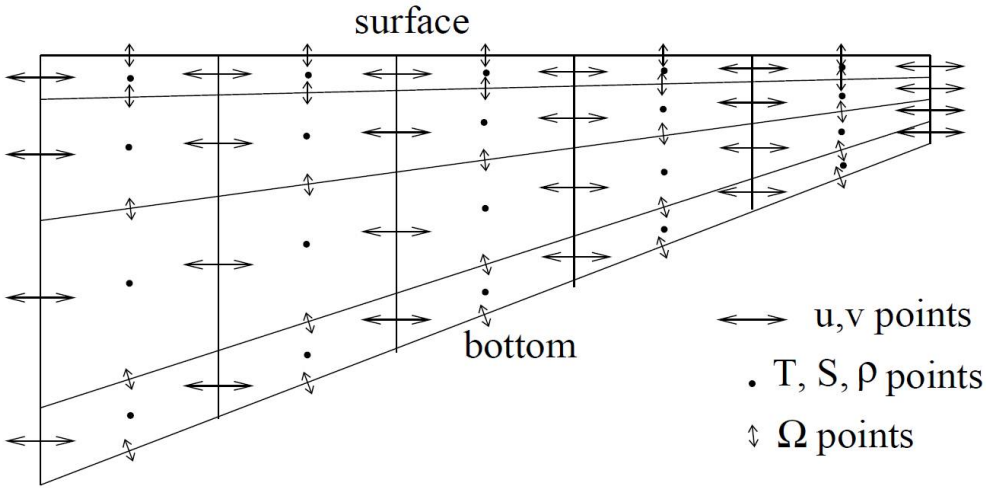

Figure 5.3: *The vertical placement of variables in ROMS.*

5.1.7 Advection Scheme

The advection scheme implemented in ROMS is a third order, upstream-biased scheme. This scheme enhances the effective resolution of the solution for a given grid size by allowing the generation of steep gradients (Shchepetkin and McWilliams, 1998). Marchesiello et al. (2009) showed that the implementation of high-order diffusive advection schemes in sigma-coordinate models leads to spurious diapycnal mixing. A solution to this problem proposed by Marchesiello et al. (2009) is a split of the diffusion from the advection calculation and to represent diffusion by a rotated bi-harmonic diffusion scheme.

5.1.8 Turbulent Closure Schemes

In ROMS, a non-local, K-profile planetary (KPP) boundary layer scheme is implemented to parametrize the unresolved physical vertical mixing processes (Large et al., 1994). This scheme uses several distinct parametrizations to resolve the distinct mixing processes of the ocean interior and the ocean surface boundary layer. At each grid point, the boundary layer depth is determined based on a critical value of turbulent processes which is parametrized by a bulk Richardson number relative to the surface. The depth of the boundary layer depends on buoyancy, mixing, surface forcing and the velocity profile. Vertical mixing below the boundary layer is regarded as the sum of internal wave breaking, double diffusion and vertical shear. Diffusivity in the surface layer is formulated to be consistent with the similarity theory of turbulence (Blackadar, 1962; Louis, 1979). Diffusivity and its gradient at the base of the surface layer are matched to their values in the interior ocean.

5.2 Model Configuration

In this thesis, the AGRIF (Adaptive Grid Refinement in FORTRAN) embedding capabilities (Debreu et al., 2008) of the ROMS model are used to maximize the computing efficiency of a higher resolution simulation over the Comoros Basin. The 1-way embedding approach is designed so that the boundary conditions of the higher resolution domain (child domain) are obtained from the coarser resolution domain (parent domain) but the parent solution is not updated with the results from the child. By evaluating a 1-way embedded configuration of the central California upwelling system, Penven et al. (2006b) showed that the embedding approach significantly improved the solution of the inner grid compared to only using open boundaries while increasing the computational cost only slightly. The 2-way embedding

approach allows for the coarse resolution domain to provide boundary conditions for the higher resolution domain and additionally allows the higher resolution domain to feed into the coarser resolution domain. This procedure was recently implemented in the AGRIF package (see Debreu et al., 2008) and is used in this study. The AGRIF package for mesh refinement (Blayo and Debreu, 1999) is a FORTRAN 90 program that runs independent of the type of ocean model.

5.2.1 Parent configuration

The parent configuration used in this thesis is based on the eddy-resolving Southern African Experiment (SAfE) but with an extended domain. The SAfE configuration, designed by Penven et al. (2006a) to simulate the salient oceanographic features around southern Africa, has a $\frac{1}{4}^\circ$ horizontal resolution and encompasses the region 2.5°W-54.75°E and 4.8°S-46.75°S. Likewise, the parent configuration used in this study also has a $\frac{1}{4}^\circ$ horizontal resolution but the domain encompasses the region 0°W-70°E and 4°N-44°S and thus covers most of the tropical western Indian Ocean (Figure 5.4). The domain includes the Agulhas and Benguela Currents, the Mozambique Channel, and the East African Coastal Current. In the vertical, there are 40 s-coordinate levels which are stretched, increasing the resolution near the surface. The stretching parameters used are $\theta_s = 6$ and $\theta_b = 0$ which results in a 3m and 500m vertical resolution in the surface and bottom layers, respectively. In this configuration, the effects of the strong western boundary current, the Agulhas Current, is dampened through the parametrization of horizontal viscosity based on the Smagorinsky formulation (Smagorinsky, 1963):

$$A_h = 0.025 \times \frac{\delta x \delta y}{2} \times \mid deformation tensor \mid$$

where A_h is the horizontal turbulent viscosity coefficient and δx, δy represents the lateral grid size.

In ROMS, the bottom boundary layer dynamics can be specified as wave-current sub-models which incorporate bottom bed roughness or as a drag-coefficient expression which can be either linear or quadratic (Haidvogel et al., 2008). In the current configuration, the latter method is used and the bottom stress is applied as a quadratic function of bottom velocity with the non-dimensional drag coefficient ranging from 0.0025 to 0.02. The parent configuration uses monthly climatological forcing and is not concerned with small-scale processes such as sediment transport which would require the use of the wave-current sub-model method. Therefore, the simpler method is appropriate for this configuration. At each of the lateral boundaries of the parent configuration, a sponge layer with a width of 200km is specified. Within the sponge layer, the viscosity increases in a half cosine curve from 0 at the inner edge of the sponge layer to 1000$m^2 \cdot s^{-1}$ at the boundary (Penven et al., 2006b). The sponge layer allows for enhanced diffusivity at the lateral boundaries ensuring that no discontinuities are introduced at the boundaries. Additionally, within the sponge layer, when information passes into the model domain through the open boundaries, the model solution is nudged toward World Ocean Atlas 2009 (WOA09) climatological data.

5.2.1.1 Bathymetry

The topography for the parent configuration is derived from the 1' GEBCO (GEneral Bathymetric Chart of the Oceans) product. The higher resolution topography from GEBCO is coarsened to reach the resolution of the parent grid in order to prevent the generation of noise

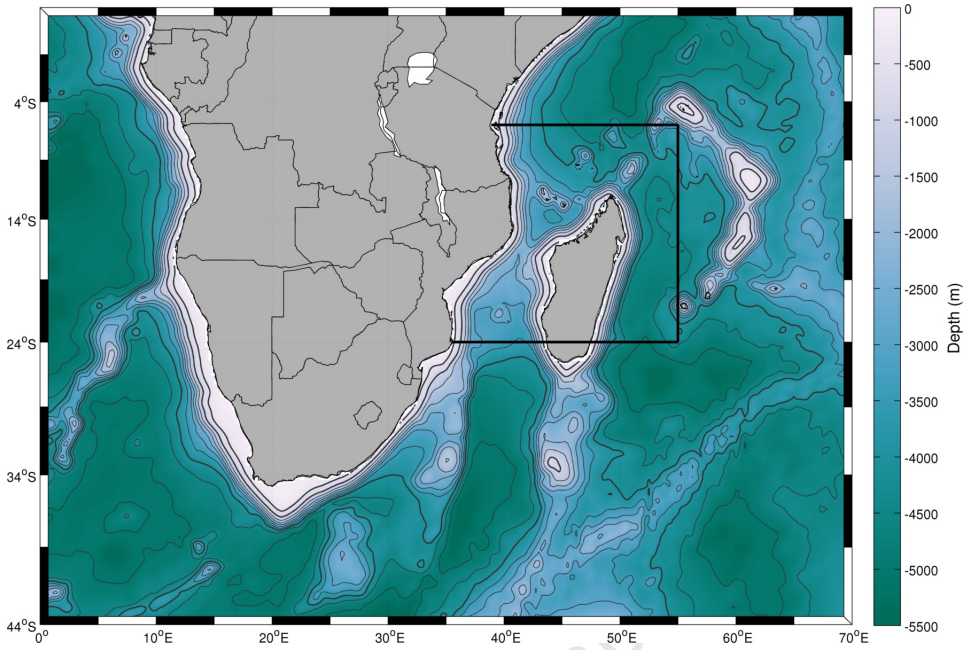

Figure 5.4: *Bathymetry (m) of the parent configuration. The child domain is indicated by the black square. The contours are shown for every 500m.*

due to under-sampling. Subsequently, the new topography is interpolated onto the parent grid. Additional smoothing of the new topography with a hanning filter is applied to reduce any remaining noise and to avoid pressure gradient errors. The smoothing applied to the topography is to keep the slope parameter ($r = \frac{\nabla h}{h}$) below a threshold of 0.2.

5.2.1.2 Surface Forcing and Initialization

The parent configuration is forced at the surface with heat and salt fluxes (Figures 5.5,5.6) based on the monthly climatological means derived from the Comprehensive Ocean-Atmosphere Data Set (COADS; da Silva et al., 1994) which has a 0.5° spatial resolution. Objective analysis is used to replace missing values and interpolation of the data onto the ROMS grid is accomplished using a cubic interpolation method. The sea surface temperature (SST) used

to force the model is obtained from a satellite-derived SST climatology which is based on Pathfinder Advanced Very High Resolution Radiometer (AVHRR) data (Figure 5.7). This SST climatology has a resolution of ~9km and was generated from version 4 NOAA-NASA AVHRR Oceans Pathfinder fields for the period 1985-1995 (Casey and Cornillon, 1999). The wind forcing (Figure 5.8) used for this configuration was obtained from a 0.5° resolution QuikSCAT climatology (Liu et al., 1998) constructed from 8 years (2000-2007) of data.

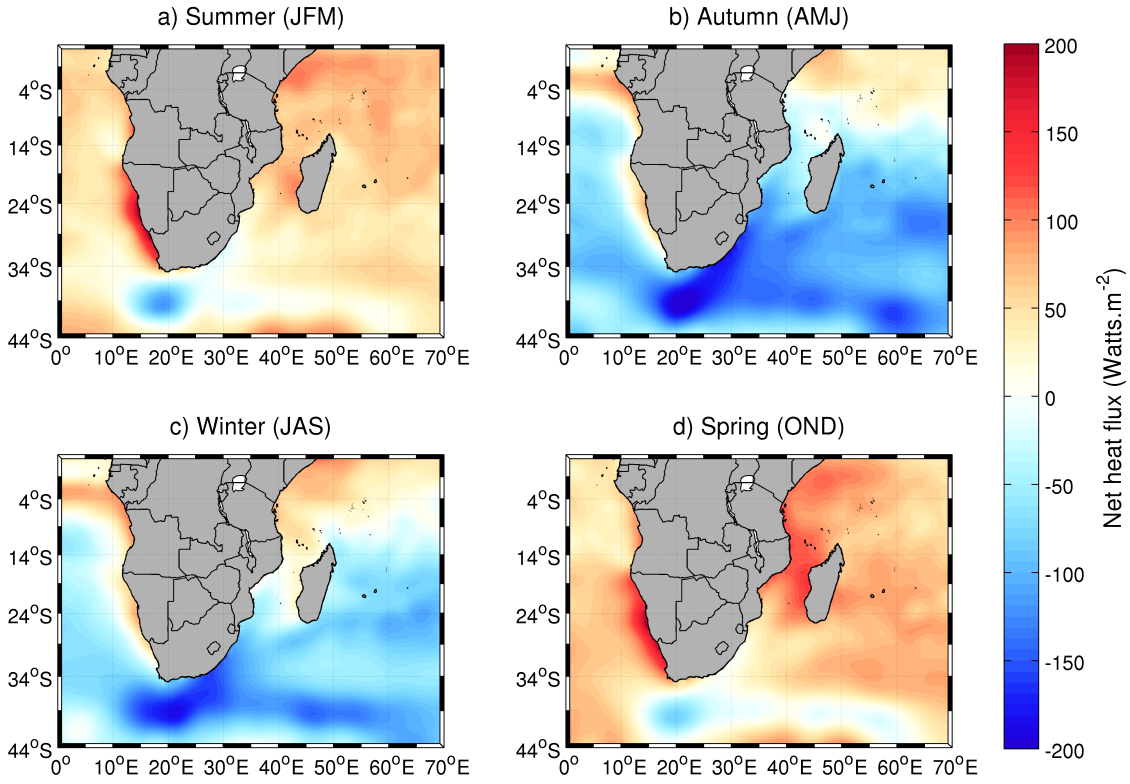

Figure 5.5: *The seasonal mean COADS net surface heat fluxes (positive=net gain into the ocean, negative=net loss from the ocean).*

Initial and boundary conditions are obtained from World Ocean Atlas 2009 (WOA09;

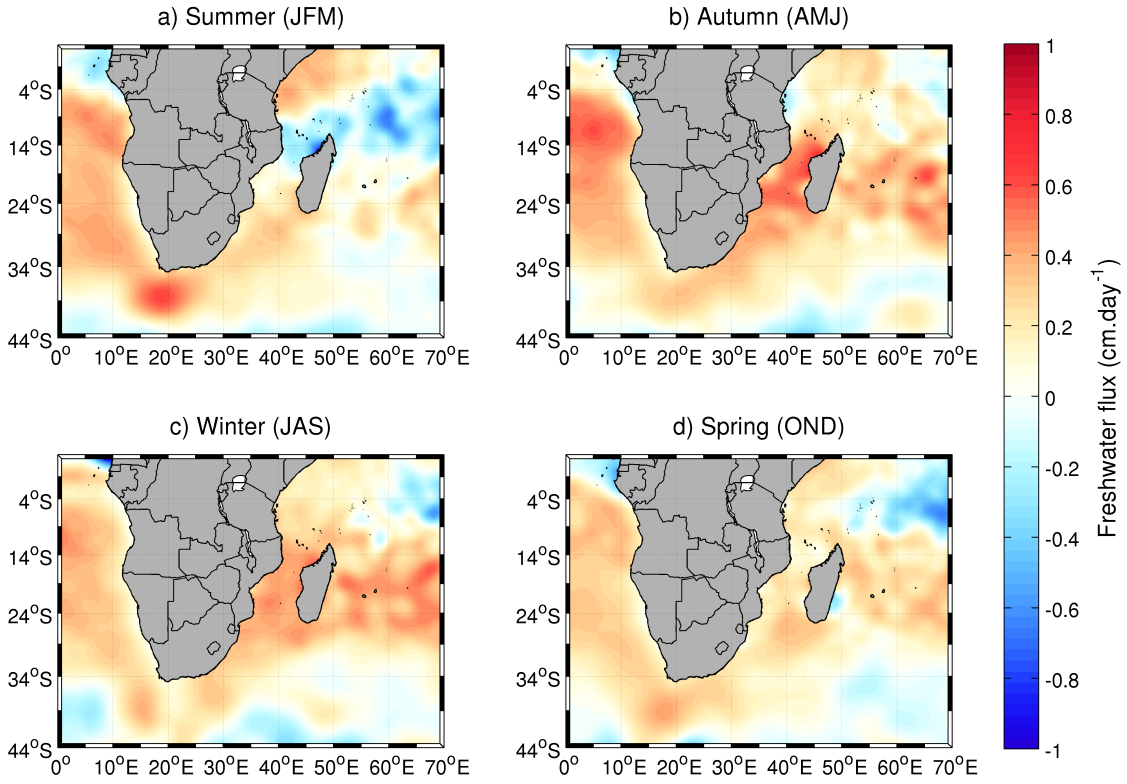

Figure 5.6: *The seasonal mean COADS freshwater flux (evaporation-precipitation).*

Conkright et al., 2002) which has a 1° spatial resolution. Temperature and salinity for January is used to initialize the model which is started from rest. Furthermore, geostrophic velocities at the open boundaries are calculated from temperature and salinity at a reference level of 1000m while Ekman velocities are estimated from the wind field.

5.2.2 Child configuration

The embedded child domain was designed to encompass the Mozambique Channel and range from 30°E to 55°E and 6°S to 24°S. The child domain (TWIO), refining the model solution

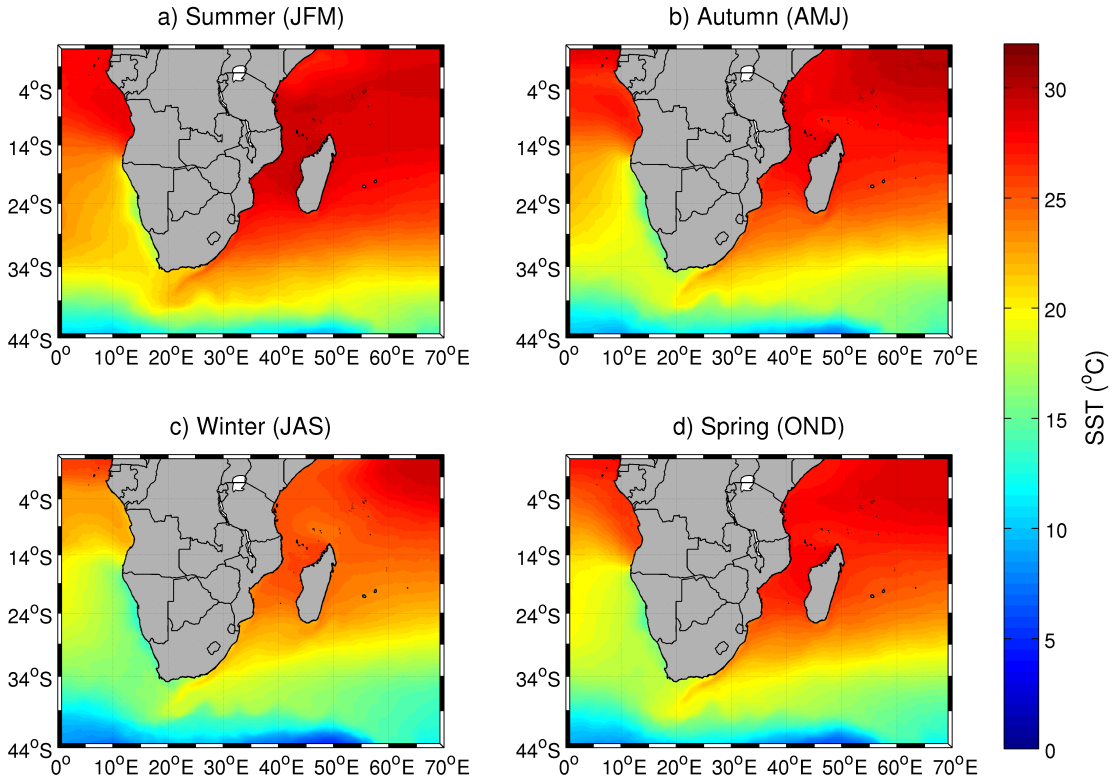

Figure 5.7: *The seasonal mean Pathfinder sea surface temperature (SST)* .

by a factor of three (coefficient of refinement (r_{coef})=3), resolves the Mozambique Channel and the Comoros Basin at 1/12° (~ 9km) and, similar to the parent configuration, has 40 stretched vertical levels. The topography of the child grid is interpolated from the original GEBCO dataset and not from the coarser parent topography in order to obtain finer resolution bathymetry. The interpolation and smoothing methods used is similar to that of obtaining the parent grid topography. At the coast minimum depth is set at 30m. Differences in the topographies of the parent and child configurations occur due to the fact that the topography of the parent configuration is smoothed more than that of the child configuration. To prevent

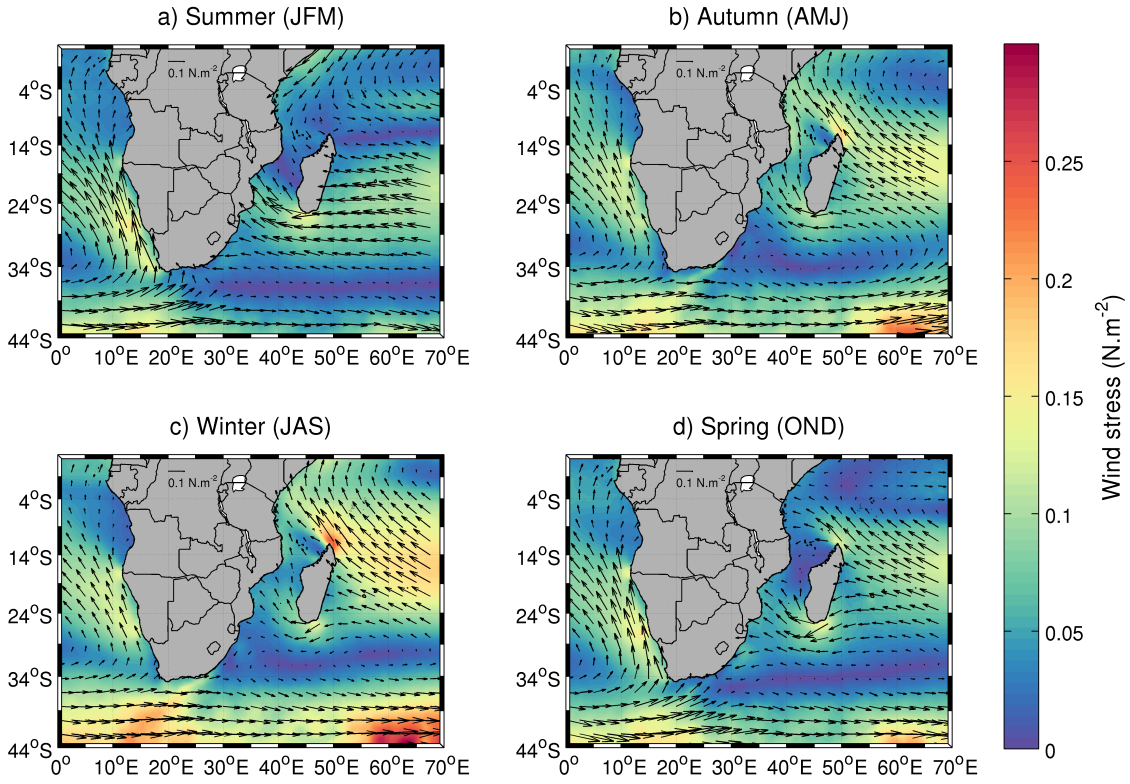

Figure 5.8: *The seasonal mean QuikSCAT surface wind stress and direction.*

discontinuities between the parent and child domains, a smooth connection between the different grid levels is needed. The topography of the child domain is smoothly connected to the topography of the parent domain using the relation

$$h_{child} = \alpha h_{parent} + (1-\alpha) h_{fine}$$

where the bottom topography of the child and the parent domains are defined by h_{child} and h_{parent}, respectively; h_{fine} is the high-resolution bathymetry, and α is a parameter that ranges from zero to 1 within a number of grid points ("nband") at the lateral parent-child

boundary. In this configuration, the width of the connection band is set to 20 grid points. The child topography is kept identical to the parent topography for the first two parent grid points close to the parent-child boundary (Penven et al., 2006b). It is also necessary to conserve the volume at the parent-child boundary. Therefore, a special treatment is applied in this band to force the child grid to have the same vertical sections and volume as the parent domain (Penven et al., 2006b).

The surface forcing as well as the initial and boundary conditions of the child domain are interpolated from that of the parent domain. Vertical re-interpolation of the initial conditions for the child domain is necessary due to the different topographies of the child and the parent domains. Mass and energy conservations through the 4 open boundaries of the child domain, which are forced by the parent solution, are obtained through the open boundary conditions described by Penven et al. (2006b). Dirichlet (i.e. fixed) boundary conditions are used for the baroclinic variables of the child domain while boundary conditions based on the method of characteristics (Hedstrom, 1979; Thompson, 1987, 1990) are used for the barotropic radiation conditions at the parent-child boundaries. A sponge layer with a width of 50km between the parent and child domains allows for a smooth transition at the boundaries. Similar to the parent domain, the horizontal viscosity of the child domain is zero. Viscosity within the sponge layer increases in a half cosine curve from 0 to $100 m^2 \cdot s^{-1}$.

The time evolution of the child domain takes place within the time step of the parent domain through a recursive integration procedure (Penven et al., 2006b). To maintain the CFL criteria, it is necessary to decrease the time step of the child domain by the same factor as the coefficient of refinement, r_{coef}. In this simulation, the coefficient of refinement is three and therefore, for each parent step, the child time step is advanced by the parent time step divided by three. The result of this procedure is three child time steps for every parent

time step. The parent-child coupling is located at the baroclinic level, i.e. the boundary conditions are interpolated in space and time for each parent time step to obtain the boundary conditions for the child domain (Penven et al., 2006b). Along each sigma level, the baroclinic prognostic variables (temperature, salinity and the horizontal momentum components (u,v)) are interpolated bi-linearly for each parent time step and linearly for each child time step. Therefore, to conserve properties, the topographies of both the parent and child domain sigma levels have to correspond in the vicinity of the parent-child boundary.

5.2.2.1 Model Spin-up

The nested simulation, starting from rest, reaches a statistical equilibrium after a spin-up of about 8-12 months. The model was run for a total of 10 years to obtain a robust, repeating seasonal signal. Figure 5.9 depicts the time varying surface-averaged kinetic energy, volume-averaged kinetic energy, surface-averaged temperature, volume-averaged temperature, surface-averaged salinity and volume-averaged salinity for the child domain. For all of these variables, except volume-averaged salinity, the model exhibits no significant temporal drift after a spin-up period of about 1 year. The volume-averaged kinetic energy displays a rapid adjustment of the currents to the initial conditions within the first 5-6 months of the simulation followed by an increase in the level of kinetic energy during the latter half of the first year of the simulation due to increasing eddy activity. After the first year of the simulation the kinetic energy stays relatively stable indicating that the wind-driven circulation of the model has reached equilibrium and is stable. The temperature and salinity fields of the model have a slow drift, but nevertheless provide a good representation of the general circulation (see Chapter 6). In order to account for the spin-up time, the results presented in the following chapter(s) are based on seasonal and monthly climatologies derived from model

years 3 to 10.

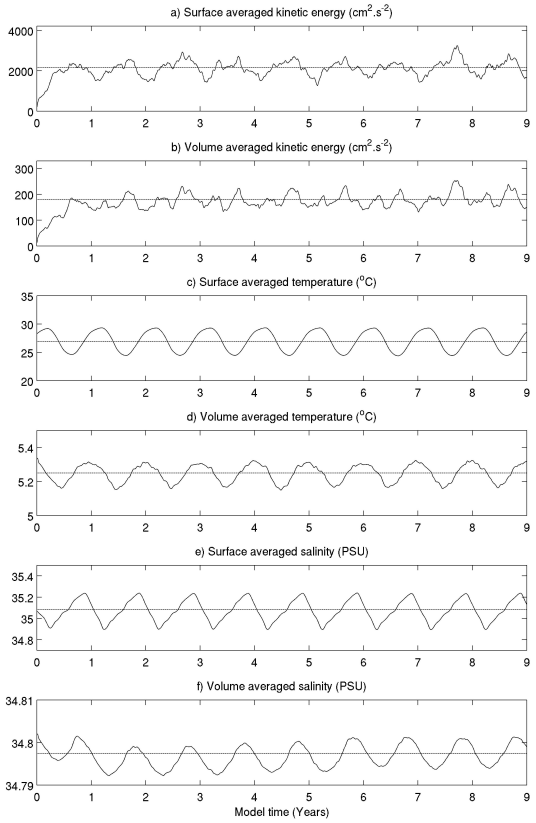

Figure 5.9: *Monthly mean surface averaged eddy kinetic energy, volume averaged eddy kinetic energy, surface averaged temperature, volume averaged temperature, surface averaged salinity and volume averaged salinity for the 10-year model simulation.*

5.3 Description of AG01

In addition to the ROMS simulation described above, the circulation in the Comoros Basin was also analysed using a nested model simulation based on the numerical framework of the

"Nucleus for European Modelling of the Ocean" (NEMO, v2.3) which utilises the AGRIF package for grid refinement as described in section 5.2 (Biastoch et al., 2009b). This model simulation, AG01, is an interannual, high-resolution, "two-way nesting" model of the greater Agulhas region spanning the time period 1968-2004 (Figure 5.10; Biastoch et al., 2008a). AG01 is nested within ORCA05, a global ocean/sea-ice model that has a nominal grid resolution of 0.5° and uses 46 layers in the vertical (Biastoch et al., 2008a). ORCA05 is forced at the surface by CORE data (Griffies et al., 2009), a consistent dataset that consists of a combination of NCEP/NCAR atmospheric reanalysis and independent observations which are used to correct known biases. Bulk formulae, used to compute the turbulent fluxes, allow for some feedback of the ocean on atmospheric fluxes. AG01, with a refinement factor of 5 compared to ORCA05, incorporates the domain 20°W-70°E and 47°S-7°S and resolves the baroclinic Rossby radius of ~30km (Biastoch et al., 2009b). The CORE forcing data used for ORCA05 is interpolated on the 1/10° grid of AG01. A full description of the nested model configuration is provided by Biastoch et al. (2008a; 2009b).

The AG01 configuration has been shown to successfully resolve the salient features of the Agulhas regime (Biastoch et al., 2008b) and has been used in a number of studies to examine the inter-ocean exchange between the Indian and Atlantic Oceans (Biastoch et al., 2008a,b, 2009b). In this thesis, the region of the AG01 configuration used to examine the circulation in the Comoros Basin extends from 30°E to 55°E and 6°S to 24°S. In the next chapter (Chapter 6), TWIO as well as the region of AG01 corresponding to that of the ROMS child grid is validated using the data sets described below.

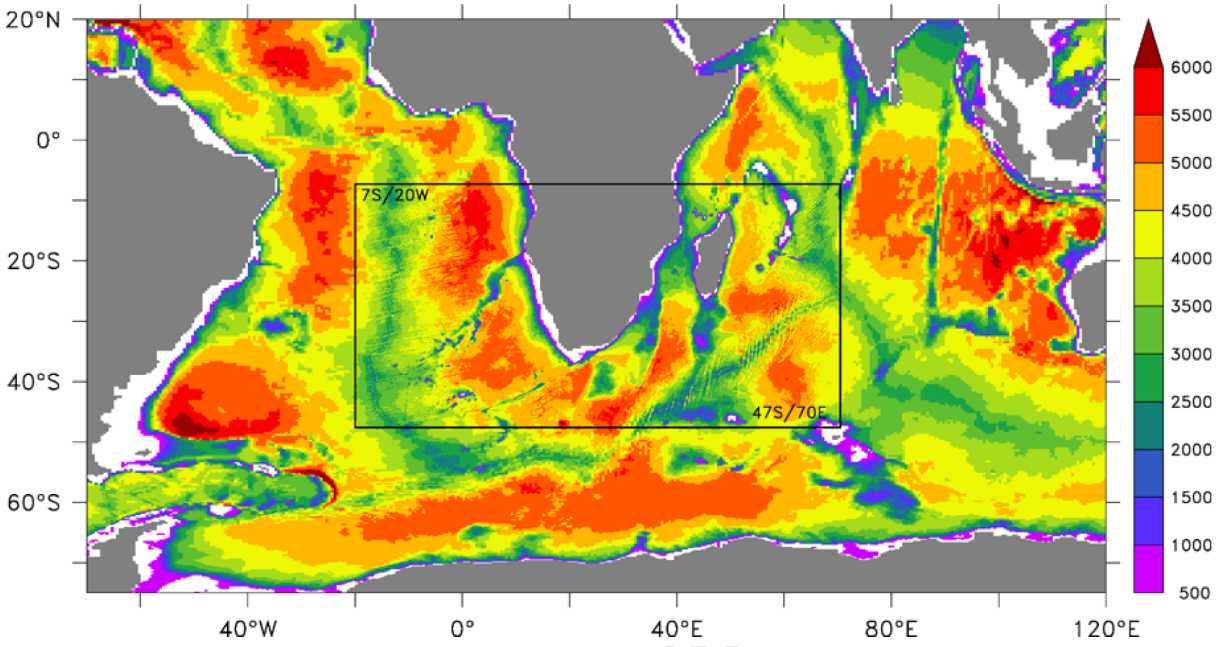

Figure 5.10: *The domain of the AG01 simulation (black box) nested with in ORCA05. Only part of the ORCA05 domain is displayed. The color bar denotes water depth (m), with white denoting areas of water depth shallower than 500m (After Biastoch et al. (2009a)).*

5.4 Model validation data sets

5.4.1 Satellite data

5.4.1.1 TMI Sea Surface Temperatures

Sea surface temperature (SST) data derived from observations made by the radiometer on-board the Tropical Rainfall Measuring Mission (TRMM) satellite were used in the model validation process. The TRMM has a low inclination (35°) equatorial orbit, allowing for global coverage between latitudes 40°S-40°N (Simpson et al., 1988). The TRMM Microwave Imager (TMI), a multi-channel passive microwave radiometer, has a swath width of 880 km and is capable of measuring SST through clouds.The SST data (available at www.remss.com),

with a 0.25° spatial resolution, has a daily, 3-daily, weekly and monthly temporal resolution for the period December 1997 to July 2012, however for the purpose of this thesis only data from 1998 to 2011 are used.

5.4.1.2 AVISO Altimetry

The absolute dynamic topography and sea level anomalies used for model-data comparisons were obtained from the SSALTO/DUACS gridded data products (www.aviso.oceanobs.com). These products were generated through the near-real time and delayed mode multi-mission altimeter data processing system at the Centre National d'Etudes Spatiales (CNES). The gridded data, merged from multiple altimeter missions, TOPEX/Poseidon, Jason-1, ERS-1/2, GFO and ENVISAT, has a 1/3° horizontal resolution and span the period 18 October 1992 to 12 July 2012. The absolute dynamic topography is calculated as the sum of the mean dynamic topography and satellite-observed sea level anomalies. The mean dynamic topography is calculated as the difference between the mean sea surface height and the geoid. The model-data comparisons include comparison of root mean square of sea level anomalies, surface geostrophic velocities, and eddy kinetic energy (EKE). The SSALTO/DUACS gridded data products provide a rich data source for comparison with model output, however data within 50km from the coast are not reliable.

5.4.2 Observational data

5.4.2.1 CARS

The CSIRO Atlas of Regional Seas (CARS) is a digital climatology of ocean water properties (Ridgway et al., 2002). It comprises gridded fields of mean ocean properties (temperature,

salinity, oxygen) derived from an archive of historical subsurface ocean measurements. The measurements are primarily from research vessel instrument profiles and autonomous profiling buoys. The latest versions, CARS2009, has a global spatial resolution of 0.5°. The temperature and salinity fields of this dataset are based on a number of data sets available up to 2008 including World Ocean Database 2005 (WOD05), surface-pressure-corrected Argo global archives, WOCE Global Hydrographic Program. The aim of CARS is to provide an estimate at every location and every depth in the world's oceans. Therefore, due to lack of data to resolve any one year, CARS is created by averaging/interpolating all available oceanographic profile data. The data are fitted onto a uniform grid using a locally weighted least squares (loess) filter while simultaneously fitting annual and semi-annual harmonics to the data (Ridgway et al., 2002). This filter is designed to allow for the influence of bathymetry on the mapped fields and it also compensates for missing values.

Chapter 6

Model Validation

Improved methods, global data sets and faster computers have resulted in more realistic ocean numerical models over the past several years. However, despite the increased realism of ocean models, validation of the models against observational data is still necessary to ensure that the simulated processes are a realistic representation of the actual processes occurring in the real system.

In this chapter, the ROMS and NEMO model simulations are compared with observational and satellite data in order to establish whether the salient features of the western Indian Ocean and the Mozambique Channel, as described in Chapter 2, are realistically simulated. Detailed descriptions of the models as well as the observational and satellite data sets are provided in Chapter 5. Throughout this chapter and the following chapters, the ROMS simulation will be referred to as TWIO and AG01 will be used to refer to the nested NEMO simulation.

Biastoch et al. (2008b) showed that the AG01 configuration, encompassing the region 20°W-70°E and 47°S-7°S, realistically simulates the salient features of the Agulhas Current

system. However, this conclusion was based solely on the representation of the Agulhas Current, Agulhas Undercurrent, Agulhas Return Current in terms of current location, speed and transport estimates as well as the formation and characteristics of Agulhas rings and Mozambique Channel eddies. In this chapter, AG01 and TWIO will be validated for the domain 30°E-55°E and 6°S-24°S based on the seasonal mean states of, among other things, sea surface temperature (SST) and velocity fields. The vertical structure of the main currents and the representation of the different water masses in the models are evaluated using vertical velocity, temperature and salinity profiles at selected key locations.

Monthly climatological data were used to force the nested ROMS simulation, therefore it is not expected that this simulation will simulate variability other than the annual cycle and the internal ocean variability. On the other hand, AG01 is forced with interannual data and will likely simulate anomalous climate events and display interannual variability. Therefore, in this chapter both AG01 and TWIO will be used to determine the climatological structure of the domain 30°E-55°E and 6°S-24°S. The validation of the 1/4° parent domain (0°W-70°E and 4°N-44°S) of the ROMS simulation is presented in Appendix B.

6.1 Water mass properties and distribution

6.1.1 Sea Surface Temperature

The seasonal mean sea surface temperatures of TWIO and AG01 are evaluated using satellite derived seasonal mean surface temperatures. Both models adequately represent the seasonal variability of SSTs in the Mozambique Channel (Figure 6.1 and 6.2). However, the SSTs of AG01 are, in general, about 1-2°C cooler compared to TMI and TWIO, resulting in a negative

SST bias of 0.5-1.5°C (Figure 6.2).

The summer SSTs in the Mozambique Channel range from ~28.6° to 31°C with the cooler (28.6°-29°C) SSTs occurring south of 20°S (Figure 6.1a and e and Figure 6.2a). TWIO overestimates the summertime SST values in the centre of the Mozambique Channel by ~0.2°C while there appears to be an underestimation close to the coast (Figure 6.1i). The underestimation may arise due to the limitation of the TRMM satellites to sample close to the coast. East of Madagascar, there is an increase in SST towards the north throughout the whole domain, which is reasonably well represented in TWIO and AG01(Figure 6.2a).

The pattern of SSTs in the Mozambique Channel during autumn and spring are very similar to that of summer but with slightly lower temperatures (25°-29°C; Figure 6.1b, d, f, h and Figure 6.2b and d). The coldest (25°-26°C) SSTs occur east of Madagascar while during spring extend more equatorward than during autumn. In TWIO, the cold water propagating from the east past the tip of Madagascar during spring, has an increased northwest extent compared to the observations resulting in a negative SST bias of 0.4°-0.8°C along the east coast of Tanzania (Figure 6.1l). During autumn, there is a negative SST bias of 0.4°-1.2°C in TWIO northeast of Madagascar (Figure 6.1j) due to the propagation of colder water from the east which is not observed in the observations.

In winter there is a decrease in SST by ~5°C and temperatures range from 24°-26.5°C and 23°-25.5°C in the Mozambique Channel and east of Madagascar, respectively (Figure 6.1c and g and Figure 6.2c). The northwestward propagation of cold water from east of Madagascar has a broader northward and east-westward extent in TWIO compared to what is observed in TMI, resulting in a negative SST bias of 0.4°-1°C north of Madagascar (Figure 6.1k).

During all four seasons, TWIO displays a negative SST bias east of Madagascar of vary-

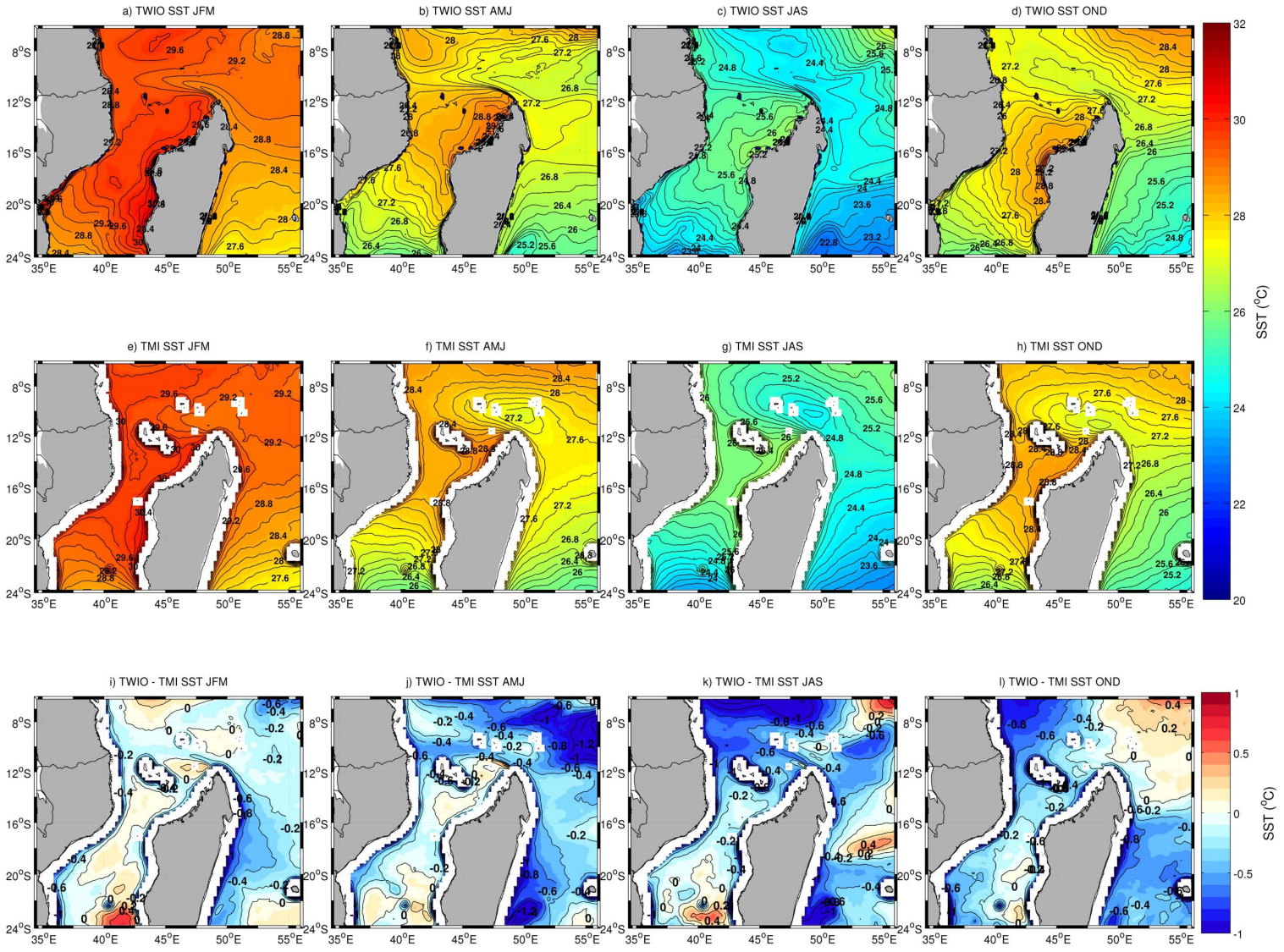

Figure 6.1: *The seasonal mean SSTs (°C) for TWIO (a-d) and TMI (e-h) where the contour interval is 0.2°C. The difference between TWIO and TMI are shown in (e)-(h), where the contour interval is 0.2°C. Positive (negative) values indicate an over-estimation (under-estimation) of SSTs by the model.*

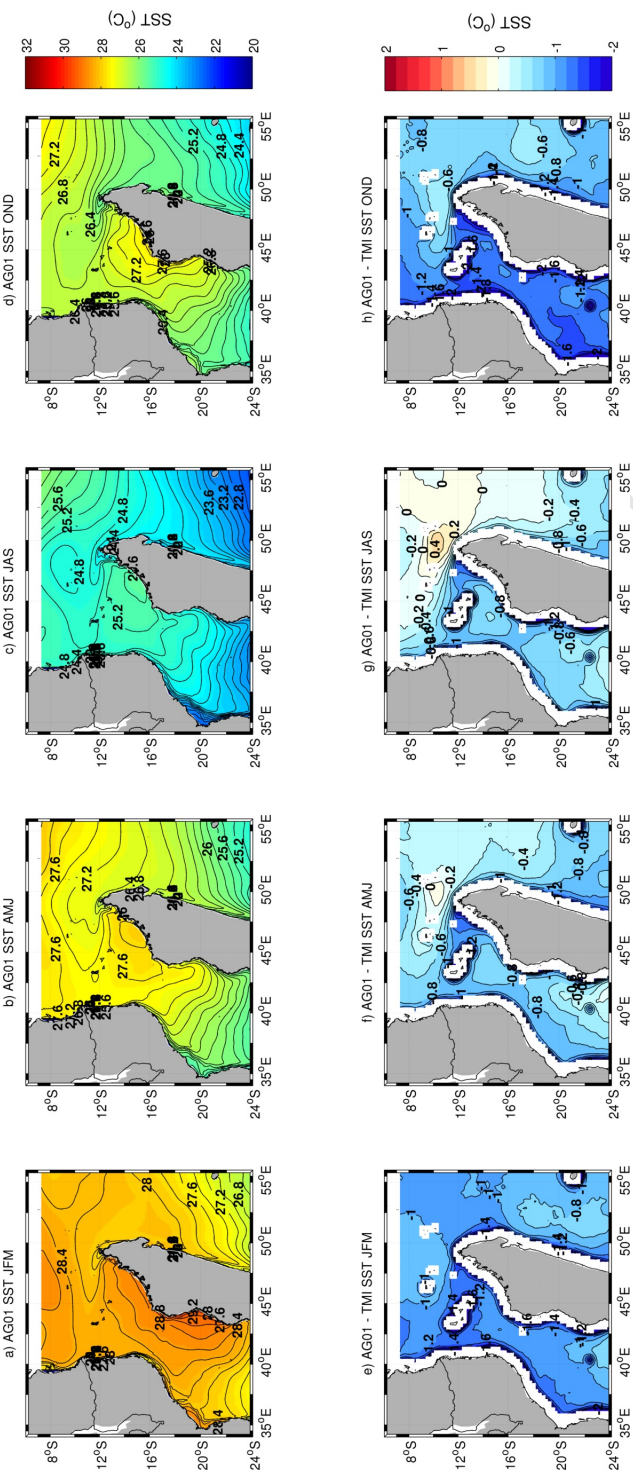

Figure 6.2: *The seasonal mean SSTs (°C) for AG01 (a-d) where the contour interval is 0.2°C. The difference between AG01 and TMI are shown in (e)-(h), where the contour interval is 0.2°C. Positive (negative) values indicate an over-estimation (under-estimation) of SSTs by the model.*

ing north-south extent (Figure 6.1), indicating that in the model the warmer tropical waters do not penetrate as far south as the observations suggest. The underestimation of SST in AG01 is more pronounced during summer and spring within the Mozambique Channel (Figure 6.2a and d). Furthermore, the warmer SST located along the west coast of Madagascar during all four seasons has a limited south- and westward extent in AG01 compared to TWIO and TMI.

6.1.2 Vertical structure of temperature and salinity

The representation of the different water masses of the western Indian Ocean, and particularly the Mozambique Channel, in the two models (TWIO and AG01) are evaluated based on the annual mean temperature and salinity along a number of vertical profiles. The vertical zonal profiles were chosen as representative of the North East Madagascar Current (NEMC), the South East Madagascar Current (SEMC), the Comoros Basin (CB) and the southern Mozambique Channel (SMC; Figure 6.3). A vertical meridional section west of the Mascarene Plateau was chosen to represent the South Equatorial Current (SEC).

The meridional section representing the SEC is located at 54°E and 10-20°S (Figure 6.3). The annual mean vertical thermal and salinity structures of the SEC in TWIO and AG01 are in relative good agreement with that of observations (Figures 6.4 and 6.5). However, AG01 underestimates the salinity of the SEC and all other sections by roughly 1 psu (Figure 6.5e). The water masses within the SEC, clearly distinguishable in the temperature-salinity (T-S) profiles derived from TWIO, AG01 and CARS, are TSW, STSW, SICW, AAIW and NADW (Figure 6.4). These water masses were also identified by New et al. (2007) from hydrographic data collected along meridional transects east and west of the Mascarene Plateau.

The isotherms in the upper 600-700m of TWIO, AG01 and CARS slope steadily down

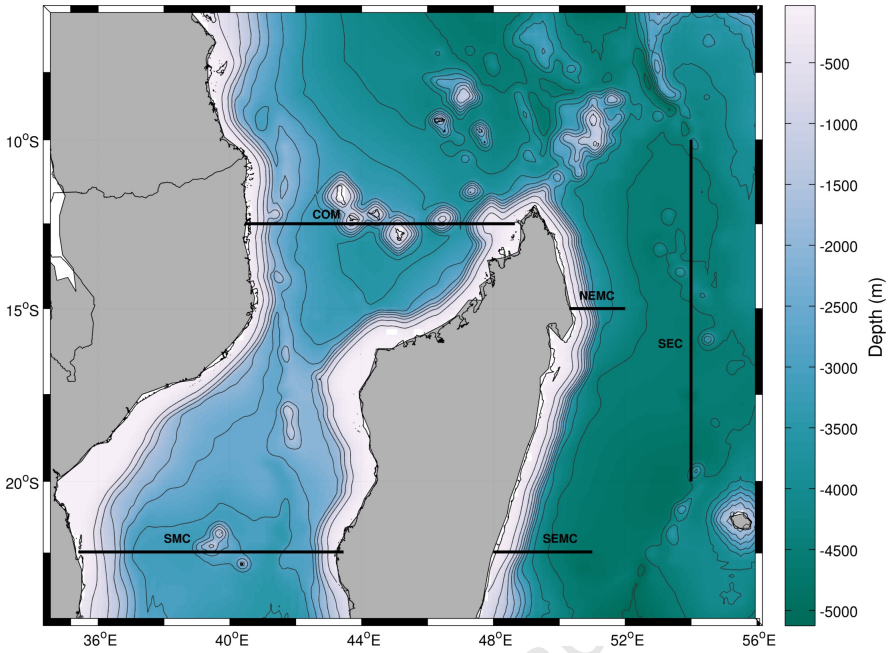

Figure 6.3: *The location of vertical profiles of temperature and salinity.*

towards the south, particularly between 10° and 14°S, and 16° and 20°S (Figure 6.5) corresponding to the double core structure of the SEC after it has crossed the Mascarene Plateau (New et al., 2007). The salinity values in the top 100m are in the range 34.7-35psu in CARS and TWIO (Figure 6.5a and c) whereas in AG01 they range from 34.2 to 34.5psu (Figure 6.5b). These salinity values together with the warm surface temperatures (20-26°C) are indicative of TSW. The most notable feature of the vertical salinity structure is the salinity maximum layer at approximately 100-400m (Figure 6.5). The temperature (12-18°C) and salinity (35.2-35.4psu in CARS and TWIO, 34.4-34.5psu in AG01) range of this salinity maximum layer is characteristic of Subtropical Surface Water (STSW). Consistent with the findings of New et al. (2007) for a transect west of the Mascarene Plateau, the STSW in TWIO, AG01 and CARS display a reduced salinity maxima to the north of ~16°S (Figure

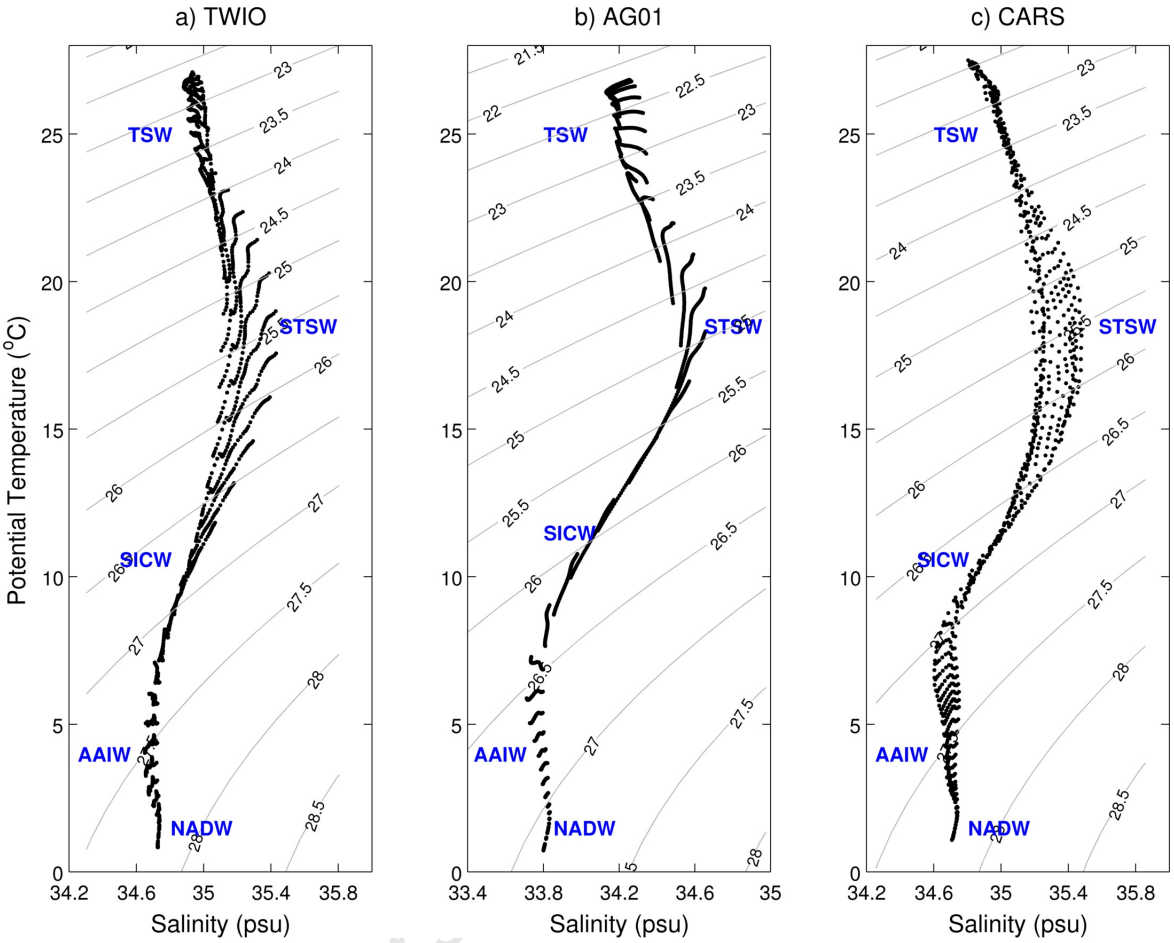

Figure 6.4: *θ-S diagram showing the water mass properties extracted along a zonal section across the SEC for a) TWIO, b) AG01 and c) CARS. Due to the overall lower salinity of AG01 (b) is plotted on a different scale for clarity.*

6.5). Low salinity water (>34.8psu) located between 700-2000m with a temperature range of 2-8°C suggests the presence of Antarctic Intermediate Water (AAIW) south of 12°S.

The vertical structure of the NEMC is analysed along a meridional section at 49.2°E off the tip of Madagascar (Figure 6.3). The meridional section corresponds to the transect S6 sampled during the Comoros Cruise (see Figure 3.1, Chapter 3). The vertical temperature and salinity structures of the NEMC along the east coast of Madagascar and off the tip of

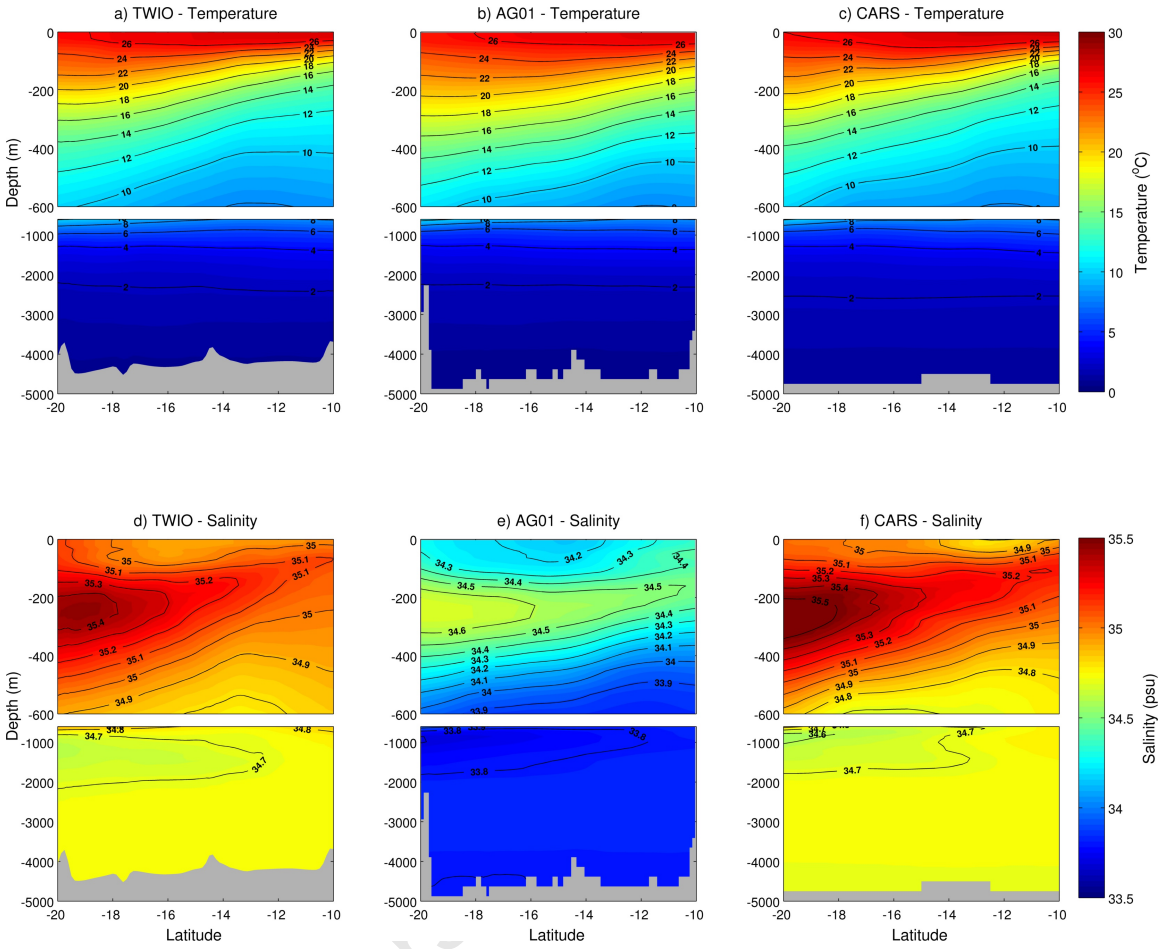

Figure 6.5: *Vertical profile of temperature (a-c) and salinity (d-f) of the South Equatorial Current (SEC) in TWIO, AG01 and CARS. The contour interval for temperature and salinity is 2°C and 0.1psu, respectively.*

Madagascar as resolved by TWIO and AG01 are comparable to that of CARS (Figures 6.6 and 6.7). The water masses identifiable in the T-S diagrams of both sections through the NEMC are TSW, STSW, SICW, and AAIW (Figure 6.6). The presence of these water masses in the NEMC are consistent with the water masses identified during the Comoros Cruise as well as the findings of Swallow et al. (1988). An additional water mass identified in the NEMC off the tip of Madagascar from the data collected during the Comoros Cruise is

ASHSW which is also present in both models and CARS.

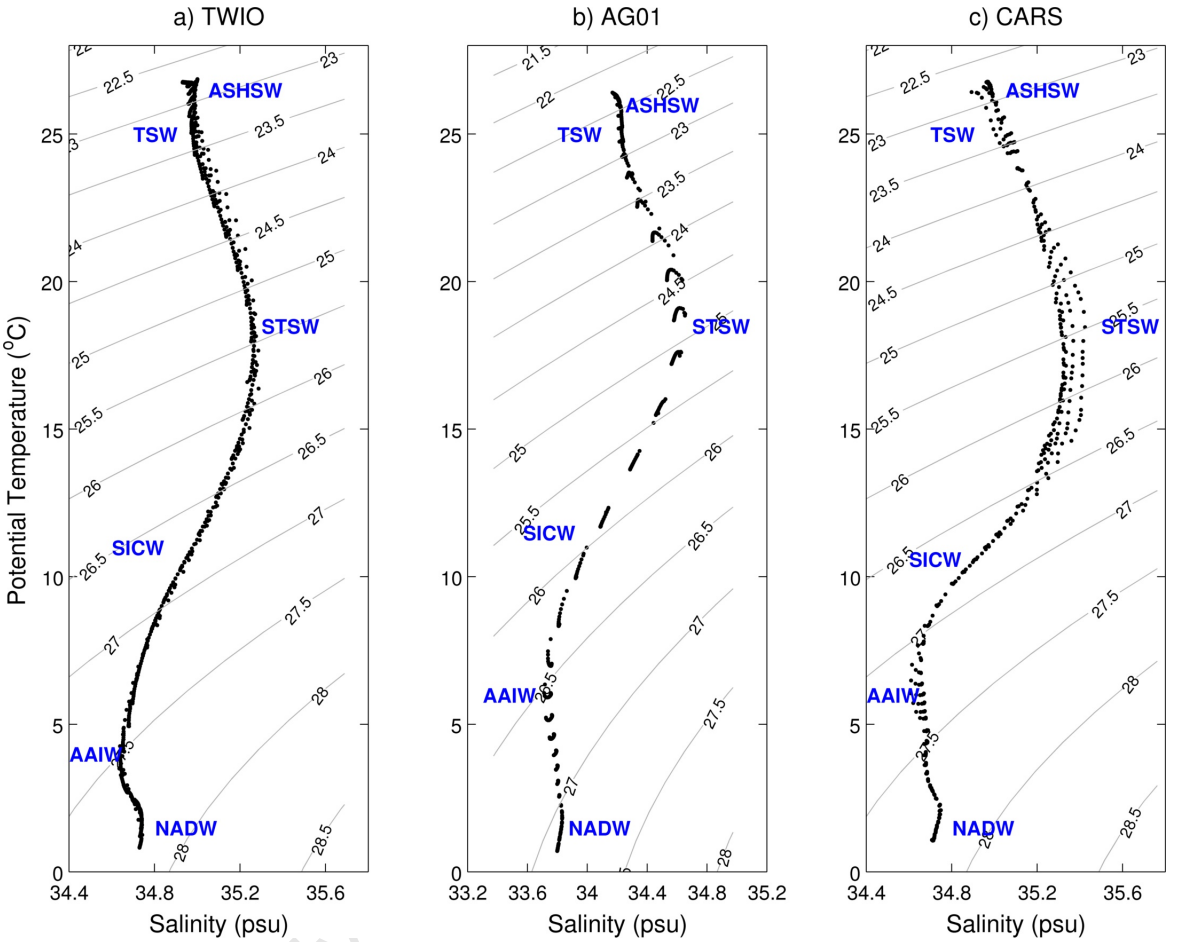

Figure 6.6: *θ-S diagram showing the water mass properties extracted along a meridional section across the NEMC for a) TWIO, b) AG01 and c) CARS. Due to the overall lower salinity of AG01 (b) is plotted on a different scale for clarity.*

The surface temperatures (23-25°C) and salinity values (34.3-35.1psu) indicate the presence of TSW in the upper ~100m. The most noticeable feature of the vertical salinity structure of the NEMC is the high salinity layer of STSW centred at about 200m (Figure 6.7). In agreement with Swallow et al. (1988), mixing with lower salinity waters such as ITW from the eastern Indian Ocean results in a reduced high salinity core of STSW. The STSW layer

north of Madagascar in TWIO display lower salinities compared to CARS and can most likely be attributed to excess mixing in the model (Figure 6.7). Between depths of 1000-2000m along the east coast of Madagascar, the salinity minimum layer of AAIW is observed in both models as well as in CARS (Figure 6.7). There are indications of this water mass off the tip of Madagascar as well, however it is less pronounced.

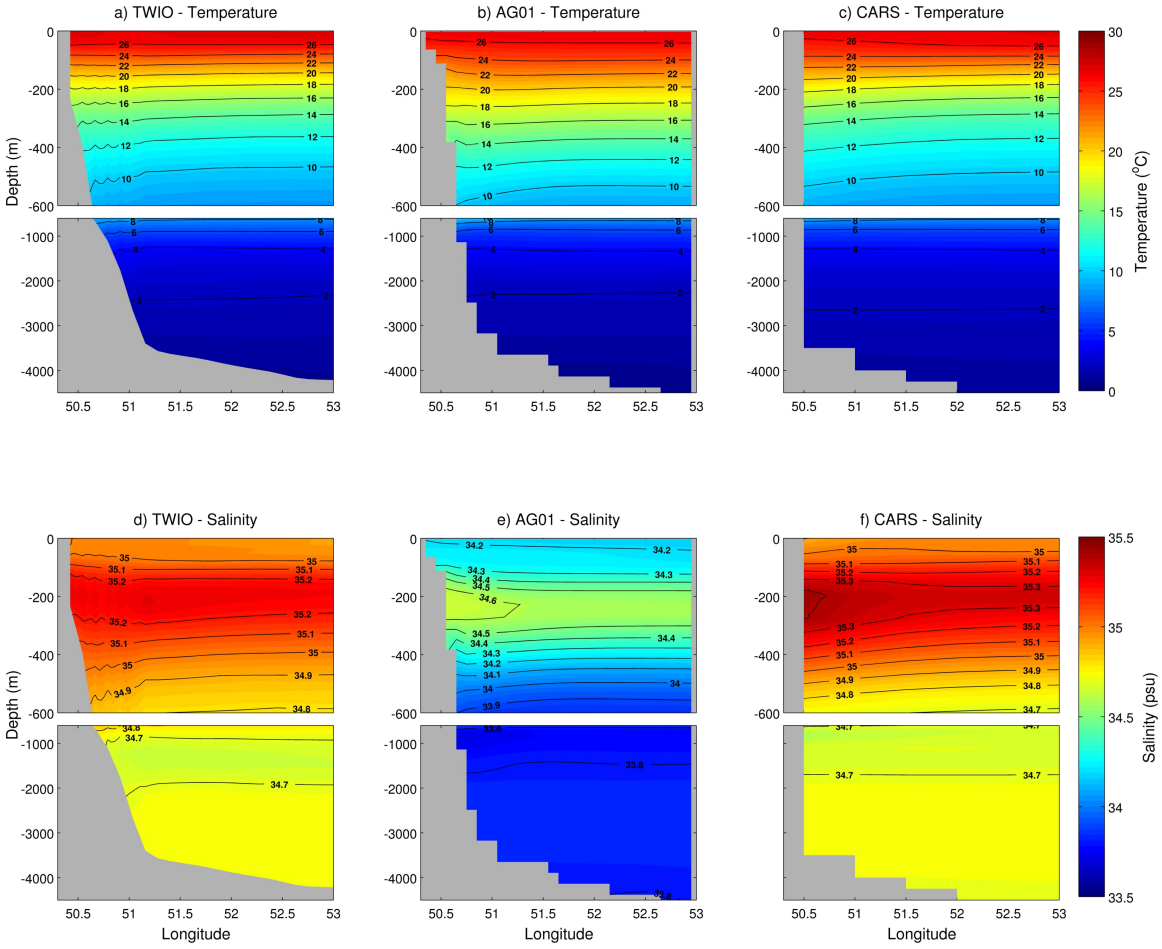

Figure 6.7: *Vertical profile of temperature (a-c) and salinity (d-f) of the NEMC in TWIO, AG01 and CARS. The contour interval for temperature and salinity is 2°C and 0.1psu, respectively.*

A zonal section at 22°S off the east coast of Madagascar is used to evaluate the water

masses within the SEMC. In TWIO, AG01 and CARS, there is a slightly upward sloping of the isopleths towards the coast indicative of the southward flowing SEMC (Figure 6.8). Analogous to the NEMC, the water masses of the SEMC comprise of TSW in the upper ~100m, high salinity STSW centred around 200m, SICW, and low salinity AAIW between depths of 1000-2000m (Figure 6.8). In accordance with Swallow et al. (1988), the high salinity STSW present in the SEMC is slightly more saline than the STSW in the NEMC off the northern tip of Madagascar. In contrast, the AAIW within the SEMC is slightly fresher compared to that within the NEMC. The salinity minimum layer of AAIW has an increased vertical distribution in TWIO compared to CARS and AG01 (Figure 6.8).

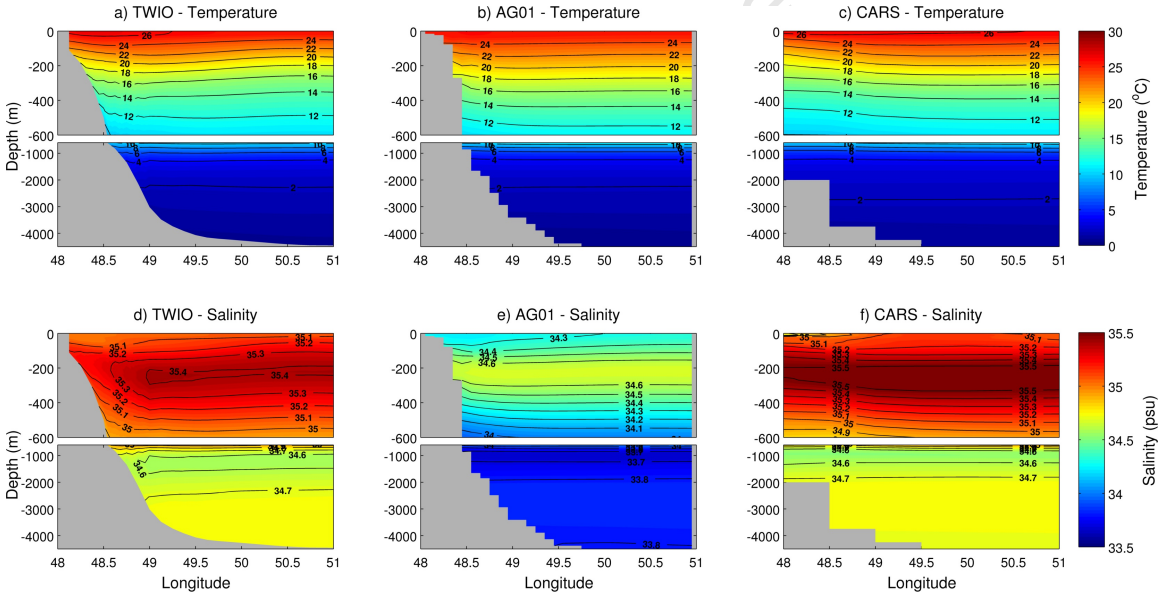

Figure 6.8: *Vertical profile of temperature (a-c) and salinity (d-f) of the South East Madagascar Current (SEMC) in TWIO, AG01 and CARS. The contour interval for temperature and salinity is 2°C and 0.1psu, respectively.*

The vertical structure of the Mozambique Channel is assessed along two zonal sections: one in the Comoros Basin at ~12.5°S and one at about 22°S (Figure 6.3). The vertical struc-

tures along both sections are similar and unless explicitly stated the results presented here, pertains to both. Consistent with water masses previously identified in the Mozambique Channel from observational (e.g. Ullgren et al., 2012, Donohue and Toole, 2003 and Chapter 3 of this thesis), the T-S diagrams of TWIO, AG01 and CARS indicate that the water masses in the Mozambique Channel consist of TSW, ASHSW, STSW, SICW and AAIW (Figure 6.9 and 6.10).

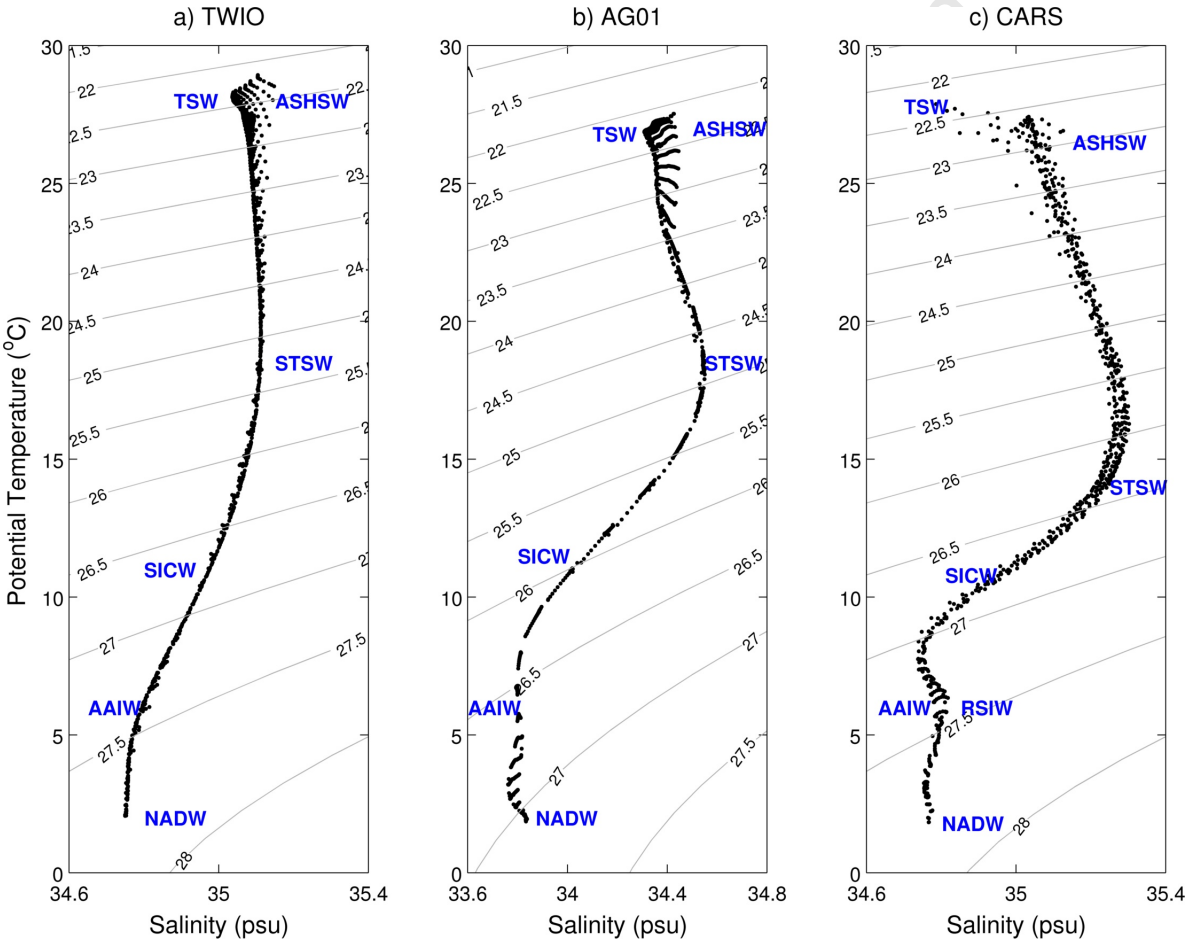

Figure 6.9: *θ-S diagram showing the water mass properties extracted along a zonal section across the Comoros Basin for a) TWIO, b) AG01 and c) CARS. Due to the overall lower salinity of AG01 (b) is plotted on a different scale for clarity.*

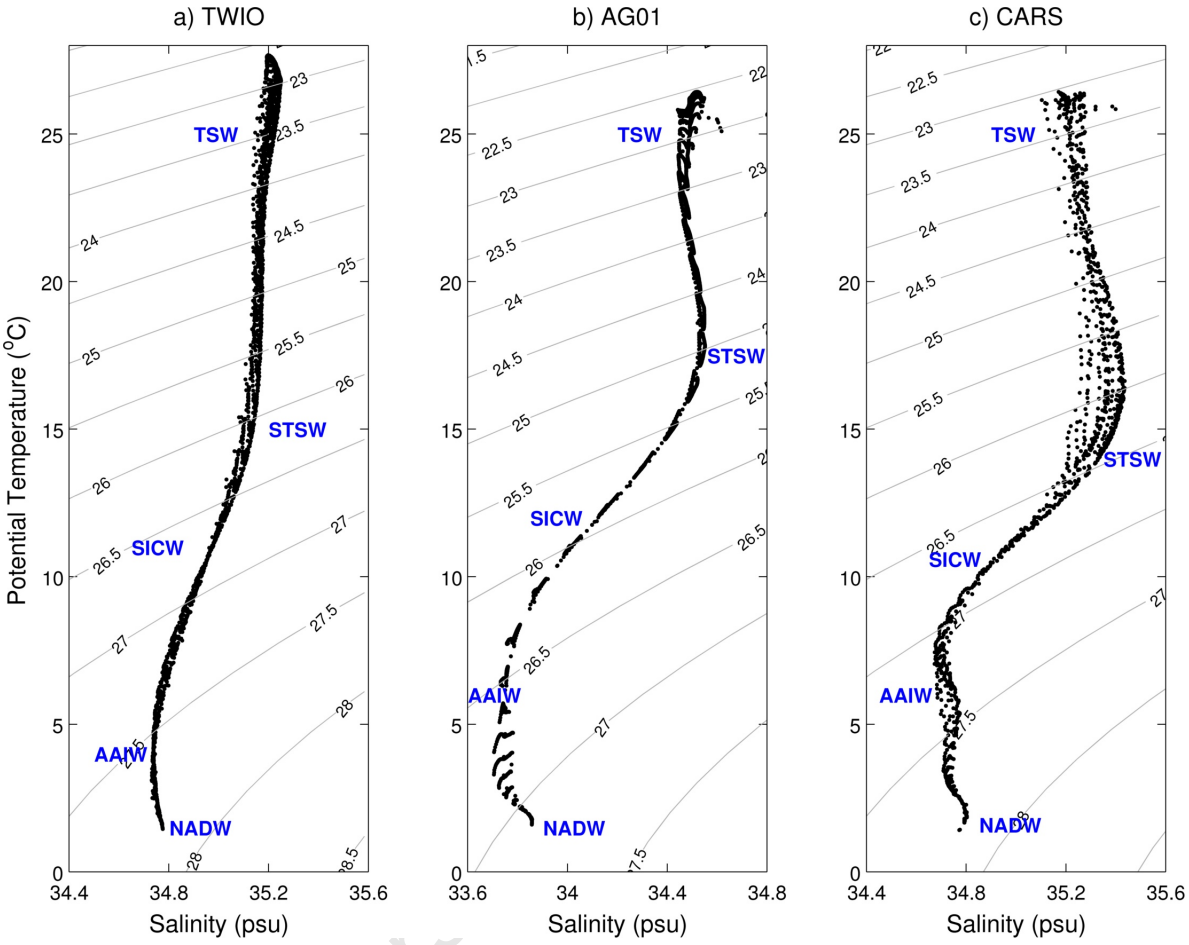

Figure 6.10: *θ-S diagram showing the water mass properties extracted along a zonal section across the SMC for a) TWIO, b) AG01 and c) CARS. Due to the overall lower salinity of AG01 (b) is plotted on a different scale for clarity.*

The upper 100m of the Mozambique Channel is characterized by TSW with surface temperatures and salinities of about 23-27°C and <35.1psu in CARS and TWIO (Figures 6.11 and 6.12a, c, d, e). As previously noted, the salinity in AG01 is significantly underestimated and as such it displays salinities of <34.5psu for TSW in the Mozambique Channel (Figures 6.11e

and 6.12e). Below the surface layer of TSW, a high salinity layer characteristic of STSW is observed in both models as well as in CARS (Figure 6.11 and 6.12). However, in TWIO the high salinity layer (35.1psu), located between 50 and 100m, is less conspicuous compared to CARS. In AG01, the STSW layer (>34.44psu) is confined to between 150-320m, whereas in CARS it occurs between 50-320m. The influence of RSIW is evident in the Comoros Basin in the observational data but not in the models (Figures 6.11 and 6.12). Similarly, in the southern Mozambique Channel, the influence of AAIW is only evident in the observational data (Figure 6.11 and 6.12)

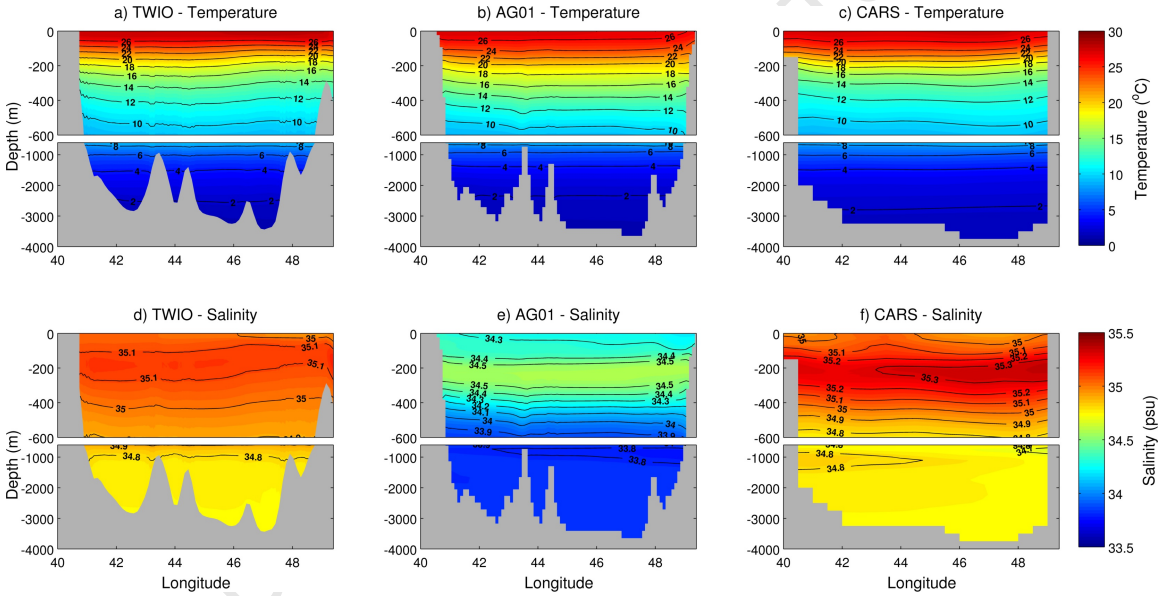

Figure 6.11: *Vertical profile of temperature (a-c) and salinity (d-f) of the Comoros Basin (CB) in a) TWIO, b) AG01 and c) CARS. The contour interval for temperature and salinity is 2°C and 0.1psu, respectively.*

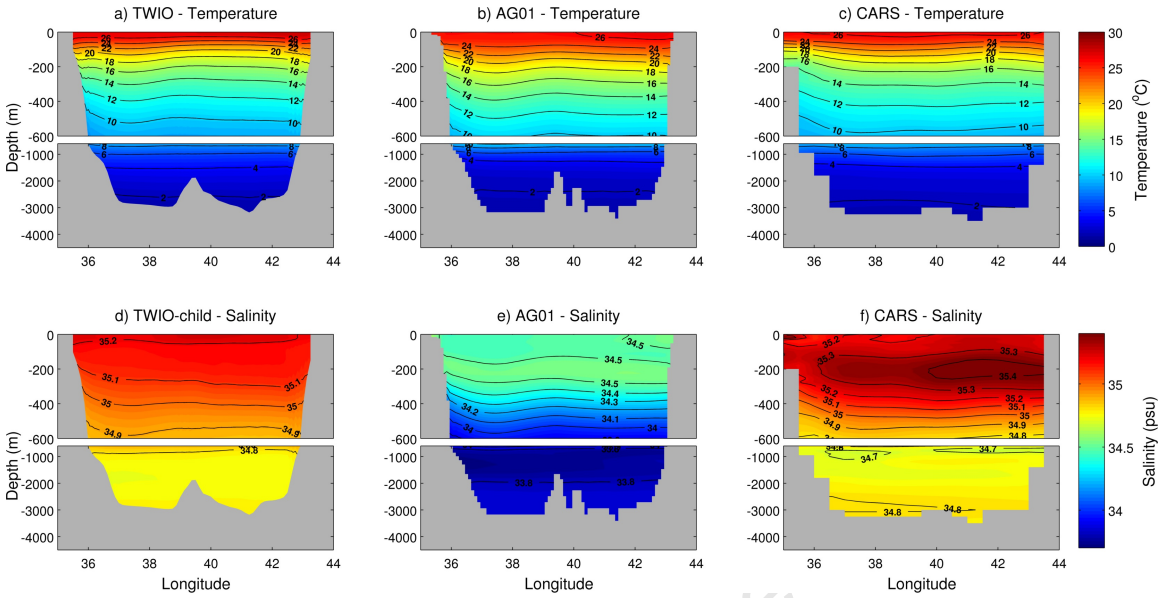

Figure 6.12: *Vertical profile of temperature (a-c) and salinity (d-f) of the Southern Mozambique Channel (SMC) in a) TWIO, b) AG01 and c) CARS. The contour interval for temperature and salinity is 2°C and 0.05psu, respectively.*

6.2 Velocity Field

6.2.1 Surface Currents

The seasonal mean surface velocity fields of TWIO and AG01 are compared to the satellite derived mean surface geostrophic velocities for the period 1993-2011 (Figure 6.13). The geographic location of the main oceanographic features evident in the altimeter surface geostrophic velocities are well represented in TWIO and AG01.

In TWIO and AG01, the main flow into the western Indian Ocean is via the broad, westward flowing SEC located between 10 and 20°S (Figure 6.13). This current has velocities in

the range of 0.1-0.2m·s^{-1} in AG01 which is similar to the velocities measured by the altimeter. TWIO, on the other hand, reproduces the SEC with velocities of 0.1-0.2m·s^{-1} stronger than measured by the altimeter (Figure 6.13). New et al. (2007) demonstrated that the SEC, with a total transport of ~50-55Sv, bifurcates into a northern (10-14°S) and southern core (17-20°S), each of which transports ~25Sv, as it flows over the Mascarene Plateau. Consistent with these findings, AG01 and the surface geostrophic velocities indicate that the SEC consists of a southern and broad northern branch located between 17-20°S and 10-14°S, respectively (Figure 6.13). During spring and summer (Figure 6.13a and d), the surface currents of TWIO appear to resolve the SEC as a single broad current extending from 10-20°S, however up to three branches of more intense westward flow, in the latitude ranges 10-12°S, 13-15°S and 16-18°S, are evident during winter (Figure 6.13c).

The SEC has a mean transport of 53.19±10.41Sv and 49.28±13.89Sv in TWIO and AG01, respectively (Figure 6.14). This transport estimate is considerably higher than the geostrophic transport estimate in the upper 1000m of 25Sv reported by Stramma and Lutjeharms (1997) but is consistent with the 40-50Sv estimated by Schott and McCreary (2001) for the SEC between 10-20°S at 60°E. The hydrographic sections used by Stramma and Lutjeharms (1997) only extended to about 12°S, and thus the northernmost part of the northern branch of the SEC was excluded from their calculations resulting in a lower transport estimate.

In agreement with the altimeter data and previous literature (Lutjeharms et al., 2000), the SEC in TWIO and AG01 bifurcates into the equatorward NEMC and poleward SEMC (Figure 6.13). Consistent with the findings of Nauw et al. (2008), Palastanga et al. (2009) and Chapman et al. (2003), the bifurcation of the SEC into the NEMC and SEMC occurs at about 17°S in TWIO (Figure 6.13a); however, in AG01 the split occurs about 3° further south at 20°S (Figure 6.13b). Therefore, in both models part of the southern core of the SEC

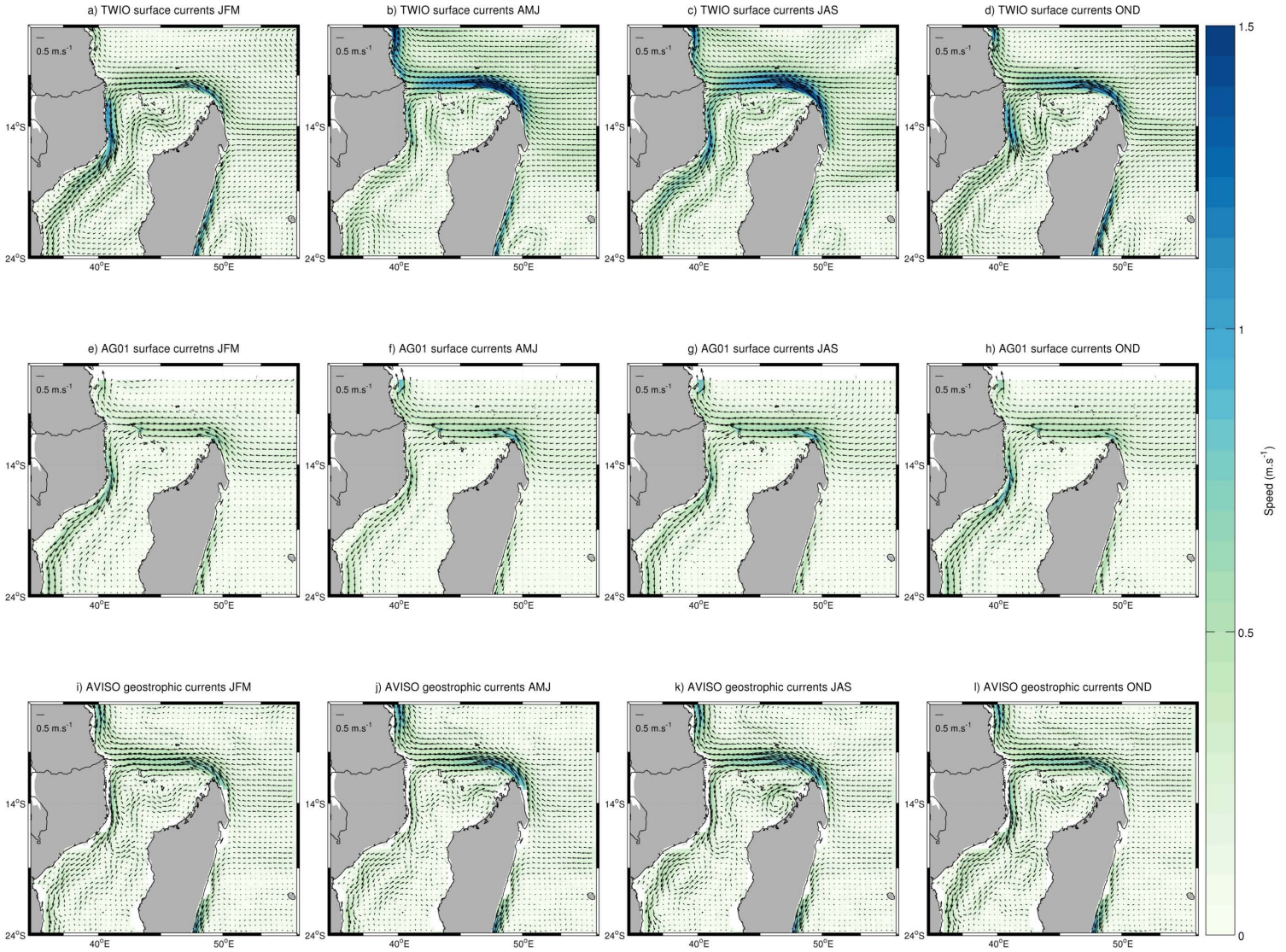

Figure 6.13: *The seasonal mean surface velocities from TWIO (a-d), AG01 (e-h) and the surface geostrophic velocities from AVISO (i-l).*

turns north as the NEMC, contradicting the suggestion of New et al. (2007) that the northern core of the SEC turns north at Madagascar as the NEMC and the southern core turns south as the SEMC. The bifurcation at the coast of Madagascar displays no seasonality in AG01 or the altimeter data (Figure 6.13); however in TWIO, the bifurcation occurs ~2° further south during autumn and winter compared to summer and spring (Figure 6.13a, b, and c).

The surface velocities of both branches along the east Madagascar coast are stronger (weaker) in TWIO (AG01) than is suggested by the surface geostrophic velocities (Figure 6.13). In both models as well as the altimeter data, the NEMC intensifies during autumn and winter (Figure 6.13). This current intensifies by as much as $0.6 m \cdot s^{-1}$ in TWIO-child whereas in the altimeter data and AG01, there is an increase in velocity of only about $0.2 m \cdot s^{-1}$. The increased strength of the NEMC results in an increased westward extent of the core of the current north of Madagascar which subsequently results in an intensification of the EACC (Figure 6.13). The NEMC resolved by AG01 is limited in its northward trajectory as it flows past the tip of Madagascar and even though it stretches west across the Mozambique Channel its core (i.e. maximum speed) is limited to east of 45°E during all four seasons (Figure 6.13).

The SEMC, flowing south along the east coast of Madagascar, closely follows the shelf edge which separates from the coast south of Madagascar so that the SEMC is steered away and intensifies, reaching a maximum speed of about $1 m \cdot s^{-1}$. The SEMC resolved by AG01 also displays an increase in poleward velocities reaching maximum speeds of approximately $0.5 m \cdot s^{-1}$ which are considerably weaker than the maximum speed displayed by TWIO and the altimeter data (Figure 6.13).

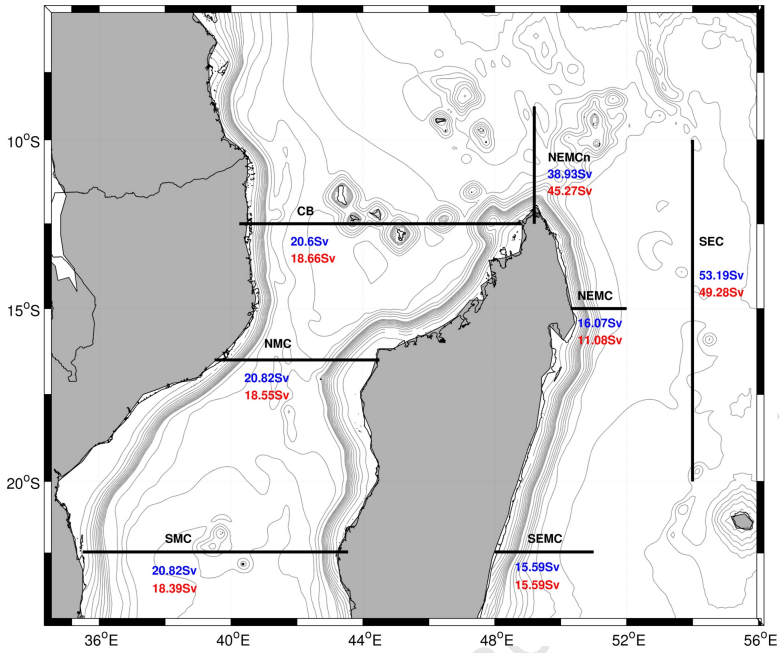

Figure 6.14: *The mean volume transports in Sverdrups (Sv), calculated in the upper 1500m for the South Equatorial Current (SEC), North East Madagascar Current at 15°S (NEMC) and 49.2°E (NEMCn), South East Madagascar Current (SEMC) at 22°S, the Comoros Basin (CB), the Mozambique Channel at 17°S (NMC) and 22°S (SMC). The blue and red values were calculated from TWIO and AG01, respectively.*

The NEMC transports about 38.93±10.36Sv and 45.27±14.96Sv past the northern tip of Madagascar in TWIO and AG01, respectively while 19±9.38Sv and 15.75±8.82Sv are transported poleward in the SEMC (Figure 6.14). The transport estimates of TWIO are in good agreement with the transports of 30Sv and 20Sv for the NEMC and SEMC, respectively, calculated from hydrographic data (Swallow et al., 1988). However, AG01 overestimates the transport of the NEMC while that of the SEMC is underestimated.

In the Comoros Basin, a strong southward current is evident along the north coast of

Mozambique in the altimeter data as well as in the two models (Figure 6.13). In TWIO, this current reaches speeds of up to $1 m \cdot s^{-1}$ while in AG01 and AVISO it has a maximum speed of about $0.5 m \cdot s^{-1}$. The surface velocities and surface geostrophic currents suggest that this feature continues as a well-defined southward flowing current along the east coast of Africa that eventually feeds into the northern Agulhas Current (Figure 6.13). This southward flow appears to be weakest during the autumn in TWIO, AG01 and AVISO (Figure 6.13b, f, j).

As mentioned in Chapter 2, numerous studies have shown that the flow in the Mozambique Channel consists of a number of meso-scale eddies which propagate southward along the western side of the channel. Southward propagating anti-cyclonic eddies, as previously documented by Schouten et al. (2003), de Ruijter et al. (2002), and Ridderinkhof and de Ruijter (2003), are evident in the weekly averaged surface velocities of TWIO and AG01 and in the surface geostrophic velocities (Appendix C). The horizontal scale of the Mozambique Channel eddies simulated in TWIO and AG01 are comparable in size to those observed from altimetry. The average diameter of the eddies are approximately 300km, which is consistent with previous literature (e.g. Schouten et al., 2003; Harris, 1972; de Ruijter et al., 2002).

The annual mean transport through the Mozambique Channel in TWIO and AG01 is 20.82±13.43Sv and 18.55±8.46Sv, respectively (Figure 6.14). These transport estimates through the channel are in good agreement with recent transport estimates of 16.7-18.66Sv based on a long term mooring in the narrows of the channel (Ridderinkhof et al., 2010; Ullgren et al., 2012).

6.2.2 Vertical structure of currents

The vertical structure of the major currents in the western Indian Ocean and the flow in the Mozambique Channel as reproduced by the models are compared against the vertical structures presented in the literature. The vertical structure of the SEC, SEMC, NEMC and the flow in the Mozambique Channel are analysed along the sections indicated in Figure 6.3 based on the annual mean meridional and zonal velocities for the latitudinal and longitudinal sections, respectively.

The annual mean zonal (east-west) velocity of the SEC as resolved by TWIO and AG01 along a section between 10° and 20°S at 55°E are compared against ADCP measurements between the same latitudes at ~57°E analysed by (New et al., 2007). In the upper 800m, the westward velocities of the SEC resolved in TWIO-child and AG01 are in the range 0.04-0.3m·s^{-1}s and 0.03-0.2m·s^{-1}, respectively (Figure 6.15). The SEC resolved in both models appears to be comprised of two cores: a broad current between 8°S and 16°S and a weaker core between 17° and 19°S. The northern core of the SEC has typical westward velocities in the range 0.1-0.3m·s^{-1} in both models whereas the southern core in AG01 with velocities of 0.05-0.1m·s^{-1} is slightly weaker compared to the velocities of 0.06-0.2m·s^{-1} in TWIO (Figure 6.15). The double core structure of the SEC observed in the models is consistent with the findings of New et al. (2007); however, the northern core identified by New et al. (2007) only extends as far north as 11°S. Furthermore, the velocities of both cores are weaker compared to the typical speed of 0.3-0.4m·s^{-1} observed for both cores by New et al. (2007).

The vertical structure of the velocity of the NEMC is analysed along a zonal profile at 15°S off the east coast of Madagascar and a meridional profile at 49.2°E off the tip of Madagascar. The meridional profile is compared against the vertical structure presented by Swal-

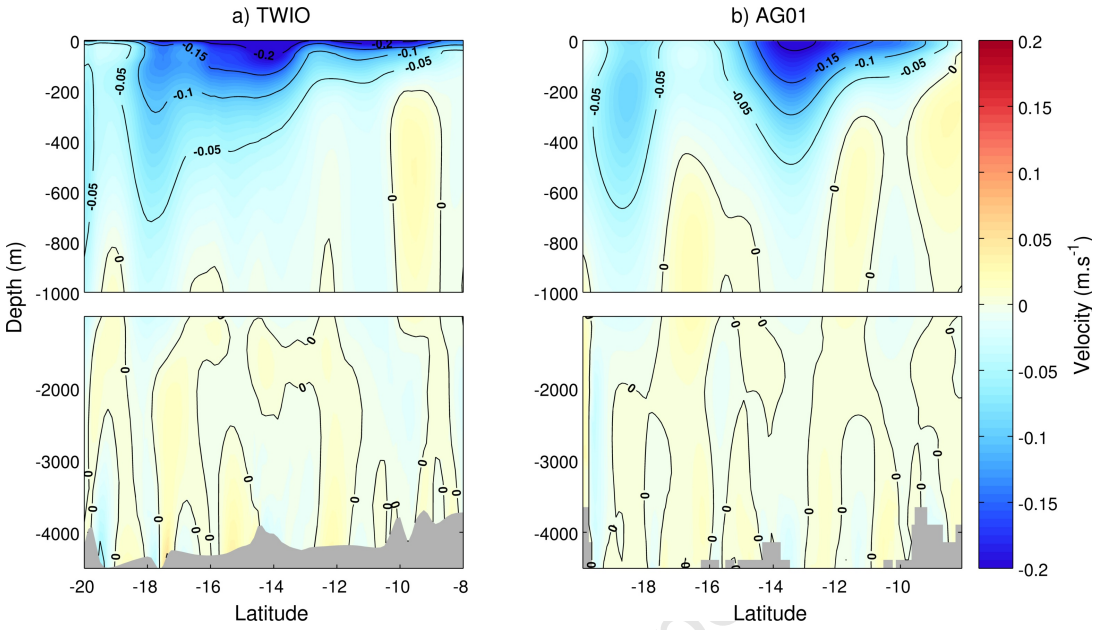

Figure 6.15: *Vertical profile of the annual mean zonal velocity ($m{\cdot}s^{-1}$) along a meridional section through the South Equatorial Current (SEC) in a) TWIO and b) AG01. The contour interval is 0.05$m{\cdot}s^{-1}$. Negative (positive) values indicate westward (eastward) flow.*

low et al. (1988) based on observational data. The highest velocities of the NEMC, both north of Madagascar and along the east coast, are confined close to the coast (Figure 6.16 and 6.17). Consistent with the findings of Swallow et al. (1988), both models resolve the highest westward velocities of the NEMC north of Madagascar within the upper 100m where they exceed 0.7$m{\cdot}s^{-1}$ and remain above 0.3$m{\cdot}s^{-1}$ up-to a depth of ~600m (Figure 6.16c and d). In AG01, velocities exceeding 0.7$m{\cdot}s^{-1}$ are also observed between ~130-240m. Along the east coast of Madagascar, the NEMC in TWIO has maximum northward velocities of 0.3$m{\cdot}s^{-1}$ at the surface as well as between depths of 100-430m (Figure 6.17a). In AG01, the maximum northward velocities of 0.3$m{\cdot}s^{-1}$ along the east coast of Madagascar are centred around 400m and at the surface it obtains speeds of only 0.05$m{\cdot}s^{-1}$ (Figure 6.17b). North of Madagascar, the 0.5$m{\cdot}s^{-1}$ isotach of the NEMC obtains a depth of ~450m in both models and surfaces at

~165km and ~122km offshore in TWIO and AG01, respectively (Figure 6.16a and b). In comparison, Swallow et al. (1988) found that the 0.5m·s^{-1} isotach of the NEMC northeast of Cape Amber reached a depth of approximately 300m and surfaced at 92km offshore. The overall horizontal extent of the NEMC north of Madagascar exceeds 300km in both models, whereas the vertical extent of the current in AG01 at ~1300m is 700m less than the 2000m vertical extent in TWIO (Figure 6.16a and b). On the other hand, east of Madagascar the width of the NEMC is less than 250km in both models, and the vertical extent in TWIO at ~1700m is 300m less than the 2000m vertical extent in AG01 (Figure 6.17a and b). The shallower maximum depth of the NEMC east of Madagascar in TWIO can be attributed to the presence of a southward undercurrent between 2000-3500m which is absent in AG01.

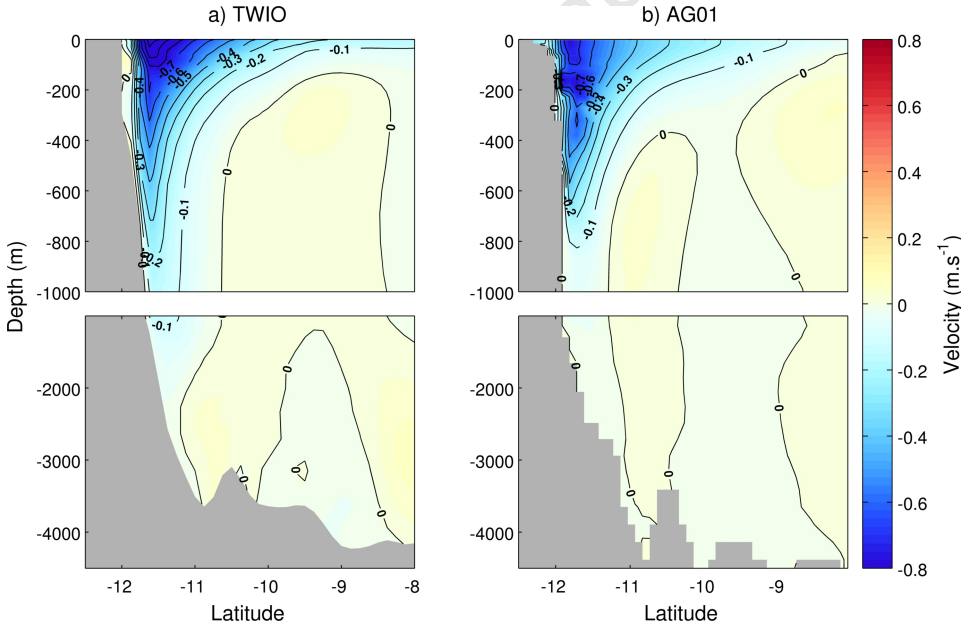

Figure 6.16: *Vertical profile of the annual mean zonal velocity (m·s^{-1}) along a section through the NEMC at the northern tip of Madagascar in a) TWIO and b) AG01. The contour interval is 0.1m·s^{-1}. Negative (positive) values indicate westward (eastward) flow.*

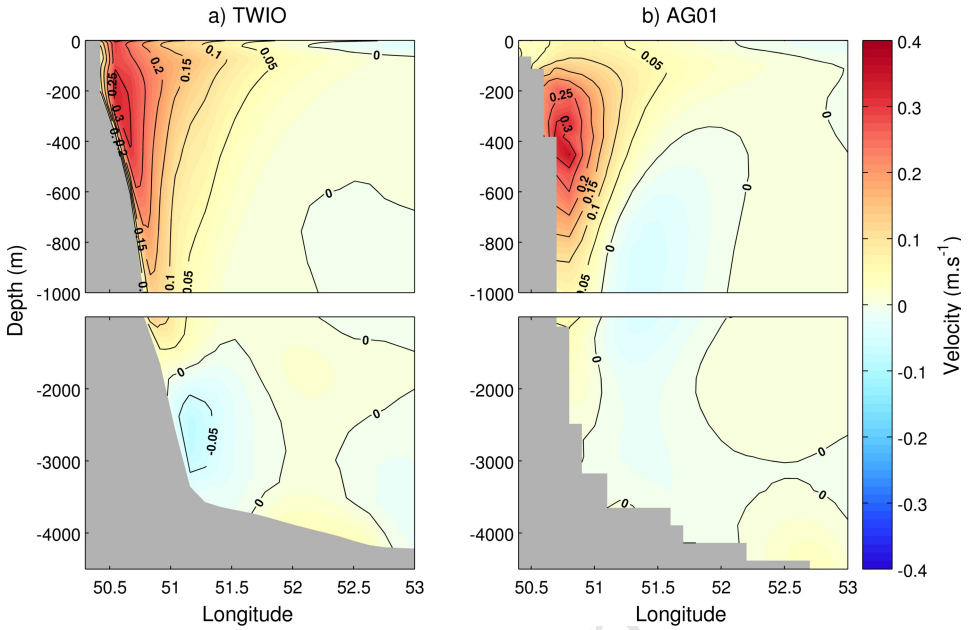

Figure 6.17: *Vertical profile of the annual mean meridional velocity (m·s^{-1}) along a section through the NEMC east of Madagascar in a) TWIO and b) AG01. The contour interval is 0.05m·s^{-1}. Negative (positive) values indicate southward (northward) flow.*

The vertical structure of the meridional velocity of the SEMC at 22°S between 48° and 51°E is similar to that observed for the NEMC along the east coast of Madagascar. The maximum southward surface velocities of >0.7m·s^{-1} and >0.5m·s^{-1} in TWIO and AG01, respectively (Figure 6.18), are comparable to that observed by Swallow et al. (1988) from observational data at 23°S. The 0.5m·s^{-1} isotach, confined to within 45km of the coast in TWIO, obtains a maximum depth of ~500m (Figure 6.18a), whereas in AG01 it is located between 36km and 44km offshore and reach a maximum depth of 30m (Figure 6.18b). Swallow et al. (1988) found the 0.5m·s^{-1} isotach of the SEMC at 23°S to be confined to within 74km of the coast, reaching no deeper than 200m. In both models, the SEMC has a width of less than

150km; however in AG01, the SEMC is confined to the upper 1000m whereas in TWIO it extends to a depth of ~3300m.

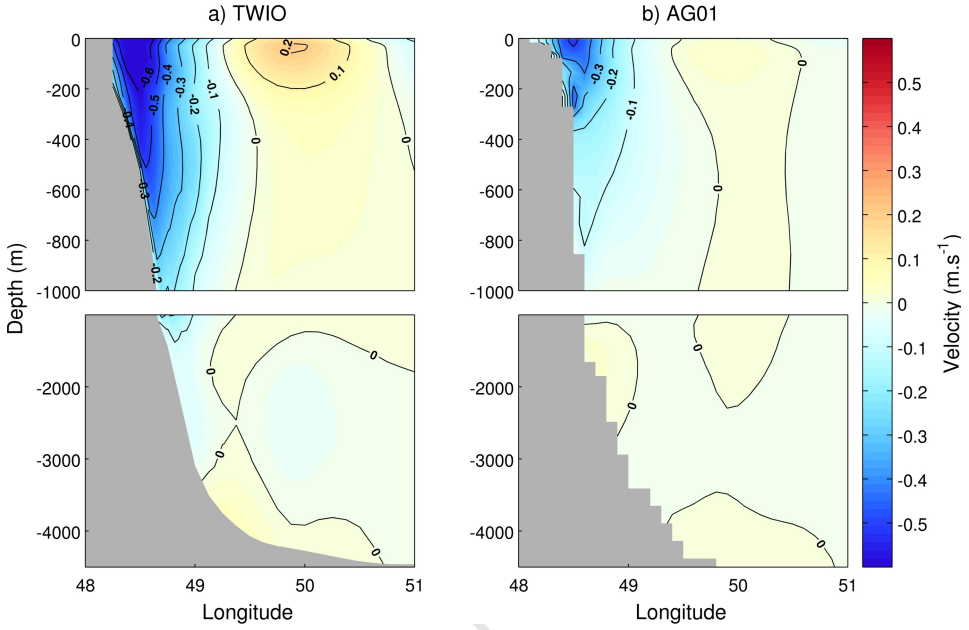

Figure 6.18: *Vertical profile of the annual mean zonal velocity ($m{\cdot}s^{-1}$) along a meridional section through the SEMC in a) TWIO and b) AG01. The contour interval is 0.1$m{\cdot}s^{-1}$. Negative (positive) values indicate southward (northward) flow.*

The vertical structure of velocity in the northern Mozambique Channel is analysed along the same section as the temperature and salinity profiles in order to compare it with the vertical structure obtained from the LOCO mooring array (Harlander et al., 2009; Ridderinkhof et al., 2010; Ullgren et al., 2012). Both models show that the meridional flow in the northern Mozambique Channel consists of a strong (0.05-0.5$m{\cdot}s^{-1}$) southward flow along the coast of Mozambique that extends ~160km offshore and weaker (0.05-0.1$m{\cdot}s^{-1}$) eastward flow in the east of the channel (Figure 6.19). In TWIO and AG01, the core of the southward flow is

confined to the upper 100m where velocities exceed 0.4m·s^{-1}. In the vertical, the southward flow extends to the bottom of the channel, however along the continental slope there is an indication of the northward undercurrent between 1500-2000m in TWIO (Figure 6.19a) and between about 1100-2600m in AG01 (Figure 6.19b). These findings are consistent with those of Harlander et al. (2009), Ridderinkhof et al. (2010) and Ullgren et al. (2012).

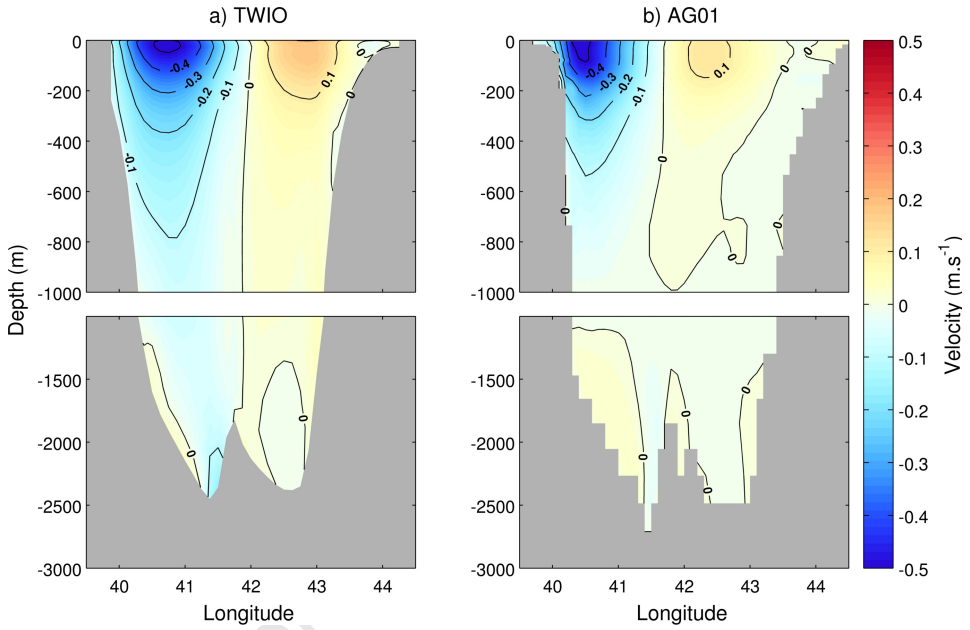

Figure 6.19: *Vertical profile of the annual mean zonal velocity (m·s^{-1}) along a meridional section through the northern Mozambique Channel in a) TWIO and b) AG01. The contour interval is 0.1m·s^{-1}. Negative (positive) values indicate southward (northward) flow.*

In the southern Mozambique Channel (22°S; Figure 6.20), the meridional flow shows a very similar pattern to that observed in the northern Mozambique Channel (Figure 6.19); however, in both TWIO and AG01, the southward and northward flows are confined closer to the coast (Figure 6.20). In addition, the velocity of the southward flow, ranging from 0.05 to

0.4m·s^{-1} (Figure 6.20), is similar to that in the northern Mozambique Channel. On the other hand, the northward flow is slightly stronger with velocities in the range 0.04-0.12m·s^{-1} in AG01 (Figure 6.20b) and 0.05-0.2m·s^{-1} in TWIO (Figure 6.20a). The vertical extent of the southward flow in AG01 does not exceed 1000m while the northward flow is limited to the top 700m (Figure 6.20a). In TWIO, the southward flow extends to a depth of 2000m and the northward flow is confined to the upper 1100m (Figure 6.20b). In both models, there is evidence at depth of northward flow along the continental slope. In AG01, this northward flow, occurring between 1200m and the bottom of the channel, is more pronounced compared to TWIO where it occurs at depths greater than 2000m (Figure 6.20).

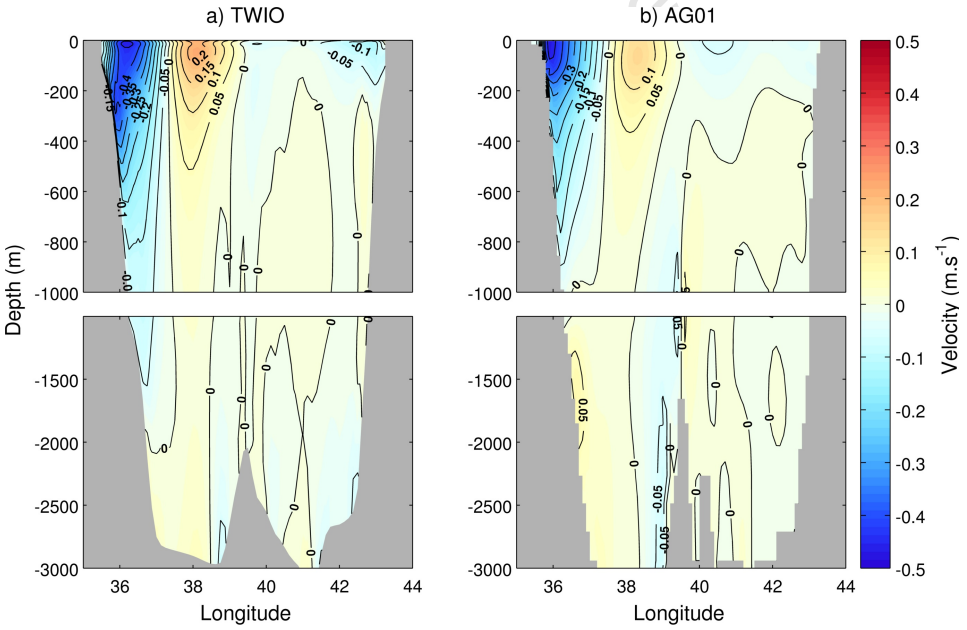

Figure 6.20: *Vertical profile of the annual mean zonal velocity (m·s^{-1}) along a meridional section through the southern Mozambique Channel in a) TWIO and b) AG01. The contour interval is 0.05m·s^{-1}. Negative (positive) values indicate southward (northward) flow.*

6.3 Meso-scale variability

6.3.1 Mean Eddy Kinetic Energy

Figure 6.21 shows the annual mean eddy kinetic energy calculated for the satellite altimeter data and the two models (AG01 and TWIO). The pattern of EKE calculated for AG01 and TWIO is comparable to that derived from the altimeter data, however the magnitudes are not (Figure 6.21). Overall, the EKE derived from AVISO is considerably lower than that of AG01 and TWIO. Similar to EKE values calculated from ship's drift data Lutjeharms et al. (2000), energy levels in the Mozambique Channel in the models and altimeter data exceeds $400cm^2 \cdot s^{-2}$.

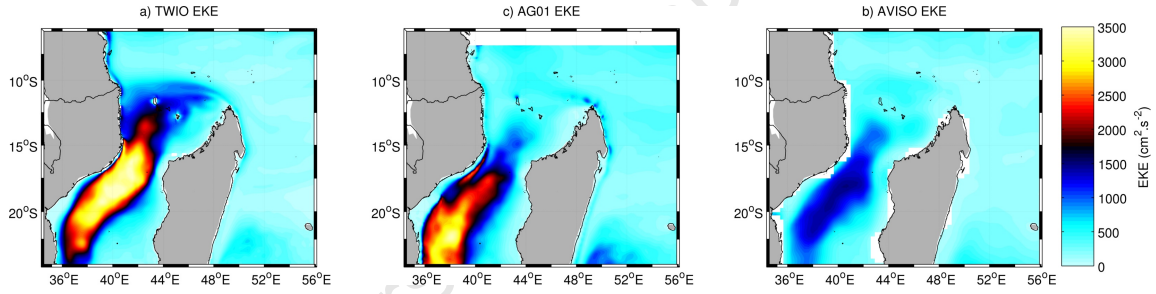

Figure 6.21: *The annual mean eddy kinetic energy (EKE) from a) TWIO, b) AG01 and c) AVISO.*

In TWIO, energy levels exceeding $600cm^2 \cdot s^{-2}$ extends from north of the Comoros Islands throughout the Mozambique Channel (Figure 6.21a). In comparison, EKE in excess of $600cm^2 \cdot s^{-2}$ extend from south of the Comoros Islands into the Mozambique Channel in AG01 and AVISO (Figure 6.21b and c). Maximum energy ($>800cm^2 \cdot s^{-2}$) occurs along the east coast of Mozambique (Figure 6.21) coinciding with the southward migration of Mozambique Channel eddies (Harlander et al., 2009). The altimeter data display maximum energies in the range $1000\text{-}1400cm^2 \cdot s^{-2}$ along the western boundary of the Mozambique Channel,

whereas in the models maximum EKE of 2000-3200cm^2·s^{-2} indicates and overestimation of about 40%.

6.3.2 Sea Level Anomalies

The meso-scale variability can also be inferred from enhanced values of the root-mean square (RMS) of sea surface height (SSH) which is calculated as

$$RMS = \sqrt{\frac{\sum SSH^2}{n}}$$

where n is the number of observations. The RMS of SSH derived from TWIO, AG01 and the altimetry date are displayed in Figure 6.22.

There is relatively good agreement between the sea surface height variability calculated for TWIO, AG01 and the altimeter data (Figure 6.22). The variability in the Mozambique Channel ranges from 6 to 30cm with enhanced variability (>10cm) occurring throughout the Mozambique Channel. The highest variability (>15cm) in the channel is confined to the western part and corresponds to the southward passage of meso-scale eddies through the channel (Harlander et al., 2009). The patterns of SSH variability in the Mozambique Channel observed in TWIO and AVISO are in good agreement with the variability calculated from altimetry data by Quartly et al. (2006), Palastanga et al. (2006), and Swart et al. (2010) as well as the variability calculated by Srinivasan et al. (2009) for observed and modeled SSH.

In TWIO, AG01 and AVISO, RMS values in the Mozambique Channel are in the range 10-25cm, 10-20cm and 10-15cm, respectively indicating that there is a slight overestimation of the maximum variability in TWIO whereas in AG01 there is an underestimation (Figure 6.22). In both TWIO and the altimeter data, the variability within the Mozambique Chan-

nel extends south from about 12°S; however, in AG01 the variability only extends south from ~16°S with little variability in the Comoros Basin. Furthermore, in TWIO maximum variability (>15cm) in the Mozambique Channel extends from south of the Comoros Islands whereas in the altimeter data its northern limit is ~14°S (Figure 6.22).

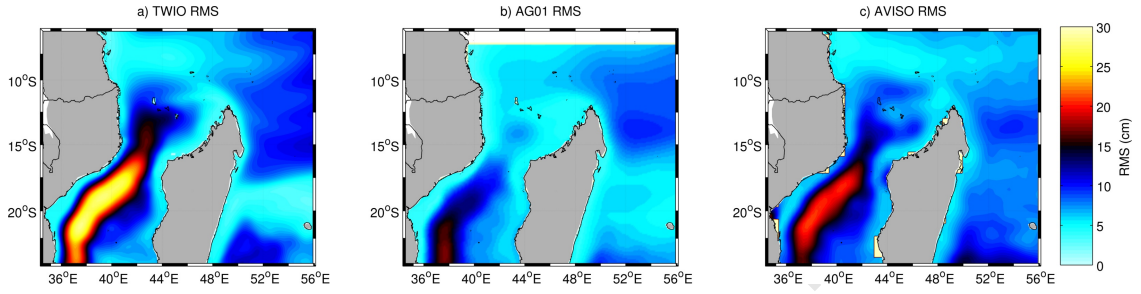

Figure 6.22: *The annual mean RMS of sea level anomalies for a) TWIO, b) AG01 and c) AVISO.*

6.4 Synthesis and Discussion

In this chapter, the TWIO and AG01 simulations described in Chapter 5 were compared against several observational data sets (CARS, TMI, LOCO and satellite altimetry) to determine whether these models reproduce the main features of the real system realistically. The performance of the models was evaluated based on their reproduction of the water mass structure, surface currents, vertical structure of the main currents and the meso-scale variability in terms of EKE and the RMS of SSH.

6.4.1 Water masses

The salient SST features of the western Indian Ocean and the Mozambique Channel are well resolved by TWIO and AG01 (Figure 6.1). Warm, saline water dominates the western Indian

Ocean with a gradual decrease in SST towards the south.

The slight overestimation of SST in the Mozambique Channel in TWIO compared to the SST of TMI (Figure 6.1) can possibly be attributed to the coarser spatial resolution of the satellite data. The underestimation of SST in AG01 (Figure 6.1) can, in part, be attributed to the coarser NCEP/NCAR atmospheric reanalysis that is included in the forcing fields of AG01. As shown in Chapter 4, NCEP/NCAR reanalysis wind data fails to reproduce small-scale wind induced features such as wind-induced meso-scale eddies, wind shadows and jets which all could potentially have large impacts on meso-scale SST. In addition, the initial and boundary conditions of AG01 are derived from the Levitus World Ocean Atlas which, compared to satellite derived SST, underestimates the SST of the Mozambique Channel and surrounds (Appendix D).

The main water masses of the tropical western Indian Ocean are well represented in TWIO and AG01; however, the latter underestimates the salinity values by about 1psu. The most notable discrepancies between the models and observations are the absence of RSIW in the northern Mozambique Channel and AAIW in the southern Mozambique Channel (Figure 6.11). The absence of these water masses can be attributed to biases introduced due to the interpolation of the model solution to observational data at the open boundaries. Furthermore, the absence of the intermediate water masses in the Mozambique Channel in the models suggest that the models do not accurately resolve the spreading of these water masses.

6.4.2 Velocity Field

The main circulation features of the western Indian Ocean, i.e. the SEC, NEMC and SEMC, and their associated transports as well as vertical structures are relatively well resolved by

TWIO and AG01. However, the surface velocities of TWIO are slightly stronger than the satellite derived geostrophic velocities while those of AG01 are slightly weaker (Figure 6.13). The weaker altimeter derived velocities could be due to the sub-sampling of the altimeter and the absence of ageostrophic velocities which may contribute substantially to the overall flow. Furthermore, the altimeter satellite tracks are not always perpendicular to the main flow direction and thus do not always capture the maximum slope and surface geostrophic current. Therefore, the more intense surface velocities in TWIO are not necessarily unrealistic.

The most apparent difference between surface velocities of TWIO, AG01 and the altimetery derived data is the structure of the SEC (Figure 6.13). In the latter two, the SEC clearly consists of two branches, a northern (10-14°S) and southern (17-20°S) branch. In TWIO, however, the SEC appears as a single broad current during summer and spring whereas in winter it consists of three branches (Figure 6.13c).

In AG01, the transport associated with the NEMC is overestimated while that of the SEMC is underestimated (Figure 6.14). This discrepancy in the estimated transport can be attributed to the bifurcation of the SEC along the coast of Madagascar which occurs at ~20°S compared to ~17°S in TWIO and the altimeter data (Figure 6.13). The more southward location of the bifurcation in AG01 results in a greater portion of the SEC turning northward with less flowing poleward.

6.4.3 Meso-scale activity

The patterns of RMS and EKE of TWIO and AG01 are in relatively good agreement with that calculated from AVISO satellite data but there are some differences in the magnitudes (Figure 6.21 and 6.22). The RMS and EKE indicates that the Mozambique Channel is a region of high

variability. Both models display higher variability in the Mozambique Channel compared to the satellite derived variability (Figure 6.21).

The higher eddy kinetic energy levels observed in the Mozambique Channel in the models (Figure 6.21) suggests that either the dissipation of energy in the Mozambique Channel is not adequately resolved or the eddies produced are larger than those observed by the satellite altimeters. Numerous studies have shown that larger eddies are likely to have higher energy levels compared to smaller eddies (Rhines, 1975; McWilliams, 1984; Eden, 2007).

6.5 Conclusion

Despite some differences between observational, satellite derived data and the models, in terms of the surface patterns and vertical structure, the models reproduce the salient features of the western Indian Ocean with reasonable accuracy. Therefore, both models can be used with relative confidence to improve the current knowledge of the circulation patterns in the Comoros Basin, the focus of Chapter 7.

Chapter 7

Meso-scale eddies in the Comoros Basin

Characteristically, the circulation in the Comoros Basin is depicted as a single, large anti-cyclonic feature known as the "Comoros Gyre" (Lutjeharms, 2006a). Based on hydrographic data, Harris (1972) suggested the presence of a deep anti-cyclonic vortex in the Comoros Basin with a diameter of about 300km and an estimated volume transport of ~10-20Sv. Sætre and da Silva (1984), analysing a different hydrographic dataset, concluded that a quasi-stationary anti-cyclonic gyre dominates in the Comoros Basin. Similarly, Donguy and Piton (1991) inferred, from geostrophic and absolute current measurements, a distinct anti-cyclonic eddy in the Comoros Basin, which consists, in the north, of the westward flowing SEC while northward flow along the Madagascan coast constitutes the eastern boundary.

More recently, Biastoch and Krauss (1999), using an eddy-permitting numerical model, noted an anti-cyclonic loop in the Comoros Basin which pinches off anti-cyclonic eddies that subsequently propagate into the Mozambique Channel. On the contrary, studies based on high resolution models and satellite altimetry data found that the circulation in the basin consists of anti-cyclonic eddies generated at the tip of Madagascar (Backeberg and Reason,

2010; van der Werf et al., 2010). Van der Werf et al. (2010) found that the eddies observed in the satellite data dissipated in the Comoros Basin and new eddies were generated at the narrows of the channel, whereas the simulated eddies propagated from the basin into the channel. This difference in eddy behaviour between the model and observations were attributed to the interaction of the eddies with the Comoros Islands which are not correctly resolved in the models. Backeberg and Reason (2010) determined, from satellite altimetry data and an eddy resolving model, that the formation of anti-cyclonic eddies at the northern tip of Madagascar is related to pulses in the transport of the SEC. Contrary to the findings of van der Werf et al. (2010), these authors showed that the anti-cyclonic eddies propagate westward across the basin to the coast of Mozambique with subsequent southward flow into the Mozambique Channel.

In recent years, the circulation in the Mozambique Channel south of 15°S has been the focus of numerous studies (e.g. di Marco et al., 2002; Chapman et al., 2003; de Ruijter et al., 2002; Ridderinkhof and de Ruijter, 2003; Schouten et al., 2003; Harlander et al., 2009; Swart et al., 2010; Ullgren et al., 2012). Deep reaching anti-cyclonic eddies with diameters of ~300-350km and speeds exceeding 10cm·s^{-1} dominate the flow in the Mozambique Channel (Harris, 1972; de Ruijter et al., 2002; Schouten et al., 2003). These eddies propagate southward through the channel at ~4.5km·day^{-1} (de Ruijter et al., 2002) resulting in three successive eddies throughout the channel at a time. Schouten et al. (2003) showed that eddy formation north of 16°S occurs at a frequency of 6-7 per year decreasing to 4-7 per year in the Mozambique Channel. The 55 day period at which eddies in the Comoros Basin are generated coincides with the dominant period of the barotropic instability of the SEC north of Madagascar (Schott et al., 1988; Quadfasel and Swallow, 1986). Similarly, Biastoch and Krauss (1999), using an eddy permitting ocean model and LaCasce and Isachsen

(2007), using a flat bottom, barotropic model, determined that the eddies generated at the tip of Madagascar are a result of barotropic instability of the NEMC. Another mechanism proposed for the formation of Mozambique Channel eddies is the interaction of baroclinic Rossby waves with Madagascar (Schouten et al., 2002b)

In Chapter 3, it was determined through the analysis of hydrographic and satellite derived altimetery data that the circulation in the Comoros Basin consists of numerous cyclonic and anti-cyclonic eddies. The former are primarily generated along the northwest coast of Madagascar and display no preferential propagation patterns. In agreement with previous studies (Backeberg and Reason, 2010; van der Werf et al., 2010), the anti-cyclonic eddies, with an average diameter of 160km, are primarily formed at the northern tip of Madagascar from where they propagate across the Comoros Basin and into the Mozambique Channel. The hydrographic and altimetry data presented in Chapter 3 have limited spatio-temporal resolution and the vertical structure of the eddies could not be determined using this data. Therefore, the objective of this chapter is to improve the current understanding of the circulation in the Comoros Basin through the spatially, temporally and dynamically coherent data sets obtained from the two high resolution model simulations (TWIO and AG01) described in Chapter 5. Furthermore, the dominant eddy formation mechanism at play in the two models will also be investigated.

7.1 Eddy Physical Characteristics

In order to investigate the physical properties of the eddies generated in the Comoros Basin, both TWIO and AG01 were subjected to the eddy detection and tracking algorithm described in Chapter 3. The eddies simulated in TWIO were tracked for the entire 8 years (years

3-10 of the climatological run) after equilibrium was obtained. Initially, an 8 year period was also considered for the eddies simulated in the interannual AG01 simulation, however this period yielded a significantly lower number of eddies compared to TWIO. Most of the statistics presented below were calculated as frequencies and therefore it was decided to track the eddies in AG01 for the last 25 years (1980-2004) of the 37 year interannual simulation (1968-2004) in order to obtain a similar total amount of tracked eddies compared to TWIO. The same values for maximum diameter (400km), minimum amplitude (0.2m) and lifespan (30 days) used to track the eddies in the altimeter data were used to track the eddies in the two model simulations. Eddies generated throughout the child domain, 30°E-55°E and 6°S-24°S, were tracked, however the focus will be placed on eddies generated in the Comoros Basin.

7.1.1 Eddy Genesis and Propagation

In TWIO, only 16% of the total number of eddies tracked had lifespans exceeding 30 days whereas in AG01 more than a quarter of the tracked eddies had lifespans longer than 30 days (Table 7.1). These eddies consisted of roughly equal numbers of anti-cyclonic and cyclonic eddies in AG01, whereas in TWIO slightly more anti-cyclonic eddies had lifespans exceeding 30 days (Table 7.1).

Table 7.1: *The percentage (%) of eddies tracked in the two models with lifespans exceeding 30 days and the percentage of these which are anti-cyclonic and cyclonic.*

	TWIO	**AG01**
Lifespans >30 days	16	27
Anti-cyclonic	58	52
Cyclonic	42	48

In the domain 6-24°S and 32-55°E, an increased number of eddies occur in the Comoros Basin, the Mozambique Channel and east of Madagascar (Figures 7.1a and b). More specif-

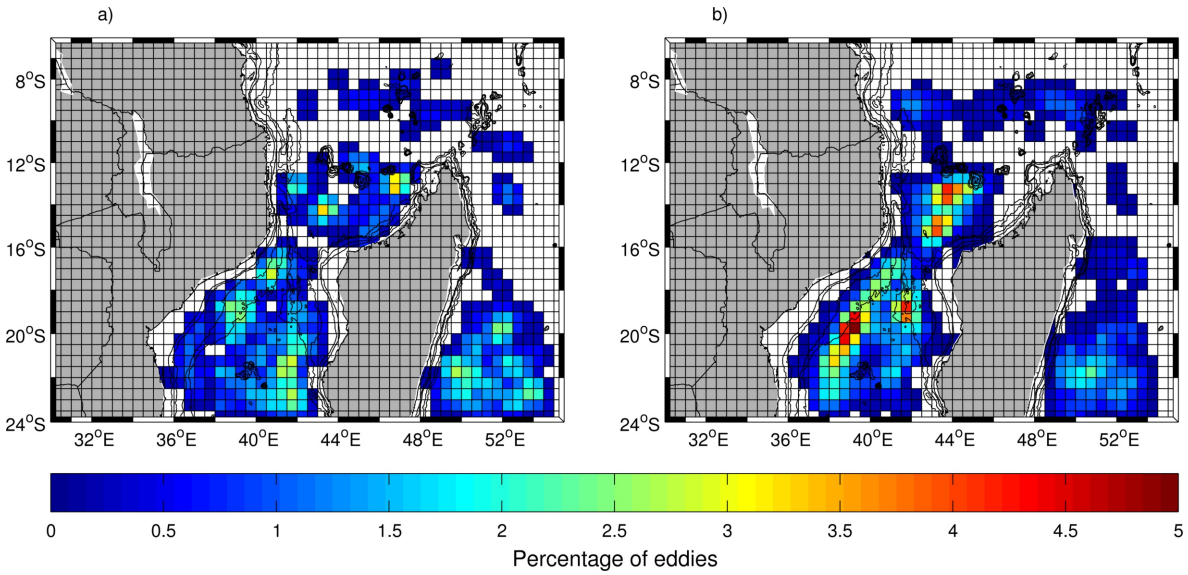

Figure 7.1: *The spatial distribution of the percentage of eddies with lifespans exceeding 30 days calculated within each 0.5°x0.5° for a) TWIO and b) AG01.*

ically, in the Comoros Basin the high number of eddies is observed west of the northern tip of Madagascar and north of the narrows of the channel in TWIO, whereas in AG01 increased eddy numbers occur south of ~13°S extending into the narrows. In the Mozambique Channel, elevated eddy activity is observed along the western boundary, with additional areas of high eddy activity east of 41°E in AG01 and along the west coast of Madagascar south of 20°S in TWIO (Figures 7.1a and b) . East of Madagascar, elevated eddy numbers occur south of 18°S, with the highest eddy activity along the east coast of Madagascar.

The eddy activity evident north of Madagascar and the Comoros Basin in Figure 7.1 can be attributed to the generation of cyclonic eddies which mainly propagate westward (Figures 7.2). Within the Mozambique Channel, both models display three general areas of anti-cyclonic eddy formation (Figures 7.2a and c): the Comoros Basin, the narrows of the channel and the eastern Mozambique Channel corresponding to areas of high eddy activity (Figures

7.1a and b). Consistent with the altimeter data and previous studies (Schouten et al., 2003; de Ruijter et al., 2005; Backeberg and Reason, 2010; van der Werf et al., 2010), anti-cyclonic eddies are mainly formed west of the tip of Madagascar in the Comoros Basin propagating west across the basin and into the Mozambique Channel.

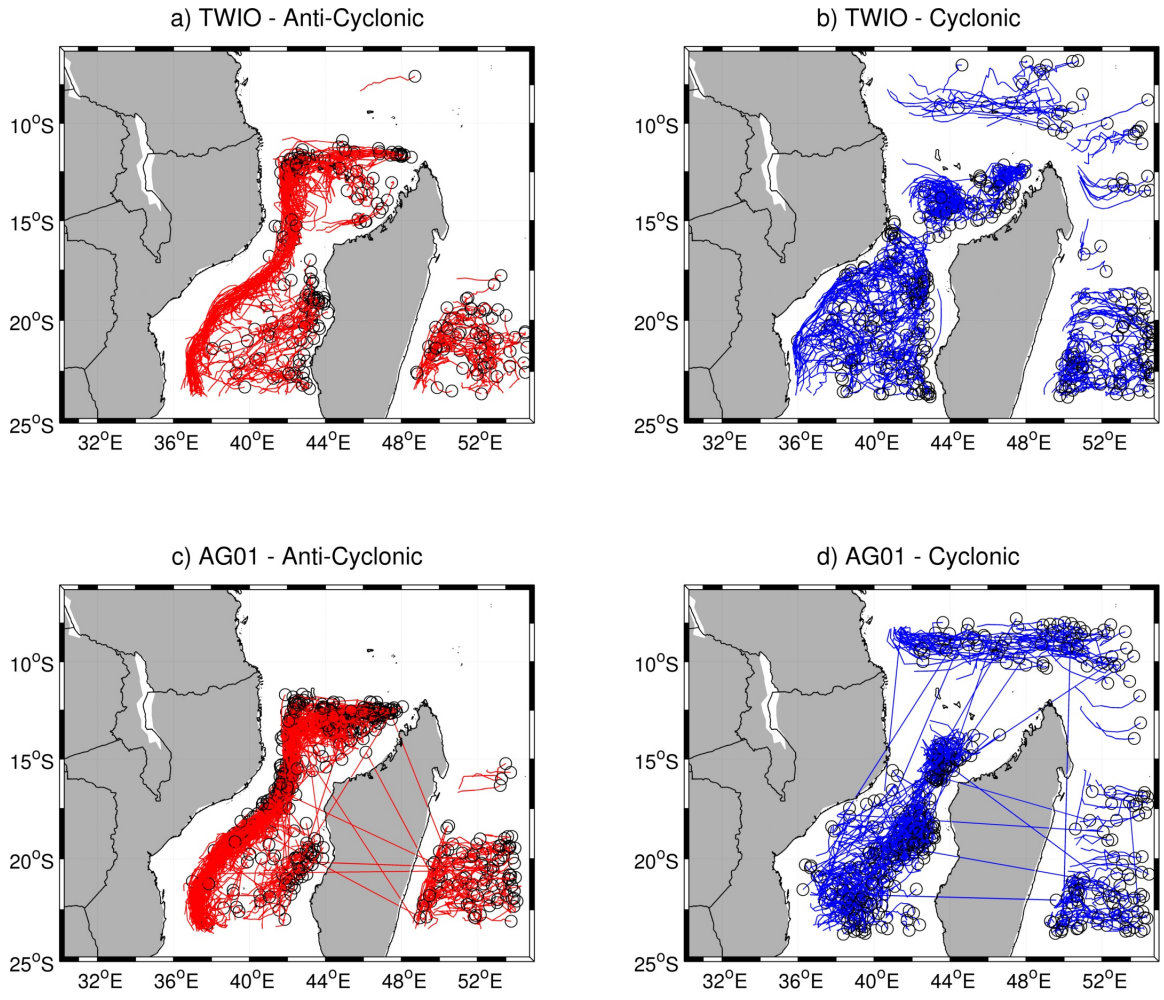

Figure 7.2: *The generation sites (open black circles) and trajectories (lines) of all anti-cyclonic eddies (a and c) and cyclonic eddies (b and d) with lifespan exceeding 30 days tracked in TWIO (top panel) and AG01 (bottom panel).*

Cyclonic eddies in the Comoros Basin are formed primarily along the northwest coast

of Madagascar in TWIO (Figure 7.2b) indicating that the high concentration of eddies along the northwest coast of Madagascar (Figures 7.1a) can be attributed mainly to cyclonic eddy activity. In AG01, cyclonic eddies in the Comoros Basin are formed in a localized area to the northwest of Cape St. Andre (Figure 7.2d) resulting in increased eddy occurrence (Figures 7.1b). The cyclonic eddies tracked in the altimeter data as presented in Chapter 3 also show preferential generation along the northwest coast of Madagascar. Cyclonic eddies generated throughout the rest of the Mozambique Channel display no preferential areas of formation in either of the models. In agreement with the altimeter data, the trajectories of the cyclonic eddies tracked in the models show no coherent pattern (Figures 7.2b and d).

The region of interest is the Comoros Basin and therefore all subsequent analyses focus on eddies generated within the Comoros Basin (39°E-50°E and 11°S-16°S; Figures 7.3). In both models, 21% of the eddies tracked with lifespans longer than 30 days were generated in the Comoros Basin. In TWIO, these eddies consisted of 60% anti-cyclonic and 40% cyclonic eddies. On the other hand, anti-cyclonic eddies constituted 90% of the eddies generated in the Comoros Basin in AG01 with only 10% cyclonic eddies.

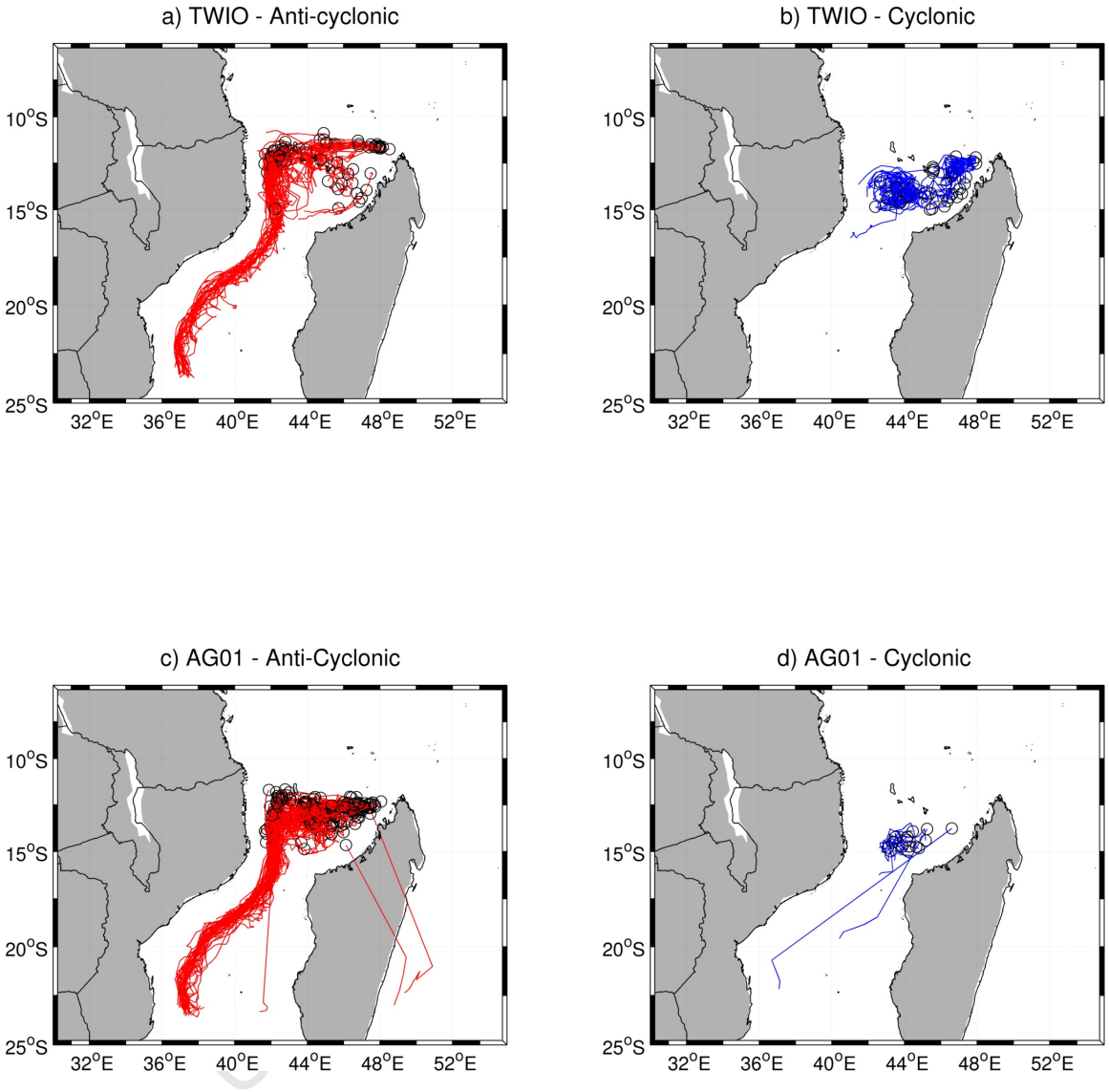

Figure 7.3: *The generation sites (open black circles) and trajectories (lines) of anti-cyclonic eddies (a and c) and cyclonic eddies (b and d) generated in the Comoros Basin in TWIO (top panel) and AG01 (bottom panel).*

7.1.2 Eddy Lifespan and Retention time

The lifespan of an eddy is defined as the number of days between the date it was first detected and the date on which it dissipated. Retention time of the eddies in the Comoros Basin, on the other hand, refers to the number of days spent within the basin and is calculated as the difference between the date it was generated and the date on which it left the Comoros Basin.

Table 7.2: *The mean lifespan (days) of eddies generated in the Comoros Basin and their mean retention time (days).*

	Overall	**Anti-cyclonic**	**Cyclonic**
TWIO			
Lifespan	87±63	98±71	71±45
Retention Time	58±35	50±25	70±44
AG01			
Lifespan	81±57	84±59	48±22
Retention time	48±23	48±22	43±29
AVISO			
Lifespan	91±67	85±63	102±72
Retention time	60±46	50±28	80±65

Comparable to the altimetry data, anti-cyclonic eddies generated in the Comoros Basin in the two models have, on average, a lifespan exceeding 80 days (Table 7.2) and remain in the Comoros Basin for roughly half of their lifespan. Unlike the cyclonic eddies tracked in the altimeter data, the cyclonic eddies formed in the basin in the models have shorter lifespans compared to their anti-cyclonic counterparts and remain in the basin over almost their whole lifespan (Table 7.2). The discrepancy between the cyclonic eddies in the model and the altimeter data can be attributed to a number of cyclonic eddies tracked in the altimeter data with lifespans exceeding 200 days which traveled into the Mozambique Channel. A quarter of the satellite derived cyclonic eddies generated in the Comoros Basin proceeded southwards

into the Mozambique Channel (Chapter 3, Figure 3.15). In AG01, on the other hand, only two cyclones propagated through the narrows of the channel (Figure 7.3d). while in TWIO a single eddy propagated as far south as ~16°S (Figure 7.3b).

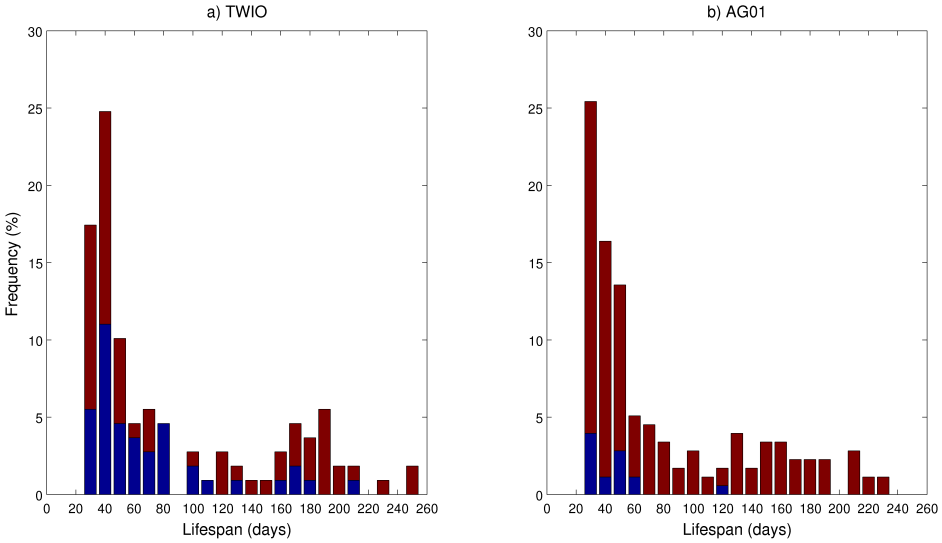

Figure 7.4: *The lifespan of eddies generated in the Comoros Basin in a) TWIO and b) AG01. Blue (red) bars represent cyclonic (anti-cyclonic) eddies.*

In agreement with the altimeter data, more than half of the eddies generated in the Comoros Basin in both models, consisting mainly of anti-cyclonic eddies, have lifespans shorter than 60 days (Figure 7.4). Lifespans between 100 and 200 days are obtained by about 30% and 24% of the anti-cyclonic eddies generated in the Comoros Basin in TWIO and AG01, respectively. Similar to the eddies tracked in the altimeter data, eddies with lifespans exceeding 200 days are rare and consist primarily of anti-cyclonic eddies (Figure 7.4). In the models as well as the altimeter data, the majority of the anti-cyclonic eddies generated in the Comoros Basin remain there for less than 50 days. Less than 5% of the anti-cyclonic eddies generated in the Comoros Basin spend more than 100 days in the basin (Figure 7.5).

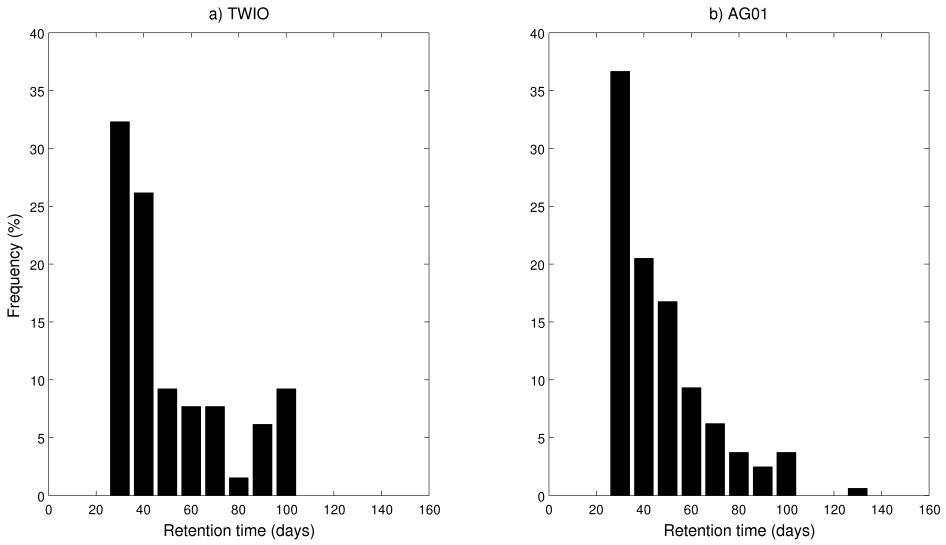

Figure 7.5: *The retention time of anti-cyclonic eddies generated in the Comoros Basin tracked in a) TWIO and b) AG01.*

7.1.3 Eddy Translation speed

Anti-cyclonic eddies generated in the Comoros Basin have higher translation speeds (>6km·day^{-1}) and shorter advective timescales while residing in the basin compared to their cyclonic counter parts (Table 7.3). In the two models the translation speeds of the anti-cyclonic eddies are more than double that of the cyclonic eddies while in the altimeter data the translation speed of the anti-cyclonic eddies are slightly less than double that of the cyclonic eddies. The advective timescales of the cyclonic eddies generated in the Comoros Basin are about three times longer than that of their anti-cyclonic counter parts (Table 7.3).

Table 7.3: *Mean translation speed and advective timescale of eddies generated in the Comoros Basin.*

	Translation Speed (km·day^{-1})	Advective Timescale (days)
TWIO		
Anti-cyclonic	8.4±5.5	34±27
Cyclonic	2.5±1.9	99±81
AG01		
Anti-cyclonic	7.5±4.2	33±21
Cyclonic	2.7±2.1	103±76
AVISO		
Anti-cyclonic	6.3±3.6	39±29
Cyclonic	3.5±2.6	99±90

7.1.4 Eddy Kinematic Properties

Eddy Scale

As defined in Chapter 3, section 3.2.3.4, eddy scale (L_s) in this study is the radius of an eddy based on the maximum average geostrophic speed of the eddy (Chelton et al., 2011). The eddy scale, an important statistical property of variability (Beckmann et al., 1994), is a better measure of eddy size as no assumption is made about the structure of the eddy (Chelton et al., 2011).

Anti-cyclonic eddies generated in the Comoros Basin are larger than their cyclonic counterparts and while residing in the basin obtain an average size of 105km in both models (Table 7.4). The anti-cyclonic eddies tracked in the altimeter data have a slightly smaller average size while retained in the Comoros Basin. Cyclonic eddies generated in the Comoros Basin have, on average, eddy scales less than 70km (Table 7.4).

Table 7.4: *Mean eddy scale and rotational speed of the eddies while residing in the Comoros Basin.*

	Eddy Scale (km)	**Rotational Speed ($m \cdot s^{-1}$)**
TWIO		
Anti-cyclonic	105±29	0.9±0.7
Cyclonic	62±21	0.4±0.2
AG01		
Anti-cyclonic	105±22	0.4±0.1
Cyclonic	58±20	0.3±0.1
AVISO		
Anti-cyclonic	83±20	0.5±0.2
Cyclonic	62±13	0.4±0.2

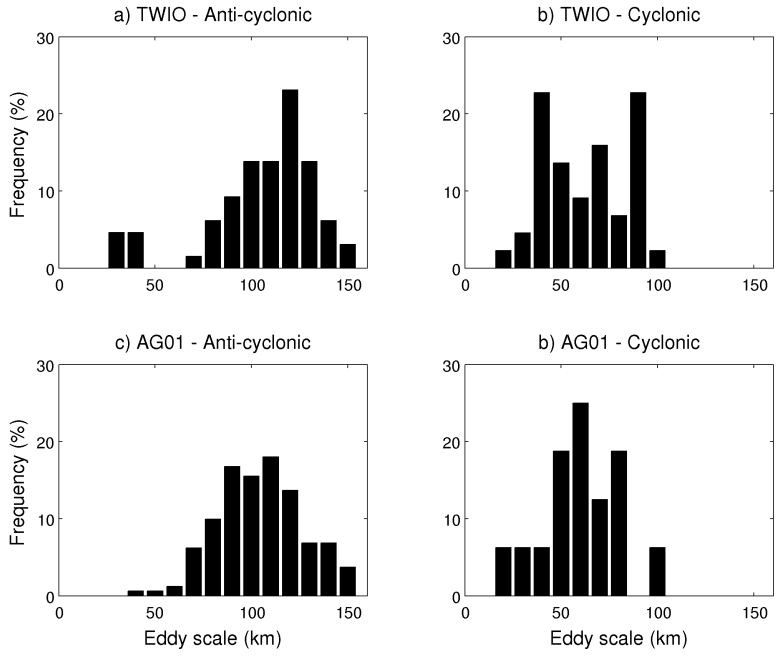

Figure 7.6: *The frequency distribution of eddy scale (km) for anti-cyclonic (a and c) and cyclonic (b and d) eddies residing in the Comoros Basin in TWIO (top panel) and AG01 (bottom panel).*

Consistent with the altimeter data, the majority of the cyclonic eddies generated in the

Comoros Basin in the two models have eddy scales in the range 50-100km (Figure 7.6). Less than 10% of the cyclonic eddies in the Comoros Basin have eddy scales exceeding 100km. Roughly more than half of the anti-cyclonic eddies generated in the Comoros Basin have eddy scales exceeding 100km while residing in the basin (Figure 7.6). Conversely, the majority of the satellite derived anti-cyclonic eddies have eddy scales in the range 50-100km (Figure 3.18). Anti-cyclonic eddies with eddy scales smaller than 50km are rare accounting for less than 10% of the anti-cyclones generated in the basin.

Rotational Speed

The rotational speed of an eddy as defined in Chapter 3, section 3.2.3.4 by Chelton et al. (2011) can roughly be characterized as proportional to the ratio of eddy amplitude to eddy scale.

Cyclonic eddies generated in the Comoros Basin have mean rotational speeds of ~0.4m·s^{-1} (Table 7.4). In AG01 and the altimeter data, anti-cyclonic eddies generated in the Comoros Basin have similar rotational speeds to their cyclonic counterparts while residing in the basin. However, the anti-cyclonic eddies generated in the Comoros Basin in TWIO-child have rotational speeds almost twice that of their cyclonic counter parts while in the basin (Table 7.4).

Consistent with the altimeter data, the majority of the cyclonic eddies generated in the Comoros Basin in the two models have rotational speeds slower than 0.5m·s^{-1} (Figure 7.7). Similarly, the majority of anti-cyclonic eddies generated in the basin in the altimeter data and AG01 have rotational speeds less than 0.5m·s^{-1} while residing in the basin. On the contrary, in TWIO-child roughly a quarter of the eddies formed in the Comoros Basin have rotational speeds slower than 0.5m·s^{-1} and in excess of 1m·s^{-1} while contained within the basin (Figure

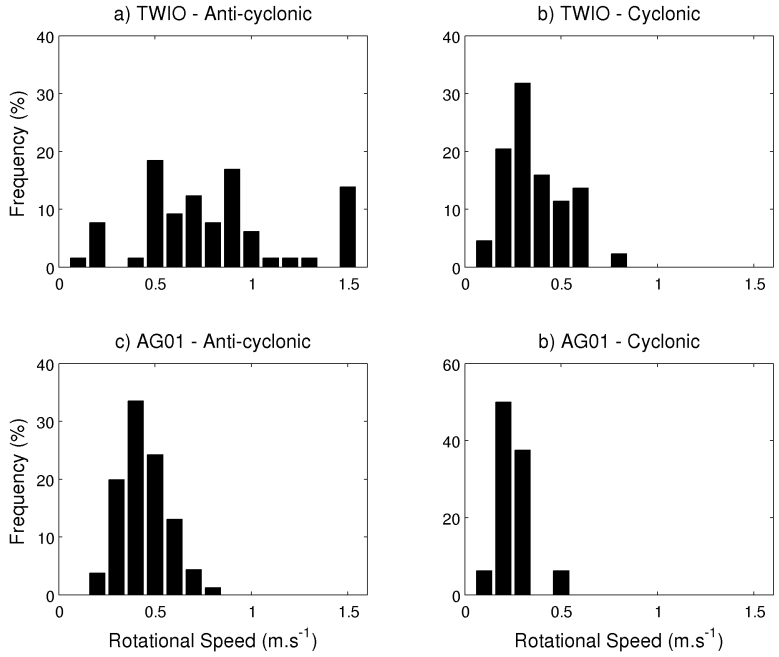

Figure 7.7: *Frequency distribution of the eddy rotational speed ($m{\cdot}s^{-1}$) of anti-cyclonic (a and c) and cyclonic (b and d) eddies residing in the Comoros Basin in TWIO (top panel) and AG01 (bottom panel).*

7.7).

7.2 Mechanisms of Eddy Formation

The mechanisms responsible for eddy generation in the Comoros Basin in both TWIO and AG01 are investigated by means of two energy interaction terms. These two terms, contained within the energy equation, which is derived from the zonal and meridional velocity component (u,v) equations, describe the interaction between the eddies and the mean flow (Beckmann et al., 1994; Biastoch and Krauss, 1999). The one term (T1), formulated as

$$T1 = g \int\int\int \frac{\overline{u'\rho'}(\partial\overline{\rho}/\partial x) + \overline{v'\rho'}(\partial\overline{\rho}/\partial y)}{d\tilde{\rho}/dz} dV \tag{7.1}$$

describes the conversion of mean potential energy to eddy potential energy and positive values for this term can be used as an indicator of baroclinic instability (Böning and Budich, 1992; Beckmann et al., 1994). The other term,

$$T2 = -\int\int\int \overline{u'u'}\frac{\partial\overline{u}}{\partial x} + \overline{u'v'}(\frac{\partial\overline{v}}{\partial x} + \frac{\partial\overline{u}}{\partial y}) + \overline{v'v'}\frac{\partial\overline{v}}{\partial y} dV \tag{7.2}$$

also referred to as "shear production" (Cushman-Roisin and Beckers, 2009), represents the effect of the Reynolds stresses on the shear and positive values suggest the occurrence of barotropic instability (Beckmann et al., 1994). This equation represents the conversion of kinetic energy of the mean flow to eddy kinetic energy and therefore, negative values indicate that energy is transferred from the eddies to the mean flow (Dewar and Bane, 1985). In the above equations, the overbar represents the time-mean and the prime the deviation from the mean. In equation 7.1, $\tilde{p}(z)$ represents the reference state for potential density.

Overall, the energy conversion rates of both terms are about an order of magnitude lower in AG01 compared to TWIO (Figures 7.8 and 7.9). Term T1 is derived from the meridional and zonal velocity fields as well as temperature and salinity whereas term T2 is derived from only the velocity fields. The lower conversion rates in AG01 can be attributed to the lower velocities and salinities of this model simulation as discussed in Chapter 6.

At the northern tip of Madagascar and westwards into the Comoros Basin, negative conversion rates for term T1 is observed in both models. This transfer of potential energy from eddies to the mean flow suggests that eddies dissipate at this location instead of being generated as suggested by the eddy tracking scheme (Figures 7.2b and d). On the other hand, the

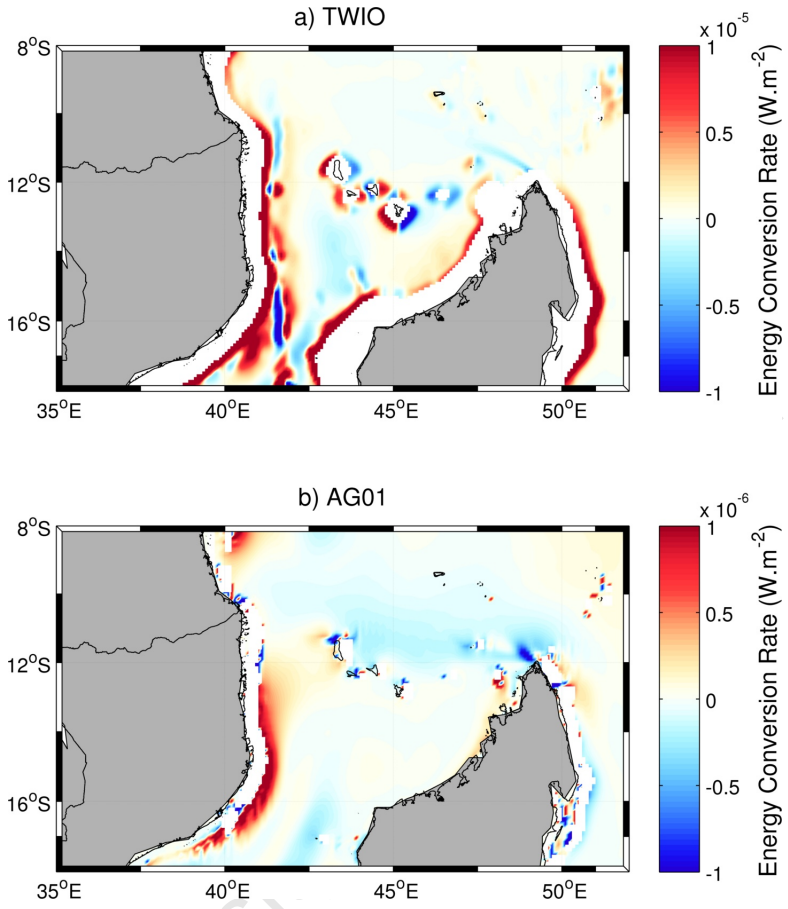

Figure 7.8: *The spatial distribution of the energy transfer term T1 (W·m^{-2}) vertically integrated over the upper 1000m for a) TWIO and b) AG01. Due to the lower conversion rates of AG01 (b) is plotted on a different scale for clarity.*

transfer of mean kinetic energy to eddy kinetic energy as indicated by the positive conversion rates of term T2 observed in the same location, suggests that eddy formation takes place at the northern tip of Madagascar.

In order to determine which energy conversion term plays the most important role in eddy activity at the northern tip of Madagascar the two energy terms were averaged meridionally between 11°-12°S from 45° to 49°E. In both models, the barotropic instability (term T2)

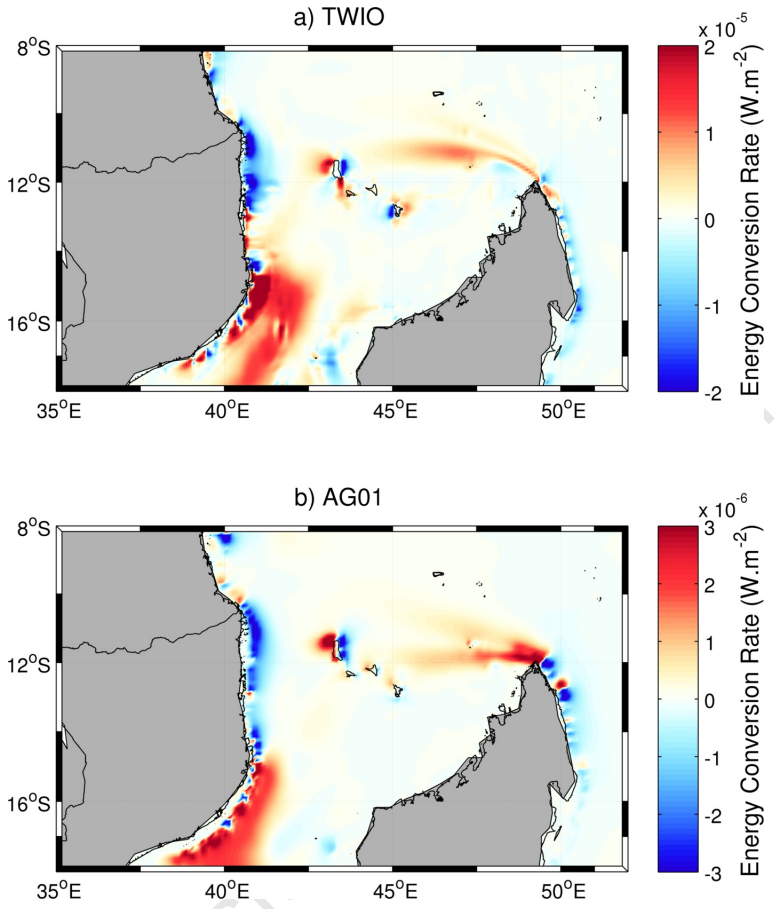

Figure 7.9: *Spatial distribution of the energy transfer term T2 ($W{\cdot}m^{-2}$) vertically integrated over the upper 1000m for a) TWIO and b) AG01. Due to the lower conversion rates of AG01 (b) is plotted on a different scale for clarity.*

is greater than the baroclinic instability (term T1; Figure 7.10), indicating that there is a preponderance of eddy generation at the northern tip of Madagascar due to the barotropic instability associated with the NEMC as it flows past the tip. The formation of eddies at the northern tip of Madagascar due to barotropic instability of the NEMC is consistent with the findings of previous observational (Schott et al., 1988; Quadfasel and Swallow, 1986) and modelling studies (Biastoch and Krauss, 1999; LaCasce and Isachsen, 2007).

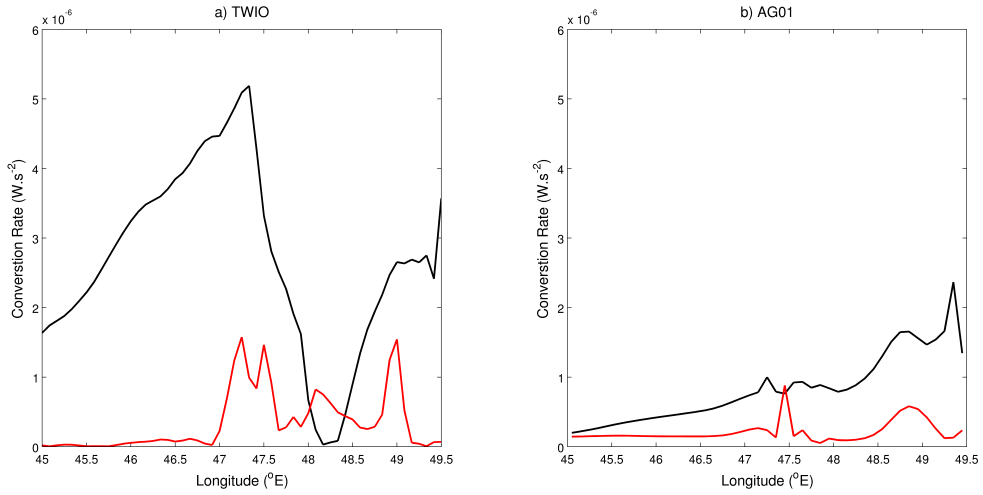

Figure 7.10: *The absolute meridional average of terms T1 (red lines) and T2 (black lines) between 11°-12°S for a) TWIO and b) AG01.*

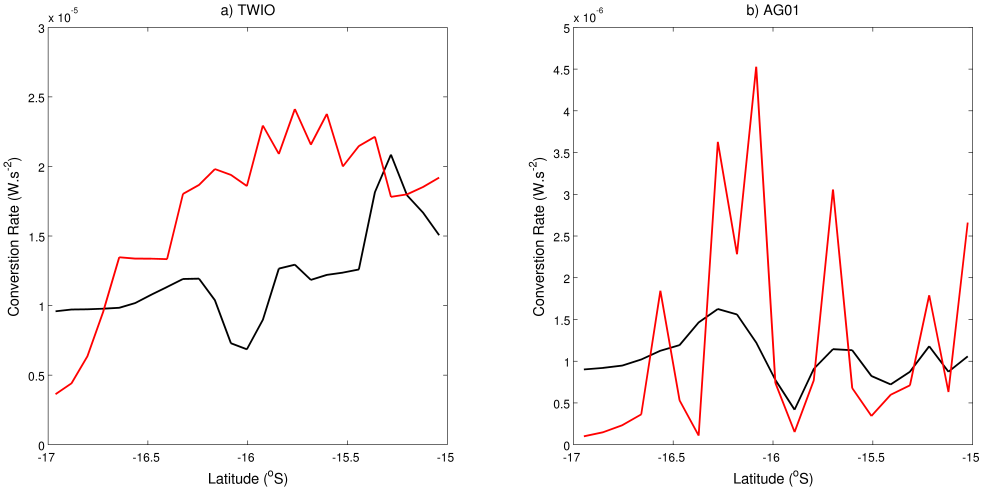

Figure 7.11: *The absolute zonal average of terms T1 (red lines) and T2 (black lines) between 40.2°-42°E for a) TWIO and b) AG01.*

The strongest positive conversion rate for mean potential energy to eddy potential energy in the Comoros Basin occurs along the east coast of Mozambique from ~12°S into the Mozambique Channel (Figure 7.8). Positive conversion rates for term T2, indicative of shear production, are also observed along the western boundary of the Comoros Basin between ~15°S and 18°S. In both models, the shear production and the conversion of mean potential to eddy potential energy in the narrows of the Mozambique Channel coincide with the generation of anti-cyclonic eddies as determined by the eddy tracking scheme (Figures 7.2b and d). Ridderinkhof and de Ruijter (2003) argued that anti-cyclonic eddies in the Mozambique Channel are not generated in the northern part of the channel but rather in the narrowest part of the channel as a result of local instabilities, however the exact nature of the instability was not investigated. Harlander et al. (2009), however, linked the current variability in the narrow of the channel resulting from southward migrating anti-cyclonic eddies to a baroclinic Rossby normal mode. The meridional average of the two energy conversion terms between 40.2°-42°E from 15°S to 17°S suggests that in TWIO the baroclinic instability dominates along most of the Mozambican coast (Figure 7.11a), whereas in AG01 it dominates mainly between 15-16°S and south of 16.5°S (Figure 7.11b).

In TWIO, positive conversion rates for mean potential energy to eddy potential energy are observed along the northwest coast of Madagascar extending into the narrows of the channel (Figure 7.8a) coinciding with a region of cyclonic eddy generation as determined by the eddy tracking scheme (Figures 7.2b and d). The meridional average of the two energy conversion terms between 45.5°-48°E from 13.5°S to 15°S, indicates that in both models, the term representing baroclinic instability greatly exceeds the term for barotropic instability, suggesting that the cyclonic eddies in the Comoros Basin are formed as a result of baroclinic instability (Figure 7.12b).

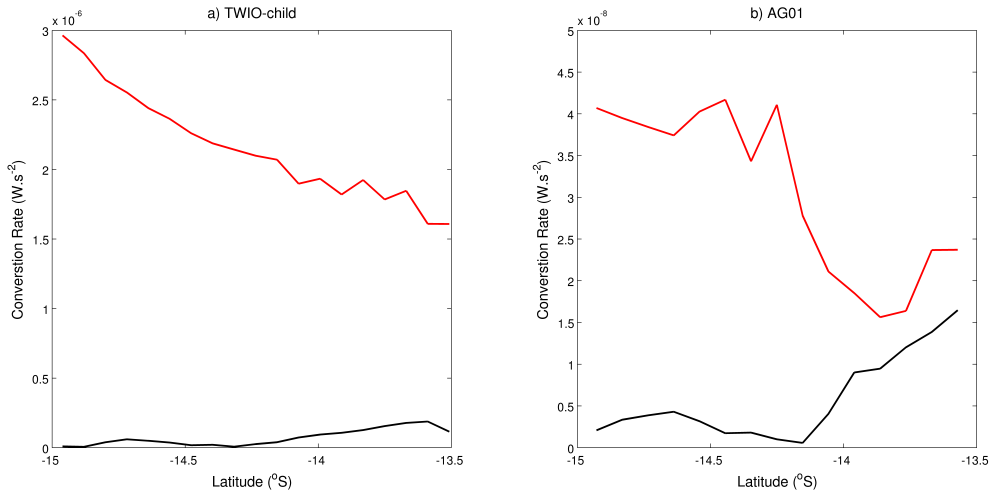

Figure 7.12: *The absolute zonal average of terms T1 (red lines) and T2 (black lines) between 45.5°-48°E for a) TWIO and b) AG01.*

7.3 Anti-cyclones with long and short retention times

In the following section, anti-cyclonic eddies with a long retention time in the Comoros Basin are compared against ones with a short retention time for both TWIO and AG01. Anti-cyclonic eddies with retention times longer than 100 days are considered as long retention eddies whereas eddies with retention times shorter than 80 days are considered as short retention eddies.

A comparison of the two types of eddies are made based on their translation speeds, rotational speeds, area, and eddy scales while residing in the Comoros Basin. Furthermore, vertical structure of the anti-cyclonic eddies with long and short retention times were also analysed at the time of formation, when residing in approximately the centre of the Comoros Basin and upon leaving the basin. The vertical structure between eddies of the same type were found to be similar and for ease only one eddy of each type for each of the models are

presented in section 7.3.2. The tracks of the selected eddies are shown in Figure 7.13.

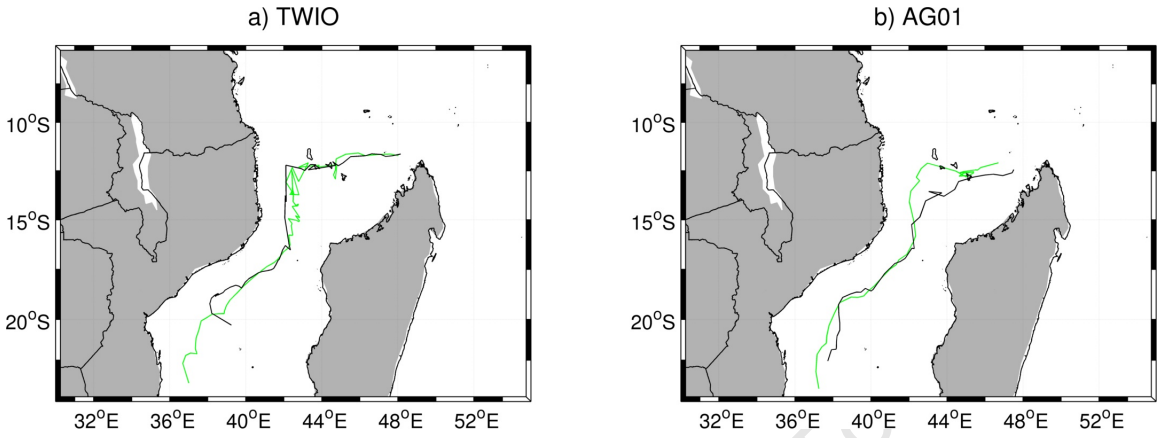

Figure 7.13: *Trajectories of anti-cyclonic eddies with long (green) and short (black) retention times in the Comoros Basin selected from a) TWIO and b) AG01.*

7.3.1 Eddy Properties

The anti-cyclones with long retention spans selected for analysis from AG01 and TWIO had average lifespans of 133 and 190 days, respectively. The long retained eddies selected from TWIO remained in the Comoros Basin for an average of 96 days whereas that selected from AG01 had a mean retention time of 101 days. The short retained eddies selected from the two models, with average lifespans of 127 and 136 days in TWIO and AG01 respectively, remained in the Comoros Basin for an average of 65 days.

On average, the long retention eddies in TWIO have stronger propagation speeds compared to the short retention eddies (Table 7.5). The long retained anti-cyclones also have stronger rotational speeds at the time of formation compared to the short retained anti-cyclones whereas the latter have stronger mean rotational speeds. The long and short retained

anti-cyclones have similar areas and eddy scales at the time of formation; however, the former has a larger area and eddy scale upon leaving the Comoros Basin (Table 7.5).

Table 7.5: *The average initial, final and properties of the ten short and long retained anti-cyclones in the Comoros Basin selected from TWIO.*

	Initial	**Final**	**Mean**
TWIO Short			
Propagation speed ($cm{\cdot}s^{-1}$)	6	11	13
Rotational Speed ($m{\cdot}s^{-1}$)	0.8	1.3	1.7
Area (km^2)	19 736	45 123	56 422
Eddy Scale (km)	78	118	132
TWIO Long			
Propagation speed ($cm{\cdot}s^{-1}$)	13	14	18
Rotational Speed ($m{\cdot}s^{-1}$)	1.5	1.1	1.1
Area (km^2)	19 996	50 489	44 506
Eddy Scale (km)	77	130	124
AG01 Short-Lived			
Propagation speed ($cm{\cdot}s^{-1}$)	11	14	13
Rotational Speed ($m{\cdot}s^{-1}$)	0.3	0.5	0.5
Area (km^2)	16 281	28 604	32 631
Eddy Scale (km)	67	90	107
AG01 Long-Lived			
Propagation speed ($cm{\cdot}s^{-1}$)	16	13	12
Rotational Speed ($m{\cdot}s^{-1}$)	0.3	0.5	0.4
Area (km^2)	13 851	37 641	33 047
Eddy Scale (km)	70	116	112

In AG01, the long and short retained anti-cyclones selected for comparison have similar mean propagation speeds as well as similar mean, initial and exiting propagation and rotational speeds (Table 7.5). The initial and mean area and eddy scale of the long retained anti-cyclones are comparable to that of the short retained anti-cyclones. However, the area and eddy scale of the long retained eddies are larger than that of the short retained anti-cyclones upon leaving the Comoros Basin (Table 7.5).

7.3.2 Eddy vertical structure

The long and short retained eddies selected from TWIO were first identified west of the northern tip of Madagascar (Figure 7.14a and d). At this location, both anti-cyclones were deep reaching but had a weak signal throughout the water column with maximum surface meridional velocities (>0.6m·s^{-1}) confined to the upper 100m (Figure 7.15). At the time of generation the short retained anti-cyclone, with slightly stronger surface velocities, had a much greater volume transport (20Sv) compared to its long retained counterpart (~12.5Sv).

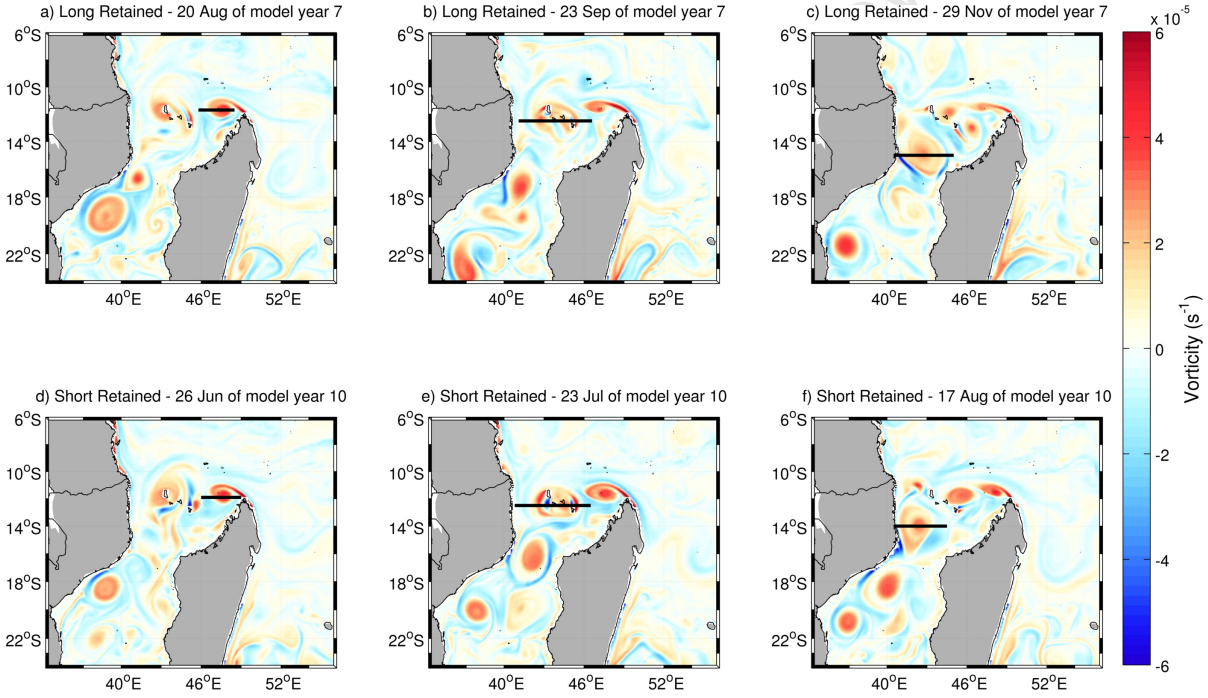

Figure 7.14: *The surface vorticity (s^{-1}) of the long (top panel) and short (bottom panel) retained anti-cyclones selected from TWIO at the time of formation (a, d), when occupying the central Comoros Basin (b,d) and when leaving the basin (c,f). The black lines indicate the location of the transects used to investigate the vertical structure.*

About a month after each of these anti-cyclones were identified, they had propagated westward to the centre of the Comoros Basin surrounding the Comoros Islands (Figure

7.14b). The poleward flow of both anti-cyclones appear to bifurcate around the island of Grand Comoros with stronger (weaker) poleward velocities on the western (eastern) side (Figure 7.15b). Similarly, the equatorward flow appears to split around Mayotte with stronger (weaker) velocities on the eastern (western) side. Both anti-cyclones are still deep reaching with meridional velocities on either side of the islands extending to the bottom of the channel. Even though, the long retained anti-cyclone had intensified obtaining maximum velocities of ~1m·s^{-1}, it is still weaker than the short retained eddy which has a volume transport (~50Sv) five times greater than the long retained anti-cyclone (~10Sv).

The long retained eddy reached the narrows of the Mozambique Channel about three months after it was first identified (Figure 7.14c) whereas the short retained eddy reached the narrows about two months after it was first identified. At ~15°S, the long retained anti-cyclone occupied about half of the channel extending from the east coast of Mozambique to about ~45°E (Figure 7.15c). The short retained anti-cyclone had a slightly reduced horizontal extent, extending only to about 44.5°E. Both anti-cyclones, extending to the bottom, were strongly surface intensified with maximum poleward and equatorward velocities in excess of 1m·s^{-1}. Poleward velocities of 0.1m·s^{-1} associated with the long retained anti-cyclone slope downward to the east due to the presence of an equatorward undercurrent along the continental shelf. This undercurrent displays two cores, one between ~50-320m with velocities of 0.1m·s^{-1} and the other below 500m with velocities between 0.1-0.2m·s^{-1} (Figure 7.15c).

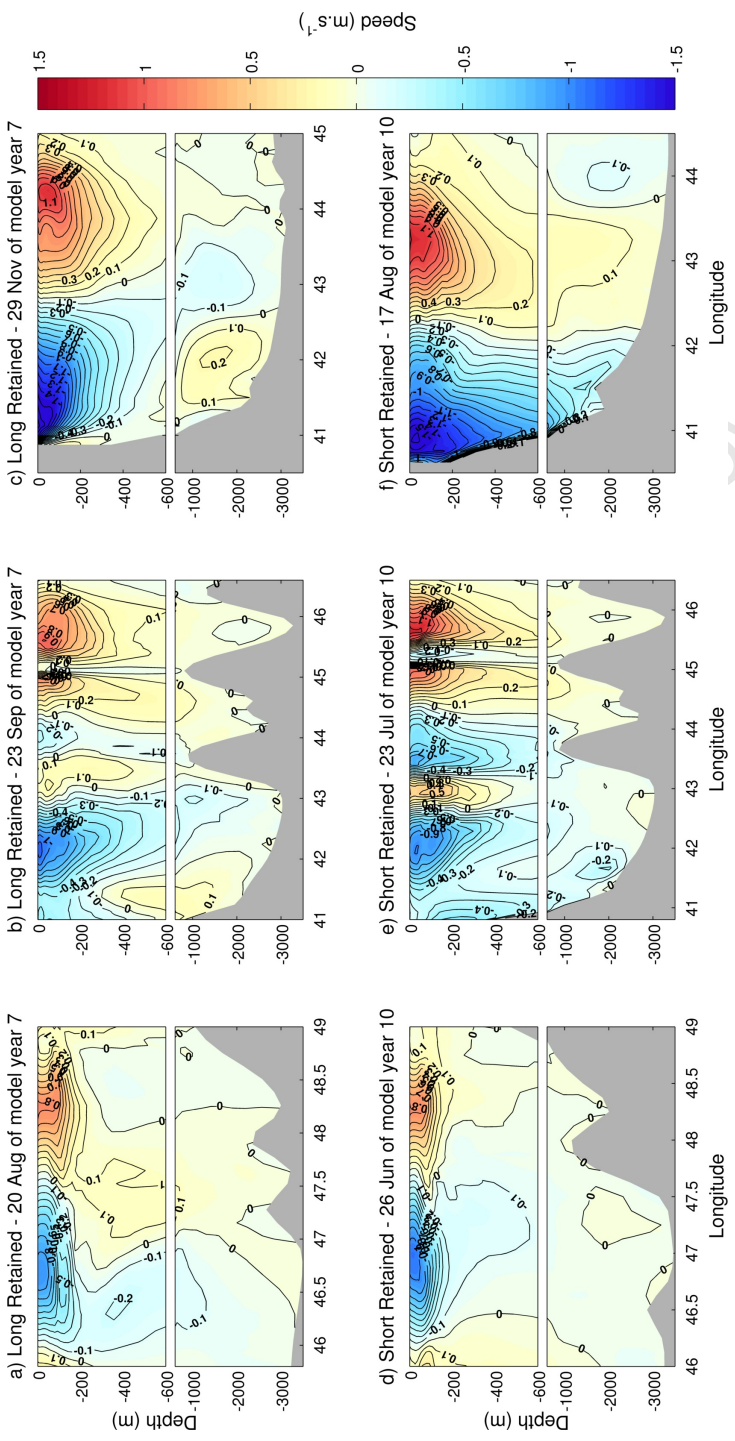

Figure 7.15: *Vertical profiles of the meridional velocity of the long (left panel) and short (right panel) retained anti-cyclones selected from TWIO at the time of formation (a), when occupying the central Comoros Basin (b) and when leaving the basin (c). The contour interval is 0.1m·s^{-1}. Negative (positive) values indicate westward (eastward) flow.*

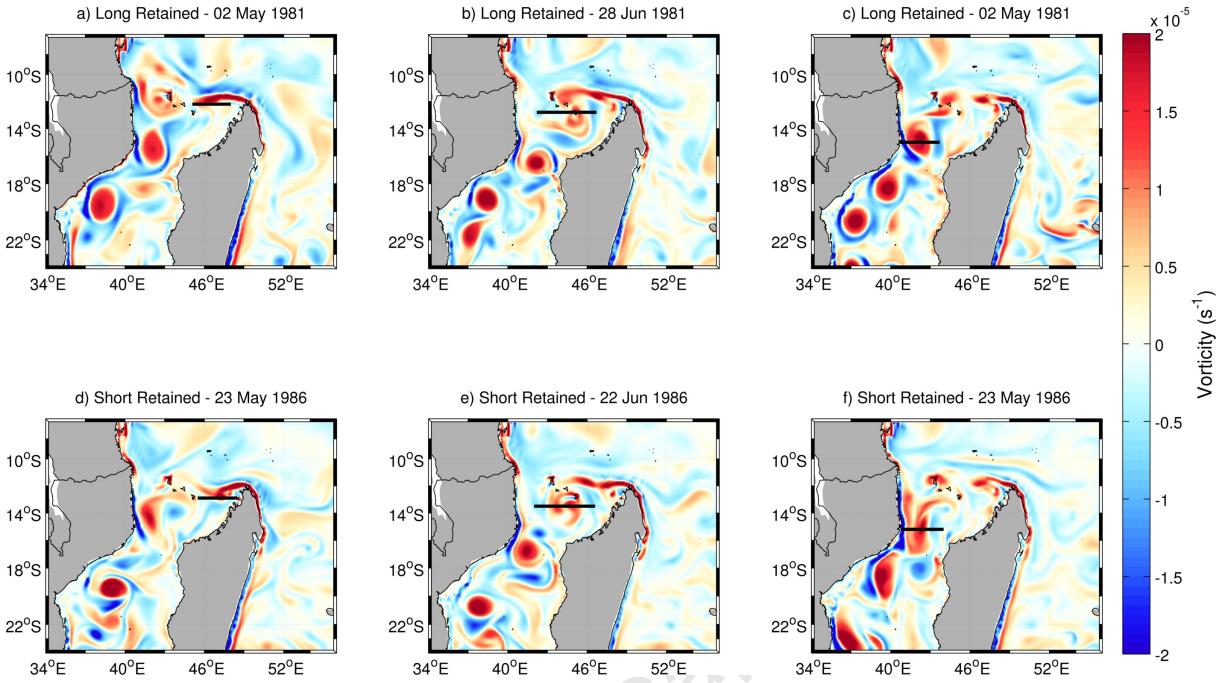

Figure 7.16: *The surface vorticity (s^{-1}) of the long (top panel) and short (bottom panel) retained anti-cyclones selected from AG01 at the time of formation (a, d), when occupying the central Comoros Basin (b,d) and when leaving the basin (c,f). The black lines indicate the location of the transects used to investigate the vertical structure.*

Both the long and short retained anti-cyclonic eddies selected from AG01 were also first identified west of Madagascar (Figure 7.16a and d). At the time of formation, both eddies had a weak signal throughout the water column with maximum meridional velocities <0.2m·s^{-1} (Figures 7.17a). The deep reaching short retained anti-cyclone has a slightly higher volume transport (~6Sv) than the long retained anti-cyclone (~2Sv) which has poleward and equatorward velocities of 0.1m·s^{-1} confined to the upper 400m and 50-100m, respectively (Figure 7.17a).

Both anti-cyclones propagated westwards and after ~1-2 months were located in the cen-

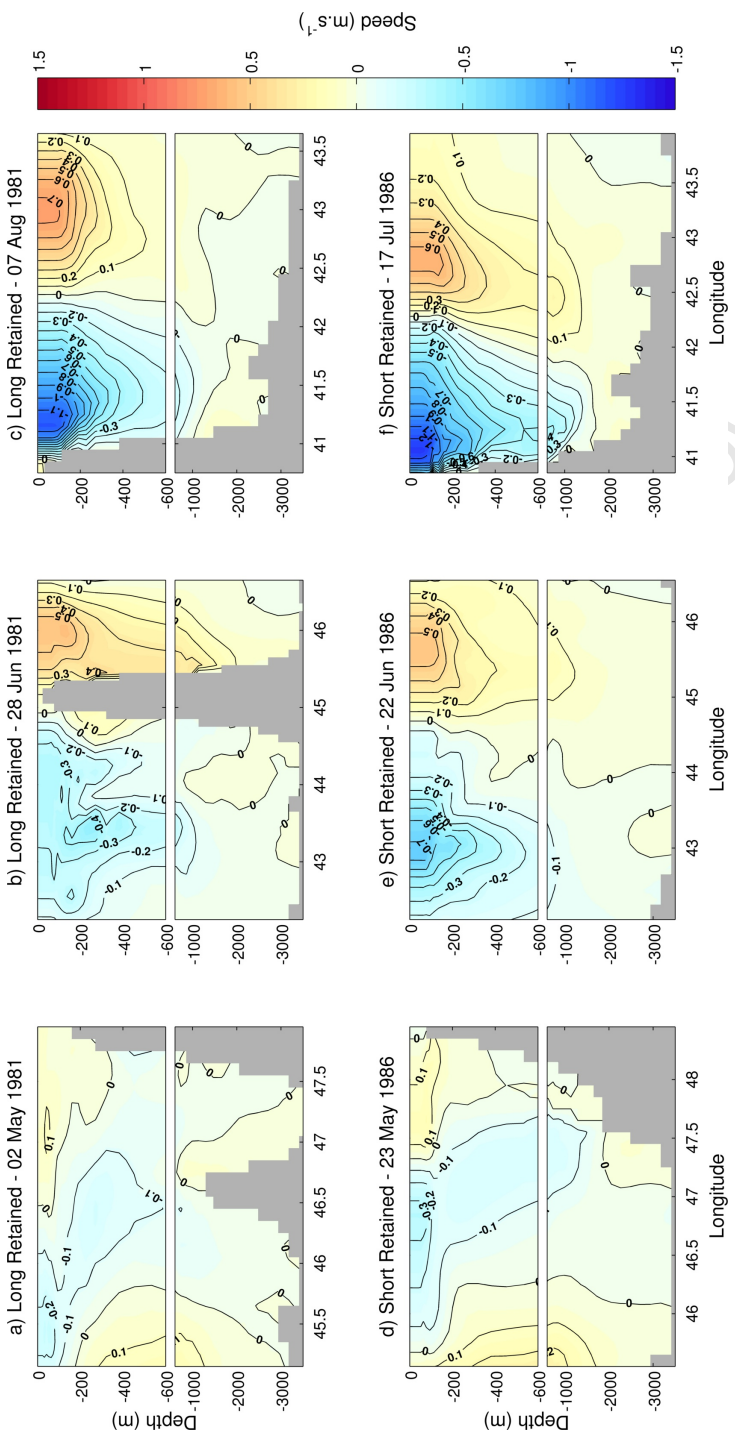

Figure 7.17: *Vertical profiles of the meridional velocity of the long (left panel) and short (right panel) retained anti-cyclones selected from AG01 at the time of formation (a), when occupying the central Comoros Basin (b) and when leaving the basin (c). The contour interval is 0.1m·s^{-1}. Negative (positive) values indicate westward (eastward) flow.*

tre of the Comoros Basin surrounding the Comoros Islands (Figure 7.16b and d). At this location, both the long and short-lived anti-cyclones have increased strength with maximum meridional velocities exceeding $0.3 m \cdot s^{-1}$. These anti-cyclones are still deep reaching with meridional velocities $0.1 m \cdot s^{-1}$ extending below 600m (Figure 7.17b). The short and long retained anti-cyclones, respectively, started leaving the Comoros Basin two and three months after they were first identified (Figure 7.16c and f). Upon leaving the basin, both these deep reaching, anti-cyclones were strongly surface intensified with maximum poleward and equator ward velocities exceeding $1 m \cdot s^{-1}$ and $0.6 m \cdot s^{-1}$, respectively (Figure 7.17c).

7.4 Summary

Despite recent increased research efforts dedicated to the meso-scale activity in the Mozambique Channel, a detailed investigation into the meso-scale activity in the Comoros Basin, a key source region of meso-scale activity in the channel, is still lacking. Therefore, considerable attention is paid in this chapter to the meso-scale activity in the Comoros Basin as resolved by two high-resolution, eddy resolving models. One of the model simulations used is based on a topographic-following (σ) coordinate model, while the other simulation is based on a isopycnal (z) coordinate model. The two models with different vertical coordinate systems are compared in order to determine whether there is a difference in the reproduction of the eddies in the models and also to obtain a more robust description of the eddy activity in the Comoros Basin.

Similar to the altimeter data presented in Chapter 3, anti-cyclonic eddies generated in the Mozambique Channel in both models are preferentially formed west of the northern tip of Madagascar (Cape Amber), close to the narrowest part of the channel and along the west coast

of Madagascar (Figures 7.2a and c). The models also realistically reproduce the generation of cyclonic eddies in the Comoros Basin and throughout the rest of the Mozambique Channel (Figures 7.2b and d). At the northern tip of Madagascar, anti-cyclonic eddies are generated as a result of the barotropic instability associated with the NEMC flowing westward past Cape Amber (Figure 7.9). These anti-cyclonic eddies propagate across the Comoros Basin, following the trajectory of the NEMC and subsequently into the Mozambique Channel. The cyclonic eddies in the Comoros Basin, mainly generated along the northwest coast of Madagascar, appear to form as a result of baroclinic instability (Figure 7.8) and display no coherent trajectory pattern.

The barotropic instability at the northern tip of Madagascar has previously been suggested as a mechanism of anti-cyclonic eddy formation west of Cape Amber (Schott et al., 1988; Quadfasel and Swallow, 1986; Biastoch and Krauss, 1999; LaCasce and Isachsen, 2007). Penven et al. (2006c) demonstrated, using a numerical ocean circulation model, that Madagascar interrupts the integrated wind stress curl over the South Indian Ocean and thus plays a fundamental role in the generation of instabilities favouring anti-cyclonic eddy generation. The mechanism behind the generation of cyclonic eddies in the Comoros Basin, however, has not been explored previously.

Overall, the characteristics of the eddies simulated in the two models in the Comoros Basin are consistent with the satellite derived eddies described in detail in Chapter 3. However, there is a discrepancy between the lifespan of the simulated and satellite derived cyclonic eddies. The simulated cyclonic eddies generated in the Comoros Basin have shorter mean lifespans (<80 days) than their anti-cyclonic counterparts (>80 days) whereas the satellite derived cyclonic eddies tracked in the Comoros Basin have longer mean lifespans (~100 days) than their anti-cyclonic counter parts (~90 days). Furthermore, in the models, the cy-

clonic eddies generated in the Comoros Basin are retained within the basin for most of their lifetime and very few propagate into the Mozambique Channel. Even though, the satellite derived cyclonic eddies also remain in the basin for most of their lifespan, a quarter propagate into the Mozambique Channel (see Chapter 3). Similar to the satellite derived anti-cyclonic eddies, simulated anti-cyclonic eddies generated in the Comoros Basin are retained within the basin for roughly half of their lifespans and the majority remain in the basin for about two months.

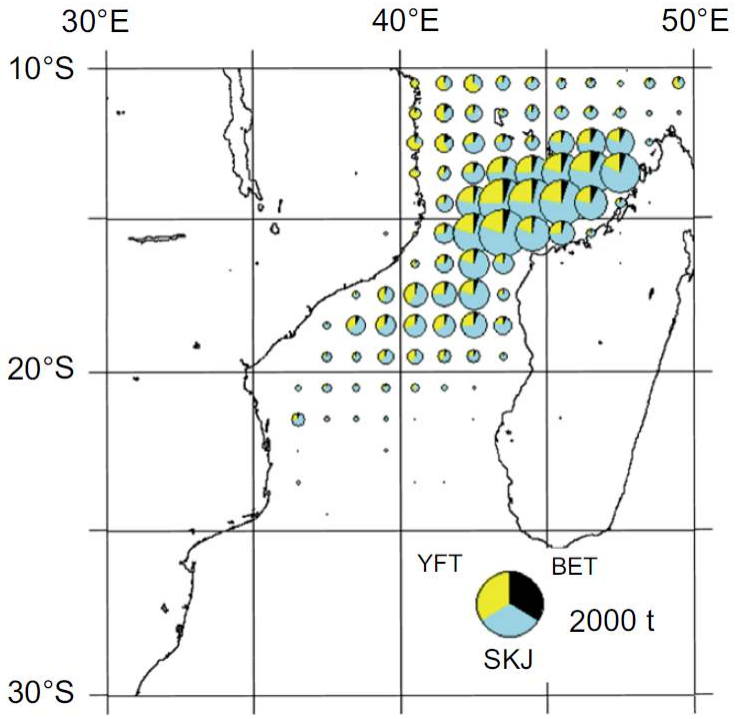

Figure 7.18: *Map of tuna catches by the purse-seine fishery in the Mozambique Channel according to species (YFT: Yellowfin tuna, SKJ: Skipjack tuna and BET: Bigeye tuna) (AfterTew-Kai and Marsac (2010)).*

The major fishing area for tuna by purse-seiners in the Mozambique Channel is located in the Comoros Basin (Figure 7.18; Tew-Kai and Marsac, 2010) and coincides with the primary

generation site of cyclonic eddies in the basin (Figures 7.2b and d). The cyclonic eddy sampled during the Comoros Cruise, showed evidence of upwelling (see Chapter 3). This suggest that the cyclonic eddies along the northwest coast of Madagascar could provide favourable conditions for the aggregation of tuna schools. However, this needs to be confirmed by an in-depth study into the role cyclonic eddies play in attracting the tuna schools which aggregate along the northwest coast of Madagascar.

The anti-cyclones generated in the Comoros Basin have higher mean translation speeds and slower advective time scales while residing in the basin than their cyclonic counter parts. The translation speeds of the anti-cyclones (>6km·day^{-1}), while in the Comoros Basin, are slightly higher than that observed for anti-cyclonic eddies in the Mozambique Channel (4.5km·day^{-1}; de Ruijter et al., 2002). Cyclonic eddies generated in the Comoros Basin, with eddy scales of ~60km and rotational speeds of ~0.4m·s^{-1}, are smaller than their anti-cyclonic counterparts. The majority of cyclonic eddies in the Comoros Basin have eddy scales of 50-100km, whereas the majority of the anti-cyclones have eddy scales exceeding 100km. Based on eddy scale, the anti-cyclonic eddies tracked in both models and the altimeter data in the Comoros Basin, appear to be slightly smaller than the 300km diameter suggested by Harris (1972) for an anti-cyclone in the basin from observations and is also smaller than the 300-350km diameters estimated for anti-cyclonic eddies in the Mozambique Channel (de Ruijter et al., 2002; Schouten et al., 2003).

A comparison of anti-cyclonic eddies with long and short retention times in the Comoros Basin revealed that in the σ-coordinate model (TWIO) the anti-cyclonic eddies with longer retention times tend to have weaker rotational speeds than those with shorter retention times. In the σ-coordinate model, the longer retained anti-cyclonic eddies, while having mean eddy scales and areas similar to those of the shorter retained anti-cyclones, tend to attain larger

sizes by the time they leave the basin. Contrary to the σ-coordinate model, the anti-cyclonic eddies with long and short retention times simulated in the Comoros Basin in the z-coordinate model (AG01) have similar propagation and rotational speeds. However, in the z-coordinate model, longer retained anti-cyclones also tend to attain larger sizes upon leaving the Comoros Basin compared to the shorter retained anti-cyclones.

In both models, the vertical structure of the two types of anti-cyclones were similar indicating that anti-cyclones in the Comoros Basin are deep-reaching and surface intensified with speeds exceeding $10 cm \cdot s^{-1}$. However, in the z-coordinate model, both the long retained and short retained eddies have weaker surface velocities at the time of formation compared to the eddies from the σ-coordinate model (TWIO). The vertical structure previously noted for anti-cyclonic eddies in the Mozambique Channel (de Ruijter et al., 2002; Schouten et al., 2003) are similar to that observed for the anti-cyclones generated in the Comoros Basin indicating that these eddies retain their vertical structure as they propagate into the channel. As the anti-cyclonic eddies travel west across the Comoros Basin they increase in size and surrounds the Comoros Islands when they reach the centre of the basin. At this time, the anti-cyclones have diameters close to 600km and therefore can give the false impression of a large anti-cyclonic vortex.

Chapter 8

Summary and Conclusion

Despite recent increased interest in the circulation of the Mozambique Channel, the current knowledge on the circulation in the Comoros Basin, located in northern part of the channel is limited. The contemporary understanding of the circulation in the Comoros Basin is that it consists of a single large anti-cyclonic cell, the Comoros Gyre. The notion of a single large anti-cyclonic cell is mainly based on temporally and spatially sparse hydrographic data (Harris, 1972; Sætre and da Silva, 1984; Donguy and Piton, 1991). More recent studies, using high-resolution models and satellite data, showed that anti-cyclonic eddies are generated at the northern tip of Madagascar (Backeberg and Reason, 2010; van der Werf et al., 2010). The circulation in the Comoros Basin were not the focus of these studies, per se, therefore the notion of the Comoros Gyre, was not unequivocally confirmed nor denied. Furthermore, these studies did not delve into the characteristics of the anti-cyclonic eddies generated in the basin nor whether cyclonic eddies are present in the basin. Thus, the main objective of this research was to examine the circulation in the Comoros Basin through a combination of observational and satellite derived data as well as two realistic, high-resolution model

simulations. In this chapter, the work presented on the circulation in the Comoros Basin are summarised and some areas for future research are suggested.

8.1 Wind forcing over the Comoros Basin

The wind forcing over the Comoros Basin displays a strong annual cycle which can be attributed to the changing monsoonal winds (Chapter 4). During the Northeast monsoon (DJFM), the northwesterlies prevail over the Comoros Basin and change to southeasterlies at the onset of the Southwest monsoon (Figure 4.11). Overall, the southeasterlies are associated with anti-cyclonic wind stress curl over the Comoros Basin whereas cyclonic wind stress curl is associated with the northwesterlies (Figure 4.12).

In addition to the large scale wind pattern, several meso-scale wind features are also present in the Comoros Basin. During the southwest monsoon a wind jet of strong southeasterlies develop off the northern tip of Madagascar and a wind shadow forms over the Comoros Basin perpendicular to the northwest coast of Madagascar (Figure 4.11). The combination of the wind jet and wind shadow is a result of the interaction of the trade winds, prevailing over the Southwest Indian Ocean during the Southwest monsoon with the landmass of Madagascar which acts as a barrier to the trade winds. Associated with the wind jet and wind shadow is a wind stress curl dipole (Figure 4.12) which in-turn results in an Ekman pumping dipole (Figure 4.13). The positive wind stress curl associated with the wind jet results in upwelling whereas the negative wind stress curl associated with the wind shadow results in downwelling perpendicular to the northwest coast of Madagascar.

Additionally, a wind stress curl and upwelling dipole is associated with the Comoros Islands (Figure 4.14). This wind stress curl dipole displays a seasonal reversal in response

to the changing monsoon winds. Anti-cyclonic (cyclonic) wind stress curl driving upwelling (downwelling) occurs to the north (south) of the islands under the influence of the Southwest monsoon whereas the pattern is reversed during the Northeast monsoon (Figure 4.14).

8.2 Circulation in the Comoros Basin

8.2.1 Hydrography

The upper ocean (0-600m) water masses in the Comoros Basin, consisting of Tropical Surface Water, Subtropical Surface Water, Arabian Sea High Salinity Water, Equatorial Indian Ocean Water and South Indian Central Water (Figure 3.4), all enter the basin from the east (Chapter 3). These water masses are transported further into the Comoros Basin and the Mozambique Channel along the coast of Mozambique. The water masses at intermediate levels (600-1500m) consists of Antarctic Intermediate Water and Red Sea Intermediate Water (Figure 3.4). In the Comoros Basin, the RSIW spreads southwards primarily between the Comoros Islands and the African continent (Figure 3.6). This is congruent with previous studies which showed that this water mass enters the Mozambique Channel from the north along the western boundary (Beal et al., 2000). The freshest AAIW was found north of Madagascar in the recently collected hydrographic data (Chapter 3, Figure 3.6). This confirms that this water mass enters the Comoros Basin from the east past the tip of Madagascar as proposed by di Marco et al. (2002) but does not eliminate the northward spreading of this water mass within the Mozambique Undercurrent as suggested by de Ruijter et al. (2002). North Atlantic Deep Water, Lower Circumpolar Deep Water and Upper Circumpolar constitute the deep and bottom water masses of the Comoros Basin (Figure 3.4). NADW is generally assumed to be

absent from the Comoros Basin due to the topographic constrain imposed by the Davie Ridge on the northward flow of this water mass. However, the presence of NADW in the southern part of the Comoros Basin indicates that this water mass is capable of spreading northward over the ridge into the Comoros Basin as proposed by van Aken et al. (2004).

8.2.2 Circulation

The main current, evident in the altimeter, hydrographic, and model data, transporting upper ocean water masses into the Comoros Basin is the westward flowing NEMC (Chapter 3). Originating along the east coast of Madagascar, the NEMC intensifies as it flows past the northern tip of Madagascar obtaining maximum velocities in excess of $0.6 m \cdot s^{-1}$ (Figures 3.10 and 6.13). At the northern tip of Madagascar, the NEMC displays a distinct seasonal cycle, strengthening during the Southwest monsoon (Figure 3.11a). This intensification of the NEMC occurs in response to a wind jet of strong southeasterlies which develops off the northern tip of Madagascar during the Southwest monsoon (Figure 4.11).

A strong poleward current, with mean velocities of $0.4 m \cdot s^{-1}$, flows along the northern coast of Mozambique and into the Mozambique Channel (Figures 3.10 and 6.13). This current is weakest during the Southwest monsoon and displays increased intensity during the Northeast monsoon. The weakening of the poleward current coincides with increased wind speeds along the Mozambique Coast, whereas the increased intensity coincides with decreased wind speeds (Figure 3.11b). During the Northeast monsoon, northwesterlies dominate over the Comoros Basin (Figure 4.11) which act to strengthen the poleward flow along the east coast of Mozambique. Conversely, southwesterlies dominate over the basin during the Southwest monsoon (Figure 4.11) which exert an opposing force on the poleward current,

thus weakening it. In addition to the aforementioned currents, the circulation in the Comoros Basin comprise of anti-cyclonic as well as cyclonic eddies.

8.2.2.1 Meso-scale eddies in the Comoros Basin

In the altimeter data and the high resolution models, anti-cyclonic eddies in the Comoros Basin are generated primarily west of the northern tip of Madagascar (Figures 3.15 and 7.2). The models suggest that the generation of the anti-cyclonic eddies west of the tip of Madagascar is due to barotropic instabilities associated with the NEMC (Chapter 7, Figure 7.9). Both the satellite derived as well as simulated anti-cyclonic eddies have a mean lifespan exceeding 80 days and remain in the basin for roughly half this time (~50 days) before propagating into the Mozambique Channel (Table 7.2). The majority of the anti-cyclonic eddies propagate due west towards the coast of Mozambique and subsequently southwards along the coast into the Mozambique Channel (Figures 3.15 and 7.2). Even though the maximum residence time of anti-cyclonic eddies in the Comoros Basin is four to six months for the satellite derived and simulated eddies, the majority have retention times in the range 30-50 days (Figures 3.16 and 7.4).

Simulated and satellite derived cyclonic eddies in the Comoros Basin are primarily generated along the northwest coast of Madagascar (Figures 3.15 and 7.2) and the models suggest that the mechanism of formation is baroclinic instabilities (Chapter 7, Figure 7.8). This generation site of cyclonic eddies coincides with the highest concentration of tuna catches by the purse-seine fishery operating in the Mozambique Channel (Tew-Kai and Marsac, 2010). The hydrographic data collected during a recent cruise in the Comoros Basin indicated that upwelling occurs within the cyclonic eddies formed in the Comoros Basin (Chapter 3, Figure 3.3). The upwelling associated with the cyclonic eddies might play an important role in the

aggregation of tuna schools which are exploited by the purse-seine fishery, however to what extent is still unresolved.

The mean lifespans of the satellite derived cyclonic eddies generated in the Comoros Basin are longer (~100 days) than that of their anti-cyclonic counter parts whereas the simulated cyclonic eddies generated in the Comoros Basin have shorter mean lifespans (<80 days) than their anti-cyclonic counterparts (Table 7.2). In addition, both the satellite derived and simulated cyclonic eddies remain in the Comoros Basin for most of their lifetime. However, very few of the simulated cyclonic eddies propagate into the Mozambique Channel (Figure 7.2) whereas a quarter of the satellite derived eddies do (Chapter 3, Figure 3.15). Half of the simulated and satellite derived cyclonic eddies generated in the Comoros Basin have residence times in the basin of between 30-50 days while a quarter have retention times exceeding 100 days (Figures 3.16 and 7.4).

Anti-cyclonic eddies formed in the Comoros Basin have a mean translation speed of 6-8km/day and with a mean effective radius of 80-100km, have advective timescales of 30-40 days (Table 7.3). Similar to anti-cyclonic eddies elsewhere in the Mozambique Channel (de Ruijter et al., 2002; Schouten et al., 2003), those generated in the Comoros Basin in the high resolution models are deep-reaching and surface intensified with speeds exceeding 10cm·s^{-1}. The translation speeds of cyclonic eddies in the Comoros Basin are 2.5-3.5km·day^{-1} resulting in advective time scales of about 100 days for an average effective radius of ~60km (Table 7.3). The majority of the simulated and satellite derived cyclonic eddies generated in the Comoros Basin have effective radii in the range 50-100km (Figures 3.18 and 7.6). Similarly, the majority of the satellite derived anti-cyclonic eddies have effective radii in this range (Figure 3.18), however half of the simulated anti-cyclonic eddies have effective radii exceeding 100km (Figure 7.6). The size of the eddies in the Comoros Basin is

likely influenced by the steep bathymetry of the islands in the basin as well as the presence of the Davie Ridge. The larger size attained by the simulated anti-cyclonic eddies could possible be attributed to the bathymetry of the Comoros Islands and the Davie Ridge which is not accurately represented in the models; however, further studies are needed to confirm this.

In conclusion, the circulation in the Comoros Basin consists of the strong westward flowing NEMC, a strong poleward flow along the western boundary and meso-scale eddies of both polarities. None of the model or observational data sets analysed showed evidence of a Comoros Gyre; however the anti-cyclonic eddies generated in the Comoros Basin can obtain diameters of ~600km when located in the centre of the basin and can thus give the false impression of an anti-cyclonic gyre. The primary generation site of anti-cyclonic eddies in the Comoros Basin is west of Cape Amber where they are formed as a result of barotropic instability associated with the NEMC. Cyclonic eddies, on the other hand, are generated mainly along the northwest coast of Madagascar due to strong baroclinic instability. The anti-cyclonic eddies generated in the Comoros Basin remain in the basin for roughly half of their lifetime while the majority of the cyclonic eddies remain there indefinitely.

8.3 Suggestions for future work

Many aspects of the dynamics and processes in the Comoros Basin still need to be clarified. The westward propagation of anti-cyclonic eddies formed in the Comoros Basin mainly occurs to the north of the Comoros Island while the southward propagation occurs along the western boundary. This behaviour leads to the question: What role does the topography of the Comoros Basin play in these propagation routes? Idealised model simulations in which the topography of the basin are altered would elucidate how the topography influences the

trajectories of the eddies generated in the Comoros Basin.

It has been shown that the Mozambique Channel eddies play an important role in the dynamics of the Agulhas Current (Schouten et al., 2002a). The majority of the anti-cyclonic eddies generated in the Comoros Basin propagate into the Mozambique Channel and presumably interact with the Agulhas Current. Further studies should investigate the impact of the eddies generated in the Comoros Basin on the dynamics in the Mozambique Channel and subsequently on the Agulhas Current.

Meso-scale eddies have a significant impact on the production, distribution and densities of marine life as they mix, advect and redistribute water masses (Lévy et al., 2001). Meso-scale eddies are also associated with mechanisms of enrichment (e.g. upwelling), concentration (e.g. convergence) and retention of nutrients as well as marine organisms (Bakun, 2006). The biological response to meso-scale eddies are well documented (e.g. Falkowski et al., 1991 and Seki et al., 2002). Similar studies in the Mozambique Channel, showed that upwelling in the core of cyclonic eddies resulted in enhanced phytoplankton production (Tew-Kai and Marsac, 2009) which in turn influence the distribution of top marine predators such as Great Frigatebirds which frequented the frontal zones between anti-cyclonic and cyclonic eddies during foraging while avoiding the centres. The primary generation site of cyclonic eddies in the Comoros Basin coincide with a purse-seine fishery hot spot. Furthermore, the hydrographic data collected during the Comoros Cruise, shows upwelling associated with a cyclonic eddy. Is the congregation of the tuna schools (exploited by the purse-seine fishery) at the generation site of cyclonic eddies in response to the upwelling or is it coincidental? One way of investigating this is to couple the ROMS simulation with a bio-geochemical model to determine what the response of the primary production is to the upwelling associated with the cyclonic eddies and whether the resulting primary production is favourable for

the aggregation of tuna.

Furthermore, meso-scale eddies enhance the transport of biotic and abiotic material trapped within their cores as they act as barriers to exchanges between their cores and the external background turbulence (Elhmaïdi et al., 1993; Provenzale, 1999). The periphery of eddies on the other hand, where strain prevails over vorticity, aids in the redistribution of tracer particles. What role do the anti-cyclonic and cyclonic eddies play in the retention of biotic and abiotic material within the Comoros Basin? Are anti-cyclonic eddies with short or long retention times more effective in transporting material out of the Comoros Basin? As a starting point, this can be achieved by releasing and tracking particles within the model simulations.

This thesis has been the first dedicated study of the Comoros Basin using remote sensing, in-situ observations and modelling. The work has shown that contrary to the Comoros Gyre, which is in fact an artefact of temporal averaging and of snap-shot studies, the circulation in the basin consists of anti-cyclonic and cyclonic eddies which are generated at a frequency of about 12 and 8 times per year, respectively. The results presented in this thesis will help in addressing the questions posed above which mainly deal with the implications of the circulation in the Basin on the bio-geochemistry and marine ecosystem of the region.

Bibliography

Allan, R. J.; J. A. Lindesay; and C. J. C. Reason (1995): Multidecadal Variability in the Climate System over the Indian Ocean Region during the Austral Summer. *Journal of Climate*, 8(7):1853–1873.

Allan, R. J.; C. J. C. Reason; J. A. Lindesay; and T. J. Ansell (2003): Protracted ENSO episodes and their impacts in the Indian Ocean region. *Deep Sea Research Part II: Topical Studies in Oceanography*, 50(12-13):2331–2347.

Annamalai, H. and R. Murtugudde (2004): Role of the Indian Ocean in regional climate variability. *Geophysical monograph*, 147:213–246.

Annamalai, H.; J. M. Slingo; K. R. Sperber; and K. Hodges (1999): The Mean Evolution and Variability of the Asian Summer Monsoon: Comparison of ECMWF and NCEP-NCAR Reanalyses. *Monthly Weather Review*, 127(6):1157–1186.

Arakawa, A. and V. R. Lamb (1977): Computational design of the basic dynamical processes of the UCLA general circulation model. *Methods in Computational Physics*, 17:173–265.

Arístegui, J.; P. Sangrá; S. Hernández-León; M. Cantón; A. Hernández-Guerra; and J. L.

Kerling (1994): Island-induced eddies in the Canary islands. *Deep Sea Research Part I: Oceanographic Research Papers*, 41(10):1509–1525.

Ashok, K.; Z. Guan; and T. Yamagata (2001): Impact of the Indian Ocean dipole on the relationship between the Indian monsoon rainfall and ENSO. *Geophysical Research Letters*, 28(23):4499–4502.

Ashok, K.; Z. Guan; and T. Yamagata (2003): Influence of the Indian Ocean Dipole on the Australian winter rainfall. *Geophysical Research Letters*, 30(15):1821.

Backeberg, B. C.; J. A. Johannessen; L. Bertino; and C. J. Reason (2008): The greater Agulhas Current system: An integrated study of its mesoscale variability. *Journal of Operational Oceanography*, 2008(1):29–44.

Backeberg, B. C. and C. J. C. Reason (2010): A connection between the South Equatorial Current north of Madagascar and Mozambique Channel Eddies. *Geophysical Research Letters*, 37(4):L04604.

Bakun, A. (2006): Fronts and eddies as key structures in the habitat of marine fish larvae: opportunity, adaptive response and competitive advantage. *Scientia Marina*, 70(S2):105–122.

Baquero-Bernal, A.; M. Latif; and S. Legutke (2002): On Dipolelike Variability of Sea Surface Temperature in the Tropical Indian Ocean. *Journal of Climate*, 15(11):1358–1368.

Barton, E. (2001): *Island wakes*, Academic Press, New York, vol. 3 of *Encyclopedia of ocean sciences.*, pp. 1397–1403.

Baumgartner, A. and E. Reichel (1975): *The World Water Balance: Mean Annual Global, Continental and Maritime Precipitation, Evaporation and Runoff*. Elsevier, New York.

Beal, L. M. and H. L. Bryden (1997): Observations of an Agulhas undercurrent. *Deep Sea Research Part I: Oceanographic Research Papers*, 44(9-10):1715–1724.

Beal, L. M. and H. L. Bryden (1999): The velocity and vorticity structure of the Agulhas Current at 32°S. *Journal of Geophysical Research*, 104:5151–5176.

Beal, L. M.; T. Chereskin; Y. D. Lenn; and S. Elipot (2006): The sources and mixing characteristics of the Agulhas Current. *Journal of Physical Oceanography*, 36(11):2060–2074.

Beal, L. M.; W. P. M. de Ruijter; A. Biastoch; and R. Zahn (2011): On the role of the Agulhas system in ocean circulation and climate. *Nature*, 472(7344):429–436.

Beal, L. M.; A. Ffield; and A. L. Gordon (2000): Spreading of Red Sea overflow waters in the Indian Ocean. *Journal of Geophysical Research: Oceansans*, 105:8549–8564.

Beckmann, A.; C. W. Böning; B. Brügge; and D. Stammer (1994): On the generation and role of eddy variability in the central North Atlantic Ocean. *Journal of Geophysical Research*, 99(C10):20381–20391.

Behera, S. K.; J. J. Luo; S. Masson; T. Yamagata; P. Delecluse; S. Gualdi; and A. Navarra (2003): Impact of the Indian Ocean Dipole on the East African short rains: A CGCM study. *CLIVAR Exchanges*, 27(2/3):43–45.

Behera, S. K.; P. S. Salvekar; and T. Yamagata (2000): Simulation of interannual SST variability in the Tropical Indian Ocean. *Journal of Climate*, 13(19):3487–3500.

Benny, P. N. (2002): Variability of western Indian Ocean currents. *Western Indian Ocean Journal of Marine Science*, 1(1):81–90.

Biastoch, A.; C. W. Böning; and J. R. E. Lutjeharms (2008a): Agulhas leakage dynamics affects decadal variability in Atlantic overturning circulation. *Nature*, 456(7221):489–492.

Biastoch, A.; C. W. Böning; M. Scheinert; and J.R.E. Lutjeharms (2009a): *The Agulhas System as a Key Region of the Global Oceanic Circulation*, Springer, Berlin, pp. 459–469. High Performance Computing in Science and Engineering '08.

Biastoch, A.; C. W. Böning; F. U. Schwarzkopf; and J. R. E. Lutjeharms (2009b): Increase in Agulhas leakage due to poleward shift of Southern Hemisphere westerlies. *Nature*, 462(7272):495–498.

Biastoch, A. and W. Krauss (1999): The role of mesoscale eddies in the source regions of the Agulhas Current. *Journal of Physical Oceanography*, 29(9):2303–2317.

Biastoch, A.; J. R. E. Lutjeharms; C. W. Böning; and M. Scheinert (2008b): Mesoscale perturbations control inter-ocean exchange south of Africa. *Geophysical Research Letters*, 35(20):L20602.

Biastoch, A.; C. J. C. Reason; J. R. E. Lutjeharms; and O. Boebel (1999): The importance of flow in the Mozambique Channel to seasonality in the greater Agulhas Current system. *Geophysical Research Letters*, 26(21):3321–3324.

Black, E.; J. Slingo; and K. R. Sperber (2003): An Observational Study of the Relationship between Excessively Strong Short Rains in Coastal East Africa and Indian Ocean SST. *Monthly Weather Review*, 131(1):74–94.

Blackadar, A. K. (1962): The vertical distribution of wind and turbulent exchange in a neutral atmosphere. *Journal of Geophysical Research*, 67(8):3095–3102.

Blamey, R. C. and C. J. C. Reason (2012): Mesoscale Convective complexes over southern Africa. *Journal of Climate*, 25(2):753–766.

Blayo, E. and L. Debreu (1999): Adaptive mesh refinement for finite-difference ocean models: first experiments. *Journal of Physical Oceanography*, 29(6):1239–1250.

Boebel, O.; T. Rossby; J. Lutjeharms; W. Zenk; and C. Barron (2003): Path and variability of the Agulhas Return Current. *Deep Sea Research Part II: Topical Studies in Oceanography*, 50(1):35–56.

Böning, C. W. and R. G. Budich (1992): Eddy dynamics in a primitive equation model: Sensitivity to horizontal resolution and friction. *Journal of Physical Oceanography*, 22(4):361–381.

Bower, A. S.; H. D. Hunt; and J. F. Price (2000): Character and dynamics of the Red Sea and Persian Gulf outflows. *Journal of Geophysical Research*, 105(C3):6387–6414.

Brachet, S.; P. Y. Le Traon; and C. Le Provost (2004): Mesoscale variability from a high-resolution model and from altimeter data in the North Atlantic Ocean. *Journal of Geophysical Research*, 109(C12):C12025.

Bryden, H. L.; L. M. Beal; and L. M. Duncan (2005): Structure and transport of the Agulhas Current and its temporal variability. *Journal of Oceanography*, 61(3):479–492.

Cadet, D. (1979): Meteorology of the Indian summer monsoon. *Nature*, 279:761–767.

Callahan, J. E. (1972): The structure and circulation of deep water in the Antarctic. *Deep-Sea Research*, 19(8):563–575.

Casey, K. S. and P. Cornillon (1999): A comparison of satellite and in situ-based sea surface temperature climatologies. *Journal of Climate*, 12(6):1848–1863.

Chambers, D. P.; B. D. Tapley; and R. H. Stewart (1999): Anomalous warming in the Indian Ocean coincident with El Niño. *Journal of Geophysical Research*, 104(C2):3035–3047.

Chang, P.; T. Yamagata; P. Schopf; S. K. Behera; J. Carton; W. S. Kessler; G. Meyers; T. Qu; F. Schott; S. Shetye; and S. P Xie (2006): Climate Fluctuations of Tropical Coupled Systems–The Role of Ocean Dynamics. *Journal of Climate*, 19(20):5122–5174.

Chapman, P.; S. F. D. Di Marco; R. E. Davis; and A. C. Coward (2003): Flow at intermediate depths around Madagascar based on ALACE float trajectories. *Deep-Sea Research.Part 2: Topical Studies in Oceanography*, 50(12-13):1957–1986.

Chavanne, C.; P. Flament; R. Lumpkin; B. Dousset; and A. Bentamy (2002): Scatterometer observations of wind variations induced by oceanic islands: Implications for wind-driven ocean circulation. *Canadian Journal of Remote Sensing*, 28(3):466–474.

Chelton, D. B. and M. H. Freilich (2005): Scatterometer-Based Assessment of 10-m Wind Analyses from the Operational ECMWF and NCEP Numerical Weather Prediction Models. *Monthly Weather Review*, 133(2):409–429.

Chelton, D. B.; M. G. Schlax; M. H. Freilich; and R. F. Milliff (2004): Satellite measurements reveal persistent small-scale features in ocean winds. *Science*, 303(5660):978–983.

Chelton, D. B.; M. G. Schlax; and R. M. Samelson (2011): Global observations of nonlinear mesoscale eddies. *Progress in Oceanography*, 91(2):167–216.

Chen, D. and M. A. Cane (2008): El Niño prediction and predictability. *Journal of Computational Physics*, 227(7):3625–3640.

Clark, C. O.; P. J. Webster; and J. E. Cole (2003): Interdecadal Variability of the Relationship between the Indian Ocean Zonal Mode and East African Coastal Rainfall Anomalies. *Journal of Climate*, 16(3):548–554.

Clarke, A. J. and X. Liu (1993): Observations and dynamics of semiannual and annual sea levels near the eastern equatorial Indian Ocean boundary. *Journal of Physical Oceanography*, 23(2):386–399.

Clemens, S.; W. Prell; D. Murray; G. Shimmield; and G. Weedon (1991): Forcing mechanisms of the Indian Ocean monsoon. *Nature*, 353(6346):720–725.

Clift, P. D. and R. A. Plumb (2008): *The Asian Monsoon: Causes, History & Effects*. No. 3. Universtiy Press, Cambridge.

Clowes, A. J. and G. E. R. Deacon (1935): The deep-water circulation of the Indian Ocean. *Nature*, 136(3450):936–938.

Conkright, M. E.; R. A. Locarnini; H. E. Garcia; T. D. O'Brien; T. P. Boyer; C. Stephens; and J. I. Antonov (2002): World Ocean Atlas 2001: objective analyses, data statistics and figures CD-ROM documentation. *National Oceanographic Data Center Technical Report*, (17).

Cushman-Roisin, B. and J.-M. Beckers (2009): *Introduction to geophysical fluid dynamics: physical and numerical aspects*. Academic Press, New Hahmpshire.

da Silva, A. M.; C. C. Young; and S. Levitus (1994): Atlas of Surface Marine Data 1994, vol. 1, Algorithms and Procedures,. *NOAA Atlas NESDIS 6*, pp. 1–74.

Daubechies, I. (1992): *Ten Lectures on Wavelets*. Society for Industrial and Applied Mathematics, Philidelphia, Pa.

de Ruijter, W. P. M.; A. Biastoch; S. S. Drijfhout; J. R. E. Lutjeharms; R. P. Matano; T. Pichevin; P. J. van Leeuwen; and W. Weijer (1999a): Indian-Atlantic interocean exchange: dynamics, estimation and impact. *Journal of Geophysical Research*, 104:20885–20910.

de Ruijter, W. P. M.; H. Ridderinkhof; J. R. E. Lutjeharms; M. W. Schouten; and C. Veth (2002): Observations of the flow in the Mozambique Channel. *Geophysical Research Letters*, 29(10):140–140.

de Ruijter, W. P. M.; H. Ridderinkhof; and M. W. Schouten (2005): Variability of the southwest Indian Ocean. *Philosophical Transactions of the Royal Society A: Mathematical, Physical and Engineering Sciences*, 363(1826):63–76.

de Ruijter, W. P. M.; H. M. van Aken; E. J. Beier; J. R. E. Lutjeharms; R. P. Matano; and M. W. Schouten (2004): Eddies and dipoles around South Madagascar: formation, pathways and large-scale impact. *Deep Sea Research Part I: Oceanographic Research Papers*, 51(3):383–400.

de Ruijter, W. P. M.; P. J. van Leeuwen; and J. R. E. Lutjeharms (1999b): Generation and evolution of Natal pulses: solitary meanders in the Agulhas Current. *Journal of Physical Oceanography*, 29(12):3043–3055.

Debreu, L.; C. Vouland; and E. Blayo (1 2008): AGRIF: Adaptive grid refinement in Fortran. *Computers & Geosciences*, 34(1):8–13.

Dewar, W. K. and J. M. Bane (1985): Subsurface energetics of the Gulf Stream near the CB. *Journal of Physical Oceanography*, 15:1771–1789.

di Marco, S. F. D.; P. Chapman; and W. D. Nowlin Jr (2000): Satellite observations of upwelling on the continental shelf south of Madagascar. *Geophysical Research Letters*, 27(24):3965–3968.

di Marco, S. F. D.; P. Chapman; W. D. Nowlin; P. Hacker; K. Donohue; M. Luther; G. C. Johnson; and J. Toole (2002): Volume transport and property distributions of the Mozambique Channel. *Deep Sea Research Part II: Topical Studies in Oceanography*, 49(7-8):1481–1511.

Dickey, T.; D. Frye; J. McNeil; D. Manov; N. Nelson; D. Sigurdson; H. Jannasch; D. Siegel; T. Michaels; and R. Johnson (1998): Upper-ocean temperature response to Hurricane Felix as measured by the Bermuda Testbed Mooring. *Monthly Weather Review*, 126(5):1195–1201.

Donguy, J. R. and B. Piton (1991): The Mozambique Channel revisited. *Oceanologica Acta*, 14(6):549–558.

Donohue, K. A. and J. M. Toole (2003): A near-synoptic survey of the Southwest Indian Ocean. *Deep-Sea Research.Part 2: Topical Studies in Oceanography*, 50(12-13):1893–1931.

Dvorak, V. F. (1984): Tropical cyclone intensity analysis using satellite data. *NOAA Technical Report*, 11:45.

Eden, C. (2007): Eddy length scales in the North Atlantic Ocean. *Journal of Geophysical Research: Oceans*, 112:C06004.

Egbert, G. D. and S. Y. Erofeeva (2002): Efficient inverse modeling of barotropic ocean tides. *Journal of Atmospheric and Oceanic Technology*, 19(2):183–204.

Elhmaïdi, D.; A. Provenzale; and A. Babiano (1993): Elementary topology of two-dimensional turbulence from a Lagrangian viewpoint and single-particle dispersion. *Journal of Fluid Mechanics*, 257(1):533–558.

Emanuel, K. (2005): Increasing destructiveness of tropical cyclones over the past 30 years. *Nature*, 436(7051):686–688.

Falkowski, P. G.; D. Ziemann; Z. Kolber; and P. K. Bienfang (1991): Role of eddy pumping in enhancing primary production in the ocean. *Nature*, 352:55–58.

Fan, Y.; I. Ginis; and T. Hara (2009): The effect of wind-wave-current interaction on air-sea momentum fluxes and ocean response in tropical cyclones. *Journal of Physical Oceanography*, 39(4):1019–1034.

Feng, M. and G. Meyers (2003): Interannual variability in the tropical Indian Ocean: a two-year time-scale of Indian Ocean Dipole. *Deep-Sea Research Part II, Topical Studies in Oceanography*, 50(12-13):2263–2284.

Ffield, A.; J. Toole; and D. Wilson (1997): Seasonal circulation in the South Indian Ocean. *Geophysical Research Letters*, 24(22):2773–2776.

Fieux, M. and G. Reverdin (2001): *Current systems in the Indian Ocean*, Academic Press, San Diego, CA, p. 621. Encyclopedia of ocean sciences.

Findlater, J. (1971): Mean monthly airflow at low levels over the western Indian Ocean. *Geophysical Memoirs*, 115:53.

Fine, R. A. (1993): Circulation of Antarctic intermediate water in the South Indian Ocean. *Deep Sea Research Part I: Oceanographic Research Papers*, 40(10):2021–2042.

Fink, H. A. and P. Speth (1998): Tropical cyclones. *Naturwissenschaften*, 85:482–493.

Gadgil, S. (2003): The Indian monsoon and its variability. *Annual Review of Earth and Planetary Sciences*, 31:429–467.

Ginis, I. (2002): Tropical cyclone-ocean interactions. *Advances in Fluid Mechanics*, 33:83–114.

Goni, G.; M. DeMaria; J. Knaff; C. Sampson; I. Ginis; F. Bringas; A. Mavume; C. Lauer; I. Lin; and M. M. Ali (2009): Applications of satellite-derived ocean measurements to tropical cyclone intensity forecasting. *Oceanography*, 22(3):176–183.

Gordon, A. L. (1985): Indian-Atlantic transfer of thermocline water at the Agulhas Retroflection. *Science*, 227(4690):1030.

Gordon, A. L.; M. Shubin; D. B. Olson; P. Hacker; A. Ffield; L. D. Talley; D. Wilson; and M. Baringer (1997): Advection and diffusion of Indonesian throughflow water within the Indian Ocean South Equatorial Current. *Geophysical Research Letters*, 24(21):2573–2576.

Gordon, A. L.; R. F. Weiss; W. M. Smethie; and M. J. Warner (1992): Thermocline and intermediate water communication between the South Atlantic and Indian Oceans. *Journal of Geophysical Research*, (97):7223–7240.

Griffies, S. M.; A. Biastoch; C. Böning; F. Bryan; G. Danabasoglu; E. P. Chassignet; M. H. England; R. Gerdes; H. Haak; and R. W. Hallberg (2009): Coordinated ocean-ice reference experiments (COREs). *Ocean Modelling*, 26(1):1–46.

Gründlingh, M. L. (1980): On the volume transport of the Agulhas Current. *Deep Sea Research Part A.Oceanographic Research Papers*, 27(7):557–563.

Gründlingh, M. L. (1983): On the course of the Agulhas Current. *South African Geographical Journal*, 65(1).

Gründlingh, M. L. (1985): Occurrence of Red Sea water in the southwestern Indian Ocean, 1981. *Journal of Physical Oceanography*, 15(2):207–212.

Gründlingh, M. L. (1987): Cyclogenesis in the Mozambique ridge current. *Deep Sea Research Part A.Oceanographic Research Papers*, 34(1):89–103.

Gründlingh, M. L. (1993): On the winter flow in the southern Mozambique channel. *Deep Sea Research Part I: Oceanographic Research Papers*, 40(2):409–418.

Gründlingh, M. L. (1995): Tracking eddies in the southeast Atlantic and southwest Indian oceans with TOPEX/POSEIDON. *Journal of Geophysical Research*, 100:24977–24986.

Gründlingh, M. L.; R. A. Carter; and R. C. Stanton (1991): Circulation and water properties of the southwest Indian Ocean, spring 1987. *Progress in Oceanography*, 28(4):305–342.

Haidvogel, D. B.; H. Arango; W. P. Budgell; B. D. Cornuelle; E. Curchitser; E. Di Lorenzo; K. Fennel; W. R. Geyer; A. J. Hermann; and L. Lanerolle (2008): Ocean forecasting in terrain-following coordinates: Formulation and skill assessment of the Regional Ocean Modeling System. *Journal of Computational Physics*, 227(7):3595–3624.

Haidvogel, D. B.; H. G. Arango; K. Hedstrom; A. Beckmann; P. Malanotte-Rizzoli; and A. F. Shchepetkin (2000): Model evaluation experiments in the North Atlantic Basin: simulations in nonlinear terrain-following coordinates. *Dynamics of Atmospheres and Oceans*, 32(3-4):239–281.

Haidvogel, D. B. and A. Beckmann (1999): *Numerical ocean circulation modeling*. Imperial College Press London.

Halo, I (2012): *The Mozambique Channel Eddies: Characteristics and Mechanisms of Formation*. Ph.D. thesis, University of Cape Town.

Halo, I; B. Backeberg; P. Penven; I. Ansorge; C. Reason; and J.E. Ullgren (2013): Eddy properties in the Mozambique Channel: A Comparison between observations and two numerical ocean circulation models.

Han, W. and J. P. McCreary (2001): Modeling salinity distributions in the Indian Ocean. *Journal of Geophysical Research*, 106:859–877.

Haney, R. L. (1971): Surface thermal boundary condition for ocean circulation models. *Journal of Physical Oceanography*, 1(4):241–244.

Harlander, U.; H. Ridderinkhof; M. W. Schouten; and W. P. M. de Ruijter (2009): Long-term observations of transport, eddies, and Rossby waves in the Mozambique Channel. *Journal of Geophysical Research*, 114:C02003.

Harris, T. F. W. (1972): Sources of the Agulhas current in the spring of 1964. *Deep Sea Research*, 19(9):633–650.

Harrison, D. E. (1989): On Climatological Monthly Mean Wind Stress and Wind Stress Curl Fields over the World Ocean. *Journal of Climate*, 2(1):57–70.

Hart, N. C. G.; C. J. C. Reason; and N. Fauchereau (2010): Tropical-extratropical interactions over southern Africa: three cases of heavy summer season rainfall. *Monthly Weather Review*, 138(7):2608–2623.

Hastenrath, S. and L. Greischar (1991): The monsoonal current regimes of the tropical Indian Ocean: Observed surface flow fields and their geostrophic and wind-driven components. *Journal of Geophysical Research*, 96(C7):12619.

Hedstrom, G. W. (1979): Nonreflecting boundary conditions for nonlinear hyperbolic systems. *Journal of Computational Physics*, 30(2):222–237.

Hedstrom, K. S. (1997): User's Manual for an S-Coordinate Primitive Equation Ocean Circulation Model SCRUM Version 3.0. *Institute of Marine and Coastal Sciences Technical Report*.

Hellerman, S. and M. Rosenstein (1983): Normal monthly wind stress over the world ocean with error estimates. *Journal of Physical Oceanography*, 13(7):1093–1104.

Henson, S. A. and A. C. Thomas (2008): A census of oceanic anticyclonic eddies in the Gulf of Alaska. *Deep Sea Research Part I: Oceanographic Research Papers*, 55(2):163–176.

Hermes, J. C. and C. J. C. Reason (2008): Annual cycle of the South Indian Ocean (Seychelles-Chagos) thermocline ridge in a regional ocean model. *Journal of Geophysical Research*, 113(C4):C04035.

Hermes, J. C. and C. J. C. Reason (2009): The sensitivity of the Seychelles-Chagos thermocline ridge to large-scale wind anomalies. *ICES Journal of Marine Science*, 66.

Hermes, J. C.; C. J. C. Reason; and J. R. E. Lutjeharms (2007): Modeling the Variability of the Greater Agulhas Current System. *Journal of Climate*, 20(13):3131–3146.

Kalnay, E. C.; M. Kanamitsu; R. Kistler; W. Collins; D. Deaven; L. Gandin; M. Iredell; S. Saha; G. White; and J. Woollen (1996): The NCEP/NCAR 40-year reanalysis project. *Bulletin of the American Meteorological Society*, 77(3):437–471.

Kara, A. B.; A. J. Wallcraft; E. J. Metzger; H. E. Hurlburt; and C. W. Fairall (2007): Wind Stress Drag Coefficient over the Global Ocean. *Journal of Climate*, 20(23):5856–5864.

Karstensen, J. and D. Quadfasel (2002): Water subducted into the Indian Ocean subtropical gyre. *Deep-Sea Research.Part 2: Topical Studies in Oceanography*, 49(7):1441–1457.

Kelly, K. A.; S. Dickinson; M. J. McPhaden; and G. C. Johnson (2001): Ocean Currents evident in Satellite Wind Data. *Geophysical Research Letters*, 28(12):2469–2472.

Kindle, J. C. (1991): Topographic effects on the seasonal circulation of the Indian Ocean. *Journal of Geophysical Research: Oceans*, 96(C9):16827–16837.

Kistler, R.; E. Kalnay; W. Collins; S. Saha; G. White; J. Woollen; M. Chelliah; W. Ebisuzaki; M. Kanamitsu; V. Kousky; H. van den Dool; R. Jenne; and M. Fiorino (2001): The NCEP-NCAR 50-Year Reanalysis: Monthly Means CD-ROM and Documentation. *Bulletin of the American Meteorological Society*, 82(2):247–267.

Klein, S. A.; B. J. Soden; and N-C Lau (1999): Remote sea surface temperature variations during ENSO: evidence for a tropical atmospheric bridge. *Journal of Climate*, 12(4):917–932.

Kumar, S. P. and T. G. Prasad (1999): Formation and spreading of Arabian Sea high-salinity water mass. *Journal of Geophysical Research*, 104(C1):1455–1464.

LaCasce, J. H. and P. E. Isachsen (2007): On Sverdrup Discontinuities and Vortices in the Southwest Indian Ocean. *Journal of Physical Oceanography*, 37(12):2940–2950.

Ladd, C. (2007): Interannual variability of the Gulf of Alaska eddy field. *Geophysical Research Letters*, 34(11):L11605.

Lanzante, J. R. (1996): Lag relationships involving tropical sea surface temperatures. *Journal of Climate*, 9:2568–2578.

Large, W. G.; J. C. McWilliams; and S. C. Doney (1994): Oceanic vertical mixing: a review and a model with a nonlocal boundary layer parameterization. *Reviews of Geophysics*, 32(4):363–403.

Large, W. G. and S. Pond (1981): Open Ocean Momentum Flux Measurements in Moderate to Strong Winds. *Journal of Physical Oceanography*, 11(3):324–336.

Lévy, M.; P. Klein; and A. Treguier (2001): Impact of sub-mesoscale physics on production and subduction of phytoplankton in an oligotrophic regime. *Journal of Marine Research*, 59(4):535–565.

Liu, L. (2010): *Tropical cyclones, oceanic circulation and climate*, Sciyo, Rijeka, Croatia, p. 486. Climate Change and Variability.

Liu, W. T.; W. Tang; and P. S. Polito (1998): NASA scatterometer provides global ocean-surface wind fields with more structures than numerical weather prediction. *Geophysical Research Letters*, 25(6):761–764.

Louis, J. F. (1979): A parametric model of vertical eddy fluxes in the atmosphere. *Boundary-Layer Meteorology*, 17(2):187–202.

Lutjeharms, J. R. E. (1988a): On the role of the East Madagascar Current as a source of the Agulhas Current. *South African Journal of Science*, 84:236–238.

Lutjeharms, J. R. E. (12 1988b): Remote sensing corroboration of retroflection of the East Madagascar Current. *Deep Sea Research Part A.Oceanographic Research Papers*, 35(12):2045–2050.

Lutjeharms, J. R. E. (1991): The temperature/salinity relationships of the South West Indian Ocean. *South African Geographer*, 18(1/2):15–31.

Lutjeharms, J. R. E. (2006a): *The coastal oceans of south-eastern Africa (15,W)*, Harvard University Press, Cambridge MA, pp. 783–834. The Sea, Vol 14B.

Lutjeharms, J. R. E. (2006b): *The Agulhas current*. Springer, Berlin.

Lutjeharms, J. R. E. (2006c): The ocean environment off southeastern Africa: a review. *South African Journal of Science*, 102(9):419–426.

Lutjeharms, J. R. E. (2006d): Three decades of research on the greater Agulhas Current. *Ocean Science Discussions*, 3(4):939–995.

Lutjeharms, J. R. E. and I. J. Ansorge (2001): The Agulhas Return Current. *Journal of Marine Systems*, 30(1):115–138.

Lutjeharms, J. R. E.; N. D. Bang; and C. P. Duncan (1981): Characteristics of the currents east and south of Madagascar. *Deep-Sea Research*, 28A(9):879–899.

Lutjeharms, J. R. E. and H. R. Roberts (1988): The Natal pulse: an extreme transient on the Agulhas Current. *Journal of Geophysical Research*, (93):631–646.

Lutjeharms, J. R. E. and R. C. van Ballegooyen (1988): Anomalous upstream retroflection in the Agulhas Current. *Science*, 240(4860):1770–1772.

Lutjeharms, J. R. E.; P. M. Wedepohl; and J. M. Meeuwis (2000): On the surface drift of the East Madagascar and Mozambique currents. *South African Journal of Science*, 96:141–147.

Ma, P. and O. S. Madsen (2011): An Open Boundary Condition for Numerical Coastal Circulation Models. *Journal of Physical Oceanography*, 41:2363–2380.

Mantyla, A. W. and J. L. Reid (1995): On the origins of deep and bottom waters of the Indian Ocean. *Journal of Geophysical Research*, 100(C2):2417–2439.

Marchesiello, P.; B. Barnier; and A. P. de Miranda (1998): A sigma-coordinate primitive equation model for studying the circulation in the South Atlantic Part II: Meridional transports and seasonal variability. *Deep Sea Research Part I: Oceanographic Research Papers*, 45(4-5):573–608.

Marchesiello, P.; L. Debreu; and X. Couvelard (2009): Spurious diapycnal mixing in terrain-following coordinate models: The problem and a solution. *Ocean Modelling*, 26(3-4):156–169.

Marchesiello, P.; J. C. McWilliams; and A. Shchepetkin (2001): Open boundary conditions for long-term integration of regional oceanic models. *Ocean Modelling*, 3(1):1–20.

Matano, R. P.; E. J. Beier; and P. T. Strub (2008): The seasonal variability of the circulation in the South Indian Ocean: Model and observations. *Journal of Marine Systems*, 74(1-2):315–328.

Matano, R. P.; E. J. Beier; P. T. Strub; and R. Tokmakian (2002): Large-scale forcing of the Agulhas variability: the seasonal cycle. *Journal of Physical Oceanography*, 32(4):1228–1241.

McCreary, J. P. and D. L. T. Anderson (1984): A simple model of El Niño and the Southern Oscillation. *Monthly Weather Review*, 112(5):934–946.

McDonald, R. E.; D. G. Bleaken; D. R. Cresswell; V. D. Pope; and C. A. Senior (2005): Tropical storms: representation and diagnosis in climate models and the impacts of climate change. *Climate Dynamics*, 25(1):19–36.

McGillicuddy, D. J.; A. R. Robinson; D. A. Siegel; H. W. Jannasch; R. Johnson; T. D. Dickey; J. McNeil; A. F. Michaels; and A. H. Knap (1998): Influence of mesoscale eddies on new production in the Sargasso Sea. *Nature*, 394(6690):263–266.

McWilliams, J. C. (1984): The emergence of isolated coherent vortices in turbulent flow. *Journal of Fluid Mechanics*, 146:21–43.

Meinen, C. S.; R. D. Watts; and A. R. Clarke (2000): Absolutely referenced geostrophic velocity and transport on a section across the North Atlantic Current. *Deep Sea Research Part I: Oceanographic Research Papers*, 47(2):309–322.

Metzger, E. J. (2003): Upper ocean sensitivity to wind forcing in the South China Sea. *Journal of Oceanography*, 59(6):783–798.

Milliff, R. F.; J. Morzel; D. B. Chelton; and M. H. Freilich (2004): Wind Stress Curl and Wind Stress Divergence Biases from Rain Effects on QSCAT Surface Wind Retrievals. *Journal of Atmospheric and Oceanic Technology*, 21(8):1216–1231.

Mooney, P. A.; F. J. Mulligan; and R. Fealy (2011): Comparison of ERA-40, ERA-Interim and NCEP/NCAR reanalysis data with observed surface air temperatures over Ireland. *International Journal of Climatology*.

Morales, R. A.; E. D. Barton; and K. J. Heywood (1996): Variability of water masses in the western Indian Ocean. *Journal of Geophysical Research*, 101(C6):14027–14038.

Morcos, S. A. (1970): Physical and chemical oceanography of the Red Sea. *Oceanography and Marine Biology: An Annual Review*, 8:73–202.

Morrison, J. M. (1997): Inter-monsoonal changes in the T-S properties of the near-surface waters of the Northern Arabian Sea. *Geophysical Research Letters*, 24(21):2553–2556.

Morrow, R. and F. Birol (1998): Variability in the southeast Indian Ocean from altimetry: Forcing mechanisms for the Leeuwin Current. *Journal of Geophysical Research*, 103(C9):18529–18,544.

Munk, W. H. (1966): Abyssal recipes. *Deep Sea Research*, 13(4):707–730.

Murtugudde, R.; J. P. McCreary Jr; and A. J. Busalacchi (2000): Oceanic processes associated with anomalous events in the Indian Ocean with relevance to 1997-1998. *Journal of Geophysical Research*, 105(C2):3295–3306.

Nauw, J. J.; H. M. van Aken; A. Webb; J. R. E. Lutjeharms; and W. P. M. de Ruijter (2008): Observations of the southern East Madagascar Current and undercurrent and countercurrent system. *Journal of Geophysical Research*, 113:C08006.

New, A. L.; S. G. Alderson; D. A. Smeed; and K. L. Stansfield (2007): On the circulation of water masses across the Mascarene Plateau in the South Indian Ocean. *Deep Sea Research Part I: Oceanographic Research Papers*, 54(1):42–74.

Okubo, A. (1970): Horizontal dispersion of floatable particles in the vicinity of velocity singularities such as convergences. *Deep Sea Research*, 17:445–454.

Osiński, R.; P. Wieczorek; A. Beszczyńska-Möller; and I. Goszczko (2003): ADCP-referenced geostrophic velocity and transport in the West Spitsbergen Current. *Oceanologia*, 45(3):425–435.

Ou, H. W. and W. P. M. de Ruijter (1986): Separation of an inertial boundary current from a curved coastline. *Journal of Physical Oceanography*, 16(2):280–289.

Palastanga, V.; H. A. Dijkstra; and W. P. M. de Ruijter (2009): Inertially induced connections between subgyres in the South Indian Ocean. *Journal of Physical Oceanography*, 39(2):465–471.

Palastanga, V.; P. J. van Leeuwen; and W. P. M. de Ruijter (2006): A link between low-frequency mesoscale eddy variability around Madagascar and the large-scale Indian Ocean variability. *Journal of Geophysical Research*, 111(C09029).

Palastanga, V.; P. J. van Leeuwen; M. W. Schouten; and W. P. M. de Ruijter (2007): Flow structure and variability in the subtropical Indian Ocean: Instability of the South Indian Ocean Countercurrent. *Journal of Geophysical Research*, 112(C01001).

Palma, E. D.; R. P. Matano; A. R. Piola; and L. E. Sitz (2004): A comparison of the circulation patterns over the Southwestern Atlantic Shelf driven by different wind stress climatologies. *Geophysical Research Letters*, 31:L24303.

Palmer, M. D. (2005): *Decadal variability of the subtropical gyre and deep meridional overturning circulation of the Indian Ocean*. Ph.D. thesis, University of Southampton, Faculty of Engineering Science and Mathematics, School of Ocean and Earth Science.

Park, Y. H.; L. Gamberoni; and E. Charriaud (1993): Frontal structure, water masses, and circulation in the Crozet Basin. *Journal of Geophysical Research*, 98(C7):12361–12385.

Payet, R. A.; N. Soogun; E. Raniavoson; R. J. Payet; and F. Ali Abdallah (2004): Indian Ocean Islands: GIWA Regional Assessment 45b. *UNEP Technical Report*, (1).

Pedlosky, J. (1996): *Ocean Circulation Theory*. Springer, New York.

Peeters, F. J. C.; R. Acheson; G. J. A. Brummer; W. P. M. De Ruijter; R. R. Schneider; G. M. Ganssen; E. Ufkes; and D. Kroon (2004): Vigorous exchange between the Indian and Atlantic oceans at the end of the past five glacial periods. *Nature*, 430(7000):661–665.

Penven, P. (2000): *A numerical study of the Southern Benguela circulation with an application to fish recruitment*. Ph.D. thesis, University of Brest.

Penven, P.; N. Chang; and F. Shillington (2006a): Modelling the Agulhas Current using SAfE (Southern Africa Experiment). *Geophysical Research Abstract*, 8(04225).

Penven, P.; L. Debreu; P. Marchesiello; and J. C. McWilliams (2006b): Evaluation and application of the ROMS 1-way embedding procedure to the central California upwelling system. *Ocean Modelling*, 12(1-2):157–187.

Penven, P.; J. R. E. Lutjeharms; and P. Florenchie (2006c): Madagascar: A pacemaker for the Agulhas Current system. *Geophysical Research Letters*, 33(L17609).

Penven, P. and T. Tan (2007): ROMSTOOLS User's Guide.

Petit, M.; A. G. Ramos; F. Lahet; and J. Coca (2006): Satellite-Derived ERS scatterometer sea-surface wind-stress curl in the southwestern Indian Ocean. *Comptes Rendus Geosciences*, 338(3):206–213.

Pfeiffer, M. and W-C Dullo (2006): Monsoon-induced cooling of the western equatorial Indian Ocean as recorded in coral oxygen isotope records from the Seychelles covering the period of 1840-1994 AD. *Quaternary Science Reviews*, 25(9-10):993–1009.

Price, J. F. (1981): Upper ocean response to a hurricane. *Journal of Physical Oceanography*, 11(2):153–175.

Provenzale, A. (1999): Transport by coherent barotropic vortices. *Annual Review of Fluid Mechanics*, 31(1):55–93.

Quadfasel, D. R. and F. Schott (1982): Water-mass distributions at intermediate layers off the Somali Coast during the onset of the southwest monsoon, 1979. *Journal of Physical Oceanography*, 12:1358–1372.

Quadfasel, D. R. and J.C. Swallow (10 1986): Evidence for 50-day period planetary waves in the South Equatorial Current of the Indian Ocean. *Deep Sea Research Part A.Oceanographic Research Papers*, 33(10):1307–1312.

Quartly, G. D.; J. J. H. Buck; M. A. Srokosz; and A. C. Coward (2006): Eddies around Madagascar–The retroflection re-considered. *Journal of Marine Systems*, 63(3-4):115–129.

Quartly, G. D. and M. A. Srokosz (2002): SST Observations of the Agulhas and East Madagascar Retroflections by the TRMM Microwave Imager. *Journal of Physical Oceanography*, 32(5):1585–1592.

Quartly, G. D. and M. A. Srokosz (2004): Eddies in the southern Mozambique Channel. *Deep Sea Research Part II: Topical Studies in Oceanography*, 51(1-3):69–83.

Ramage, C. S. (1971): *Monsoon Metereology*. Academic Press, New York.

Rao, L. V. G. and P. S. Ram (2005): *Upper ocean physical processes in the Tropical Indian Ocean*. National Institute of Oceanography, Goa.

Rao, R. R. and R. Sivakumar (2000): Seasonal variability of near-surface thermal structure and heat budget of the mixed layer of the tropical Indian Ocean from a new global ocean temperature climatology. *Journal of Geophysical Research*, 105(C1):995–1015.

Rao, S. A.; S. K. Behera; Y. Masumoto; and T. Yamagata (2002): Interannual subsurface variability in the tropical Indian Ocean with a special emphasis on the Indian Ocean Dipole. *Deep-Sea Research Part II, Topical Studies in Oceanography*, 49(7):1549–1572.

Rasmusson, E. M. and T. H. Carpenter (1982): Variations in tropical sea surface temperature and surface wind fields associated with the Southern Oscillation/El Niño. *Monthly Weather Review*, 110(5):354–384.

Reason, C. J. C.; R. J. Allan; J. A. Lindesay; and T. J. Ansell (2000): ENSO and climatic signals across the Indian Ocean basin in the global context: Part I, Interannual composite patterns. *International Journal of Climatology*, 20(11):1285–1327.

Reason, C. J. C. and A. Keibel (2004): Tropical Cyclone Eline and its unusual penetration and impacts over the southern African mainland. *Weather and forecasting*, 19:789–805.

Reason, C. J. C. and H. Mulenga (1999): Relationships between South African rainfall and SST anomalies in the southwest Indian Ocean. *International Journal of Climatology*, 19(15):1651–1673.

Rhines, P. B. (1975): Waves and turbulence on a beta-plane. *Journal of Fluid Mechanics*, 69(3):417–443.

Ridderinkhof, H. and W. P. M. de Ruijter (2003): Moored current observations in the Mozambique Channel. *Deep Sea Research Part II: Topical Studies in Oceanography*, 50(12-13):1933–1955.

Ridderinkhof, H.; P. M. Van der Werf; J. E. Ullgren; H. M. Van Aken; P. J. Van Leeuwen; and W. P. M. De Ruijter (2010): Seasonal and interannual variability in the Mozambique Channel from moored current observations. *Journal of Geophysical Research*, 115:C06010/1–C06010/18.

Ridgway, K. R.; J. R. Dunn; and J. L. Wilkin (2002): Ocean interpolation by four-dimensional weighted least squares-application to the waters around Australasia. *Journal of Atmospheric and Oceanic Technology*, 19(9):1357–1375.

Risien, C. M. and D. B. Chelton (2008): A Global Climatology of Surface Wind and Wind Stress Fields from Eight Years of QuikSCAT Scatterometer Data. *Journal of Physical Oceanography*, 38(11):2379–2413.

Risien, C. M.; C. J. C. Reason; F. A. Shillington; and D. B. Chelton (2004): Variability in satellite winds over the Benguela upwelling system during 1999-2000. *Journal of Geophysical Research*, 109(C3):C03010.

Roman, R. E. and J. R. E. Lutjeharms (2009): Red Sea Intermediate Water in the source regions of the Agulhas Current. *Deep Sea Research Part I: Oceanographic Research Papers*, 56(6):939–962.

Sætre, R. (1985): Surface currents in the Mozambique Channel. *Deep Sea Research Part A.Oceanographic Research Papers*, 32(12):1457–1467.

Sætre, R. and A. Jorge da Silva (1984): The circulation of the Mozambique Channel. *Deep Sea Research Part A.Oceanographic Research Papers*, 31(5):485–508.

Saji, N. H.; B. N. Goswami; P. N. Vinayachandran; and T. Yamagata (1999): A dipole mode in the tropical Indian Ocean. *Nature*, 401(6751):360.

Saji, N. H. and T. Yamagata (2003a): Possible impacts of Indian Ocean dipole mode events on global climate. *Climate Research*, 25(2):151–169.

Saji, N. H. and T. Yamagata (2003b): Structure of SST and surface wind variability during Indian Ocean dipole mode events: COADS observations. *Journal of Climate*, 16(16):2735–2751.

Satheesan, K.; A. Sarkar; A. Parekh; M. R. Ramesh Kumar; and Y. Kuroda (2007): Comparison of wind data from QuikSCAT and buoys in the Indian Ocean. *International Journal of Remote Sensing*, 28:2375–2382.

Schlax, M. G.; D. B. Chelton; and M. H. Freilich (2001): Sampling Errors in Wind Fields Constructed from Single and Tandem Scatterometer Datasets. *Journal of Atmospheric and Oceanic Technology*, 18(6):1014–1036.

Schott, F. (1983): Monsoon response of the Somali Current and associated upwelling. *Progress in Oceanography*, 12(3):357–381.

Schott, F.; M. Fieux; J. Kindle; J. Swallow; and R. Zantopp (1988): The boundary currents east and north of Madagascar 2. Direct measurements and model comparisons. *Journal of Geophysical Research*, 93(C5):4963–4974.

Schott, F. A. and J. Fischer (2000): Winter monsoon circulation of the northern Arabian Sea and Somali Current. *Journal of Geophysical Research*, 105(C3):6359–6376.

Schott, F. A. and J. P. McCreary (2001): The monsoon circulation of the Indian Ocean. *Progress in Oceanography*, 51(1):1–123.

Schott, F. A.; S. P. Xie; and J. P. McCreary Jr (2009): Indian Ocean circulation and climate variability. *Reviews of Geophysics*, 47(1).

Schouten, M. W.; W. P. M. de Ruijter; and P. J. van Leeuwen (2002a): Upstream control of Agulhas Ring shedding. *Journal of Geophysical Research*, 107(C8):3109.

Schouten, M. W.; W. P. M. de Ruijter; P. J. van Leeuwen; and H. A. Dijkstra (2002b): An oceanic teleconnection between the equatorial and southern Indian Ocean. *Geophysical Research Letters*, 29(16):1812.

Schouten, M. W.; W. P. M. de Ruijter; P. J. van Leeuwen; and H. Ridderinkhof (2003): Eddies and variability in the Mozambique Channel. *Deep Sea Research Part II: Topical Studies in Oceanography*, 50(12-13):1987–2003.

Schumann, E. H. (1998): The coastal ocean off southeast Africa, including Madagascar. *The Sea*, 11:557–581.

Seki, M. P.; R. Lumpkin; and P. Flament (2002): Hawaii cyclonic eddies and blue marlin catches: the case study of the 1995 Hawaiian International Billfish Tournament. *Journal of Oceanography*, 58(5):739–745.

Shanko, D. and P. Camberlin (1998): The effects of the Southwest Indian Ocean tropical cyclones on Ethiopian drought. *International Journal of Climatology*, 18(12):1373–1388.

Shapiro, G. I. and S. L. Meschanov (1991): Distribution and spreading of Red Sea Water and salt lens formation in the northwest Indian Ocean. *Deep Sea Research*, 38(1):21–34.

Sharma, G. S. (1976): Transequatorial movement of water masses in the Indian Ocean. *Journal of Marine Research*, 34(2):143–154.

Sharma, N. and E. D'Sa (2008): Assessment and analysis of QuikSCAT vector wind products for the Gulf of Mexico: A long-term and hurricane analysis. *Sensors*, 8(3):1927–1949.

Shchepetkin, A. F. and J. C. McWilliams (1998): Quasi-monotone advection schemes based on explicit locally adaptive dissipation. *Monthly Weather Review*, 126:1541–1580.

Shchepetkin, A. F. and J. C. McWilliams (2003): A method for computing horizontal pressure-gradient force in an oceanic model with a nonaligned vertical coordinate. *Journal of Geophysical Research*, 108(C3):3090.

Shchepetkin, A. F. and J. C. McWilliams (2005): The regional oceanic modeling system (ROMS): a split-explicit, free-surface, topography-following-coordinate oceanic model. *Ocean Modelling*, 9(4):347–404.

Shetye, S. R. and A. D. Gouveia (1998): Coastal circulation in the North Indian Ocean: Coastal segment (14, SW). *The Sea*, 11:523–556.

Shum, C. K.; R. A. Werner; D. T. Sandwell; B. H. Zhang; R. S. Nerem; and B. D. Tapley (1990): Variations of global mesoscale eddy energy observed from Geosat. *Journal of Geophysical Research*, 95(C10):17865–17876.

Siedler, G.; M. Rouault; A. Biastoch; B. Backeberg; C. J. C. Reason; and J. R. E. Lutjeharms (2009): Modes of the southern extension of the East Madagascar Current. *Journal of Geophysical Research*, 114(C01005).

Siedler, G.; M. Rouault; and J. R. E. Lutjeharms (2006): Structure and origin of the subtropical South Indian Ocean Countercurrent. *Geophysical Research Letters*, 33:L24609.

Simmons, A.; S. Uppala; D. Dee; and S. Kobayashi (2007): ERA-Interim: New ECMWF reanalysis products from 1989 onwards. *ECMWF Newsletter*, 110:25–35.

Simpson, J.; R. F. Adler; and G. R. North (1988): A proposed tropical rainfall measuring mission (TRMM) satellite. *Bulletin of the American meteorological Society*, 69(3):278–295.

Singh, O. P. (2008): Indian Ocean dipole mode and tropical cyclone frequency. *Current science*, 94(1):29–31.

Slingo, J.; H. Spencer; B. Hoskins; P. Berrisford; and E. Black (2005): The Meteorology of the Western Indian Ocean, and the Influence of the East African Highlands. *Philosophical Transactions: Mathematical, Physical and Engineering Sciences*, 363(1826):25–42.

Smagorinsky, J. (1963): General circulation experiments with the primitive equations. *Monthly Weather Review*, 91:99–164.

Son, S.; T. Platt; H. Bouman; D. Lee; and S. Sathyendranath (2006): Satellite observation of chlorophyll and nutrients increase induced by Typhoon Megi in the Japan/East Sea. *Geophysical Research Letters*, 33(5):L05607.

Song, Q.; A. L. Gordon; and M. Visbeck (2004): Spreading of the Indonesian Throughflow in the Indian Ocean. *Journal of Physical Oceanography*, 34:772–792.

Song, Y. and D. Haidvogel (1994): A semi-implicit ocean circulation model using a generalized topography-following coordinate system. *Journal of Computational Physics*, 115(1):228–244.

Spall, M. A. and A. R. Robinson (1989): A new open ocean, hybrid coordinate primitive equation model. *Mathematics and Computers in Simulation*, 31(3):241–269.

Srinivasan, A.; Z. Garraffo; and M. Iskandarani (2009): Abyssal circulation in the Indian Ocean from a $1/12^\circ$ resolution global hindcast. *Deep Sea Research Part I: Oceanographic Research Papers*, 56(11):1907–1926.

Stommel, H. (1958): The abyssal circulation. *Deep Sea Research Part II: Topical Studies in Oceanography*, 5:80–82.

Stramma, L. and J. R. E. Lutjeharms (1997): The flow field of the subtropical gyre of the South Indian Ocean. *Journal of Geophysical Research*, 102(C3):5513–5530.

Sverdrup, H. U.; M. W. Johnson; and R. H. Fleming (1942): *The oceans: their physics, chemistry, and general biology*. Prentice-Hall, New York.

Swallow, J.; M. Fieux; and F. Schott (1988): The boundary currents east and north of Madagascar 1. Geostrophic currents and transports. *Journal of Geophysical Research*, 93(C5):4951–4962.

Swallow, J. C.; R. L. Molinari; J. G. Bruce; O. B. Brown; and R. H. Evans (1983): Development of near-surface flow pattern and water mass distribution in the Somali Basin

in response to the southwest monsoon of 1979. *Journal of Physical Oceanography*, 13(8):1398–1415.

Swart, N. C.; J. R. E. Lutjeharms; H. Ridderinkhof; and W. P. M. de Ruijter (2010): Observed characteristics of Mozambique Channel eddies. *Journal of Geophysical Research-Oceans*, 115:C09006/1–C09006/14.

Tew-Kai, E. and F. Marsac (2009): Patterns of variability of sea surface chlorophyll in the Mozambique Channel: A quantitative approach. *Journal of Marine Systems*, 77(1-2):77–88.

Tew-Kai, E. and F. Marsac (2010): Influence of mesoscale eddies on spatial structuring of top predators' communities in the Mozambique Channel. *Progress in Oceanography*, 86(1-2):214–223.

Thompson, K. W. (1987): Time dependent boundary conditions for hyperbolic systems. *Journal of Computational Physics*, 68(1):1–24.

Thompson, K. W. (1990): Time-dependent boundary conditions for hyperbolic systems, II. *Journal of Computational Physics*, 89(2):439–461.

Thoppil, P. G.; J. G. Richman; and P. J. Hogan (2011): Energetics of a global ocean circulation model compared to observations. *Geophysical Research Letters*, 38(15):L15607.

Tomczak, M. and J. S. Godfrey (2003): *Regional Oceanography: an Introduction*. Daya Publishing House, Delhi.

Toole, J. M. and B. A. Warren (1993): A hydrographic section across the subtropical South Indian Ocean. *Deep Sea Research Part I: Oceanographic Research Papers*, 40(10):1973–2019.

Torrence, C. and G. P. Compo (1998): A practical guide to wavelet analysis. *Bulletin of the American Meteorological Society*, 79:61–78.

Tourre, Y. M. and W. B. White (1995): ENSO signals in global upper-ocean temperature. *Journal of Physical Oceanography*, 25:1317–1332.

Tourre, Y. M. and W. B. White (1997): Evolution of the ENSO Signal over the Indo-Pacific Domain. *Journal of Physical Oceanography*, 27:683–696.

Trenberth, K. E.; W. G. Large; and J. G. Olson (1990): The mean annual cycle in global ocean wind stress. *Journal of Physical Oceanography*, 20(11):1742–1760.

Tyson, P.D. and R. A. Preston-Whyte (2000): *The weather and climate of southern Africa*. Oxford University Press.

Ullgren, J. E.; H. M. van Aken; H. Ridderinkhof; and W. P. M. de Ruijter (2012): The hydrography of the Mozambique Channel from six years of continuous temperature, salinity, and velocity observations. *Deep Sea Research I*, 69:36–50.

van Aken, H. M.; H. Ridderinkhof; and W. P. M. de Ruijter (2004): North Atlantic deep water in the south-western Indian Ocean. *Deep Sea Research Part I: Oceanographic Research Papers*, 51(6):755–776.

van der Werf, P. M.; M. W. Schouten; P. J. van Leeuwen; H. Ridderinkhof; and W. P. M. de Ruijter (2009): Observation and origin of an interannual salinity anomaly in the Mozambique Channel. *Journal of Geophysical Research*, 114(C03017).

van der Werf, P. M.; P. J. van Leeuwen; H. Ridderinkhof; and W. P. M. de Ruijter (2010): Comparison between observations and models of the Mozambique Channel transport: Seasonal cycle and eddy frequencies. *Journal of Geophysical Research*, 115(C2):C02002.

Vásquez, S.; M. Correa-Ramírez; C. Parada; and A. Sepúlveda (2013): The influence of oceanographic processes on jack mackerel (Trachurus murphyi) larval distribution and population structure in the southeastern Pacific Ocean. *ICES Journal of Marine Science: Journal du Conseil*, 70:1097–1107.

Vecchi, G. A.; S. P. Xie; and A. S. Fischer (2004): Ocean-atmosphere covariability in the western Arabian Sea. *Journal of Climate*, 17(6):1213–1224.

Vinayachandran, P. N. (2004): Summer cooling of the Arabian Sea during contrasting monsoons. *Geophysical Research Letters*, 31(13):L13306.

Vinayachandran, P. N.; N. H. Saji; and T. Yamagata (1999): Response of the equatorial Indian Ocean to an unusual wind event during 1994. *Geophysical Research Letters*, 26(11):1613–1616.

Warren, B.; H. Stommel; and J. C. Swallow (1976): Water masses and patterns of flow in the Somali Basin during the southwest monsoon of 1964. *Deep Sea Research and Oceanographic Abstracts*, 13(5):825–860.

Warren, B. A. (1981): Transindian hydrographic section at Lat. 18S: Property distributions and circulation in the South Indian Ocean. *Deep Sea Research Part A.Oceanographic Research Papers*, 28(8):759–788.

Webster, P. J.; A. M. Moore; J. P. Loschnigg; and R. R. Leben (1999): Coupled ocean-atmosphere dynamics in the Indian Ocean during 1997-98. *Nature*, 401(6751):356–360.

Weijer, W.; W. P. M. de Ruijter; H. A. Dijkstra; and P. J. van Leeuwen (1999): Impact of interbasin exchange on the Atlantic overturning circulation. *Journal of Physical Oceanography*, 29(9):2266–2284.

Weimerskirch, H.; M. Le Corre; S. Jaquemet; M. Potier; and F. Marsac (2004): Foraging strategy of a top predator in tropical waters: great frigatebirds in the Mozambique Channel. *Marine Ecology Progress Series*, 275:297–308.

Weiss, J. (1991): The dynamics of enstrophy transfer in two-dimensional hydrodynamics. *Physica D: Nonlinear Phenomena*, 48(2):273–294.

Withee, G. W. and A. Johnson (1976): Data Report: Buoy observations during hurricane Eloise (September 19 to October 11, 1975).

Woodberry, K. E.; M. E. Luther; and J. J. O'Brien (1989): The wind-driven seasonal circulation in the southern tropical Indian Ocean. *Journal of Geophysical Research*, 94(C12):17985.

Wyrtki, K. (1973a): An equatorial jet in the Indian Ocean. *Science*, 181(4096):262.

Wyrtki, K. (1973b): *Physical oceanography of the Indian Ocean*, Springer-Verlag, New York, pp. 18–36. The Biology of the Indian Ocean.

Wyrtki, K.; E. B. Bennett; and D. J. Rochford (1971): *Oceanographic atlas of the international Indian Ocean expedition*. National Science Foundation, Washington, D.C.

Xie, S. P; H. Annamalai; F. A. Schott; and J. P. McCreary (2002): Structure and mechanisms of South Indian Ocean climate variability. *Journal of Climate*, 15(8):864–878.

Xie, S. P; W. T. Liu; Q. Liu; and M. Nonaka (2001): Far-reaching effects of the Hawaiian Islands on the Pacific ocean-atmosphere system. *Science*, 292(5524):2057.

Yamagata, T.; S. K. Behera; J-J Luo; S. Masson; M. R. Jury; and S. A. Rao (2004): Coupled ocean-atmosphere variability in the tropical Indian Ocean. *Earth Climate: The Ocean-Atmosphere Interaction, Geophysical Monograph Series*, 147:189–211.

Yamagata, T.; S. K. Behera; and S. A. Rao (2003): Comments on "Dipoles, Temperature Gradients, and Tropical Climate Anomalies". *Bulletin of the American Meteorological Society*, 84(10):1418–1425.

Yamagata, T.; S. K. Behera; S. A. Rao; Z. Guan; K. Ashok; and H. N. Saji (2002): The Indian Ocean dipole: A physical entity. *CLIVAR exchanges*, 24:15–18.

Yamagata, T.; K. Mizuno; and Y. Masumoto (1996): Seasonal variations in the equatorial Indian Ocean and their impact on the Lombok throughflow. *Journal of Geophysical Research*, 101(C5):12465–12473.

Yin, X.; Z. Wang; Y. Liu; and Y. Xu (2007): Ocean response to Typhoon Ketsana traveling over the northwest Pacific and a numerical model approach. *Geophysical Research Letters*, 34:L21606.

Yoo, S-H; J. Fasullo; S. Yang; and C-H Ho (2010): On the relationship between Indian Ocean sea surface temperature and the transition from El Niño to La Niña. *Journal of Geophysical Research*, 115:D15114.

Yoshida, S.; B. Qiu; and P. Hacker (2010): Wind-generated eddy characteristics in the lee of the island of Hawaii. *Journal of Geophysical Research*, 115(C3):C03019.

You, Y. (2000): Implications of the deep circulation and ventilation of the Indian Ocean on the renewal mechanism of North Atlantic Deep Water. *Journal of Geophysical Research*, 105(C10):23895–23,926.

You, Y. and M. Tomczak (1993): Thermocline circulation and ventilation in the Indian Ocean derived from water mass analysis. *Deep Sea Research Part I: Oceanographic Research Papers*, 40(1):13–56.

Appendix A

Inter-annual variability: relation to large-scale climate modes

In addition to the seasonal variability discussed in Chapter 3, the Comoros Basin is also subjected to strong interannual variability as illustrated by the strong year to year differences in Figures A.1 and A.2. For example, during the years 1994, 1995, 1998 and 1999 there is no identifiable area of high EKE north of the Comoros Islands. A time series of monthly averaged EKE for the region north of the Comoros Islands (10-12°S, 44-46°E) indicate that during these years, with the exception of 1995, the EKE does not exceed $500cm^2 \cdot s^{-2}$ whereas in other years the EKE range from 500 to more than $700cm^2 \cdot s^{-2}$ (Figure A.5b). The lower than normal EKE during the four aforementioned years suggests a decrease in eddy activity north of the Comoros Islands during these years compared to other years. A visual inspection of SLAs, where eddies were only identified as such when it had a close to circular contour associated with it and if the anomaly was equal to or exceeded +/- 10cm, revealed that during the lower-than-normal-EKE years, an average of 8 eddies per year occurred north of the

Comoros Island while an average of 13 eddies per year occurred in other years.

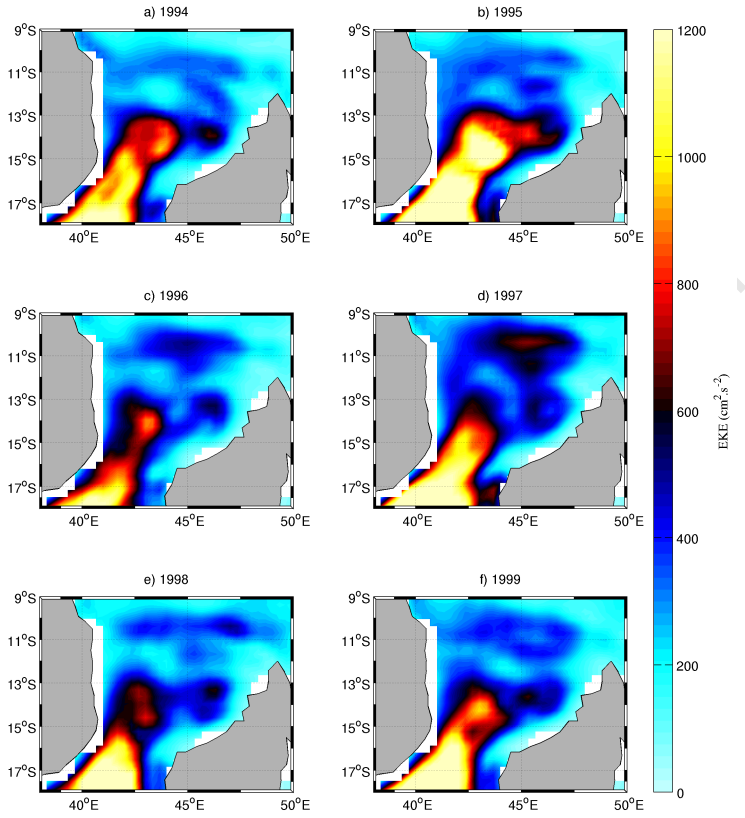

Figure A.1: *Year by year mean EKE for the period 1994-1999.*

Another example of the interannual variability is the maximum EKE in the narrows of the channel which display the lowest energies during 1994 and 1996 and is limited in its northward extent to the south of 15°S during 1998, 2003-2004, 2007 and 2011. The low EKE during 1994 and 1996 suggests a decrease in the number of eddies passing through the narrows of the channel. The limited northward extent of EKE during 1998, 2003-2004, 2007

and 2011 coincide with low EKE values throughout these years in the region 13.5-15°S, 42-44°E (Figure A.5d) suggesting a decrease in eddy activity to the north of ~15°S. The visual inspection of SLAs described above reveal that during the years with limited northward EKE extend, an average of 10 eddies per year are generated in the region compared to an average of 14 eddies per year in other years.

In order to investigate whether the year-to-year variation within the Comoros Basin is related to large scale climate modes such as the IOD and ENSO, a 19 year time series (1993-2011) of monthly averaged satellite derived SLAs and EKE were correlated with monthly time series of the ENSO and IOD indices for the same period. The Niño 3.4 index, used as representative of ENSO is based on SST anomalies for the region bounded by 120°W-170°W and 5°S-5°N. Niño 3.4 values exceeding the threshold ±0.4°C represent positive (negative) ENSO events indicative of El Niño (La Niña) events. The IOD index is calculated as the difference between the SST anomaly of the western (50°E-70°E and 10°S-10°N) and eastern (90°E-110°E and 10°S-0°S) tropical Indian Ocean (Saji et al., 1999). Positive (negative) IOD events are characterized by warmer (cooler) than normal SSTs in the western tropical Indian Ocean and cooler (warmer) than normal SSTs in the eastern tropical Indian Ocean. The Hadley Centre Sea Ice and Sea Surface Temperature dataset (HadISST) was used to calculate both indices. Before the correlations were carried out, all time series were smoothed with a 5-month running average to remove any intraseasonal variations.

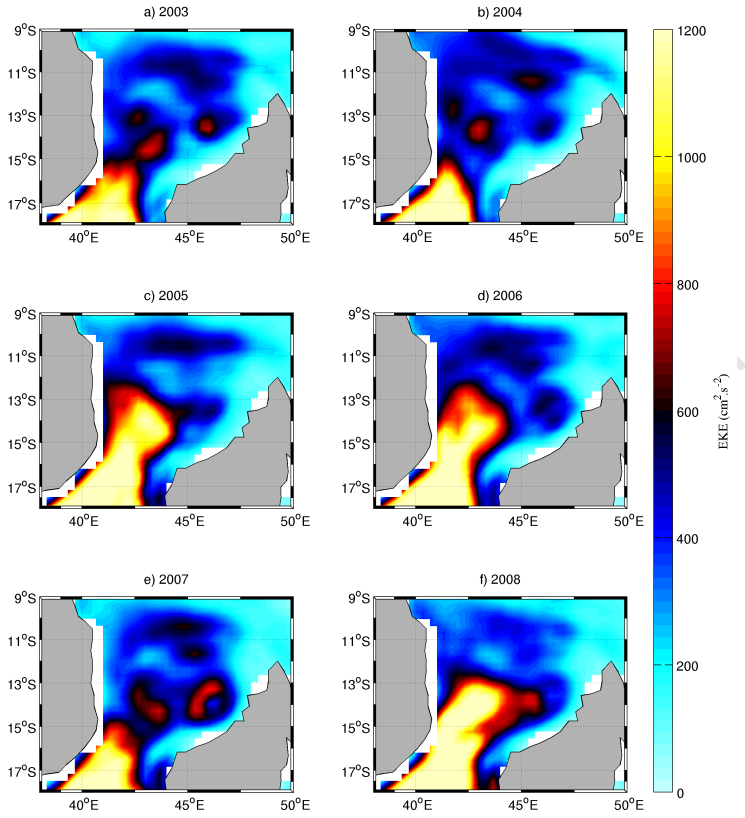

Figure A.2: *Year by year mean EKE for the period 2003-2008.*

The correlation between the satellite derived data and the climate indices were performed over three regions of high EKE within the basin as well as the basin as a whole (11-15°S and 41-47°E). The northern region (hereafter northern Comoros Basin), 10-12°S and 44-46°E (Figure A.3), was selected as it represents the area where eddies are formed due to the instability of the NEMC jet (Quadfasel and Swallow, 1986). The western region (hereafter western Comoros Basin), 13.5-15°S and 42-44°E, represents an area were EKE, generally,

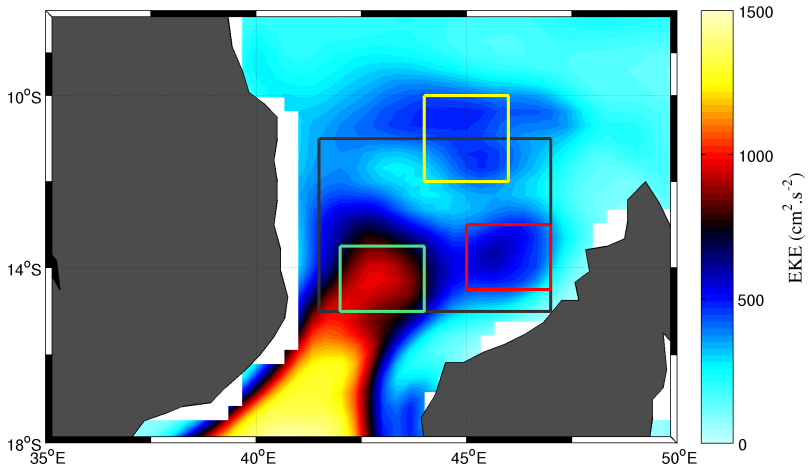

Figure A.3: *The annual mean EKE in the Comoros Basin. The regions of the Comoros Basin, northern Comoros Basin, western Comoros Basin and eastern Comoros Basin are indicated by the black, yellow, green and red boxes, respectively.*

exceeds 700cm^2·s^{-2} (Figure A.3) and the eastern region (hereafter eastern Comoros Basin), 13-14.5°S and 45-47°E (Figure A.3), comprise a region of regular cyclonic eddy formation. During the 19 years of the altimeter data analysed here, there were 6 El Niño and 7 La Niña events as well as 5 (4) years in which the IOD was in its positive (negative) phase (Table A.1).

The first negative IOD, which peaked in November 1993, was followed, 6 months later, by negative SLAs in the Comoros Basin as well as in all three sub-regions (Figure A.4). The strongest negative anomaly, peaking at about 9cm, occurred in the western Comoros Basin (Figure A.4d) 6 months after this IOD event reached its peak. Similarly, this negative IOD event preceded a period of decreased EKE (<500cm^2·s^{-2}) in the whole Comoros Basin as

Table A.1: *List of the year of onset of El Niño, La Niña, positive IOD and negative IOD events during the period 1993-2011.*

El Niño	**La Niña**	**+ IOD**	**- IOD**
1994	1995	1994	1993
1997	1998	1997	1996
2002	1999	2006	1999
2004	2000	2007	2011
2006	2007	2008	
2009	2010		
	2011		

well as in the three individual subregions (Figure A.5) by 2-6 months. In the Comoros Basin and in all three sub-regions, the first positive IOD event, peaking in September 1994, was followed by positive SLAs 3-5 months later and EKE values in excess of $500cm^2 \cdot s^{-2}$ 4-12 months later. The highest SLAs and EKE of about 8cm and $>1600cm^2 \cdot s^{-2}$, respectively, is observed in the western Comoros Basin 4 months after the peak of the 1994 IOD event.

The 1996 negative IOD event coincides with negative SLAs which persists into the following year in the whole Comoros Basin and in the northern Comoros Basin. The negative SLAs in the Comoros Basin and northern Comoros Basin reach a peak 6-7 months after the peak of the IOD event with the SLAs in the latter peaking at ~10cm. In the eastern and western Comoros Basin, negative SLAs peak about 1-3 months before the peak of the IOD event. EKE values in the Comoros Basin display no significant increase or decrease during or following the 1996 IOD event. The 1997 positive IOD event, peaking in November, precedes a strong positive SLA in the Comoros Basin as a whole and in all three sub-regions by 1-6 months. This positive IOD event is accompanied by EKE values less than $500cm^2 \cdot s^{-2}$ in the Comoros Basin including all the subregions. During the three consecutive positive IOD years of 2006, 2007 and 2008 positive SLAs dominated in the Comoros Basin; however no distinct

pattern is observed in the EKE during these three positive IOD years.

The above suggests a positive correlation between SLAs in the Comoros Basin and the IOD index at a lag of about 2 months to a year. The correlation analysis shows that the SLAs in the Comoros Basin as a whole is negatively correlated ($r=-0.28$, $p<0.05$) with the IOD index at a lag of 4-6 months (Figure A.4a). Similarly, SLAs in the northern and western Comoros Basin display a negative correlation ($r=-0.30$, $p<0.05$ and $r=-0.28$, $p=<0.05$ for the northern and western Comoros Basin respectively) with the IOD index at a 2-8 month lag (Figures A.4a and d). This indicates that in the Comoros Basin, more specifically in the northern and western parts of the basin, an increase (decrease) in SLAs occur 4-6 months after the IOD has peaked in its negative (positive) phase. EKE within the Comoros Basin as a whole and in the western Comoros Basin also display a negative correlation ($r=-0.30$, $p<0.05$ and $r=-0.21$, $p<0.05$) with the IOD index at a lag of 6-12 months (Figures A.5a and d). The EKE in the northern and eastern Comoros Basin, on the other hand, displays no clear association with the IOD index (Figures A.5b and c).

Ridderinkhof et al. (2010) found a negative correlation between the IOD and southward transport through the Mozambique Channel with increased (decreased) transport occurring during negative (positive) IOD events. This negative correlation was ascribed to the weakening (strengthening) of the tropical gyre associated with positive (negative) IOD events. Following this, it can be argued that a strengthening of the tropical gyre, and by extension the SEC, during the negative phase of the IOD would result in a strengthening of the NEMC which in turn could lead to increased eddy activity in the Comoros Basin. The geostrophic speed of the NEMC is negatively correlated with the IOD index ($r=-0.27$, $p<0.05$) suggesting that there is an intensification of the current during negative IOD events. Subsequently, from the negative correlation between EKE in the Comoros basin and the IOD index, it can be

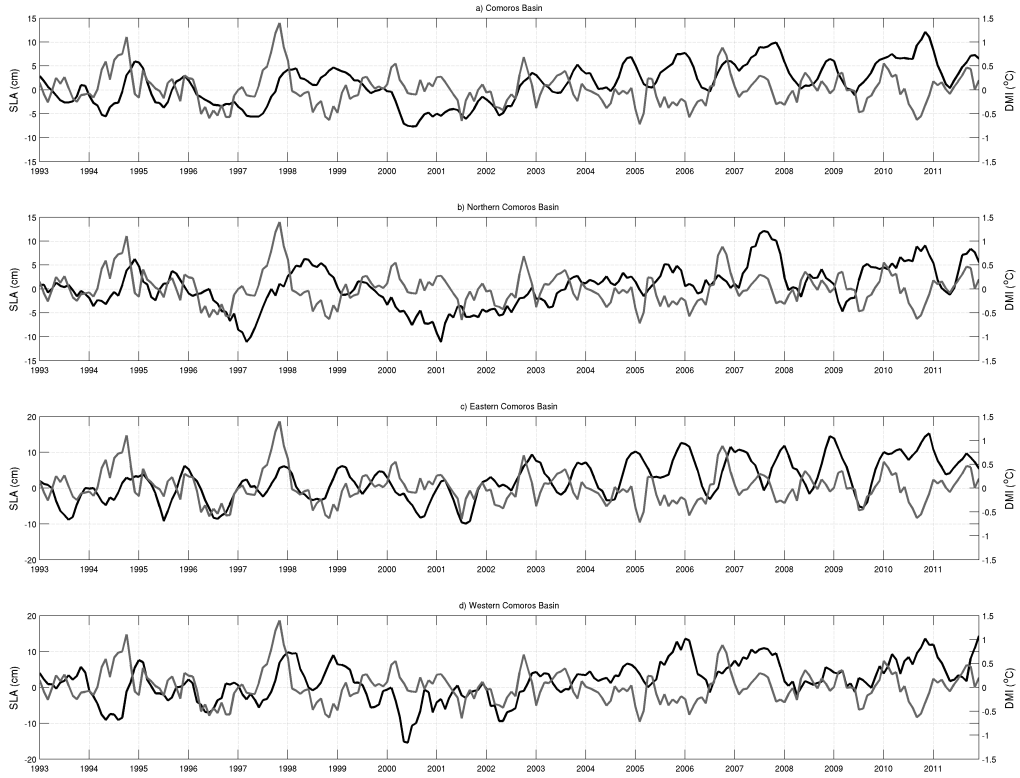

Figure A.4: *Monthly time series of the IOD index (gray line) and sea level anomalies (black line) for the a) Comoros Basin, b) northern Comoros Basin, c) eastern Comoros Basin and d) western Comoros Basin.*

inferred that the strengthening of the NEMC leads to increased eddy activity in the Comoros Basin.

The first El Niño event of the time series under investigation here coincides with positive SLAs in the Comoros Basin as a whole as well as in the three subregions, and is preceded and followed by negative SLAs. Similarly, positive SLAs coincide with the first La Niña event and is followed by negative SLAs. SLAs in the Comoros Basin as a whole and in the

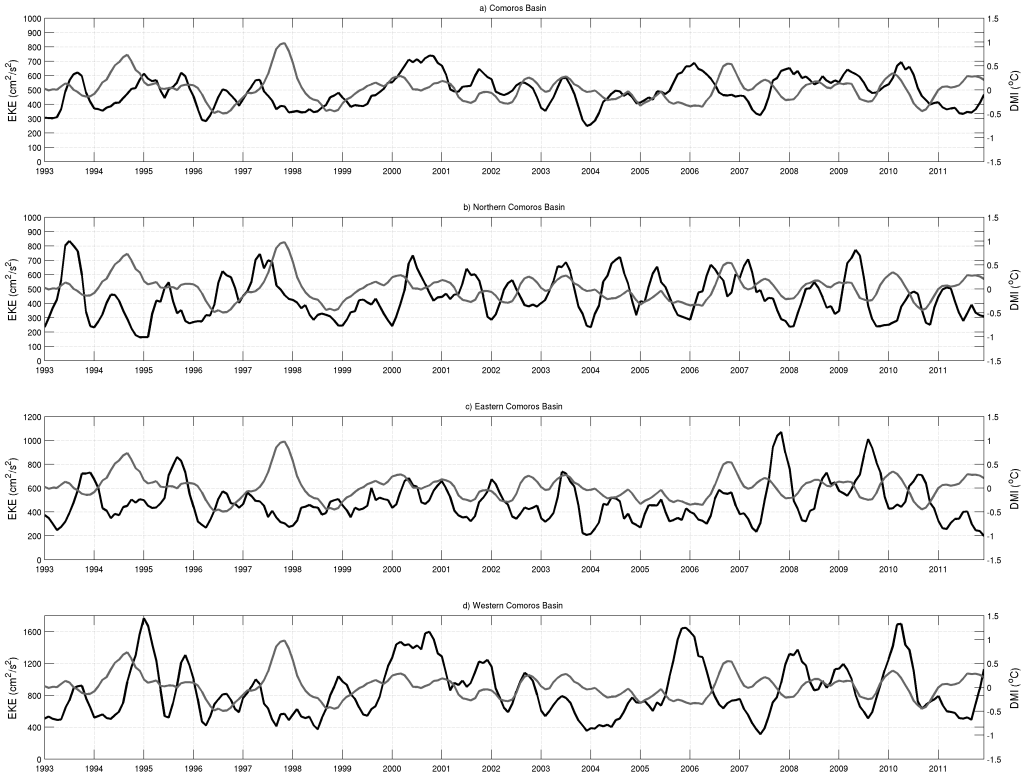

Figure A.5: *Monthly time series of the IOD index (gray line) and satellite derived EKE (black line) for the a) Comoros Basin, b) northern Comoros Basin, c) eastern Comoros Basin and d) western Comoros Basin.*

three sub-regions display a transition from negative SLAs to positive anomalies during the 1997 El Niño year. The consecutive La Niña years of 1998, 1999 are dominated by positive SLAs in the Comoros Basin as a whole as well as in the three sub-regions. On the other hand, negative SLAs dominate during the 2000 La Niña year. Similar to the 1997 El Niño year, the SLAs in the Comoros Basin and the western and eastern subregions, transition from negative to positive anomalies during the 2002 El Niño year. During the 2004, 2006 and

2009 El Niño year, positive SLAs dominated in the Comoros Basin and its subregions, with the exception of the eastern Comoros Basin which display both positive and negative SLAs. In the Comoros Basin as well as in the three subregions, the La Niña years of 2010 and 2011 are dominated by positive SLAs. In general, it appears that there is a decrease in EKE in the Comoros Basin and its three subregions during El Niño years and an increase during La Niña years.

The correlation analysis shows that the SLAs of the Comoros Basin as a whole and the northern Comoros Basin are negatively correlated with ENSO index at a lag of between 3-16 months ($r=-0.42$, $p<0.05$ and $r=-0.51$, $p<0.05$; Figures A.6a and b). This, along with the absence of significant correlations for the eastern and western Comoros Basin (Figures A.6c and d) suggests that the ENSO mainly influence the northern Comoros Basin resulting in more positive (negative) SLAs 2 to 12 months after a negative (positive) ENSO event. The correlation analysis also shows a negative correlation between EKE in the Comoros Basin as well as the western and eastern Comoros Basin subregions, with ENSO lagging the EKE by 0-24 months (Figure A.7).

The results presented above suggest a negative correlation between the meso-scale variability in the Comoros Basin and the ENSO and IOD with increased eddy activity during negative IOD/La Niña events due to an intensification of the NEMC and the reverse for positive IOD/El Niño events. However, the link between the meso-scale activity in the Comoros basin and large scale climate modes established here is a tenuous one as the 19 year time series of satellite derived data, spans only 9 IOD and 13 ENSO events. Therefore, in order to obtain more robust results, a longer time series of sea level anomaly data needs to be considered.

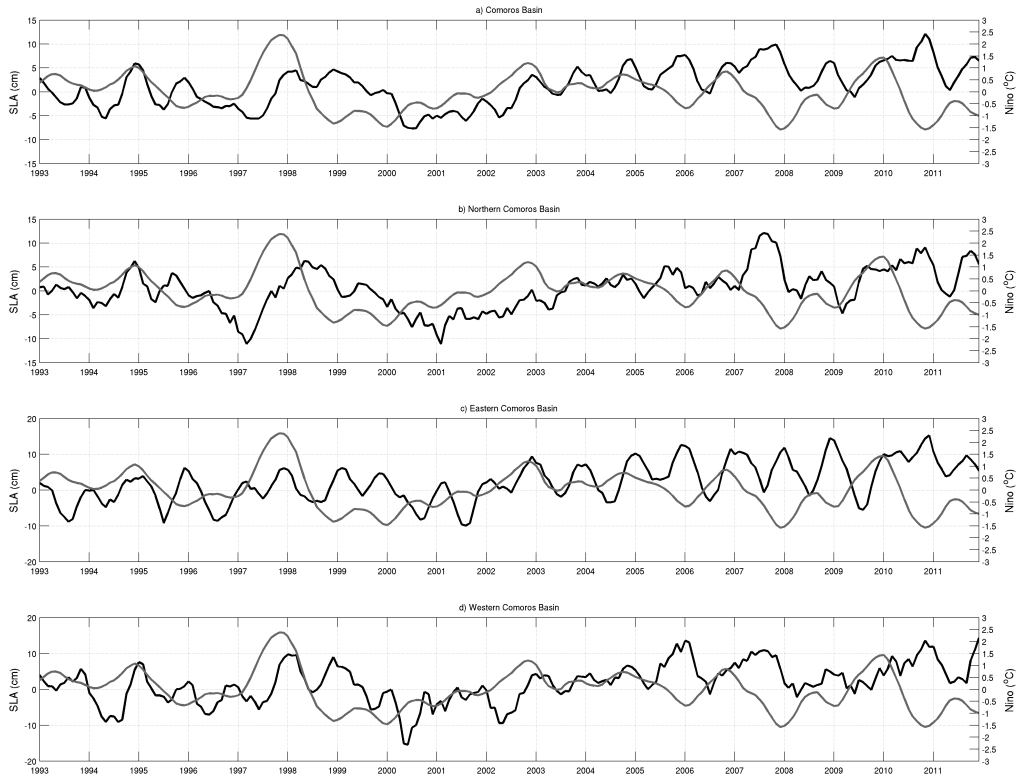

Figure A.6: *Monthly time series of the ENSO index (gray line) and sea level anomalies (black line) for the a) Comoros Basin, b) northern Comoros Basin, c) eastern Comoros Basin and d) western Comoros Basin.*

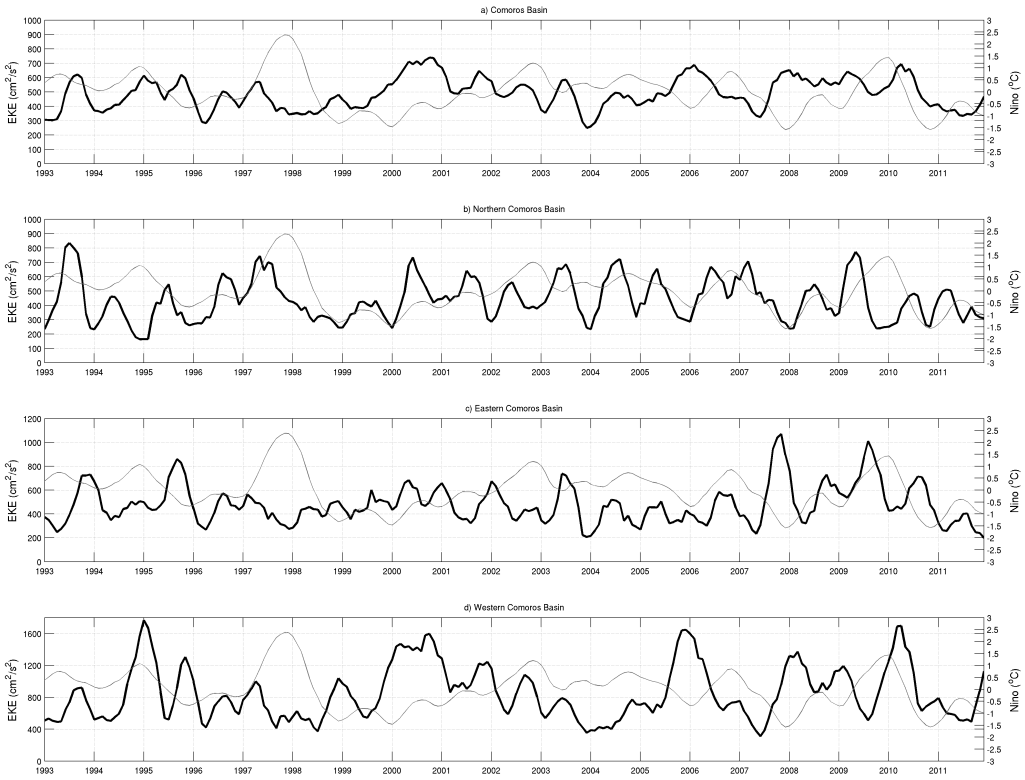

Figure A.7: *Monthly time series of the ENSO index (gray line) and satellite derived EKE (black line) for the a) Comoros Basin, b) northern Comoros Basin, c) eastern Comoros Basin and d) western Comoros Basin.*

Appendix B

Validation of Parent domain

The parent domain (0°W-70°E and 4°N-44°S) of the ROMS simulation (TWIO-parent) is compared with observational and satellite data in order to establish whether the salient features of the western Indian Ocean are realistically simulated. The focus is on the Agulhas Current which is not represented in the child domain validated in Chapter 6.

Water mass properties and Distribution

Sea surface Temperature

TWIO-parent reproduces the seasonal SST patterns of the western Indian Ocean and around southern Africa reasonably well. Winter SSTs are, in general, 4°C colder than summer SSTs, while those in autumn and spring are about 2°C colder than summer SSTs. There appears to be an increased penetration of the Agulhas Current into the south Atlantic in TWIO-parent which is more pronounced during autumn and winter (Figure B.1j and k). In the South Indian Ocean, the isotherms slope towards the southwest reflecting the Agulhas Current. In the

southeast Atlantic, the cooler waters are associated with the equatorward flowing Benguela Current and coastal upwelling. All data sets show similar representation of the Angola-Benguela Frontal Zone which separates the Benguela Current from the warm, tropical Angola Current. In TWIO-parent, there is an overestimation of the SST associated with this current by ~1-2°C in winter and autumn (Figure B.1j and k) whereas in the other seasons there is an underestimation of about 0.5-1°C (Figure B.1i and l). Furthermore, the TWIO-parent simulation overestimates the SST in the coastal upwelling system suggesting that the strength of the upwelling is underestimated in the model. The underestimation of the Benguela upwelling in TWIO-parent is more pronounced during autumn and winter (Figure B.1j and k) during which the temperatures associated with the Benguela upwelling are overestimated by 0.5-2°C.

In the Indian Ocean, the warmest SST (~28°C) is observed stretching zonally across the northeastern part of the domain and is part of the Pacific warm pool (Tomczak and Godfrey, 2003). In CARS, this warm pool stretches to about 54°E; however in TMI and TWIO-parent, it extends further west to beyond 50°E. The SST of the model as well as the satellite data display a decrease in SST to the south of the domain indicative of the cold waters of the Southern Ocean which are separated from the subtropical waters of the Atlantic and Indian Oceans (Figure B.1) by the Subtropical Frontal Zone observed between 36°-44°S. The 14.2° and 17.9°C isotherms, reveal the meandering nature of this Frontal Zone as well as its extent across the South Indian and Atlantic Oceans. Southwest of the southern tip of Africa, TWIO-parent underestimates the northward extent of the Frontal Zone into the South Atlantic Ocean resulting in a positive SST bias of between 1-3°C (Figure B.1d and e).

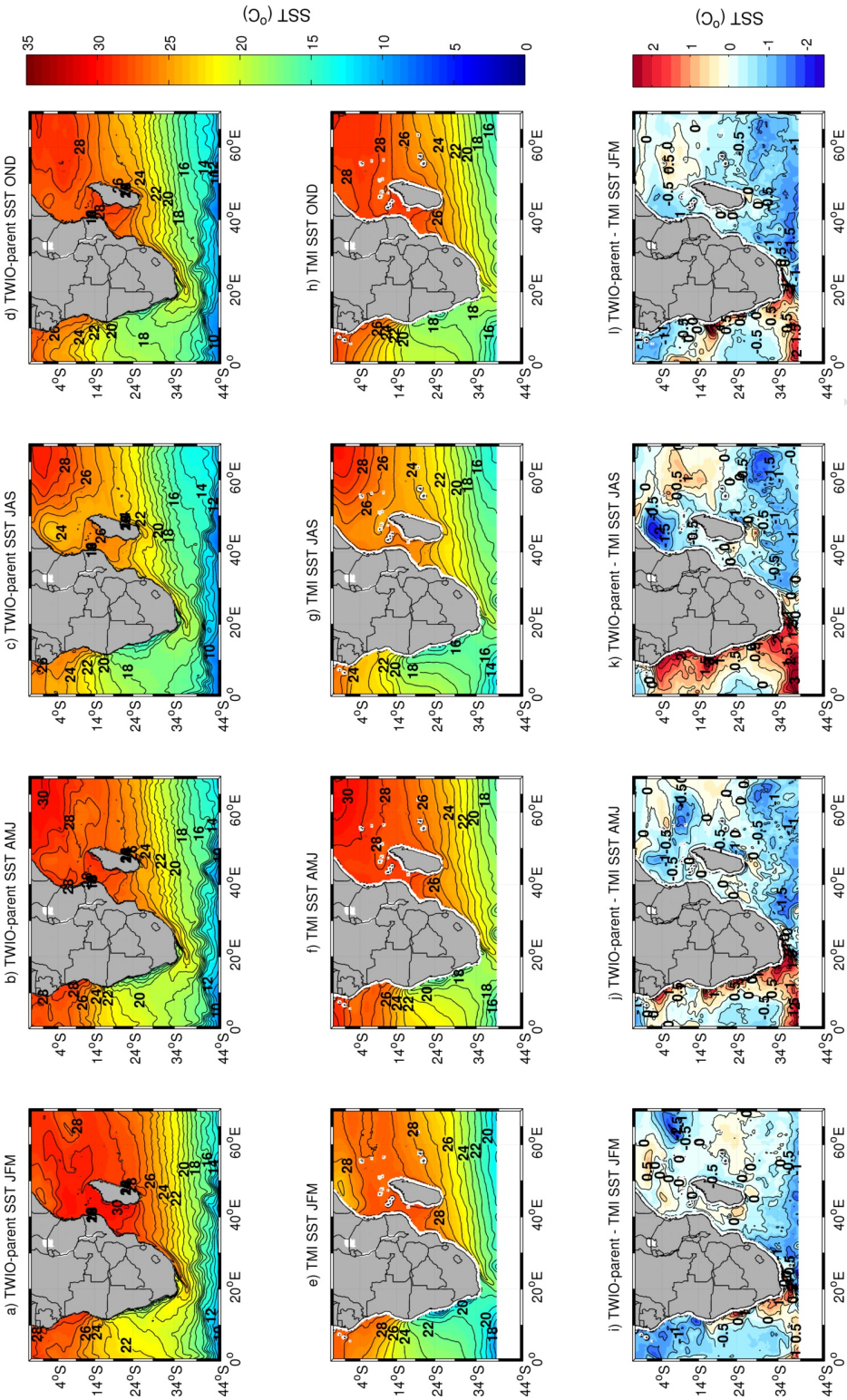

Figure B.1: *Seasonal SSTs (°C) for TWIO-parent (a-d), and TMI (e-h) where the contour interval is 0.5°C. The difference between TWIO-parent and TMI are shown in the bottom panel (i-l), where the contour interval is 0.5°C. Positive (negative) values indicate an over-estimation (underestimation) of SSTs by TWIO-parent.*

Water masses

The vertical profile representing the AC is located at 31°S and extends from the coast to ~46°E. The vertical profile of temperature and salinity of the AC in TWIO-parent and CARS display a high degree of verisimilitude (Figure B.3). In both TWIO-parent and CARS, distinct upward sloping isotherms at the coast reflect the strong poleward velocities associated with the AC (Beal and Bryden, 1999). The temperature-salinity diagram, based on the annual mean properties of the AC, shows that the majority of the water masses present in the observational data can also be identified in TWIO-parent (Figure B.2). These water masses are: warm, low salinity (<35.5) Tropical Surface Water (TSW; Beal and Bryden, 1999; Beal et al., 2006), South Indian Central Water (SICW) recognizable by its linear θ/S relationship, low-salinity (<34.7) Antarctic Intermediate Water (AAIW; Beal et al., 2006), high-salinity Red Sea Intermediate Water (RSIW) and high-salinity North Atlantic Deep Water (NADW).

Consistent with Beal and Bryden (1999), the permanent thermocline, represented by the 4°C isotherm, has an offshore depth of ~1500m in both CARS and TWIO-parent and shallows to a depth of ~1200m along the continental slope (Figure B.3). TWIO-parent differ most notably from CARS at the bottom of the water column with the 1° and 2°C isotherms situated higher in the water column in TWIO-parent (Figure B.3). This apparent difference can possibly be ascribed to the difference in the depth of the bottom bathymetry. Two ridges, centred roughly at 35°E and 45°E are apparent in both CARS and TWIO-parent, however in the former the ridges are coarsely resolved and about 200m deeper compared to TWIO-parent. The vertical resolution of TWIO-parent also needs to be considered, due to its effect on the structure of the bottom of the water column. At depths greater than 300m, the vertical resolution of the model grid is greater than 20m and increase with increasing depth to approximately

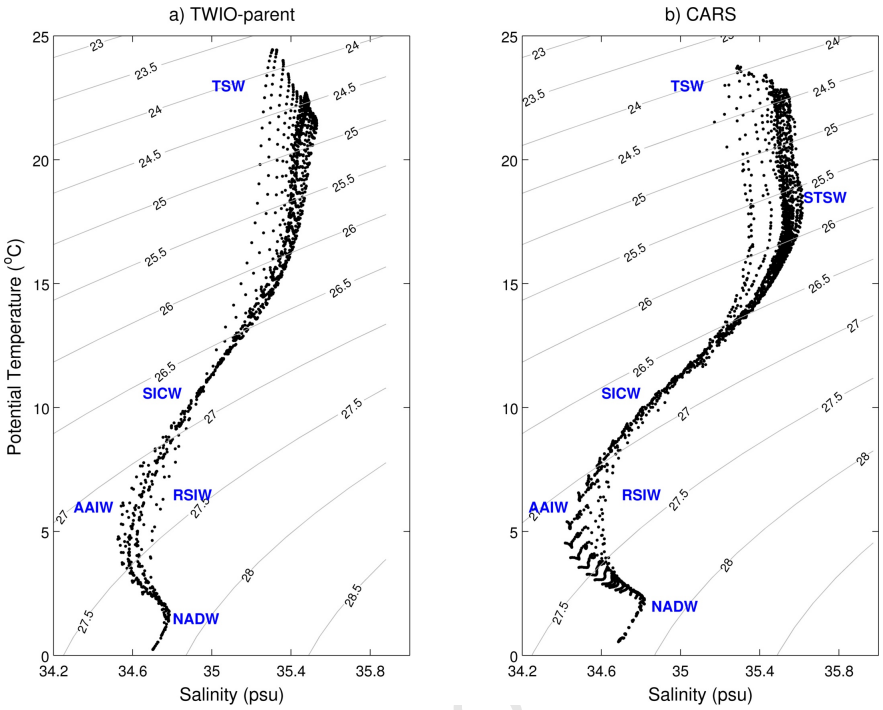

Figure B.2: *θ-S diagram showing the water mass properties extracted along a zonal section across the Agulhas Current (AC) for a) TWIO-parent and b) CARS.*

250m in depths greater than 2000m. The differences between CARS and TWIO-parent can also possibly be attributed to the coarse resolution of the observational data (0.5°) and the interpolation used in CARS to replace missing data.

In general, TWIO-parent tends to underestimate the salinity values, especially at the surface and in the bottom layers of the water column. A distinctive feature of the vertical salinity structure of the AC in both TWIO-parent and CARS is a strong salinity minimum of <34.6psu between 1000-1500m (Figures B.2 and B.3), indicative of Antarctic Intermediate Water (AAIW; Beal and Bryden, 1999). In CARS, the AAIW extends further towards the shelf than it does in TWIO-parent. AAIW enters the Indian Ocean at ~60°E from within the Sub-Antarctic Front (SAF). The southern boundary of TWIO-parent does not include

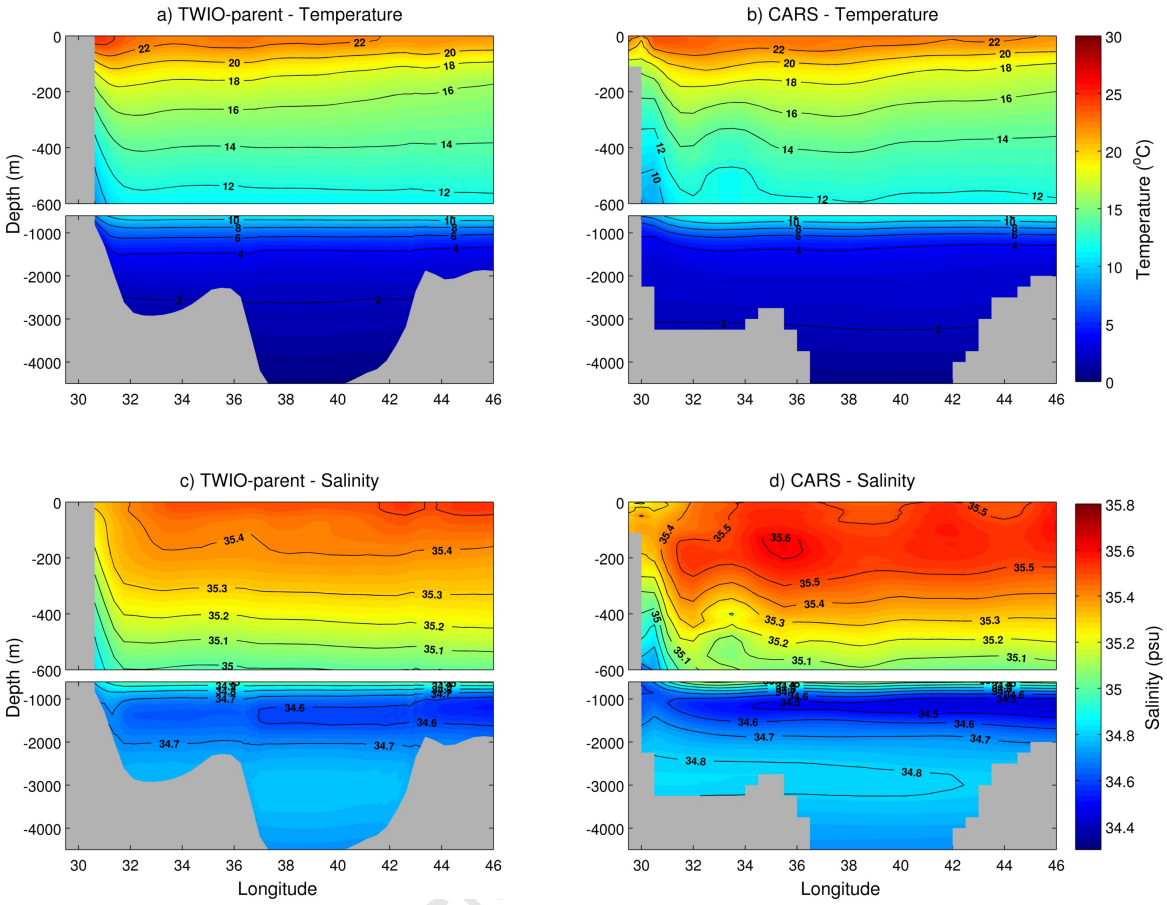

Figure B.3: *Vertical profile of the annual mean temperature (a-b) and salinity (c-d) along a zonal section through the Agulhas Current (AC) in TWIO-parent (left panel) and CARS (right panel). The contour interval for temperature and salinity is 2°C and 0.1psu, respectively.*

the whole width of the SAF and therefore the slightly more saline AAIW in TWIO-parent can most likely be attributed to boundary effects. Another distinct feature of the salinity structure of the AC is a high salinity layer in the upper 300m which is about 0.02psu less saline in TWIO-parent and only extend to about 200m. Within the high salinity layer, CARS displays a subsurface salinity maximum of 35.6 between ~50-200m, indicative of Subtropical Surface Waters (STSW; Beal and Bryden, 1999) which is absent in the vertical profile of

TWIO-parent. STSW is formed through excess evaporation east of 90°E (Wyrtki et al., 1971) between 25° and 35°S within the subtropical gyre (Beal et al., 2006) and enters the western Indian Ocean within the southern edge of the SEC (New et al., 2007). One possible reason for the absence of STSW in TWIO-parent is problems associated with the interpolation employed at the open boundaries of the model. Another possible reason is dilution of the STSW signature due to spurious mixing in the model.

Velocity Field

Surface Currents

The Agulhas Current and its main features are relatively well represented in TWIO-parent (Figure B.4 and B.5). Consistent with observations (Gründlingh, 1983) and the surface geostrophic velocities, the Agulhas Current in TWIO-parent, with speeds of ~0.2-1.5m·s^{-1}, closely follows the shelf edge in the north, intensifying to speeds in excess of 0.5m·s^{-1} at ~27°S. Near 34°S, the shelf edge separates from the coast and the current is steered away becoming increasingly unstable in its mean southwestward path (not shown). The separation of the southern Agulhas Current from the coast is evident in the surface velocity field of TWIO as well as the altimetry derived surface geostrophic velocities and, while the meandering nature of the current is not evident in the seasonal means, it is evident in the weekly averaged velocity fields (not shown). The flow of the Agulhas Current proper is highly concentrated and the TWIO-parent mean volume transport of 60.62±9.4Sv relative to 1500m at 32°S (Figure 6.14) is in reasonable agreement with previous estimates of 65-70Sv based on observations (Gründlingh, 1980; Stramma and Lutjeharms, 1997; Bryden et al., 2005).

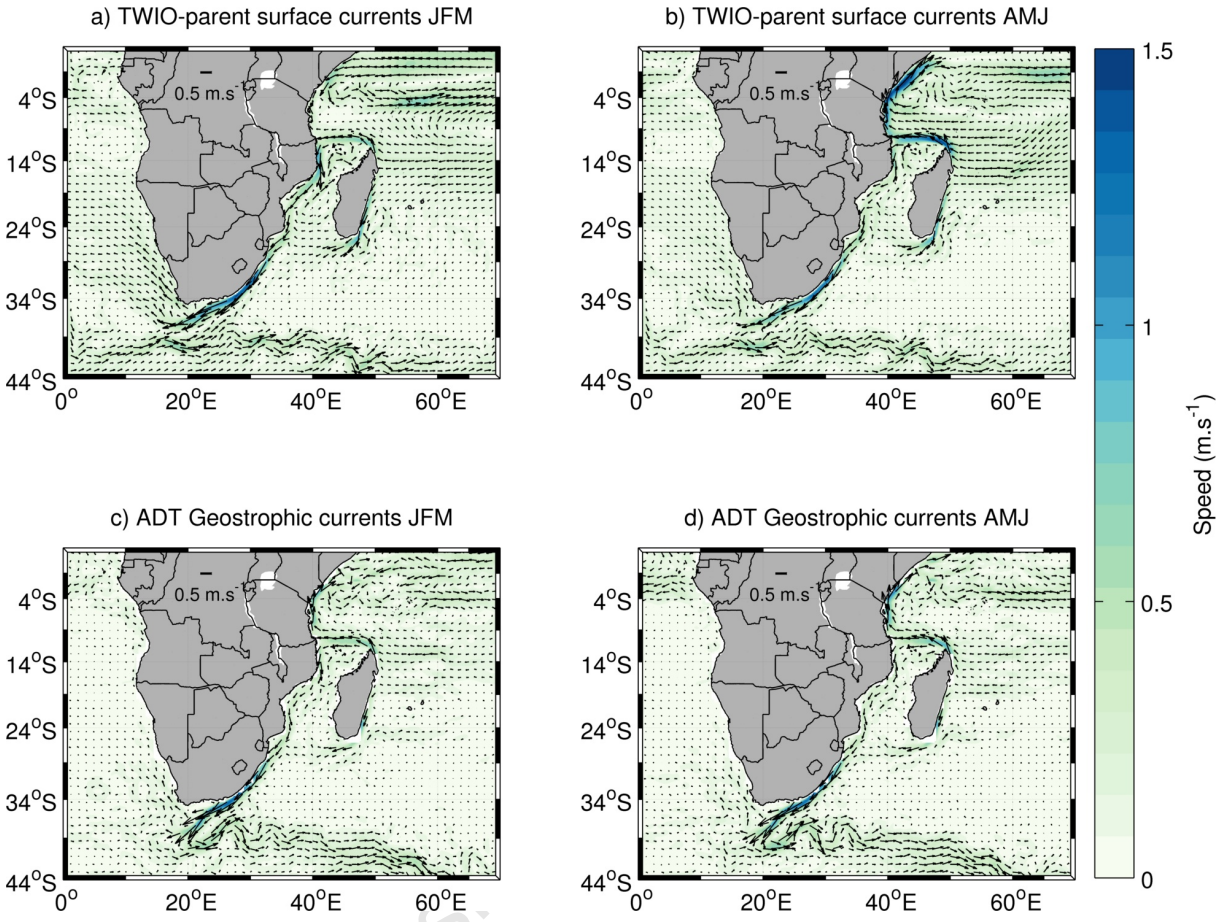

Figure B.4: *Mean surface velocities from TWIO-parent (a-b) and the seasonal mean surface geostrophic velocities from AVISO (c-d) for summer (JFM) and autumn (AMJ).*

The Agulhas Current retroflects in an anticyclonic loop roughly at about 16°E between 38° and 40°S, for which there is evidence in both the surface velocity fields of TWIO-parent and the surface geostrophic velocities (Figure B.4 and B.5). As observed in the SST, the surface velocity of TWIO-parent also overestimates the flow from the Agulhas Current into the South Atlantic Ocean compared to the leakage inferred from the altimeter data. The remainder of the waters from the Agulhas Current flow back into the South Indian Ocean in the eastward flowing Agulhas Return Current. Consistent with previous literature (Lutjeharms

and Ansorge, 2001) and the altimeter data, the Agulhas Return Current, with speeds of up to 0.6m·s^{-1}, is roughly located at 39°S and a gradual shift of its core towards increased latitudes in the east is also evident in the seasonal mean surface velocity fields of TWIO-parent (Figures B.4 and B.5). TWIO-parent displays a recirculation of about 41.73±12.73Sv from the Agulhas Current into the South Western Indian Ocean (Figure 6.14) by the Agulhas Return Current which is in good agreement with the 44-54Sv transport estimates derived from observations (Lutjeharms and Ansorge, 2001; Boebel et al., 2003).

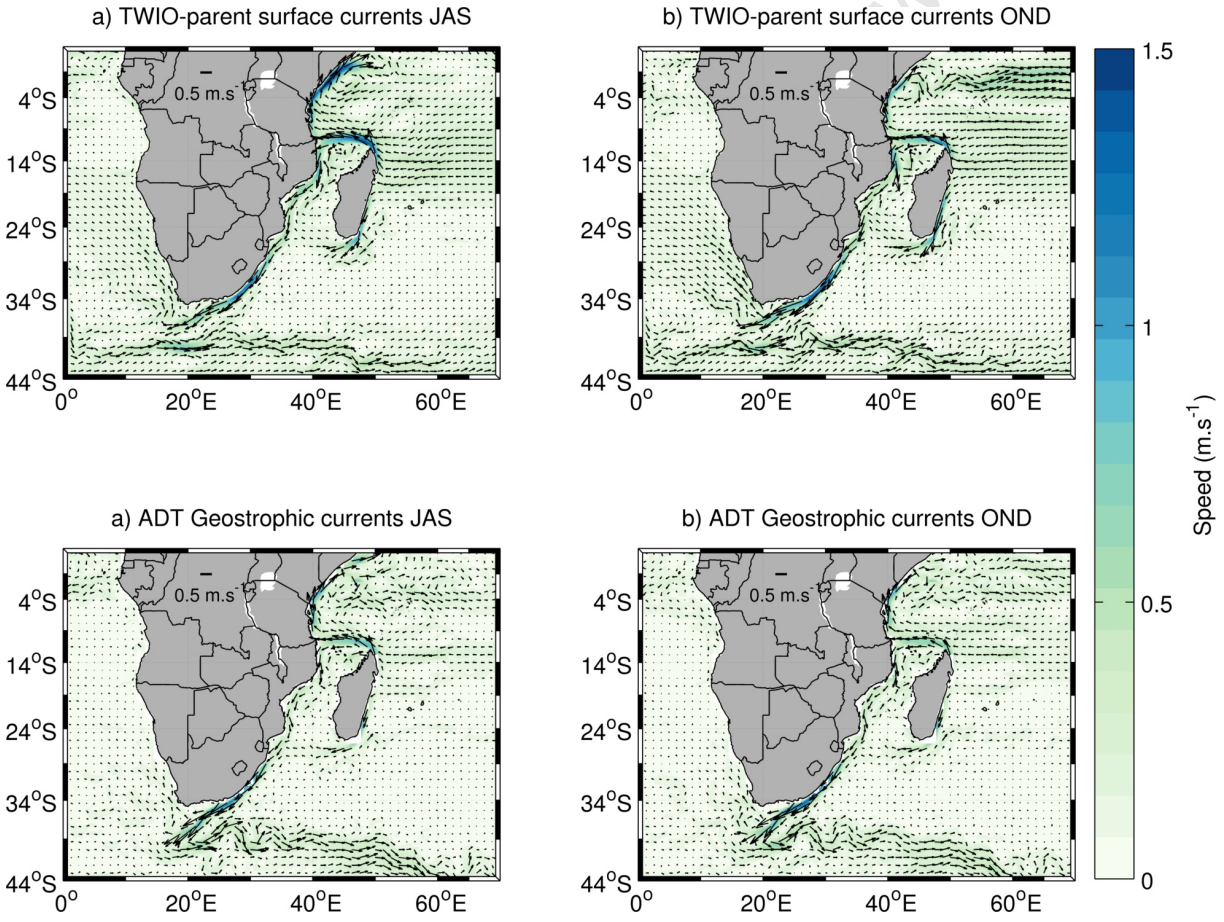

Figure B.5: *Mean surface velocities from TWIO-parent (a-b) and the seasonal mean surface geostrophic velocities from AVISO (c-d) for winter (JAS) and spring (OND).*

Consistent with the findings of Siedler et al. (2009), the SEMC as resolved in TWIO-parent displays two branches, one flowing westward into the Agulhas Current and the other retroflecting to connect with the subtropical Indian Counter Current to the east of Madagascar (Figures B.4 and B.5). While the westward flowing branch of the SEMC is clearly discernible in the annual mean surface geostrophic velocities, the retroflection of the second branch is less pronounced.

Vertical structure of the Agulhas Current

The vertical structure of the AC in TWIO at 32°S along the section 28-32°E displays a high degree of verisimilitude to the vertical structure inferred from LADCP data presented by Beal and Bryden (1999). The vertical structure of meridional velocity at 32°S reveals that TWIO reproduces a strong poleward flowing boundary current with velocities in the range 0.1-0.8m·s^{-1} (Figure B.6). In TWIO-parent, the surface core of the AC, located ~30km offshore, is about 10km further offshore compared to the findings of Beal and Bryden (1999). The AC in TWIO-parent has a width of 88km between the 0.5m·s^{-1} isotachs which is consistent with the 90km width reported by Beal and Bryden (1999).

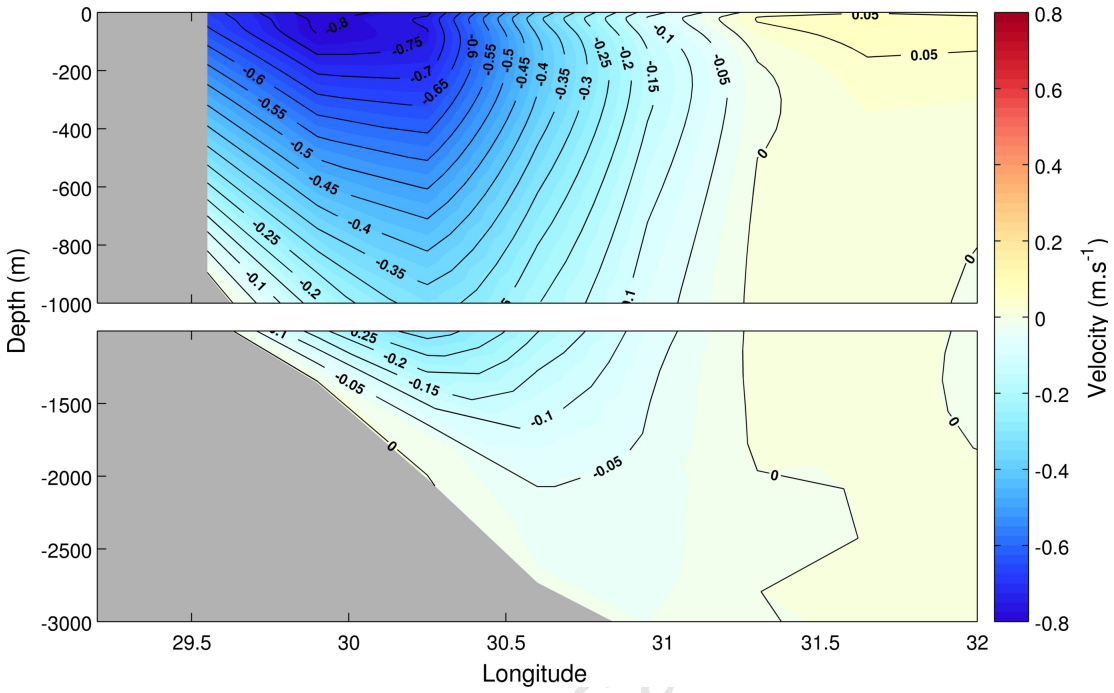

Figure B.6: *Vertical profile of the annual mean meridional velocity ($m{\cdot}s^{-1}$) along a zonal section through the Agulhas Current (AC) in TWIO-parent. The contour interval is 0.05$m{\cdot}s^{-1}$. Negative (positive) values indicate southward (northward) flow.*

Meso-scale variability

Mean Eddy Kinetic Energy

The annual mean eddy kinetic energy (EKE) calculated for TWIO-parent and for satellite altimeter data are shown in Figure B.7. While the broad patterns are similar, the model seems to overestimate (underestimate) the EKE in the Mozambique Channel and Somali Current (Agulhas Retroflection region and Agulhas Return Current). In both TWIO-parent and the

altimeter data, high energies (>500cm^2·s^{-2}) are associated with the flow in the Mozambique Channel, the Agulhas Retroflection Region and the Agulhas Return Current. The area of high energy (>2000cm^2·s^{-2}) along the coast of Somalia in TWIO-parent is completely absent in the altimeter derived EKE.

The altimeter data indicates that the Agulhas Retroflection Region is the most energetic region, with eddy kinetic energy in excess of 2400cm^2·s^{-2}. This energy appears to dissipate eastwards along the trajectory of the Agulhas Return Current. In AVISO, the EKE in excess of 1000cm^2·s^{-2} and 2000cm^2·s^{-2} associated with the Agulhas Current and the Agulhas Return Current, respectively, are in good agreement with the EKE values reported by Shum et al. (1990) and Thoppil et al. (2011). Furthermore, the EKE values of the Agulhas Current are also comparable with the EKE values associated with other western boundary currents (e.g. Gulf Stream (Brachet et al., 2004) and Kurishio Current (Shum et al., 1990)). In TWIO-parent, the EKE associated with the Agulhas Retroflection Region and the Agulhas Return Current are underestimated by 30-40% in comparison to the altimeter derived EKE. Along the east coast of South Africa the Agulhas Current does not display high variability as it is mostly stable where the shelf is narrow.

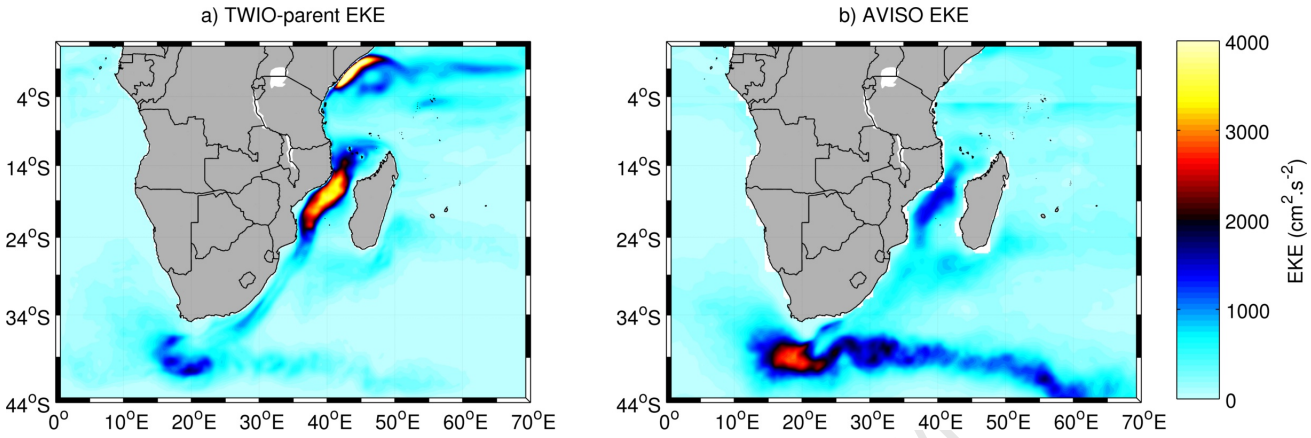

Figure B.7: *Annual mean eddy kinetic energy (EKE) derived from a) the 7-year TWIO-parent climatology run and b) satellite altimetry data for the period 1993 to 2011.*

Sea Level Anomalies

The SSH variability derived from TWIO-parent is in relatively good agreement with that calculated for altimeter derived SSH. Similar to the pattern of EKE, enhanced variability (>20cm) is associated with the flow in the Mozambique Channel, the Agulhas Current, the Agulhas Retroflection Region and the Agulhas Return Current (Figure B.8). These areas of high SSH variability are consistent with those noted by de Ruijter et al. (2005), Schouten et al. (2002a) and Swart et al. (2010).

The variability associated with the flow in the Mozambique Channel and the Agulhas Current is slightly higher in TWIO-parent compared to AVISO. On the other hand, the variability associated with the Agulhas Return Current and the Agulhas Retroflection is higher in AVISO than in TWIO-parent. In TWIO-parent, the variability associated with the Agulhas Current appears as a narrow continuous band that follows the shelf edge of southeast Africa whereas in AVISO, the variability along the east coast of southern Africa has a broader

distribution but with a core of high variability similar to that of TWIO-parent.

Two zonal bands of relatively high sea-surface height variability, centred at ~12° and 24°S respectively, stretch east of Madagascar across the Indian Ocean (de Ruijter et al., 2005). The southern band can clearly be distinguished in the altimeter data as a band of high variability (>10cm) that rounds the southern tip of Madagascar to merge with the variability associated with the Agulhas Current. In TWIO, the southern band of SSH variability is less apparent and appears as a band of low variability (<10cm) with increased variability towards the coast of Madagascar and around the southern tip.

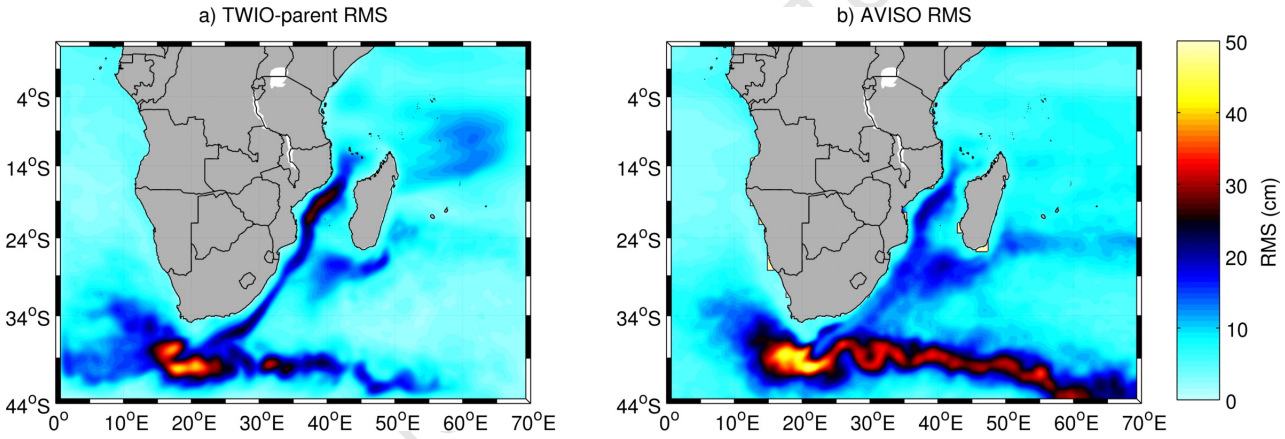

Figure B.8: *Annual mean sea surface height variability (RMS) determined from a) TWIO-parent and b) altimeter data.*

Conclusion

The comparison of TWIO-parent with observational and satellite data indicate that, despite some differences, the model reproduces the salient features of the western Indian Ocean with reasonable accuracy. Therefore the parent domain (TWIO-parent) was considered suitable for two-way nesting of a higher resolution child domain.

Appendix C

Snap-shots of velocity field

Similar to the weekly surface geostrophic velocities shown in Figure C.1, Figures C.2 and C.3 indicate that in TWIO and AG01 the flow in the Mozambique Channel is simulated as a number of meso-scale eddies which propagate southward along the eastern boundary of the channel. This is consistent with previous observational studies (de Ruijter et al., 2002; Ridderinkhof and de Ruijter, 2003).

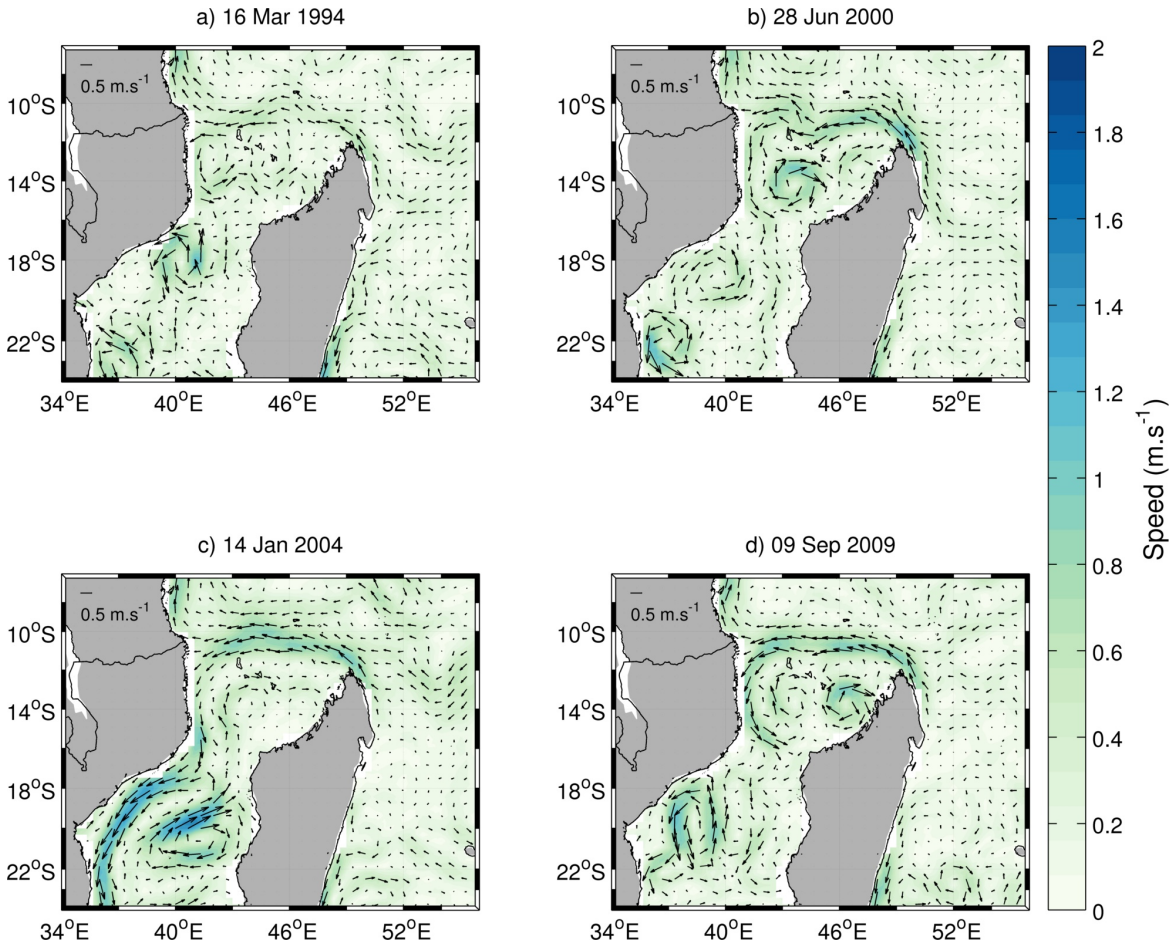

Figure C.1: *Snap-shots of the velocity field of AVISO.*

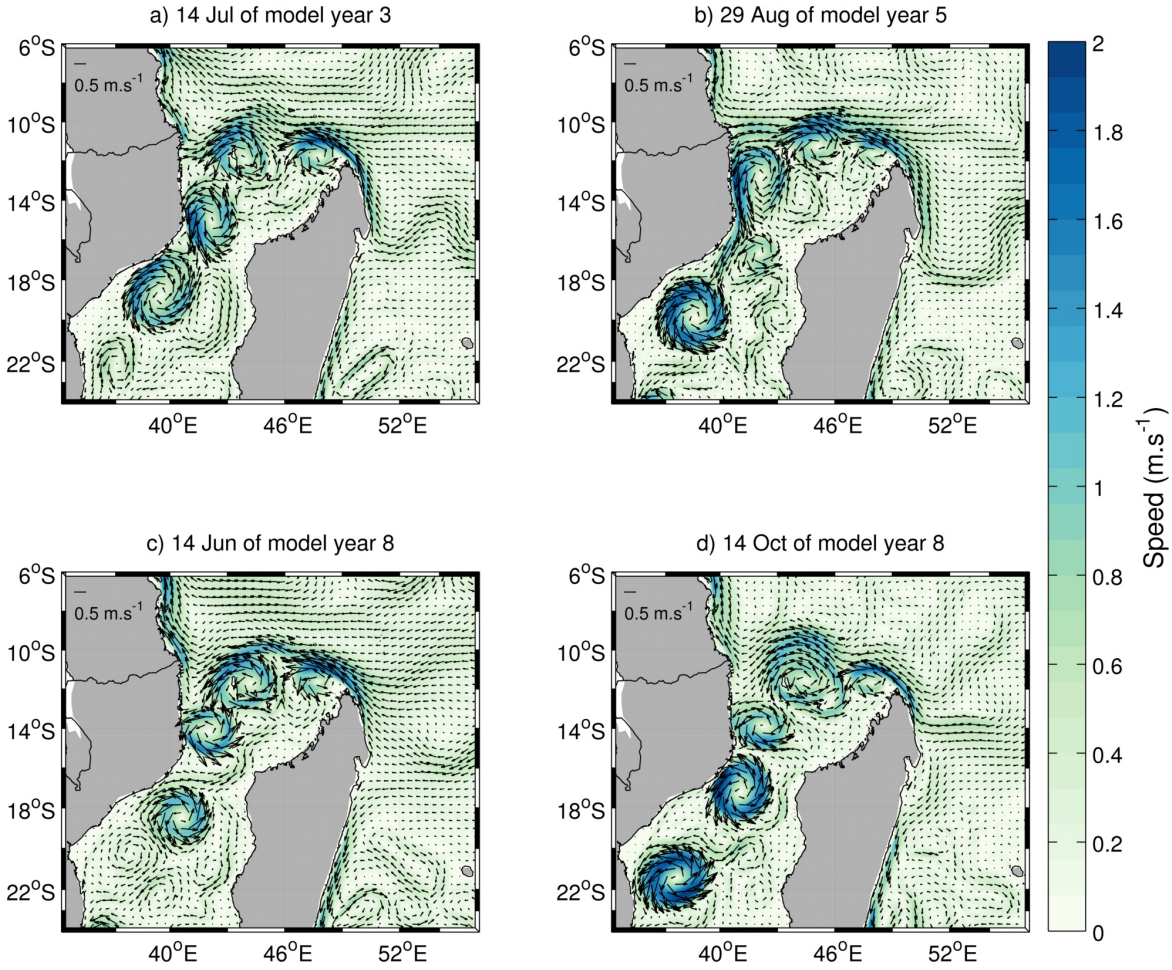

Figure C.2: *Snap-shots of the velocity field of TWIO.*

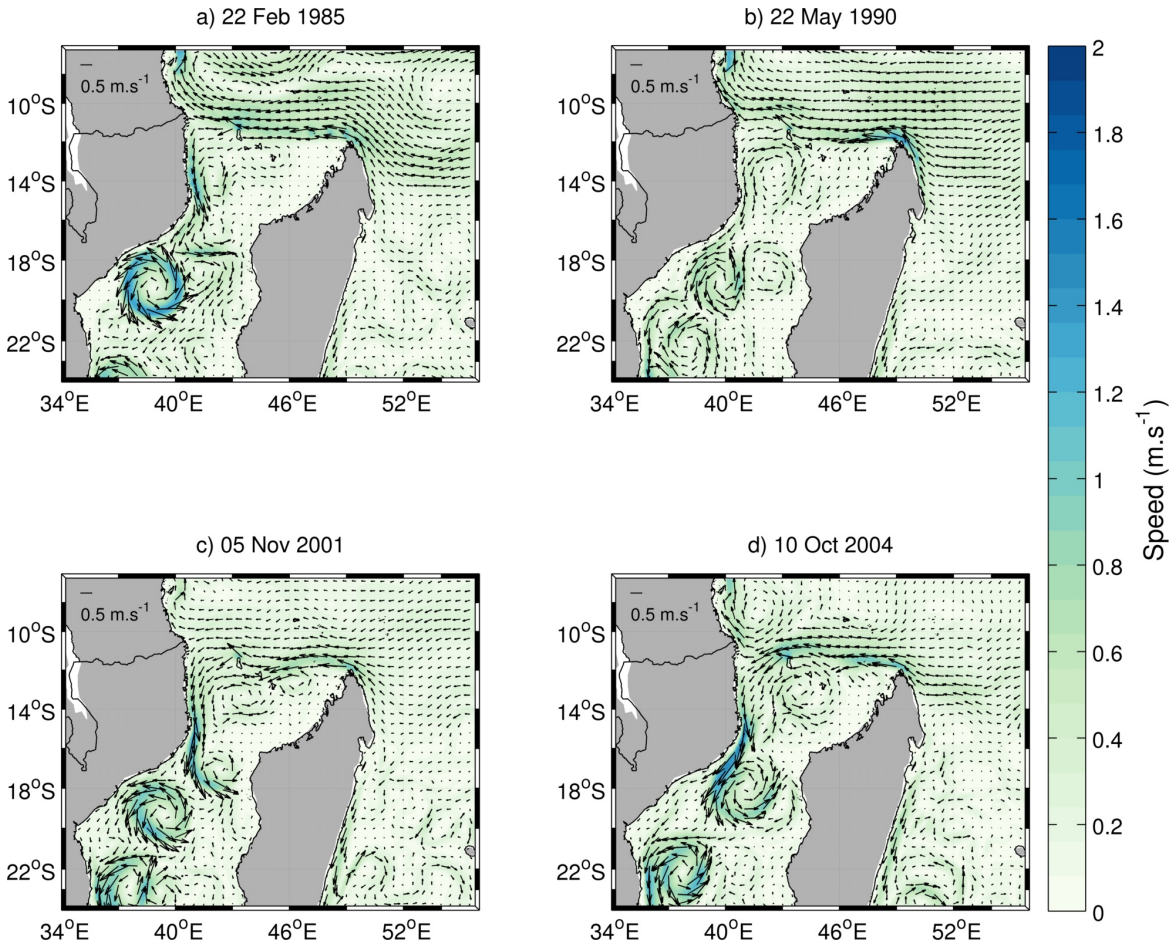

Figure C.3: *Snap-shots of the velocity field of AG01.*

Appendix D

Comparison of Levitus SST and TMI SST

Figure D.1 indicates that, compared to satellite derived SSTs, the Levitus World Ocean Atlas, which is used in AG01 as initial and boundary conditions, underestimates the SST of the Mozambique Channel and surrounds.

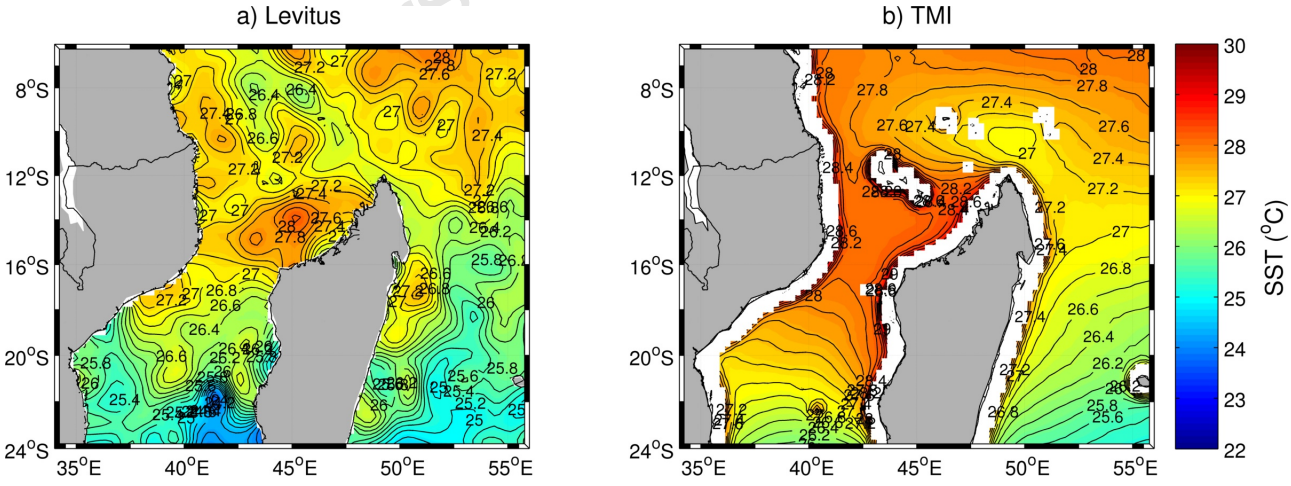

Figure D.1: *Annual mean SSTs (°C) for a) Levitus World Ocean Atlas and b) TMI. The contour interval is 0.2°C.*